High speed mask-less laser-controlled precision micro-additive manufacture

Jyi Sheuan Ten

Hughes Hall

University of Cambridge

This dissertation is submitted for the degree of

Doctor of Philosophy

September 2018

High speed mask-less laser-controlled precision micro-additive manufacture

Jyi Sheuan Ten

Abstract

A rapid, mask-less deposition technique for writing metal tracks has been developed. The technique was based on laser-induced chemical vapour deposition. The novelty in the technique was the usage of pulsed ultrafast lasers instead of continuous wave lasers in pyrolytic dissociation of the chemical precursor. The motivation of the study was that (1) ultrafast laser pulses have smaller heat affected zones thus the deposition resolution would be higher, (2) the ultrashort pulses are absorbed in most materials (including those transparent to the continuous wave light at the same wavelength) thus the deposition would be compatible with a large range of materials, and (3) the development of higher frequency repetition rate ultrafast lasers would enable higher deposition rates.

A deposition system was set-up for the study to investigate the ultrafast laser deposition of tungsten from tungsten hexacarbonyl chemical vapour precursors. A 405 nm laser diode was used for continuous wave deposition experiments that were optimized to achieve the lowest track resistivity. These results were used for comparison with the ultrafast laser track deposition. The usage of the 405 nm laser diode was itself novel and beneficial due to the low capital and running cost, high wall plug efficiency, high device lifetime, and shallower optical penetration depth in silicon substrates compared to green argon ion lasers which were commonly used by other investigators.

The lowest as-deposited track resistivity achieved in the continuous wave laser experiments on silicon dioxide coated silicon was 93±27 μΩ cm (16.6 times bulk tungsten resistivity). This deposition was done with a laser output power of 350 mW, scan speed of 10 μm/s, deposition pressure of 0.5 mBar, substrate temperature of 100 °C and laser spot size of approximately 7 μm. The laser power, scan speed, deposition pressure and substrate temperature were all optimized in this study. By annealing the deposited track with hydrogen at 650 °C for 30 mins, removal of the deposition outside the laser spot was achieved and the overall track resistivity dropped to 66±7 μΩ cm (11.7 times bulk tungsten resistivity).

For ultrafast laser deposition of tungsten, spot dwell experiments showed that a thin film of tungsten was first deposited followed by quasi-periodic structures perpendicular to the linear polarization of the laser beam. The wavelength of the periodic structures was approximately half the laser wavelength ($\lambda/2$) and was thought to be formed due to interference between the incident laser and scattered surface waves similar to that in laser-induced surface periodic structures. Deposition of the quasi-periodic structures

was possible on stainless steel, silicon dioxide coated silicon wafers, borosilicate glass and polyimide films.

The thin-films were deposited when the laser was scanned at higher laser speeds such that the number of pulses per spot was lower ($\eta \leq 11{,}000$) and using a larger focal spot diameter of 33 μm. The lowest track resistivity for the thin-film tracks on silicon dioxide coated silicon wafers was 37±4 μΩ cm (6.7 times bulk tungsten resistivity). This value was achieved without post-deposition annealing and was lower than the annealed track deposited using the continuous wave laser.

The ultrafast tungsten thin-film direct write technique was tested for writing metal contacts to single layer graphene on silicon dioxide coated silicon substrates. Without the precursor, the exposure of the graphene to the laser at the deposition parameters damaged the graphene without removing it. This was evidenced by the increase in the Raman D peak of the exposed graphene compared to pristine. The damage threshold was estimated to be 53±7 mJ/cm^2 for a scanning speed of 500 μm/s. The deposition threshold of thin-film tungsten on graphene at that speed was lower at 38±8 mJ/cm^2. However, no graphene was found when the deposited thin-film tungsten was dissolved in 30 wt% H_2O_2 that was tested to have no effect on the graphene for the dissolution time of one hour. The graphene likely reacted with the deposited tungsten to form tungsten carbide which was reported to dissolve in H_2O_2. Tungsten carbide was also found on the tungsten tracks deposited on reduced graphene oxide samples. The contact resistance between tungsten and graphene was measured by both transfer length and four-point probe method with an average value of 4.3±0.4 kΩ μm. This value was higher than reported values using noble metals such as palladium (2.8±0.4 kΩ μm), but lower than reported values using other metals that creates carbides such as nickel (9.3±1.0 kΩ μm).

This study opened many potential paths for future work. The main issue to address in the tungsten ultrafast deposition was the deposition outside the laser spot. This prevented uniform deposition in successive tracks close to one another. The ultrafast deposition technique also needs verification using other precursors to understand the precursor requirements for this process. An interesting future study would be a combination with a sulphur source for the direct write of tungsten disulphide, a transition metal dichalcogenide that has a two-dimensional structure similar to graphene. This material has a bandgap and is sought after for applications in high-end electronics, spintronics, optoelectronics, energy harvesting, flexible electronics, DNA sequencing and personalized medicine. Initial tests using sulphur micro-flakes on silicon and stainless-steel substrates exposed to the tungsten precursor and ultrafast laser pulses produced multilayer tungsten disulphide as verified in Raman measurements.

Declaration

This dissertation is the result of my own work and includes nothing which is the outcome of work done in collaboration. It is not substantially the same as any that I have submitted, or, is being concurrently submitted for a degree or diploma or other qualification at the University of Cambridge or any other University or similar institution. I further state that no substantial part of my dissertation has already been submitted, or, is being concurrently submitted for any such degree, diploma or other qualification at the University of Cambridge or any other University or similar institution. It does not exceed the prescribed 65,000 words and 150 figures of the Engineering Degree Committee.

Jyi Sheuan Ten

September 2018

Acknowledgements

I would like to take this opportunity to thank the people who without their help this journey would not have been completed.

I would like to thank Prof William O'Neill, my supervisor, for his grand experiment suggestions especially the encouragement to experiment with the ultrafast lasers for the LCVD experiments. I would like to thank Dr Martin Sparkes, my supervisor, for his creative cost effective technical advice and thorough analysis of my writings. I would like to thank Dr Krste Pangovski for his insights into ultrafast laser interaction and inspiration for my temperature model.

I would like to thank Sophie Fuller, the group administrator, who helped me smoothen this journey by handling all the necessary administrative work. I would like to thank Dr Richard Langford and Dr Ronan Daly for their expertise in using the FIB/SEM machines that this work heavily depended on.

I would like to thank Franco Ussi who always had time for me to tinker and conjure up solutions to the technical challenges in my experiments, and to teach me the Italian language and culture. I would like thank Dr Andrew Cockburn, Dr Andrew Payne, Francisco Orozco, Dr Wenhe Feng, Dr David Hopkinson, Dr Karen Yu, Dr Jiho Han, Jonathan Parkins, Tianqi Dong, Laurant Michaux, and Nicky Sloane who joined the research group before me and gave me valuable advice regarding my PhD journey and how best to work with my supervisors. I would like to thank Dr Clare Collins, Yoanna Shams, Sam Brown, Chris Wright, Matt Pryn and George Meakin, my cohort peers with whom I started this journey together, for their companionship in this journey.

I would like to thank Dr Davor Copic, Dr Philipp Braeuninger-Weimer, Hadi Moderas and Sarah Jessl from other research groups who I have depended on for experiment advice and materials.

I would like to thank Daniel Gortat, Alex Diaz, Diego Punin, Nadeem Gabbani and Katjana Lange, who started their PhD journey after me, for the opportunity to reflect on my own journey and advise them.

A large gratitude is owed to Sally Yu, my dearest partner. Thank you for all your love, support, and cherished moments in this journey. To you I dedicate this thesis.

I would also like to thank my other family members and those that I have forgot to mention here.

Table of contents

List of figures

List of tables

Nomenclature and abbreviations

A	=	Area
B	=	Arrhenius equation constant
C	=	Heat capacity
D	=	Raw beam diameter
E	=	Energy
F	=	Laser fluence
I	=	Laser intensity
M^2	=	Laser beam quality factor
P	=	Power
R	=	Resistance
$\mathbb{R}$	=	Reflectance
$\mathfrak{R}$	=	Gas constant
T	=	Temperature
c	=	Y-intercept
d	=	Thermal diffusivity
f	=	Frequency
h	=	Height
k	=	Thermal conductivity
l	=	Length
m	=	Gradient
n	=	Refractive index
$\dot{q}$	=	Heat flow rate
r	=	Radius, radial coordinate
t	=	Time
u	=	Uncertainty
v	=	Velocity
w	=	$1/e^2$ laser beam radius
x, y, z	=	Cartesian coordinates
α	=	Absorption coefficient, reciprocal of the optical penetration depth
γ	=	Energy exchange rate
η	=	Number of pulses
θ	=	Time advancing constant in finite volume discretization
λ	=	Wavelength
ρ	=	Resistivity
ϱ	=	Density

AFM	Atomic force microscopy
AR	Anti-reflection
CAD	Computer aided design
CV	Control volume
CVD	Chemical vapour deposition
CW	Continuous wave
EDX	Energy dispersive X-ray spectroscope
FIB	Focused ion beam
HAZ	Heat affected zone
HSFL	High spatial frequency laser-induced periodic surface structures
IR	Infrared
LCVD	Laser-induced chemical vapour deposition
LIPSS	Laser-induced periodic surface structures
LSFL	Low spatial frequency laser-induced periodic surface structures
NA	Numerical aperture
PVD	Physical vapour deposition
SEM	Scanning electron microscope
SS	Stainless steel
TLM	Transfer length method, transmission line method
TMD	Transition metal dichalcogenides
TSV	Through silicon via
UV	Ultra-violet
WLI	White light interferometry
3DCI	Three-dimensional circuit integration

Chapter 1 Introduction

One of the key future characteristics of manufacturing highlighted by Innovate UK in their 2013 Future of Manufacturing report (Foresight, 2013) is that manufacturing will be faster, more responsive and closer to customers. The main drivers of this change are advancements in technologies that are transforming manufacturing such as additive manufacturing (AM), robotics, sensors, big data, and machine learning. Developments in these technologies are predicted to enable mass personalization of low-cost products, on demand, by reducing the cost gap between cheap mass-produced products and more expensive customised products.

The current resolution of metal laser powder bed melting AM technology is approximately 0.2 mm (Roland Berger Strategy Consultants, 2013). For micro-fabrication, there are other AM technologies. Focused ion beam (FIB) and electron beam (EB) deposition are AM techniques capable of depositing metals, ceramics and insulators with feature sizes as small as 50 nm (Yao, 2007a) without masks. An electron and ion beam are focused and passed through apertures to create a spot which is scanned across the surface of the sample. By injecting a precursor gas via a needle to the focused spot (Figure 1), the collisions between the beam and the molecules of that gas will dissociate the gas molecules and impart some kinetic energy to them. Some of these energetic atoms will then impact the surface and are deposited. FIB and EB deposition are used for building prototypes of nano-devices, testing material properties, and repair works for circuits and photo-lithography masks. Even though FIB and EB deposition is capable of creating small features, the deposition rate is very low at 0.001 $\mu m^3/s$ (Morita et al., 2003).

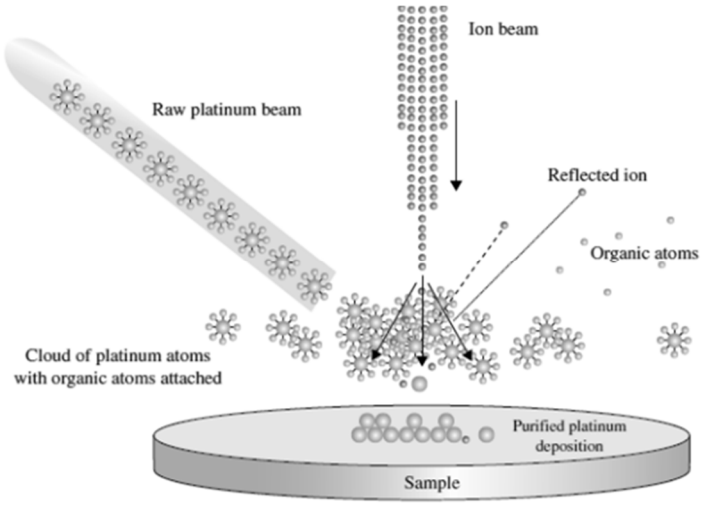

Figure 1: Schematic showing the deposition of platinum using a FIB from platinum atoms with organic ligands attached (Yao, 2007b).

Figure 2 shows the capabilities, in terms of resolution and build rate, of various micro-additive manufacturing technologies. Macro AM technologies such as laser powder bed melting are capable of

achieving high build rates of up to 10^{12} $\mu m^3/s$, however the resolution is limited to approximately 200 µm (Roland Berger Strategy Consultants, 2013). FIB and EB deposition technique can achieve a resolution of 0.05 µm, however the deposition rate is limited to approximately 1 $\mu m^3/s$. Instead of using ion and electron beams, a laser can be used cause the dissociation of the precursor and this technique is known as laser-induced chemical vapour deposition (LCVD). The resolution in LCVD is that of the focused laser beam size at 1-100 µm and the build rate achieved is approximately 1000 $\mu m^3/s$ (Duty et al., 2001) thus providing an alternative to FIB and EB deposition when the required resolution is at the order of 10 µm.

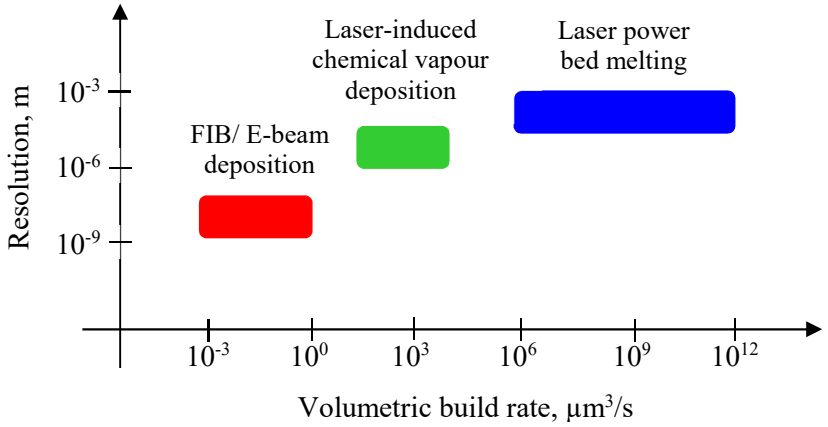

Figure 2: Graph of volumetric deposition rate against deposition resolution of various direct write additive manufacturing technologies (Roland Berger Strategy Consultants, 2013) (Duty et al., 2001) (Yao, 2007a).

1.1 Motivations for investigating ultrafast LCVD

Ultrafast laser pulses (<10 ps) are preferred for micromachining because the short intense pulse limits the energy within the optical penetration depth. Thus, the heat affected zones (HAZ) on the substrates are smaller than when longer pulse laser beams are used. Figure 3 illustrates the difference in using long and ultrafast laser pulses for micro-machining. The short intense pulse also encourages absorption in a wide range of materials such that numerous materials can be processed. Gattass and Mazur, 2008 and Rizvi, 2003, for example, demonstrated the capability of producing neat trenches on metals, glass, diamond and polymers.

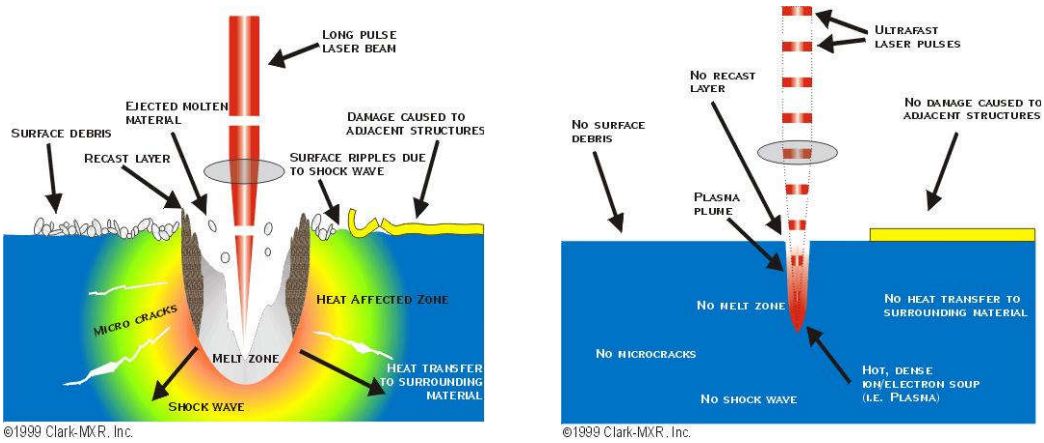

Figure 3: (Left) Illustration of machining with a conventional laser which caused numerous undesired defects. (Right) Illustration showing the much neater tracks made using an ultrafast laser (Bado et al., 2011).

Ultrafast laser pulses have not been thoroughly explored for usage in LCVD. Investigators have explored the usage of short wavelength ultrafast pulses for direct dissociation of the chemical precursor. Haight et al., 2003, Hitosugi and Mizuno, 2005 and Zhang et al., 2007 explored the usage of 400 nm 120 fs laser pulses for the deposition of chromium and tungsten. Due to the nature of the dissociation, a high intensity (>10^{12} W/cm^2) was required to achieve deposition. This high intensity limited the substrates to materials with high ablation threshold such as sapphire. Investigators have not explored the usage of ultrafast pulses for pyrolytic thermal dissociation of the precursor.

The thermal dissociation of chemical vapour precursors using ultrafast laser pulses is fundamentally possible because the temperature damage threshold of the substrate (melting point) at the order of 1500 ºC (metals, silicon, glass) is higher than the dissociation temperatures of most precursors at below 500 ºC (Lai and Lamb, 2000). The repetition rates now offered in commercially available high-power ultrafast laser systems are in the order of 1 MHz while custom built research systems are in the order of 1 GHz (Kerse et al., 2016). Chemical reactions can occur in timescales smaller than 10^{-12} s (Potter et al., 1992) thus the pulse repetition rate should be kept as high as possible to achieve a high deposition rate. Due to the high temperatures achieved in the ultrafast pulse, the deposition favours precursors with moderately high dissociation temperatures. Precursors with high deposition rates are preferred due to the short heating time during and after the ultrafast laser pulse. If deposition is possible through ultrafast laser thermal dissociation, the heating of the substrate would be minimized and the process should be compatible with a wide range of materials.

1.2 Research questions and objectives of study

The motivation of investigating ultrafast LCVD led to the following research questions.

- Can ultrafast laser pulses cause thermal dissociation of chemical vapour precursors for deposition?
- If yes, how does the ultrafast laser pulse parameters and chemical vapour precursor affect the deposition and how does the deposition compare with continuous wave (CW) deposition?

- What are the strengths and weaknesses of the process, and what are the applications of this novel process?

To answer the research questions mentioned, the objectives of this body of work has been distilled into the following:

- Objective 1: Design, build and test the LCVD system required for ultrafast laser deposition.

  At the start of the study, there was no pre-existing LCVD system available for use and there were no commercially available LCVD systems, a new deposition system was needed to be designed and built before work on ultrafast laser deposition was done. The optimisation and tests of this built deposition system will involve CW laser deposition to establish a comparison case for the ultrafast laser deposition results.

- Objective 2: Conduct the ultrafast LCVD experiments and characterise the deposition results.

  Once the system has been optimized using the CW laser, the investigation would continue with ultrafast laser experiments. The aim would be to characterise the deposition results and capabilities with the intention of identifying and exploring potential applications of this novel LCVD deposition regime.

1.3 Publications

This body of work led to the following publications.

Journals

- Ten, J. S., Sparkes M. S. & O'Neill, W. (2018). Femtosecond Laser-induced Chemical Vapor Deposition of Tungsten Quasi-periodic Structures on Silicon Substrates. *Journal of Laser Applications 30, p032606.*

Conferences

- Ten, J. S., Sparkes M. S. & O'Neill, W. (2017). Femtosecond Laser-induced Chemical Vapor Deposition of Tungsten Quasi-periodic Structures on Silicon Substrates. In *Proceedings of the The 36th International Congress on Applications of Lasers & Electro-Optics (ICALEO 2017).*
- Ten, J. S., Sparkes M. S. & O'Neill, W. (2017). Effects of process temperature in the high speed, mask-less, precision laser deposition of micro-tungsten tracks on silicon, copper and stainless-steel. In *Proceedings of the 17th International Conference of the EUSPEN.*

- Ten, J. S., Sparkes M. S. & O'Neill, W. (2017). High speed, mask-less, laser controlled deposition of microscale tungsten tracks using 405 nm wavelength diode laser. In *Proc. SPIE 10091, Laser Applications in Microelectronic and Optoelectronic Manufacturing (LAMOM) XXII.*
- Ten, J. S., Sparkes M. S. & O'Neill, W. (2016). High speed mask-less laser controlled precision deposition of metals. In *Proceedings of the 16th International Conference of the EUSPEN.*

The following journal papers are in preparation.

- Ten, J. S., Sparkes M. S. & O'Neill, W. High Speed Mask-less Femtosecond Laser-induced Chemical Vapor Deposition of Tungsten Thin Films on SiO2/Si Graphene.
- Ten, J. S., Sparkes M. S. & O'Neill, W. Femtosecond Laser-induced Chemical Vapor Deposition of Tungsten on Transparent Substrates.
- Ten, J. S., Sparkes M. S. & O'Neill, W. Direct Write of Three-dimensional Tungsten Structures via Femtosecond Laser-induced Chemical Vapor Deposition.

Chapter 2 Review of literature

To understand the LCVD process, one must consider the precursors and lasers along with their respective delivery methods to reach the substrate where the dissociation occurs.

2.1 Dissociation mechanisms in LCVD

LCVD uses a laser beam to generate solid deposits from vapour reactants by inducing chemical reactions. The LCVD processes can be divided based on the dissociation mechanism which is either pyrolytic or photolytic.

2.1.1 Pyrolytic dissociation

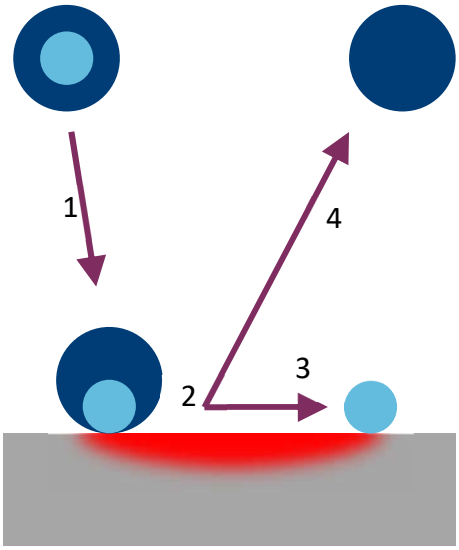

Figure 4: Illustration of the pyrolytic LCVD process showing the adsorption of precursor (1), dissociation due to laser heat (2), growth of film (3) and desorption of by-products (4).

Pyrolytic LCVD is derived from the traditional CVD process. In a CVD process the entire substrate is heated to the deposition temperature and deposition occurs on the whole substrate. Pyrolytic LCVD uses a laser to locally heat the surface of the substrate and cause localised deposition. Figure 4 shows an illustration of the pyrolytic LCVD mechanism. In the vacuum, the reactive deposition molecules first adsorb onto the surface of the substrate. Here the heat from the laser dissociates the adsorbed molecules into deposition particles and volatile by-products. The deposition particles will diffuse to nucleation sites to grow into thin films while the volatile by-products will desorb. The earliest works on pyrolytic LCVD include that of Allen, 1981 (Center of Laser Studies, University of Southern California) focusing on depositing nickel metal and titanium compounds, Baum and Jones, 1985 and Houle et al., 1985 (IBM Research Laboratory, San Jose) focusing on deposition of gold and copper, Han and Jensen, 1994

(Department of Chemical Engineering, Massachusetts Institute of Technology) focusing on the modelling the writing process, and various others mentioned in the review of Duty et al., 2001 (School of Mechanical Engineering, Georgia Institute of Technology). Most of the investigators used either a CO_2 laser, an Nd:YAG or an argon ion laser in continuous mode for heating the substrate. To the knowledge of the author, no investigator has used laser diodes (section 2.3.1) for pyrolytic LCVD. Laser diodes for pyrolytic LCVD are explored in this study in Chapter 4. Pulsed laser operation, especially in the nanosecond and ultrafast regimes, reduces the size of the heat affected zone (O'Neill and Li, 2009). However, to the knowledge of the author, no investigators have looked at using ultrafast lasers for pyrolytic LCVD. The case for using ultrafast lasers for pyrolytic LCVD is explored in section 2.1.4.

2.1.2 Photolytic dissociation

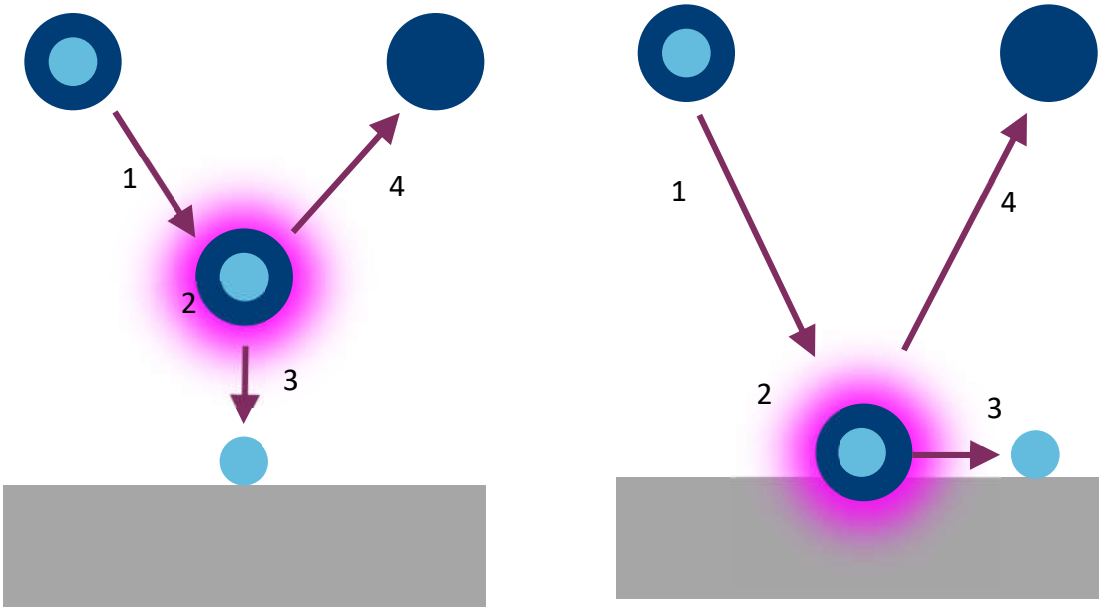

Figure 5: Illustration of the laser deposition mechanism via photolysis: (1) the precursor diffuses to a site above (left) or adsorbs on the surface (right), (2) the photons cleave the ligands of the molecule, (3) particles are deposited, and (4) the volatile by-products remain in vacuum (left) or desorb from the substrate (right).

For photolytic LCVD, energetic photons from the laser beam directly cleaves the precursor molecule (Duty et al., 2001). Most bond energies in molecules used as precursors have an energy of 2-6 eV (207-620 nm) (Jackson et al., 1989). Figure 5 shows an illustration of the laser deposition via photolysis where the precursor molecule is dissociated by photons from the laser to yield deposition particles and volatile by-products. The dissociation can either occur in the gas phase (Figure 5 left) or on the surface of the substrate (Figure 5 right). The earliest reported investigation known to the author that used this mechanism was that of Deutsch et al., 1979. The work was built upon by Ehrlich and Tsao, 1983 (Lincoln Laboratory, Massachusetts Institute of Technology), Jones et al., 1985 and Chen, 1987 (IBM Research Laboratories) and various others. Most of the investigators used frequency doubled argon ion lasers or excimer lasers in continuous mode. A few researchers have investigated the use of ultrafast lasers for multiphoton absorption to dissociate the precursor. Haight et al., 2003 and Zhang et al., 2007

deposited chromium and tungsten from carbonyl precursors using this technique, however no conductivity results of the deposits have been reported so far.

2.1.3 Comparison between pyrolytic and photolytic dissociation

A comparison between the pyrolytic and photolytic LCVD characteristics is listed in Table 1. In terms of deposition rate, pyrolytic LCVD typically has a higher deposition rate (Duty et al., 2001). This is due to the higher reaction temperature in pyrolytic LCVD that promotes a higher reaction rate. Ultraviolet (UV) excimer lasers can be focused to sub-micron radii to produce intense spots for higher dissociation rates, however the gas in the path of the laser may dissociate at such intensities. With regards to the feature size, photolytic LCVD is capable of producing smaller features. Sub-micron deposited widths are possible because the shorter wavelength of the UV laser can be focused down to a smaller diffraction limited spot. Features smaller than 2 μm have been reported for photolytic LCVD (Deutsch et al., 1979).

In terms of material dependence, pyrolytic LCVD is generally less dependent on precursor type while photolytic LCVD is less dependent on substrate material. Pyrolytic LCVD dissociates the precursor by heating the substrate. Thus, the deposition is more dependent on the substrate material properties. The substrate material needs to have low reflectivity and a low thermal diffusivity. A low light penetration depth is also needed for surface heating. For example, Han and Jensen, 1994 managed to heat up silicon and deposit copper but failed to deposit copper on silicon dioxide substrates, which was transparent at the wavelength used. Photolytic LCVD dissociates the precursor by direct photon absorption of the precursor thus it is less dependent on substrate material. Ehrlich et al., 1982 managed to use a 257 nm laser to deposit zinc on aluminium (absorbing at 257 nm) and silicon dioxide substrates (transparent) at the same laser power. However, since the absorption peaks of the precursor varies there is less flexibility in choosing the wavelength-precursor combination. In terms of the deposition quality, pyrolytic LCVD usually has lower deposition impurities and porosity. This is due to the higher process temperature which promotes desorption of the by-products and annealing of the deposits.

Table 1: Comparison of pyrolytic and photolytic LCVD characteristics.

	Pyrolytic LCVD	Photolytic LCVD
Deposition rate	Higher (~10-10,000 $\mu m^3/s$).	Lower (~1-1,000 $\mu m/s$).
Smallest feature size	~5 μm.	~1 μm.
Ideal substrate properties	Low reflectivity. Low thermal conductivity. Shallow light penetration depth. High thermal damage threshold.	High UV intensity damage threshold.
Precursor dependency	Absorption coefficients may affect deposition rate.	Precursor absorption peaks may have narrow wavelength bands.
Deposition quality	Less impurities. Less porous.	More impurities. More porous.

2.1.4 Effect of surfaces and catalysts

The dissociation of metal organic precursors are surface dependent (Luo and Gladfelter, 2008a). Metal surfaces are good catalysts for organic reactions thus a reduction in the activation energy for the deposition process and selective deposition on metallic surfaces are expected. On non-metallic surfaces, higher activation energies are often required for the nucleation events thus the initial growth rates are slower than steady state deposition. In addition, the probability of diffusing to an existing nucleus is higher than the formation of new nuclei on non-metallic surfaces. This results in large grain microstructures and rough films during metal organic deposition on non-metallic surfaces.

Metals, such as palladium, are active hydrogenation catalyst, thus residual carbon in the dissociation of metal organic precursors may be removed with the addition of hydrogen (Zinn et al., 1994a). Besides that, a variety of metal catalyst have been shown to promote the decomposition of host metal alkyls, these include $TiCl_4$, TiH_2, $CrCl_3$, VCl_4 and $NbCl_5$ (Simmonds and Gladfelter, 1994).

2.1.5 Unexplored dissociation regimes

A dissociation regime that has not been explored by investigators is the laser-induced plasma dissociation. In plasma enhanced chemical vapour deposition, plasmas are used to dissociate the precursor over the entire substrate (Alexandrov and Hitchman, 2008). Based on investigations by Thiyagarajan and Thompson, 2012, a 1064 nm laser at intensities of 2.5×10^{11} W/cm^2 breaks down dry air at atmospheric pressure; 6×10^{11} W/cm^2 at 100 mBar pressure; and around 3×10^{12} W/cm^2 at 10 mBar pressure. These energy levels are potentially achievable using ultrafast lasers. To the knowledge of the author, no investigator has explored using laser-induced plasmas dissociation of chemical precursors for spatially controlled deposition.

Another unexplored technique is laser-induced atomic layer deposition. Atomic layer deposition (ALD) or epitaxy is used to deposit a layer of material with precise control of the layer thickness (typically one atomic layer) over the whole substrate. Olander et al., 2005 explored using a laser to assist the ALD process over the whole substrate. However, to the knowledge of the author, no investigator has yet to attempt localized laser-induced ALD.

Pulsed ultrafast lasers have not been explored for pyrolytic LCVD and here, a few encouraging factors are considered. Recent advances in ultrafast chemistry imaging has revealed that dissociation reaction occurs at timescale of 100 fs (Zewail, 2000), which is the same order of magnitude as the ultrafast pulse duration. Secondly using ultrafast pulses, the total heat input to the substrate is lower thus the HAZ is smaller. This will lead to improvements in the deposition resolution and less damage to the substrate. Another encouraging reason is that there is a trend towards higher repetition rates for high power ultrafast systems. For example, there is the gigahertz system developed and used by Kerse et al., 2016 for work in ablation cooling. If thermal LCVD works with ultrafast lasers, higher repetition rates will likely lead to higher deposition rates. Pulsed ultrafast lasers for pyrolytic LCVD is the focus of this body of work.

2.2 Precursors and deposited materials in LCVD

The precursors are organic molecules that have the material to be deposited as one or more of the atoms attached to other ligands to stabilize the molecule. The required physical and chemical properties of the precursor are close to the required properties of CVD precursors. Thus, most of the precursors for the LCVD process are originally synthesized for CVD. The most important property of the precursor especially for pyrolytic LCVD is that the deposition temperature needs to be higher than the vaporisation temperature of the precursor. This is necessary to avoid dissociation of the precursor molecule before delivery to the substrate. Other desirable properties of the precursor include:

- High vapour pressure above sublimation/boiling temperature for high deposition rate.
- Clean dissociation above deposition temperature for high purity deposits.
- Stable and not reactive between sublimation/boiling temperature and deposition temperature to avoid degradation of molecule during transport to deposition site.

The ligands of the precursors include fluorides, chlorides, carbonyls and hydrocarbon groups. For the hydrocarbon ligands, the chain can be straight or branched and one or more branches maybe substituted with other chemical groups such as fluoro-methyls. The substitution in the synthesis of the chemical precursors are often done to achieve the desirable properties mentioned previously.

LCVD has been explored for the deposition of conductive tracks using polysilicon, nickel, copper, platinum, chromium, rhodium, tungsten, and gold (Duty et al., 2001). Most of the investigators used pyrolytic LCVD instead of photolytic LCVD for the deposition of conductors because the deposition purity was higher. Table 2 shows metals deposited and precursors used that have good resulting conductivities. Copper deposited from Cu(hfac)(tmvs) has low resistivity however the deposition rate was low. Aluminium and gold have good deposition conductivity and high deposition rate. The resistivity of the deposits from platinum and tungsten precursors were at least 10 μΩ cm.

Table 2: Best results of metal conductors deposited via pyrolytic LCVD from literature.

Metal and precursor	Properties of deposited metal	LCVD investigator	Deposition rate	Resistivity, μΩ cm
Aluminium from $Al(CH_3)_3$	Low resistance. Self-passivation by oxide formation.	Baum and Comita, 1992	50 μm/s scan. 11 μm wide. 0.7 μm thick. 385 μm^3/s volumetric rate.	3.1-7.8 (1.2-3 times bulk).
Copper from Cu(hfac)(tmvs)	High conductivity.	Han and Jensen, 1994	20 μm/s scan. <100 μm^3/s volumetric rate.	1.7-5.0 (1-3 times bulk).
Gold from $(CH_3)_2(C_5H_7O_2)$ Au	Chemical inertness. Good electrical conductivity.	Kodas et al., 1987	Stationary. 3 μm/s vertical growth rate. 100 μm diameter. 23,600 μm^3/s volumetric rate.	3.4-24 (1.4-10 times bulk).
Platinum from $C_{10}H_{14}O_4Pt$	Good elevated temperature and chemical stability. Limited diffusion into silicon.	Braichotte and van den Bergh, 1987	1-100 μm/s scan. 0.1-10 μm thickness. 10-50 μm width. 90-280 μm^3/s volumetric rate.	11-74 (1-7 times bulk).
Tungsten from $W(CO)_6$	Thermal and chemical stability. Ability to conduct high current densities.	Nambu et al., 1990	300 μm/s scan. 5-8 μm width. 0.1-0.4 μm thickness. 100-300 μm^3/s volumetric rate.	10-30 (1.8-5.4 times bulk).

Besides conductive metal tracks, LCVD has also been explored for the deposition of ceramics such as titanium carbide, titanium nitrite and silicon carbide (Duty et al., 2001); The investigators used pyrolytic LCVD and successfully deposited the ceramics below the high melting temperature of the deposits.

A few nano-materials has also been synthesized using both pyrolytic and photolytic LCVD. For pyrolytic LCVD, Longtin et al., 2007 selectively grew carbon nanotube forests on porous alumina substrates coated with nickel catalyst. Park et al., 2011 explored pyrolytic LCVD of graphene by scanning lines on nickel foils. Yeo et al., 2013 demonstrated the ability to locally grow zinc oxide nanowires on gold coated silicon substrates (Figure 6) via laser-induced hydrothermal growth, a modification to pyrolytic LCVD where the precursor was in the liquid phase and immersed the substrate. One advantage of LCVD for the synthesis of these nano-materials is the higher growth rate in the localized area. For example, graphene grown in a 10x10 μm area takes 0.2 s using LCVD but conventional CVD over a large area will take 2 hours (Park et al., 2014). The speculated reason for the higher growth rate was the rapid heating and cooling rate due to the laser exposure. Another possible reason for the higher growth rates in LCVD was the higher diffusion rates to a spot compared to the entire substrate from the gas-phase (Duty et al., 2001) or the migration of dissolved carbon atoms from the surrounding nickel catalyst on the surface. The quality of the growths is also on par to that of conventional CVD methods. For example, the graphene layer produced was single layer (Park et al., 2011) as proven by Raman inspection. However, it was not clearly stated whether the single layer graphene grown into a line was a single continuous crystal.

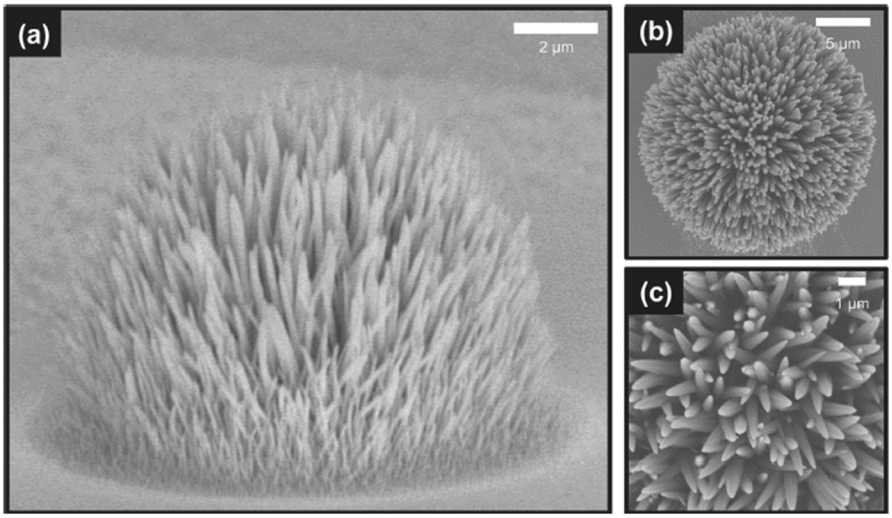

Figure 6: (a) Tilted SEM picture of the ZnO nanowires synthesized using laser induced hydrothermal growth. (b) Top view SEM picture and (c) magnified SEM picture (Yeo et al., 2013).

For photolytic LCVD, Alm, 2007 investigated the synthesis of iron, cobalt and tungsten oxide nanoparticles with an excimer laser at 193 nm. The synthesized nanoparticles were spherical in shape and had a size distribution of 1-50 nm. The challenge in the synthesis of nanoparticles via photolytic LCVD was the impurity levels in the nanoparticles. For example, the attempt by Alm et al., 2005 to produce cobalt nanoparticles resulted in carbon coated cobalt nanoparticles where the carbon content was more than ten times that of the cobalt.

2.2.1 Dissociation methods of tungsten hexacarbonyl

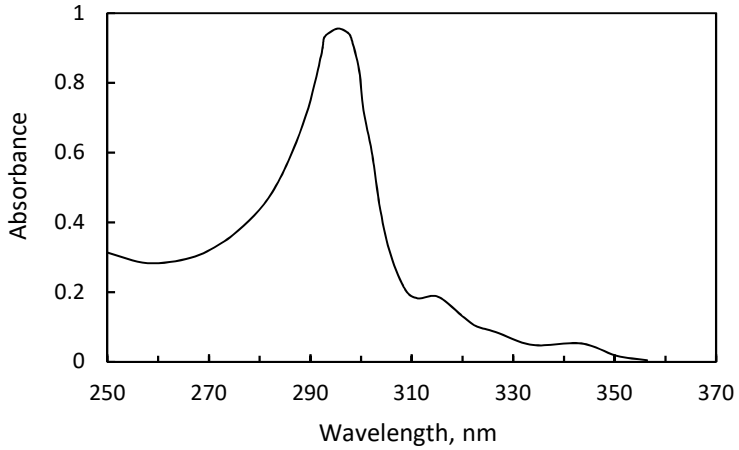

Figure 7: UV absorption spectrum of tungsten hexacarbonyl (Wrighton, 1974).

Tungsten hexacarbonyl was the precursor used in this body of work due to the high deposition rate and high conductivity of the deposited metal. In this section, the known dissociation methods of this precursor were reviewed. The absorption bands of tungsten hexacarbonyl are in the UV and infrared (IR) regions. The absorption in the UV region (Figure 7) was associated with the ligand field absorption of the bonds in the tungsten hexacarbonyl molecule (Wrighton, 1974). In the IR region, the absorption at 5 µm is linked to the CO ligand stretching vibrations (Au et al., 1984). There are no other IR

absorption bands until approximately > 16 μm, thus there was no overlap of strong fundamental absorption bands with IR lasers (HF, DF, CO or CO_2 lasers) (Gilgen et al., 1987).

A few investigators have attempted photolytic dissociation of the tungsten hexacarbonyl using CW UV lasers. Ehrlich et al., 1981 deposited tungsten on quartz substrates using a 257 nm CW laser at scan speed of 0.9 μm/s and power of 0.9 kW/cm^2. Gilgen et al., 1987 deposited tungsten on glass and gallium arsenide substrates with a 355 nm CW argon ion laser with a focal spot of 3 μm. The scan speed used was 1 μm/s, laser power was 10-70 mW corresponding to an intensity of 0.15 – 1.0 MW/cm^2. The high laser intensity also heated the substrate therefore the dissociation was a combination of photolytic and thermal mechanisms. The resistivity of the tracks on glass were low at 1-2 times bulk however the resistivity of the deposits on gallium arsenide substrate was high at 300 times bulk. The difference was associated to the lower gallium arsenide substrate temperature of 300 °C compared to 700 °C on glass. Temperatures below 400 °C promoted the nucleation of high resistivity granular β-phase tungsten. A temperature of at least 400-500 ºC was necessary to produce the low-resistivity, α-phase material (Deutsch and Rathman, 1984). Deutsch and Rathman, 1984 reported that annealing the high resistivity films at 650 °C in hydrogen reduced the resistivity from 32 to 6 times bulk.

For photolysis in the mid-IR band, investigators have attempted to dissociate tungsten hexacarbonyl using pulsed lasers. Au et al., 1984 used 50 ns frequency doubled TEA CO_2 lasers at 5 μm to cause the dissociation of tungsten hexacarbonyl at a laser intensity of 0.77 MW/cm^2 (at focus). The dissociation investigated was in a gas cell and detected through the increase in pressure due to the products of the reaction, no deposition on substrates were investigated. Windhorn et al., 2002 experimented with 5 μm ultrafast pulses for the photolytic dissociation of tungsten hexacarbonyl. The threshold for dissociation was 5x10^{11} W/cm^2 using 150 fs pulses. Similar to the previous investigation, no deposition on substrates were investigated and the dissociation was measured through IR spectrometry.

Dissociation of the tungsten hexacarbonyl outside the absorption bands of the molecule have been investigated through multiphoton dissociation, ion/electron beam bombardment and thermal dissociation. For multiphoton dissociation, investigators have attempted using 400 nm wavelength 150 fs pulses to direct write tungsten nano-gratings on sapphire, quartz, calcium fluoride, gallium nitrite, gold, copper and palladium (Zhang et al., 2007) (Tang et al., 2007). The grating had an average periodicity of 170 nm parallel to the laser linear polarization direction and was produced using a laser intensity of 7x10^{11} W/cm^2 at a scan speed up to 1 μm/s. The total dissociation energy of tungsten hexacarbonyl to ground state tungsten was 11 eV (Venkataraman et al., 1990), thus at least four photons at 400 nm (3.1 eV) were required.

Tungsten has been deposited from tungsten hexacarbonyl on substrates through ion or electron beam bombardment. For FIB deposition, (Langfischer et al., 2002) used gallium ion at 50 kV to deposit tungsten on SiO_2/Si substrates kept at temperature of 25 °C to produce tracks with a resolution of 150 nm (Figure 8). The highest deposition rate recorded was 8.4 nm/s or 1.5x10^{-4} μm^3/s. The purity of the

deposition was only 87 wt% and there was a large amount of gallium impurity (11 wt%) from the ion bombardment and a large amount of carbon (2 wt%) due to the low temperature of the deposition process. The resistivity of the deposition was high at 47 times bulk tungsten resistivity due to the high impurity and low temperature deposition. Roberts et al., 2013, Fowlkes and Rack, 2010, and Randolph et al., 2006 have attempted electron beam deposition of tungsten using tungsten hexacarbonyl. The highest deposition rate achieved was 9.5×10^{-4} $\mu m^3/s$ with a resolution of 70 nm (Fowlkes and Rack, 2010). However the resistivity of the deposit was high at >3800 times bulk due to a low tungsten purity of 30 at.%. Roberts et al., 2013 managed to improve the resistivity to approximately 41 times bulk, lower than the FIB deposition results, by pulse laser heating during the electron beam deposition. The laser power was kept to half the exposure where laser assisted deposition was observed and the deposition composition was similar to the EB deposition by heating the substrate to 150-300 °C.

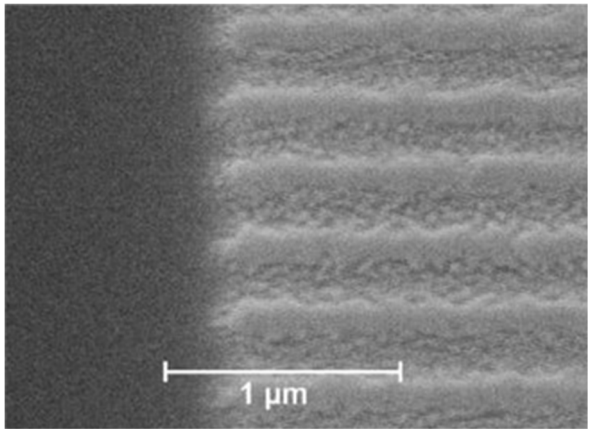

Figure 8: FIB-SEM image of tungsten deposited at a spacing of 300 nm in the vertical direction of this page showing that the deposition resolution of 150 nm (Langfischer et al., 2002).

Thermal dissociation of tungsten hexacarbonyl has been investigated using large area chemical vapour deposition (CVD) and CW LCVD. In large area CVD, Lai and Lamb, 2000 deposited tungsten from tungsten hexacarbonyl on silicon substrates. Films deposited at 375 °C were β-phase tungsten with a high resistivity of >188 times bulk tungsten. The high resistivity was reduced by vacuum annealing at 900 °C to achieve a resistivity of 3.6 times bulk tungsten. Films deposited at a higher temperature of 540 °C where of high purity (>95 at. %) polycrystalline α-phase tungsten with a low resistivity of 3.4 times bulk tungsten. These results were broadly in-line with the temperature-resistivity results reported by Gilgen et al., 1987 using UV dissociation. For direct laser writing, Nambu et al., 1990 wrote low resistivity (2-6 times bulk) tungsten lines at speeds up to 300 µm/s on silicon substrates. The wavelength of the laser was transparent to the tungsten precursor at 515 nm thus substrate heating caused the dissociation. The beam spot size was 2 µm and the lowest intensity that produced deposition was 0.54 MW/cm^2. No SEM images or phase measurements of the deposition results were reported but based on the low resistivity achieved (2-6 times bulk tungsten), it was assumed that the deposition occurred above 500 °C to produce low resistivity α-phase tungsten.

In summary, investigators have explored photolytic dissociation of tungsten hexacarbonyl through exposure to continuous wave UV lasers and pulsed IR lasers. FIB deposition of tungsten from tungsten

hexacarbonyl has also been studied. The deposited tungsten was of low purity due to the low deposition temperature, this led to high resistivity of the deposits. Large area CVD and CW laser direct writing of tungsten from tungsten hexacarbonyl produced low resistivity tungsten tracks and the results of from these investigations are used as comparison in this study.

2.2.2 Precursor delivery

The chemical precursor can either be in the form of solids, liquids or gases. For gaseous chemical precursors such as tungsten hexafluroride, the gas was either fed directly into the chamber or mixed with a carrier gas. The carrier gases were used to increase mass transport and dilute the precursor for condensation prevention (Chen et al., 1995). These gases were typically inert however hydrogen was used as a reduction gas for certain precursors such as tungsten hexafluoride (Zhang et al., 1987). For liquid chemical precursors, a carrier gas was bubbled through and vaporises the heated liquid (Mi and Lackey, 2009) as seen in Figure 9 (left). The saturated carrier gas can then be further diluted downstream before entering the deposition chamber. The liquid precursor can also be heated to cause vaporization and diffuse into the deposition chamber without a carrier gas (Maxwell et al., 1999). A liquid delivery method that has been used in CVD but not yet explored for usage in LCVD is the direct liquid injection method (Gao et al., 2004). In CVD, this liquid delivery system was used to vaporize the liquid precursor with a shower head inside the deposition chamber. For solid precursors, the precursor was heated and a carrier gas can be used to transport the vapour to the deposition chamber (Zhang et al., 2007). Alternatively, the vaporised precursor can also diffuse into the chamber without a carrier gas (Hitosugi and Mizuno, 2005) as seen in Figure 9 (right).

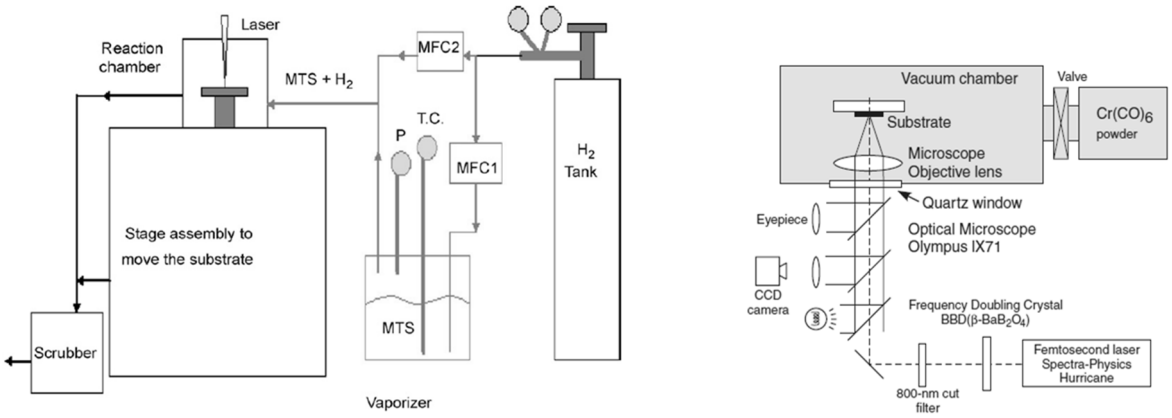

Figure 9: (left) Precursor delivered by bubbling a carrier gas through the liquid precursor (Mi and Lackey, 2009). (Right) Precursor delivered through diffusion from solid chromium hexacarbonyl powders (Hitosugi and Mizuno, 2005).

When a carrier gas was involved, the pressure of the precursor chamber was controlled by throttling the vacuum pump while the mass flow rate of the precursor was controlled by mass flow controllers in the flow of the carrier gas. The mass flow controllers were placed before the carrier gas picks up the precursor vapour because the precursor can condensate inside the mass flow controller and affect the flow measurements. When there was no carrier gas involved in the system, the temperature of the

precursor was used to control the precursor vapour pressure. To the knowledge of the author, no investigator has directly measured the amount of precursor inside the deposition chamber during experiments. All investigators assume that the precursor boils or vaporizes from a liquid or solid respectively to form a saturated vapour. An inline UV spectrometer could be used to directly measure the amount of precursor vapour. Another method of controlling the precursor amount is to use a precursor cell. Here the precursor is sealed in a cell with a small opening of known diameter that limits the flow rate. Thus, it can be assumed that inside the cell, the pressure is that of the saturated precursor pressure and the flowrate out of the cell is that of a known choked fluid flow-rate.

A few authors have mentioned employing a needle gas injection apparatus to feed the precursor directly to the deposition zone in the deposition chamber. To the author's knowledge, no investigator has reported experiment results confirming the advantage of such an apparatus. Morishige and Kishida, 1994 mentioned this set-up in their experiment but did not provide evidence that such a system was beneficial. A simulation study by Duty et al., 2003 indicated that such a system would increase deposition rate for diffusion limited reactions. If the dissociation reaction was not diffusion limited, the deposition rate would decrease due to cooling effects from the jet. Furthermore, when the needle system was included in their configuration (Lackey et al., 2002), no experiment results were published to confirm the increase in deposition rate. The main issue with using a needle injection for the precursor is the uneven precursor partial pressure over the substrate especially if the substrate and intended deposition area is large relative to the diameter of the needle outlet. In FIB deposition, the needle is always at the focus of the ion beam because the substrate is moved by a stage inside the vacuum chamber. However, in most LCVD set-ups the vacuum chamber is small, and the motion stages are outside. Thus, to keep the needle outlet at the deposition zone, a larger vacuum chamber with a stage inside is required. Alternatively, an actuator can be used to move the needle outlet around the substrate surface. However, both solutions will tremendously increase the cost of the set-up since the components would need to be vacuum compatible and resistant to the precursor vapours.

A reaction chamber was usually needed to control the deposition environment. Investigators typically use windows to let the laser in and charcoal filters or liquid nitrogen cold traps to trap the precursors at the exhaust of the vacuum pump. For precursor that do not condense at room temperature, a cold wall reactor was used, else a hot wall reactor. A few investigators have chosen not to contain the precursor within reaction chambers but to rely on suction systems to collect the by-products and unreacted precursors. Such as system is seen in Figure 10 where the chromium hexacarbonyl precursor was delivered and sucked back into a jacket around the microscope objective.

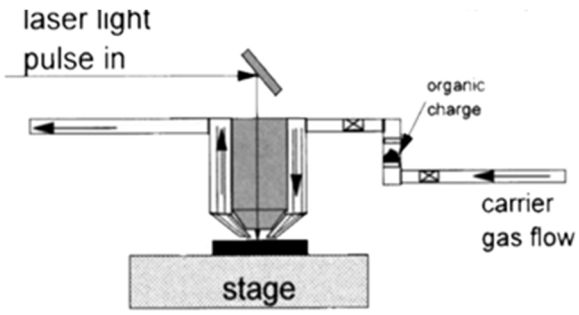

Figure 10: Schematic of precursor and laser beam delivery system used by (Haight et al., 2003) where the organic precursor is delivered from a jacket around the microscope objective.

2.3 Lasers in LCVD

The various laser sources used for LCVD include argon ion lasers, CO_2 lasers and excimer lasers. Argon ion lasers have a low laser power output to the total electrical input ratio (wall plug efficiency) of approximately 0.1 % (Paschotta, 2017). The laser emits thirteen wavelengths from UV to green (351 to 529 nm). Most LCVD investigators used the argon ion laser with wavelengths of 514 nm for pyrolytic dissociation of the precursor (Duty et al., 2001) because that wavelength has the highest output power, was suitable for coupling heat into various materials due to low reflectance and shallow optical penetration depth (section 2.3.4), and was transparent to most chemical precursors. Other investigators have used the 351 nm output or halved the 515 nm wavelength to 257 nm for UV photolysis. The argon ion laser has a good beam quality with a $M^2<1.5$ and the short wavelength makes the beam suitable for focusing to diameters <10 µm. The power output of the laser used by the investigators was in the range of 20-5000 mW.

The CO_2 laser is based on a gas mixture (primarily CO_2 with He and N_2) as the gain medium. A typical CO_2 laser emits at a wavelength of 10.6 µm and has a power conversion efficiency of 10 % (Steen and Mazumder, 2010). A few investigators have explored the usage of CO_2 lasers for pyrolytic LCVD (Cao et al., 1995). However, the absorption penetration depth at 10.6 µm was large for most materials and the large diffraction limited focal spot size was not suitable for precision localized LCVD.

Excimer lasers are usually operated in the UV region and the gain medium is a mixture of a noble gas and a halogen gas. The wall plug efficiency is low at approximately 2 % or less (Steen and Mazumder, 2010). Excimer lasers have been used by investigators for photolytic LCVD such as the deposition of tungsten using the argon fluoride laser mentioned previously (Deutsch and Rathman, 1984).

2.3.1 Laser diodes

A laser source that has not been explored for usage in LCVD are laser diodes. The electrical to optical efficiency is typically of the order of 50 % and the device lifetime is very high at the order of tens of thousands of hours (Steen and Mazumder, 2010). The cost of semiconductor laser diodes has decreased significantly due to technological developments and also mass production (Rothenbach and Gupta,

2012). There is also a drive towards higher output power to achieve higher data writing speed in Blu-ray DVD writers. These developments have encouraged investigators to explore other uses for laser diodes. (Rothenbach and Gupta, 2012), for example, explored using Blu-ray laser diodes to pattern photoresists. Features as small as 450 nm were created using the SU-8 photoresist coated on silicon wafers at a write speed of 15 mm/s.

To the knowledge of the author, no investigator has explored using high power diodes as laser sources for LCVD. For pyrolytic LCVD, the advantage of using a 405 nm wavelength blue laser diode compared to argon ion lasers at around 500 nm is the shorter optical penetration depth in silicon at that wavelength (section 2.3.4) thus heating will be more localized. A 405 nm laser diode was used for CW LCVD in this study (Chapter 4).

2.3.2 Ultrafast lasers

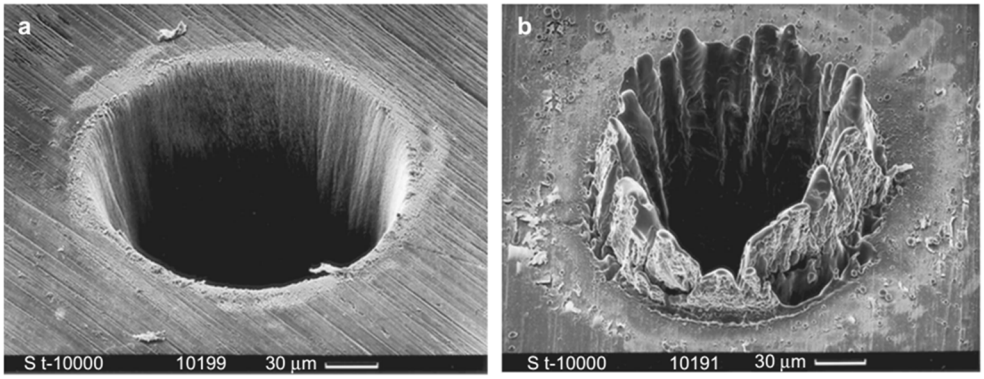

Figure 11: Drilled holes on steel by 780 nm laser ablation with (left) 200 fs pulse width, 0.5 J/cm^2 fluence and (right) 3.3 ns pulse width, 4.2 J/cm^2 fluence (Chichkov et al., 1996).

Ultrafast lasers have not been explored for usage in pyrolytic LCVD. Micro-machining with ultrafast pulses produced neater trenches and holes compared to longer pulse lasers (Figure 11). The reduction in HAZ enables clean machining of low temperature melting point materials such as polymers. For example, (Toenshoff et al., 2000) used ultrafast lasers to trim cylindrical polymers to produce stents for medical usage (Figure 12). Another advantage of machining with ultrafast lasers was the nonlinear absorption induced by the high intensity at the focal spot, which enables the processing of transparent materials such as glass (Gattass and Mazur, 2008). Ultrafast pyrolytic LCVD would use less intense pulses compared to ultrafast micro-machining, thus this method would potentially be compatible with the numerous materials investigated in ultrafast micro-machining such as metals, glass and polymers.

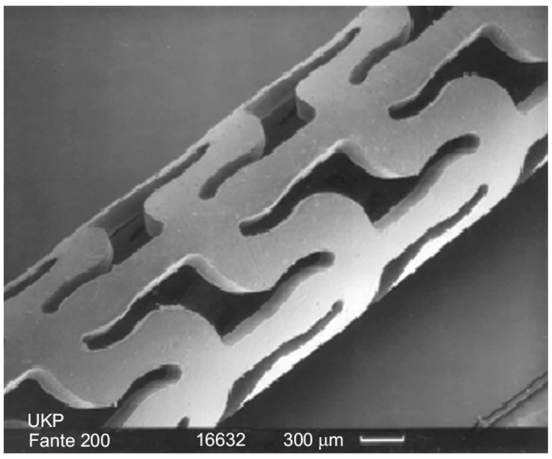

Figure 12: SEM image of bioresorbable polymer medical stent fabricated using ultrafast pulsed lasers (Toenshoff et al., 2000).

Ultrafast laser pulses have been investigated for additive manufacturing. The pulsed near-IR photopolymerizing fabrication process through multiphoton absorption was first mentioned by (Maruo et al., 1997). Common materials that can be processed using this method include liquid resins, photoresists such as SU-8 and SZ2080 (a photoresist based on zirconium propoxide sol-gel) and elastomers such as polydimethylsiloxane (PDMS) (Malinauskas et al., 2016). The smallest feature size achieved by the technology is 65 nm (Fischer and Wegener, 2011). The typical volumetric built rate is low at around 20 $\mu m^3/s$ however the speed can be increased to 720 $\mu m^3/s$ with a loss of resolution to 5 µm (Rekštytė et al., 2013). The laser intensity required for multiphoton polymerization depends on the photochemical used and were typically in the order of > $5x10^{12}$ W/cm^2. Multiphoton polymerization has been explored for use in micro-optics, micro-fluidics and micro-mechanics. An example of structures that can be produced by the technique is a photonic crystal (Figure 13) that can be used for optical sensing of liquids and gases. Ultrafast lasers have been used in photolytic LCVD and the deposition produced laser-induced periodic surface structures (Green and Her, 2013). These results are reviewed in section 2.3.5.

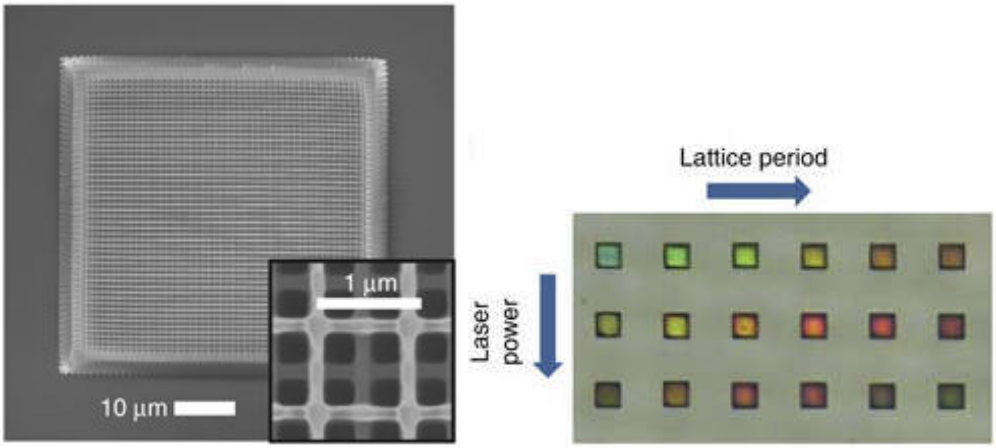

Figure 13: (Left) SEM image of 3D woodpile architecture photonic crystals fabricated using multiphoton polymerization of SZ2080 photoresist and (right) optical microscopy image of several woodpile structures having different lattice parameters thus exhibiting different structural colours (Mizeikis, 2014).

2.3.3 Laser beam delivery and scanning methods

The focused laser spot can be scanned on the substrate through various strategies. LCVD investigators have tried depositing dots through fixed exposure times on a stationary spot; growing fibres perpendicular to the surface by keeping the focus of the laser on the growing tip (Duty et al., 2001); and depositing lines by moving the substrate along the plane parallel to the substrate surface. The depositions were done in either single pass or multiple passes (Haight et al., 2003). A few investigators have explored a two-step deposition process. For example in Han et al., 1994 a nucleation step was done by scanning the beam at a speed of 1000 µm/s. Then the entire surface was exposed to a CVD precursor for 30 minutes where deposition only occurred on the nucleated regions. Without the two-step method, a slow scanning speed of 16 µm/s was required.

A scanning strategy that has not been explored by investigators is rapidly scanning the pattern of interest multiple times at a high speed to heat the whole pattern area up to the deposition temperature. For example, instead of laser scanning a circle pattern at a speed of v for a duration of t, the laser can scan the pattern at a speed of $100v$ for one hundred times for a duration of t. In this manner, the whole circle will be heated thus the LCVD deposited track would be smoother. The high-speed scanning could be achieved using galvo-scanners.

A few investigators have included a heater in their LCVD assembly such as in Lackey et al., 2002 and Chen et al., 1995. Jean et al., 1999 have explored raising the temperature to just below the deposition temperature then using the laser to locally reach the deposition temperature. This was done to reduce thermal stress and speed up the heating process. However, no results of this technique have been published. Researchers have not explored actively cooling the substrate just above the condensation temperature of the precursor. The cooling will dissipate the energy input from the laser and maintain the substrate temperature for so that the LCVD process is more repeatable and reliable.

For the deposition of two-dimensional tracks, there is also the opportunity to investigate scanning the beam at an angle (Figure 14 right) compared to the usual configuration which is perpendicular to the substrate (Figure 14 left). In this configuration, the growth direction would be closer to the scan. This technique would be relevant when depositing thick tracks.

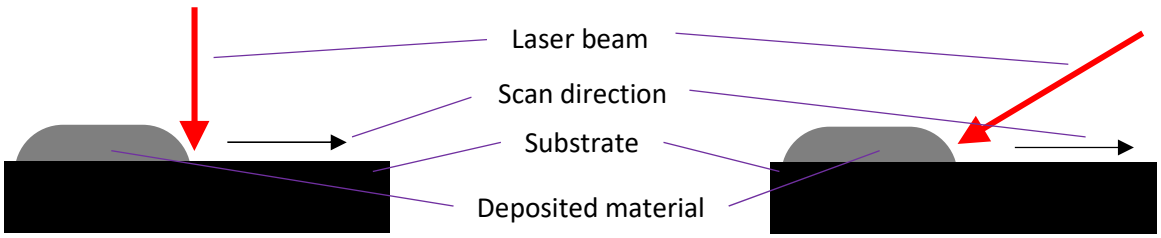

Figure 14: Configurations for depositing 2D tracks on the substrate. (Left) Laser beam perpendicular to the substrate and (right) at angle to the substrate surface.

Besides two dimensional deposition on the surface of the substrate, investigators have grown rods and fibres perpendicular to the substrate surface. Wallenberger et al., 1994 successfully synthesized boron,

carbon, silicon, SiN and SiC fibres that were amorphous, polycrystalline, glassy or single crystal via pyrolytic LCVD. Fibres made were up to 2 m long with diameter as small as 9 μm, while the growth rates were 0.3-1.1 mm/s. The high volumetric growth rates achieved, $12x10^6$ $\mu m^3/s$, were due to the growth direction being in the preferential direction which was in the direction of the laser beam; and the high pressures used in the reactor chamber (up to 7.5 bar compared with <<1 bar used by other investigators (Duty et al., 2001)). There are opportunities to explore high pressure LCVD to increase the deposition rate in other LCVD configurations besides growing fibres, such as deposition of two-dimensional tracks and three-dimensional fabrication. The challenge is finding precursors with high vapour pressures to avoid condensation at high pressures.

LCVD has also been explored for three-dimensional fabrication and all papers found by the author on this topic used pyrolytic LCVD. Due to the thermal nature of pyrolytic LCVD, the material deposited and substrate needs to have a low thermal conductivity. To the author's knowledge, no successful three-dimensional fabrication of good thermally conducting materials such as metals have been reported. At best, the investigators only managed to grow straight rods or deposit the thermally conducting material on moulds. Materials that have been reported in LCVD three-dimensional fabrication include boron (Johansson et al., 1992), aluminium oxide (Lehmann and Stuke, 1994), carbon (Dean et al., 1999), tungsten carbide (Maxwell et al., 1998), and silicon (Westberg et al., 1993). For substrate materials that have a good thermal conductivity, a larger diameter is expected when the deposit first grows on the substrate (Figure 15 left). If the thermal conductivity of the materials is even higher, such as in silicon, then a post needs to be etched to start the growth (Figure 15 right). Thus, pyrolytic LCVD for three-dimensional fabrication is limited to low thermally conducting materials.

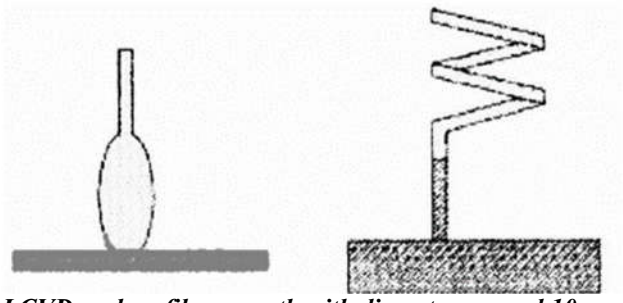

Figure 15: The start of LCVD carbon fibre growth with diameter around 10 μm on steel (left) where the deposit initially bulges and on silicon (right) where an etched post was necessary (Dean et al., 1999).

For three-dimensional fabrication, there were four common scanning strategies employed by researchers. The first method moves the focal point in the XYZ directions without changing the angle of incidence (Westberg et al., 1993) (Figure 16 a). The growth rate was higher in the direction parallel to the beam. For example, Westberg et al., 1993 achieved a maximum lateral to vertical growth ratio of 1:3 resulting in growth direction 20º perpendicular to substrate. It was difficult to create features that were parallel to the surface of the substrate. The next method scans the laser diagonal to the substrate surface while moving the focal point in the XYZ direction. For the case shown in Figure 16 (b), a rotary motor was used to provide rotation in the XY plane. With this configuration, it was possible to create features that were parallel to the surface of the substrate but it was difficult to create features that were perpendicular

to the substrate without changing the beam angle. A helical coil was the most suitable shape to create in this configuration (Westberg et al., 1993)(Maxwell et al., 1998). A modification to this configuration was the LCVD on a mould as seen in Figure 16 (c). After deposition, the mould can either be dissolved away (Lehmann and Stuke, 1991) or kept for its functional properties (Williams et al., 1999). The limitation of this technique was that the mould needs to be pre-formed before deposition. The final variation that was explored by investigators for three-dimensional fabrication was splitting the laser beam into two and focusing both on to the same spot (Lehmann and Stuke, 1994) (Figure 16 d). This method enables writing free form shapes because deposition only occurs where the laser intensity was high in the intersection of the two focal spots.

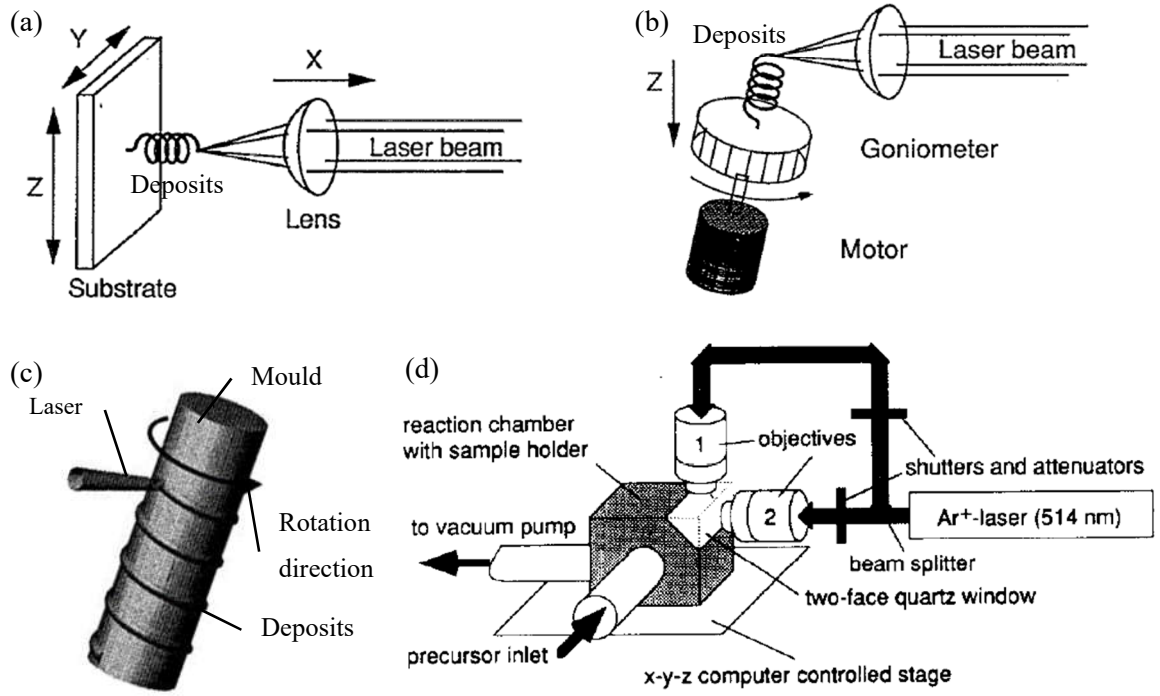

Figure 16: Scanning strategies employed for 3D fabrication using LCVD. (a) Moving the focal point in the XYZ directions while keeping the angle of incidence fixed perpendicular to the substrate (Westberg et al., 1993). (b) Moving the focal point in a rotation motion along the XY plane and down on the Z direction while the beam is slanted with respects to the substrate surface to produce helical springs (Westberg et al., 1993). (c) Deposition of 3D structures on a mould (Duty et al., 2001). (d) Free-form direct writing by splitting the beam into two and focusing both onto the same spot (Lehmann and Stuke, 1994).

2.3.4 Light absorption

Figure 17 shows the reflectivity and absorption depth spectrum of various materials used as substrates in this body of work. A low reflectance is required to reduce the total laser power output and prevent damage from back reflection of the laser beam. A shallow optical penetration depth is required to concentrate the heating to the surface of the substrate for the dissociation. This achieves a higher surface temperature with less laser power and reduces volumetric heating that increases the HAZ of the process. From Figure 7, a wavelength above 350 nm is required to avoid absorption by the tungsten hexacarbonyl precursor, however the optical penetration depth in silicon substrates increases from 0.1 μm to 100 μm

when the wavelength is increased from 400 to 1100 nm. Thus, a wavelength of 400-500 nm is the best for CW thermal LCVD on silicon substrates.

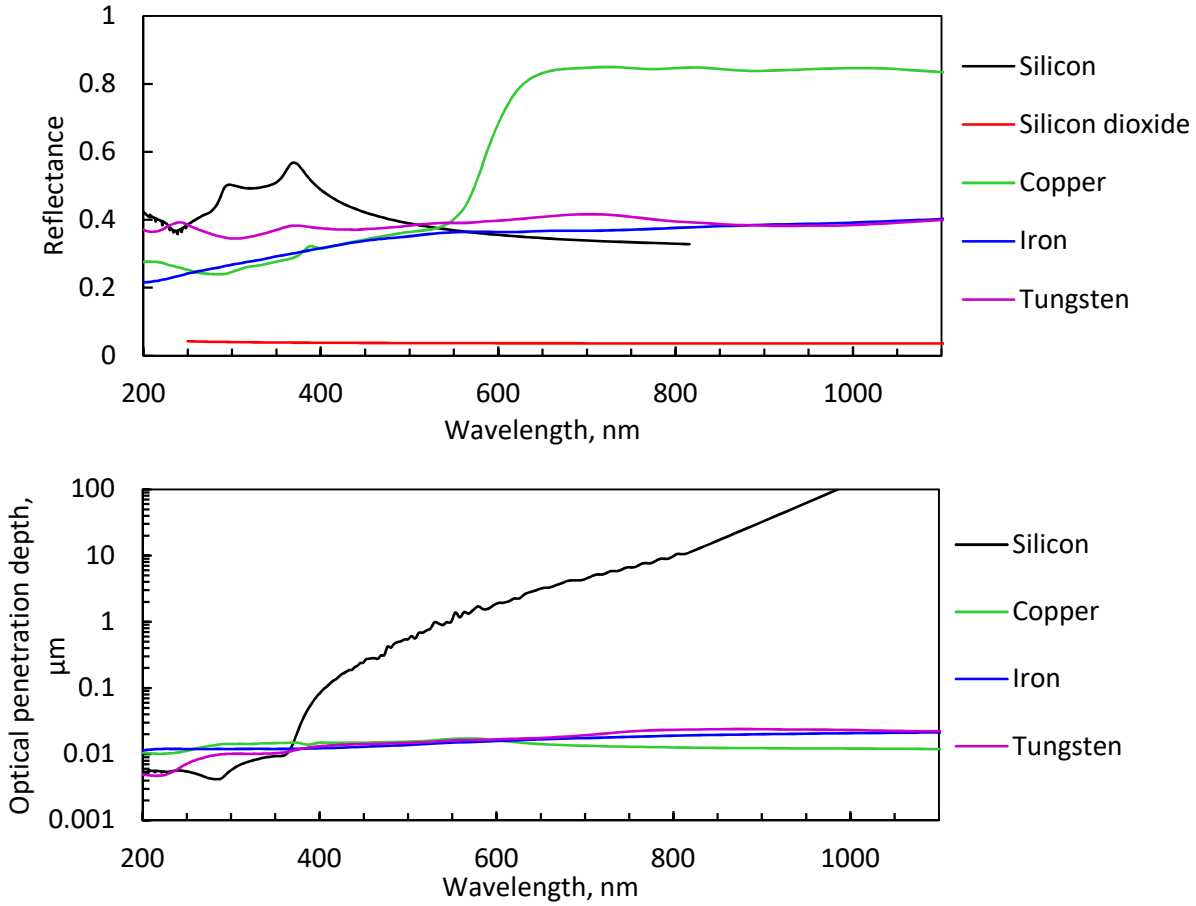

Figure 17: Reflectivity (top) and absorption depth (bottom) spectrum calculated based on data from Filmetrics Inc, 2015.

In the substrate, energy from the electromagnetic wave of the laser pulse is absorbed by electrons which then transfer the energy to the lattice through phonon vibrations. The transfer of energy between the electrons and lattice is often modelled using the two-temperature model

$$C_e \frac{\partial T_e}{\partial t} = \nabla \cdot (k_e \nabla T_e) - \gamma_{e-l}(T_e - T_l) + \dot{q} \qquad [1]$$

$$C_l \frac{\partial T_l}{\partial t} = \nabla \cdot (k_l \nabla T_l) + \gamma_{e-l}(T_e - T_l) \qquad [2]$$

where the subscripts e, l, and $e-l$ are the electron, lattice and electron-lattice sub-systems respectively, C is the heat capacity, T is the temperature, k is the thermal conductivities, γ is the energy exchange rate between electron and lattice and $\dot{q}$ is the volumetric heat source from the laser (Rethfeld et al., 2017). The two-temperature model allows theoretical prediction for instance of melting and thus ablation thresholds of materials.

The electron cooling time $\tau_e = \frac{C_e}{\gamma_{e-l}}$ in the two temperature model is at the order of $1\text{x}10^{-13}$ s (Derrien et al., 2011) and the time scale for dissociation reactions are also in the order of $1\text{x}10^{-13}$ s (Zewail, 2000). In the case of thermal LCVD investigated in this body of work, ablation temperatures were typically

avoided. Thus, it can be assumed that the electron and lattice were in equilibrium for most of the dissociation reaction and the two-temperature model can be simplified to the single temperature heat diffusion equation

$$C\frac{\partial T}{\partial t} = \nabla \cdot (k\,\nabla T) + \dot{q} \qquad [3]$$

For a laser with a Gaussian spatial distribution, the volumetric heat source can be modelled as

$$\dot{q} = P\,(1-\mathbb{R})\frac{2}{\pi w^2}\exp\left(-\frac{2\left((x-v_x t)^2+y^2\right)}{w^2}\right)\cdot\,\alpha\exp(-\alpha z) \qquad [4]$$

where P is the total laser power input, $\mathbb{R}$ is the reflectance, w is the laser beam radius, $x, y\ z$ are the coordinates, v_x is the velocity in the x-direction and α is the absorption coefficient. For ultrafast laser pulses, the laser heating will stop at the end of the pulse duration therefore there will be no heating between the pulses and $\dot{q} = 0$ during that time. During the pulse, the laser power peak intensity $I_0 = P\,(1-R)\frac{2}{\pi w^2}$ is at the order of > 10^{10} W/cm^2. The high intensity allows for non-linear absorption by transparent materials. In the regime where the pulse duration is < 10 ps, various non-linear ionization mechanisms such as multiphoton absorption, avalanche ionization, and tunnelling become important (Ben-Yakar and Byer, 2004). For example, borosilicate glass is transparent ($l_\alpha = \infty$) at a wavelength of 780 nm however using 200 fs pulses, the optical penetration depth measured experimentally was 238 nm (Ben-Yakar and Byer, 2004).

To calculate the spatial and temporal temperature distribution, the partial differential heat transfer equation 3 can be numerically solved. This is done by discretizing the domain of interest into multiple finite computation units. Thus, the numerical solution is more readily adapted for changes in the domain shape and laser source compared to an analytical solution. The heat transfer equation 3 can be discretized (Wheatley and Gerald, 2004) using finite volume cells through

$$\int_t^{t+\Delta t}\int_V^{V+CV}\rho c\frac{\partial T}{\partial t}\,dV\,dt = \int_t^{t+\Delta t}\int_V^{V+CV}\left(\frac{\partial}{\partial x}\left(k\frac{\partial T}{\partial x}\right)+\dot{q}\right)dV\,dt \qquad [5]$$

$$\rho c\frac{(T_P-T_P^0)}{\Delta t}\,\Delta V\,\Delta t = \left(\frac{\theta k_E A_E(T_E-T_P)}{\delta x_{EP}} + \frac{(1-\theta)k_E A_E\left(T_E^0-T_P^0\right)}{\delta x_{EP}} - \frac{\theta k_W A_W(T_P-T_W)}{\delta x_{PW}} - \frac{(1-\theta)k_W A_W\left(T_P^0-T_W^0\right)}{\delta x_{PW}}\right)\Delta t + \dot{q}\,\Delta V\,\Delta t \qquad [6]$$

where CV was the control volume, the subscripts P, W, E were the point, west neighbouring cell, and east neighbouring cell respectively in the single dimension, θ was the time advancing scheme weights, A was the face area of the cells and δx was the length of the cell. Here, the equations are only described in one-dimension for simplicity but can be expended for implementation in three dimensions. Equation 6 was used to build a simulation model (section 3.5.7) to determine the temperature during the pyrolytic ultrafast LCVD process.

2.3.5 Laser-induced periodic surface structures

Close to the ablation threshold of the substrate, laser induced periodic surface structures (LIPSS) as seen in Figure 18 are generally formed. The scattering of the incident light due to surface roughness generates surface electromagnetic waves (Polo and Lakhtakia, 2011) which interferes with the incident light and produces standing wave patterns on the surface (Zhang et al., 2007). LIPSS are classified based on the spatial frequency. Low spatial frequency LIPSS (LSFL) typically exhibit periods close to or slightly smaller than the irradiation wavelength while high spatial frequency LIPSS (HSFL) have periods smaller than half the irradiation wavelength. For absorbing materials, LSFL orientated perpendicular to the electric field direction of the linear polarized laser beam were more common (Buividas et al., 2014).

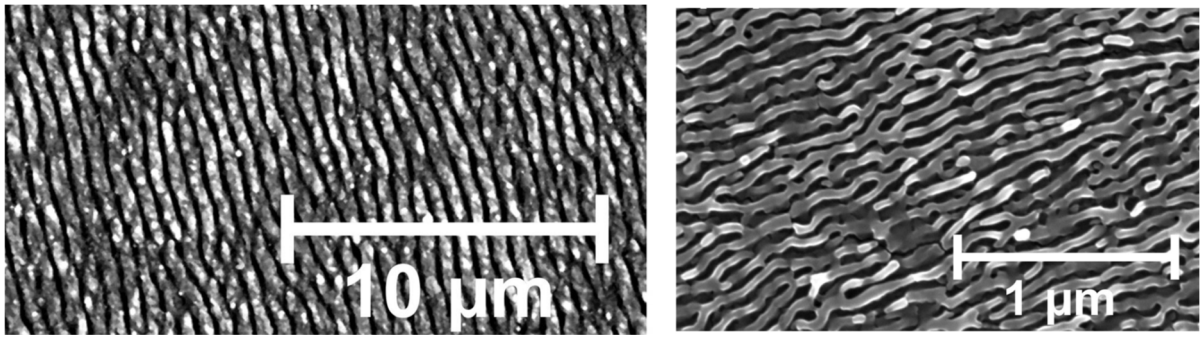

Figure 18: SEM images of two different LIPSS formed on titanium alloy (TI6Al4V) surfaces after irradiation with pulsed laser (30 fs, 800 nm, 1 kHz) at laser intensity and number of pulses of (left) 0.11 J/cm^2, 56 pulses and (right) 0.08 J/cm^2, 560 pulses (Bonse et al., 2017).

The period of the LIPSS are highly dependent on the wavelength of the laser, exhibiting a linear scaling (Le Harzic et al., 2011). This happens because the resonant spatial frequency in the surface electromagnetic wave – laser interference is dependent on the laser wavelength. Other factors that affect the period of the ripples are the pulse overlap and pulse energy. The period of the ripples reduces with increasing pulse overlap (Bonse and Krüger, 2010). On silicon irradiated with an 800 nm wavelength 130 fs laser, the period of the ripples decreased from 770 nm to 560 when the number of pulses was increased from one to a thousand pulses. According to Huang et al., 2009, the decrease in the period happens through a grating-assisted surface electromagnetic wave – laser coupling. As the grating-like surface relief deepens, the resonant wavelength of the surface electromagnetic wave undergoes a redshift, due to a change in the effective refractive index, which leads to the decrease in the spatial ripple period.

The spatial period of ripples increases with pulse energy. Okamuro et al., 2010 studied the increase in period with pulse energy for 800 nm 160 fs laser irradiation on titanium, molybdenum, platinum and tungsten. The increase of the period was from approximately 600 nm to 700 nm from the minimum to maximum fluence where the periodic structures were observed on those metals Figure 19. The increase in the period with laser fluence was attributed to the change in the plasma density formed during ablation. The change in plasma density affected the incident wavelength at the air-substrate surface interface thus affecting the resonant frequency for LIPSS formation.

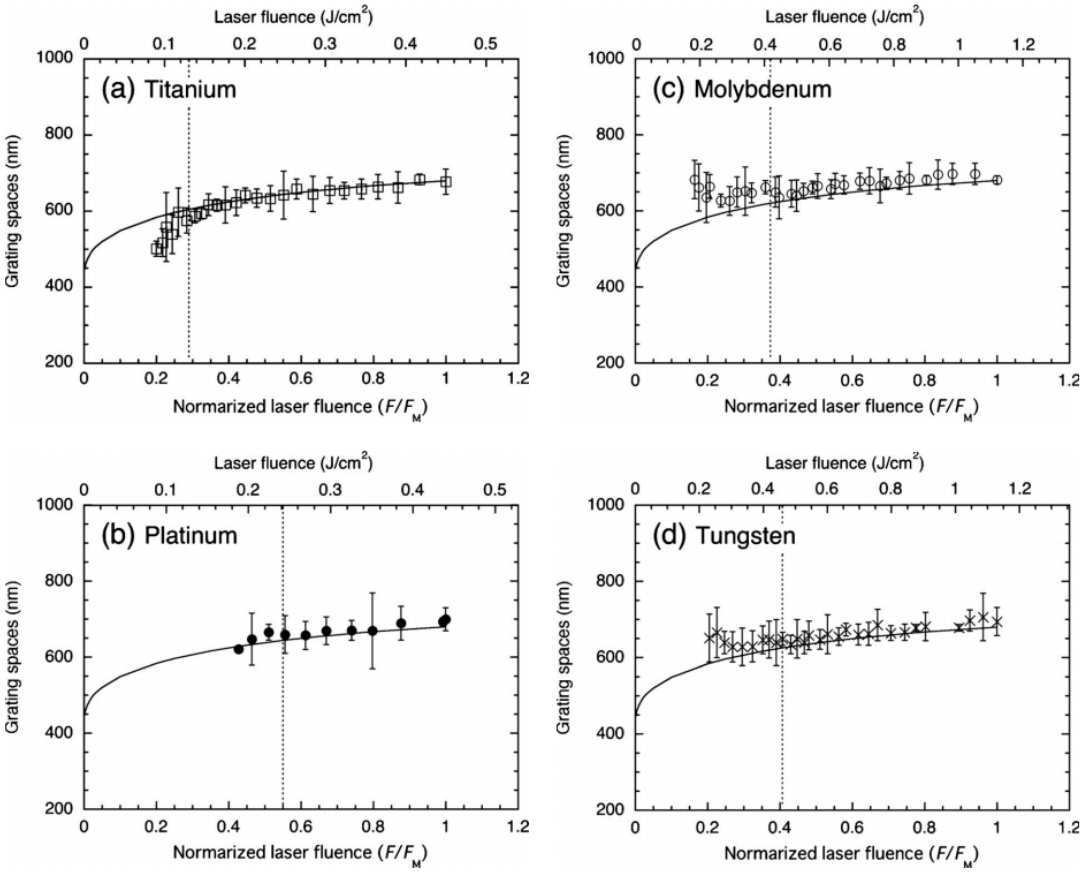

Figure 19: Graphs of ripple spatial period against laser fluence on metals made using 800 nm 160 fs pulsed laser by (Okamuro et al., 2010).

LIPSS formation are typically associated with subtractive laser ablation or surface modification through melting. LIPSS formation in LCVD has been reported for processes that employ non-thermal dissociation mechanism such as UV photolysis and multiphoton ultrafast dissociation. CW 257 nm UV lasers have been used to deposit metal ripple structures on substrates. (Singmaster et al., 1990) deposited chromium and molybdenum, (Brueck and Ehrlich, 1982) and (Osgood and Ehrlich, 1982) deposited cadmium while (Wilson and Houle, 1985) deposited copper. In these investigations, the laser intensity was less than 10^4 W/cm^2 with laser spots <10 μm. The estimated substrate temperature rise was at most 50 °C, indicating that the deposition was due to photolysis of the precursor molecules without thermal dissociation. The period of the ripples observed were that of LSFL at half to one wavelength size. The formation of tungsten LIPSS in LCVD through multiphoton absorption has been reported by investigators using 400 nm 100 fs ultrafast lasers (Tang et al., 2007), (Zhang et al., 2007), (Green and Her, 2013). These investigators were able to produce highly uniform tungsten gratings through the LIPSS (Figure 20) however the scan speed was limited to < 1 μm/s.

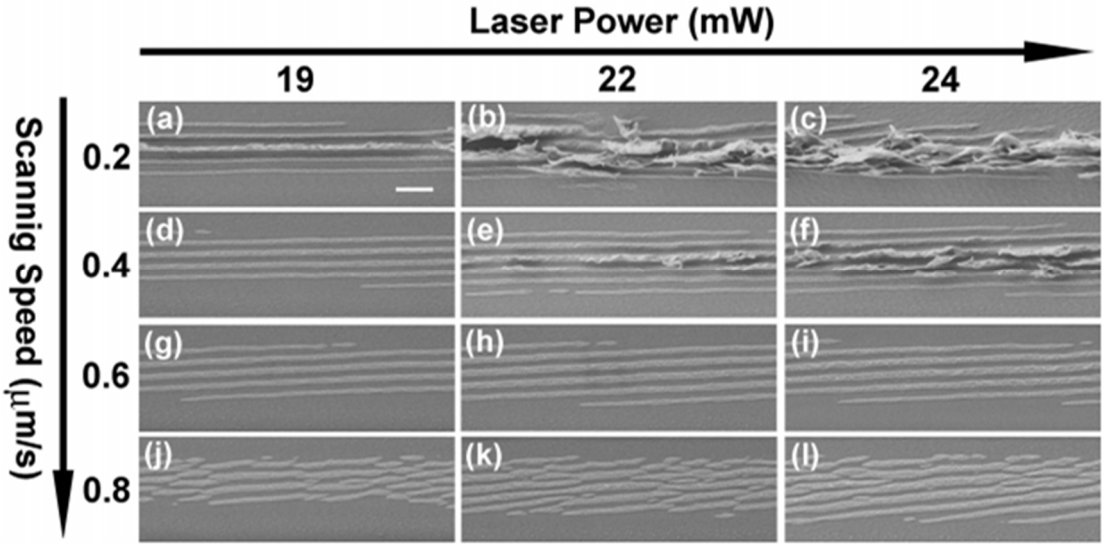

Figure 20: LIPSS through LCVD of tungsten using 400 nm 100 fs pulsed laser (Zhang et al., 2007). Scale bar is 500 nm.

2.3.6 Laser modification threshold

For ultrafast pulse duration lasers, the surface modification regions are highly dependent on the local laser intensity when the laser power was close to the ablation threshold. For example in silicon (Figure 21 a, b), the region that was exposed to the highest laser fluence experienced ablation while at lower intensities, the surface experienced other surface modifications such as annealing and oxidation (Bonse et al., 2002). When the laser power was increased the diameter of the respective regions increased in proportion to the increase of the Gaussian beam diameter with that threshold fluence. The Gaussian beam equation can thus be modified to achieve a linear plot so that the various modification thresholds can be estimated through linear regression.

$$F_{th} = F_0 \exp\left(-\frac{2r^2}{w^2}\right) \quad [7]$$

$$\ln(F_0) = \frac{1}{2w^2}(2r)^2 + \ln(F_{th}) \quad [8]$$

thus at the modification threshold (that is r=0), the threshold fluence would be the peak fluence. Figure 21 (c) shows this linear regression done to estimate the modification (squares) and melting (circles) threshold of silicon. In this study, equation 8 was used to determine the deposition threshold for the pyrolytic ultrafast LCVD process and these values are compared to the ablation threshold of the substrate.

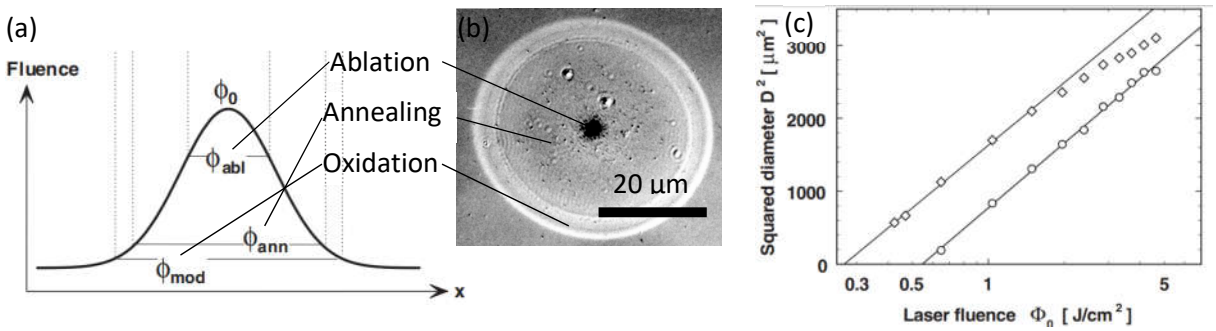

Figure 21: (a) Fluence against distance across the laser beam and (b) SEM image of laser ablation on silicon showing the different effects at various fluence levels. (c) Linear regression to estimate the fluence threshold of modification (squares) and melting (circle) on silicon (Bonse et al., 2002).

2.4 Other deposition methods

Other deposition methods for conductive materials include photolithography, laser induced forward transfer and inkjet printing.

2.4.1 Photolithography

Photolithography is a 2D pattern transfer technique from a mask to thin films on substrates which are typically silicon wafers (Madou, 2011). This method is widely adopted in the integrated circuit industry (ITRS, 2013) and continuous improvements have led to feature size of 14 nm. Microstructures are created in a process called patterning (Mack, 2007). The patterning process is either subtractive or additive. The subtractive method is more common and involves three steps: (1) deposit a film on the wafer; (2) pattern the film via lithography; and (3) etch to transfer the pattern into the film. For the additive process, lithography is first done to create the pattern that is desired then selective deposition is done into the areas not protected. The deposition technology chosen is based on the material and intended functionality of the film. The deposition step can either be direct oxide growth; physical vapour deposition (PVD); or CVD. PVD techniques usually require a direct line of sight from the target material to the deposition substrate and require a higher vacuum to increase the mean free path (Madou, 2011). CVD does not require a direct line of sight as the deposition material is carried in the gas phase. Typical deposition rates for PVD and CVD are tens of micrometres per hour.

Photolithography is used for the fabrication of microchips in industry because the technology is capable of meeting demanding specifications; has a low cost per unit in large volume production; and the technology is very reliable. Due to the demand for faster, smaller and more power efficient microchips, the number of transistors in a microchip has increased while the feature size decreased exponentially since 1970s according to Moore's law (Rothschild et al., 2003). Photolithography is capable of producing microchips according to these demanding design specifications at a production rate of around 50,000 wafers (300 mm in diameter) per month per fabrication plant (Chang, 2014). At a diameter of 300 mm, each wafer contains around 1000 microchips (Chapman, 2010). Besides meeting the

specifications, the cost of producing a high end microchip using photolithography is only around USD 5 (Handy, 2014). Furthermore, the failure rate of the fabrication process is very low at less than 300 ppm microchips (Denes, 2009) thus the technology is very reliable.

Despite the advantages of photolithography, there are limitations. Photolithography is not suitable for low volume production such as for prototyping because fixed costs such as cost of equipment, maintenance cost and cost of masks. Lithography equipment for 300 mm wafers costs around USD 4 million and the cost to build a semiconductor fabrication plant is around USD 10 billion (Clean Room Technology, 2010). The fabrication process is also resource intensive. Each 300 mm wafer uses 2,200 gallons of clean water (GWI, 2009) and 1 MWh of electrical energy (Branham, 2008). Another limitation is that photolithography is not suitable for the deposition of high aspect ratio structures because the deposition is done layer after layer. Each subsequent layer requires precise alignment to the previous layer thus the alignment errors are compounded. Modifications to the photolithography technology allows for creation of high aspect ratio structures in a single layer however these are expensive such as the LIGA (Wallace, 2013), or are limited to certain designs cases such as the SOI technique and the HEXSIL technology (Keller and Ferrari, 1994).

2.4.2 Laser induced forward transfer

Laser induced forward transfer (LIFT) is a micro-deposition process that uses a laser beam to transfer material from a "donor" substrate to a "target" substrate (Willis, 2018). The donor substrate is transparent to the laser and is in contact or located up to a few hundreds of microns away from the target. The laser is focused through the donor substrate unto the metal where it heats and propels the film to the target to cause deposition. Patterns are made by scanning the laser. LIFT can transfer a range of materials including metals, semiconductors, polymers, superconductors, electronic pastes and biological materials. The resolution of LIFT deposition of metals is in the sub-500 nm range. The resistivity of the deposit was however poor, for example copper LIFT produced deposits with approximately 3-80 times bulk resistivity due to the low deposition temperature and lack of fusion between the deposits (Figure 22). A vacuum environment is not necessary for the process, however when done in air there is a higher risk of oxidation which contributes to the high resistivity of the tracks (Grant-Jacob et al., 2013). The LIFT process can be used to create columnar structures, pillars up to a height of 2.1 mm with a diameter of 10 μm can be made (aspect ratio 1:210 (Visser et al., 2015)).

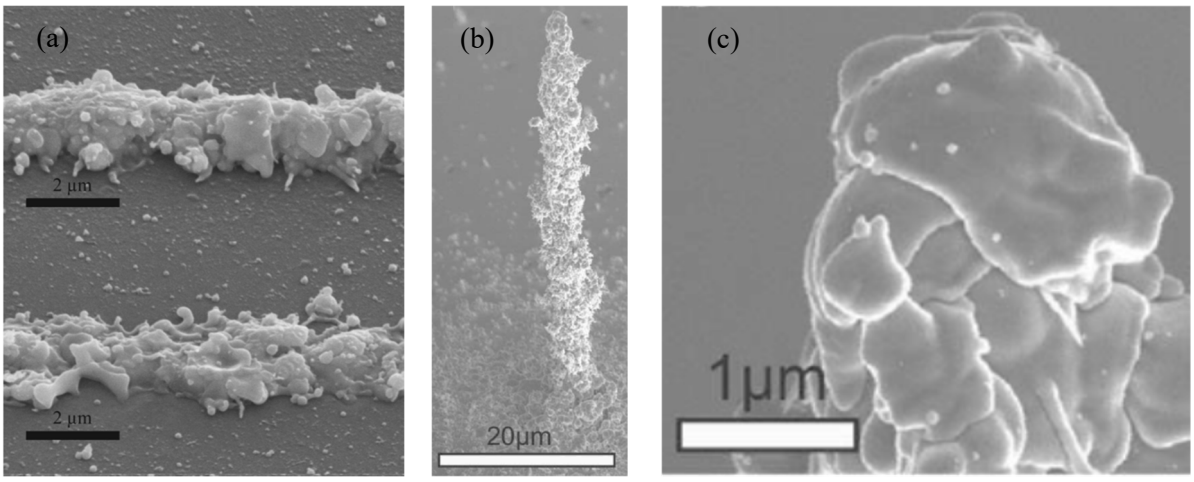

Figure 22: (a) LIFT deposition of copper tracks on silica substrates at two laser powers (Grant-Jacob et al., 2013). (b) LIFT deposition of copper to form a tower and (c) a higher resolution image of the tower tip (Visser et al., 2015).

2.4.3 Inkjet printing

Another method for micro-deposition is inkjet printing. Inkjet printing, which involves the production of small drops of liquid and their deposition in precise locations on a substrate, are typically done using drop-on-demand systems (Martin and Hutchings, 2012). Conductive tracks are printed using metal (silver or copper) nanoparticle inks. Low track resistivities can be achieved by sintering to achieve resistivities of 2.4 times bulk silver and 4.5 times bulk copper for silver and copper oxide inks respectively (Albrecht et al., 2016). The printed track widths are typically larger than 30 µm, however using techniques such as dissolution and redistribution with SU-8, track width can be reduced to 5 µm (Chu et al., 2018).

2.5 LCVD Applications

Various applications of LCVD have been mentioned by the LCVD investigators. For the deposition of conductive metal tracks, investigators have explored deposition of conductors to repair circuits (Han and Jensen, 1994), strain dependent resistors to measure deformation and sensors to measure pressure (Moilanen et al., 1994). The earliest patent found by the author, for LCVD was that of circuit repair in Baum et al., 1993 and Baum et al., 1995 filed for International Business Machines. A patent filed for Intel Corporation (Winer and Livengood, 2000) describes a method to combine LCVD with FIB deposition for editing integrated circuits (IC).

Titanium nitride and titanium carbide were deposited through LCVD as protective mechanical coatings (Cao et al., 1995). The deposition of ceramics was also used to “weld” ceramic parts together below the melting temperature. Harrison and Marcus, 1999 joined two separate silicon carbide tubes via pyrolytic LCVD below the melting temperature of 2700 ^{o}C. The deposition of semiconductors such as silicon and gallium arsenide were also explored. A gallium arsenide waveguide deposited by Boutros et al., 1996

achieved a loss of 5.4 dB/cm (compared with losses in silicon on insulators 1 dB/cm and glass 0.1 dB/cm (Janz, 2004)). LCVD was also used for fabrication of thin film capacitors as filed in a patent by Baeuerle, 1989.

The free-form direct writing of helical shapes were proposed to be used in micro mechanical springs, micro-solenoids and terahertz antennas (Dean et al., 1999), with a patent filed for terahertz antenna fabrication using LCVD by Clark and Jr, 2001. LCVD is also used to synthesize fibres and Maxwell, 2010 holds a patent for the synthesis of woven fibres using LCVD. Production of fibres was also the focus of a commercial spin-off company, Free Form Fibers, which uses pyrolytic LCVD to produce various fibres of boron, silicon carbide, tungsten, tungsten carbide and carbon.

2.6 Metal-graphene contacts through LCVD

A potential application that has not been explored is direct writing of conductive metal tracks to two-dimensional nano-materials such as graphene. Graphene is a single atomic layer of graphite with the carbon atoms organised into a hexagonal lattice. Graphene has been demonstrated to have room temperature mobility as high as 10,000 $cm^2\ V^{-1}\ s^{-1}$ (Novoselov et al., 2004) which is higher than that of expensive high performance III-IV GaAs semiconductors (6500 $cm^2\ V^{-1}\ s^{-1}$ (Beard et al., 2000)). The high mobility values permits the creation of very high frequency devices such as for radio frequency circuit applications and low noise amplifiers (Reddy et al., 2011). Besides those applications, the sensitivity of graphene to molecules and atoms enables a plethora of sensor devices including those that can detect the analyte at parts per billion (Allen et al., 2010a), gas sensors (Toda et al., 2015), and DNA, small molecules and protein detectors (Green and Norton, 2015). The nano-scale size of graphene enables high density storage of electrical charge in energy conversion and storage devices (Bonaccorso et al., 2015).

Graphene can be synthesized through mechanical exfoliation, reduction of graphite oxide, and CVD (Allen et al., 2010b). For CVD growth, graphene is grown on metal catalyst films such as copper at high temperatures (1065ºC) (Braeuninger-Weimer et al., 2016). The graphene films were then transferred to 280 nm SiO_2/Si wafers using a wet transfer method. PMMA, which was used as the sacrificial transfer layer, was then removed using acetone and isopropanol.

Typically once transferred to the substrate, the graphene would be patterned using electron beam lithography (Peng et al., 2015) (Watanabe et al., 2012). The patterned micro graphene device requires larger and more robust contact pads or wire connections to other micro electronics devices. Usually, metal thin film contacts pads or wires would be deposited on the graphene through photolithography, evaporation of the metal onto the graphene and lift-off (Wang et al., 2015) (Politou et al., 2015) (Peng et al., 2015) (Du et al., 2014).

2.6.1 Metal-graphene contact resistance

In metal-semiconductor junctions, a potential energy barrier for electrons is formed and this is known as the Schottky barrier (Tung, 2014). Metal-semiconductor junctions that have large Schottky barriers have rectifying properties and act as diodes. Junctions where the Schottky barrier is too low form Ohmic contacts that are not rectifying. The height of the Schottky barrier depends on the difference between vacuum work function of the metal and the vacuum electron affinity of the semiconductor. If the work function of the metal is close to the vacuum electron affinity of the semiconductor, the Schottky barrier will be low and Ohmic junctions with low contact resistance are expected.

However for metal-graphene contacts, the difference between the work function of the metal and graphene (4.89–5.16 eV (Song et al., 2012)) is not the only determining factor for contact resistance (Giubileo and Di Bartolomeo, 2017). The metal-graphene contact resistance is determined by chemical bonds, electronic structures and geometry of the interface. For example, palladium, gold and nickel all have approximately the same work function of 5.1-5.15 eV (Michaelson, 1977), however their metal-graphene contact resistance are different. Palladium forms weak carbide bonds with graphene, has good graphene wettability (Song et al., 2012), and has the lowest contact resistance of 2.8 kΩ μm (Politou et al., 2015). Gold has no carbide formation with graphene has a contact resistance of 3.9 kΩ μm (Politou et al., 2015). Nickel forms nickel carbide with graphene and has the highest contact resistance of 9.3 kΩ μm.

The contact resistance in metal to CVD grown graphene is typically at the order of 1 kΩ μm (Politou et al., 2015), however the contact resistance can be reduced by cleaning of source/drain contact areas before the metallization (Li et al., 2014), creating double contacts geometry (Franklin et al., 2012), and patterning of contact region (Franklin et al., 2012).

2.6.2 Laser deposition

For pyrolytic LCVD writing on graphene, the main concern is the thermal damage threshold of graphene with respect to the required deposition temperature. In vacuum, single layer graphene can survive temperatures above 2000 ^{o}C (Table 3). This temperature was higher than the estimated peak temperature reached in the ultrafast laser deposition mentioned in section 5.1.4. In reducing environments, the highest temperature reached was 700 ^{o}C and in air, it was 500 ^{o}C.

Table 3: Thermal stability of graphene in air, reducing atmosphere and vacuum conditions.

Graphene growth method	Substrate	Heating environment	Maximum stable temperature (ºC)	Reference
CVD grown on copper.	Suspended.	Joule heating in vacuum inside TEM platform.	2327	Kim et al., 2010
Mechanical exfoliation and CVD grown graphene.	Suspended.	Vacuum (<10^{-4} mBar).	2527	(Kim et al., 2015)
CVD grown on nickel.	SiO_2/Si.	Reducing atmosphere (6 sccm H_2, 144 sccm Ar at 1 Bar).	700	(Kahng et al., 2012)
Mechanical cleavage and CVD grown on copper.	SiO_2 300 nm on Si.	In air at atmosphere.	~500	(Nan et al., 2013)

The next consideration is the optical properties of graphene (Table 4). For a single layer of atoms, the absorption of a single layer of graphene in the range of 400-2480 nm is large at 2.3 %. Overall however, the absorption is small and the heating of the substrate would mainly rely on the laser absorption of the SiO_2/Si layer below. Graphene has a high thermal conductivity of approximately 5000 W/m·K (Balandin et al., 2008) compared to copper 400 W/m·K. However, the laser heating would be localised due to the ultrafast time duration of the ultrafast laser pulse used in this study.

Table 4: Optical reflectivity, absorption and transmission spectra of graphene.

Graphene growth method	Substrate	Wave-length (nm)	Reflectivity, absorption, transmission spectrum	Reference
Mechanical exfoliation.	SiO_2/Si.	1033-2480	9% increase in reflectance over base substrate. Absorption is wavelength independent at around 2.3%.	Mak et al., 2008
Mechanical cleavage.	None (suspended).	400-750	2.3% per layer of graphene.	Nair et al., 2008

2.6.3 Advantage of laser metal deposition

The processes involved in the conventional and laser-based graphene patterning and metal deposition is seen in Figure 23. The first advantage is the reduction in the number of process steps. This leads to a reduction in the process time and the process cost, enabling rapid prototyping of graphene devices. Another advantage in the laser-based graphene patterning is the elimination of alignment errors. In the conventional process, the patterned graphene would need re-alignment for the lift-off exposure phase. In the laser-based process, the patterning and laser deposition would be done in the same system without the need for re-alignment.

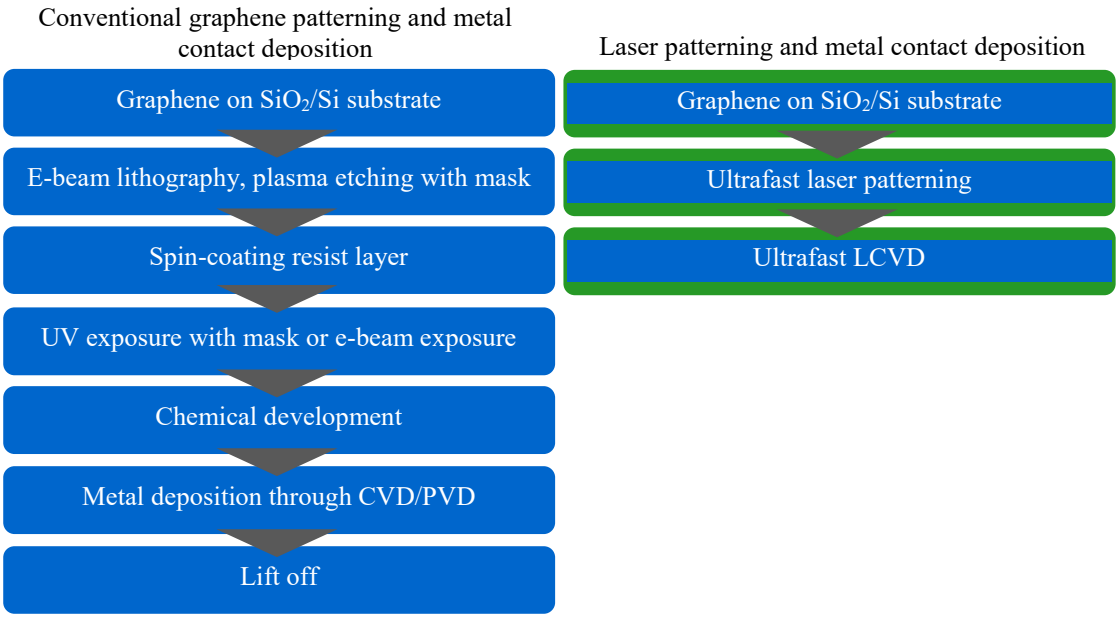

Figure 23: Process steps for (left) conventional and (right) laser-based graphene patterning and metal contact deposition. Adapted from (Feng et al., 2012) (Wang et al., 2015) (Politou et al., 2015).

2.6.4 Raman analysis

To assess the quality of graphene before and after the laser patterning and deposition processes, Raman spectroscopy would be used. Raman spectroscopy is a versatile tool for graphene research due to the ability to determine the number (Ferrari et al., 2006) and orientation of layers (Cancado et al., 2008), the quality and type of edges, doping (Beams et al., 2015), and disorder in graphene (Lucchese et al., 2010). The presence of graphene and the number of graphene layers can be inferred from the Raman 2D peak at approximately 2700 cm^{-1} as seen in Figure 24 (a). Single layer graphene exhibits a sharp 2D peak and the width of the peak increases and the peak blue shifts with increasing number of graphene layers. Amorphous carbon, for example from candle soot, does not have observable 2D peaks but has D and G peaks (Figure 24 b). The presence of edges can be deduced from the disorder-induced D and band as seen in Figure 24 (c, d). The Raman signal taken at the edge (square symbol) of the single layer graphene has D bands which were not observed in the signal taken at the centre (circle spectrum). The effect of increasing defect density in the single layer graphene can be deduced from the D and G peak (Figure 24 e). As the number of defects increased, the D peak rose while the G peak declined and broadened. The doping in graphene can be gauged from the ratio of the 2D to G peak (Figure 24 f). The ratio of the 2D to G peak decreases with increasing dopant amount.

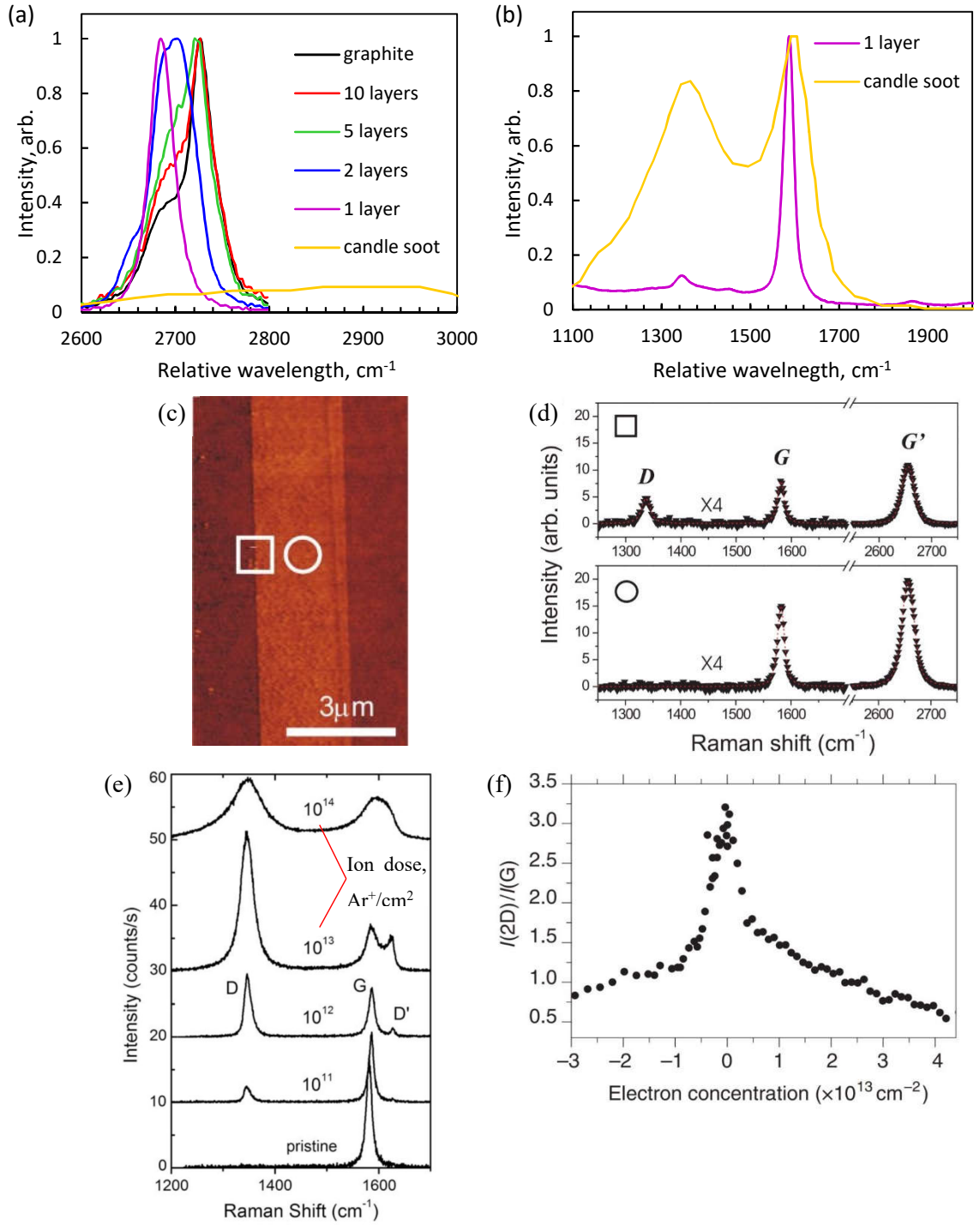

Figure 24: Raman spectrum of: (a, b) single and few layer graphene, graphite and amorphous carbon (candle soot) as reported in (Ferrari et al., 2006) and (Escribano et al., 2001); (c, d) single layer graphene at the edge and in the middle of the sample (Cancado et al., 2008); and (e) pristine and Ar^+ ion bombarded single layer graphene (Lucchese et al., 2010). (f) Ratio of Raman 2D peak to G peak intensity at various levels of doped graphene (Beams et al., 2015).

2.7 Summary

This chapter has given an overview of the theories involved in LCVD and the work of other investigators in this field. There are two main dissociation mechanisms in LCVD. In pyrolytic LCVD, the laser

indirectly dissociates the precursor by heating the substrate. In photolytic LCVD, the laser directly dissociates the precursor by cleaving chemical bonds. Pyrolytic LCVD achieves higher deposition rates and deposition purity but is more substrate dependent compared to photolytic LCVD. The precursors used in LCVD are generally precursors used in CVD. Various metals, such as aluminium, copper, gold, platinum, and tungsten can be deposited in LCVD. Other materials that can be deposited include ceramics and nano-materials.

The literature survey has showed that ultrafast lasers have only been explored for photolytic LCVD, and not pyrolytic LCVD. Due to the potentially low reaction time when using ultrafast pulses, the repetition rate of the laser should be set to the maximum to observe deposition in the pyrolytic ultrafast LCVD experiments. The literature survey also showed that tungsten hexacarbonyl would be a good precursor for this study due to the high deposition rates and good resistivity of 1.8 to 5.4 times bulk tungsten resistivity achieved by investigators. This precursor is transparent to the laser above the wavelength of 350 nm and below 5 μm, making it suitable for pyrolytic LCVD using lasers between those wavelengths. This precursor has also been extensively studied in pyrolytic LCVD, photolytic LCVD, CVD, FIB deposition and electron beam deposition thus there would be good comparison cases. The use of high wall plug efficiency laser diodes for CW pyrolytic LCVD has not been explored in the literature. Laser diodes from Blu-ray DVD drives have been used to develop photolithography resists. This study will explore using these laser diodes for CW pyrolytic LCVD and the results will be used as comparison to the pyrolytic ultrafast LCVD results.

Chapter 3 Experiment materials and methods

This chapter explains the materials, laser sources, precursor delivery components, experiment set-up, experiment procedures and analysis methods used in the experiments of this study.

3.1 Materials

The two main groups of materials used in this study were the substrates and precursors. Substrates from various groups of materials were used in this study including metals, semiconductors, glass, and polymers. Stainless steel grade 304 (SS304), from Cutting Technologies Ltd. UK, was used due to the low thermal diffusivity which was ideal for pyrolytic LCVD. Silicon was the main substrate material investigated in this study due to its prominence in micro-electronic devices and graphene electronic devices (Ferrari et al., 2015). The silicon substrate used in this study has a 280 nm thick thermally grown oxide layer and is referred to as SiO_2/Si substrate in this thesis. The insulating oxide layer on the substrate was necessary so that the conductivity of silicon did not affect the resistivity measurements. The deposited metal in this study, tungsten, has a very high melting point of 3422ºC. This indicates strong metallic bonds which are difficult to overcome for the metal atoms to diffuse into dielectrics such as silicon oxide (He and Lu, 2012). The stability of tungsten on silicon oxide is evidenced by its usage as gate metal-oxide-silicon capacitors (Shang et al., 2001) and tungsten plug diffusion barriers (Luoh et al., 2008). Glass was studied because it was transparent to CW light but opaque to ultrafast laser pulses. The glass used in this study was Pyrex 7740 borosilicate glass. Polymers have low thermal damage thresholds and would likely be damaged by the pyrolytic LCVD process. Polyimide (3M Kapton tape) was used in this study because it has one of the highest thermal damage thresholds for polymers. All substrates were cut into rectangles smaller than 20 mm on each side. The SS304 substrates were cut to size using a Struers Secotom 10. The silicon wafers were cut to size by first making a small scratch with a diamond tip then cleaving the wafer. After cutting to size the substrates were cleaned using by an isopropanol ultrasonic bath for 5 minutes and blown dry with filtered compressed air or nitrogen.

The precursors used in published works are compared in Table 5 in terms of costs and handling details. Although the aluminium precursors were low cost and produced good conductive metal tracks in Table 2, there was difficulty in handling the precursors due to spontaneous ignition behaviour in air and water. To avoid air and water, these precursors need to be loaded into the deposition system inside a glove box filled with inert gas. Due to leakages into the vacuum system, the whole system would need to be kept and operated inside the glove box to avoid degradation of the precursor. This requirement was difficult to meet in terms of resources available.

Table 5: Precursors, deposited metals, costs, deposition temperatures and important details regarding the stability and handling of these precursors.

Chemical precursor name and Chemical Abstracts Service code	Deposition metal	Cost per gram (GBP) and product code	CVD deposition temperature (ºC) and literature	Precursor stability and hazards
Trimethylaluminium Al(CH3)3	Al	2.50 (Sigma Aldrich 257222)	NA	Spontaneously ignites in air and water. Causes severe skin burns and eye damage.
Triisobutylaluminium [Al(CH2CH(CH3)2)2H]3	Al	1.11 (Sigma Aldrich 257206)	200-400 (Luo and Gladfelter, 2008b)	Spontaneously ignites in air and water. Causes severe skin burns and eye damage.
Copper(II) hexafluoroacetylacetonate Cu(CF3COCHCOCF3)2 14781-45-4	Cu	99.00 (Strem 29-2928)	340-390 (Temple and Reisman, 1989)	May be fatal if swallowed. Causes severe skin burns and eye damage.
Copper(II) acetylacetonate Cu(CH3COCHCOCH3)2 13395-16-9	Cu	0.78 (Strem 93-2968)	180-200 (Griffin and Maverick, 1994)	Requires hydrogen carrier gas. Causes skin and eye irritation.
Dimethyl (acetylacetonate) gold(III) (CH3)2(C5H7O2)Au 14951-50-9	Au	3080.00 (Strem 79-1500)	200-300 (Larson et al., 1987)	Handle and store in inert gas.
Dimethyl (trifluoroacetylacetonate) gold(III) (CH3)2Au(CF3COCHCOCH3) 63470-53-1	Au	3080.00 (Strem 79-1600)	200-300 (Larson et al., 1987)	Fatal if inhaled. Handle and store in inert gas.
Platinum(II) hexafluoroacetylacetonate Pt(CF3COCHCOCF3)2 65353-51-7	Pt	522.00 (Strem 78-1550)	NA	Causes skin and eye irritation.
Platinum(II) acetylacetonate Pt(CH3COCHCOCH3)2 15170-57-7	Pt	99.00 (Strem 78-1400)	500-600 (Zinn et al., 1994b)	Causes skin and eye irritation.
(Trimethyl) methylcyclopentadienyl platinum(IV) (CH3)3(CH3C5H4)Pt 94442-22-5	Pt	256.50 (Sigma Aldrich 645605)	90-180 (Zinn et al., 1994b)	Requires hydrogen carrier gas.
Tungsten hexacarbonyl W(CO)6 14040-11-0	W	19.00 (Strem 74-2202)	375-540 (Lai and Lamb, 2000)	Toxic if swallowed.
Vinyltriethylsilane (hexafluoroacetylacetonato) silver(I) Ag(CF3COCHCOCF3)(C8H18Si) 177279-28-6	Ag	47.00 (Strem 47-8000)	>180 (Gao et al., 2004)	Causes skin and eye irritation.
Palladium(II) hexafluoroacetylacetonate Pd(CF3COCHCOCF3)2 64916-48-9	Pd	73.30 (Sigma Aldrich 401471)	353-473 (Garcia and Goto, 2003)	Requires hydrogen carrier gas. Causes skin and eye irritation.

Both the gold precursors and platinum(II) hexafluoroacetylacetonate used in literature were relatively costly for this initial study but may be considered in the future. Tungsten hexacarbonyl was chosen as

the precursor because it was stable in air, the deposition results were good (Table 2), and the cost of the precursor was relatively low. The tungsten hexacarbonyl used in this study was of 99% purity and supplied by ACROS Organics.

A few precursors required hydrogen as a reducing gas (trimethyl methylcyclopentadienyl platinum(IV), palladium(II) hexafluoroacetylacetonate, and copper(II) acetylacetonate). These precursors can be tested in the future since the set-up was designed to work with hydrogen. The platinum precursor, platinum(II) acetylacetonate required a comparatively high deposition temperature of 500-600 °C. This precursor would be interesting to investigate with the ultrafast LCVD since high deposition temperatures of over 1000 °C were achieved in this process (section 5.1.4).

3.2 Laser sources

In pyrolytic LCVD, the focused laser spot is used to heat the substrate to the deposition temperature. A 405 nm CW laser diode was used for pyrolytic CW LCVD experiments and a 1030 nm ultrafast laser was used for pyrolytic ultrafast LCVD experiments.

3.2.1 405 nm continuous wave laser

Most pyrolytic LCVD researchers have used a wavelength of around 500 nm from argon ion lasers (section 2.3), however as mentioned previously, a wavelength closer to 370 nm is more suitable to achieve a shallow optical penetration depth in silicon.

Based on simulations of the substrate temperature exposed to a focused laser (section 3.5.6), 250 mW of power with a focused spot diameter of 8 μm ($1/e^2$) at a wavelength of 405 nm was required to raise the temperature of a silicon substrate to 527 ºC at the laser spot (section 4.1). This temperature was above most deposition temperature of the precursors of interest in this study (Table 5). Based on these requirements, quotes from commercial provides were sought and the details of their laser specifications is seen in Table 6. The cost was at least GBP 5,000 and the output power was at least 200 mW. The Vortran Stradus 405-250 laser was the best commercially available laser for use in pyrolytic LCVD with silicon based substrates because it has the lowest wavelength with the highest maximum power output.

Table 6: Cost and specifications of relevant commercially available blue diode lasers.

Laser type	Vortran Stradus 405-250	Coherent Sapphire 488-200 CW	Melles Griot 56 CRN
Cost from quotations Nov 2015 (GBP)	6,500	10,000	4,676
Wavelength (nm)	405	488	405
Maximum output power (mW)	250	200	200
M2 value	<1.25	<1.2	<1.5
Beam asymmetry /circularity ratio	0.9	0.9	0.95
Beam diameter (mm)	1.4	0.7 ± 0.05	0.69 - 1.09
Focused spot diameter with 10 mm focal length objective (µm)	4.6	10.7	8.9

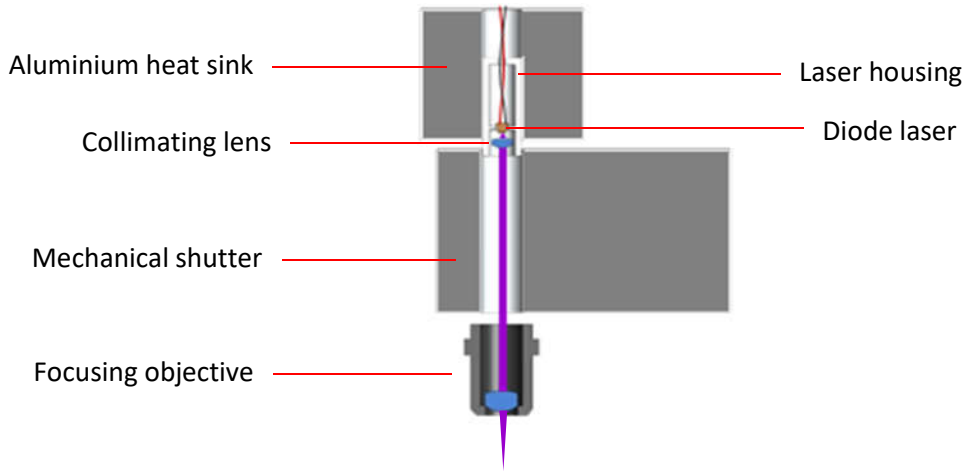

Figure 25: Diagram of CW 405 nm laser diode set-up.

Instead of purchasing the Vortran Stradus 405-250 laser, a blue laser diode from a Pioneer BDR-209DBK Blu-ray disc writer was removed and connected to a 12 V power supply with a LM317T regulator in current adjust configuration with several other diodes to protect the diode laser against reverse and excess current exposure. The laser diode was then mounted in a housing, which was fixed inside a block of aluminium that acts as a heatsink (Figure 25). Using a Spiricon LBA-FW SCOR 20 beam profiler, the beam divergence of the laser diode was measured to be 14.0 ° and 7.6 ° respectively in the fast and slow axis. An Odicforce Lasers 405 nm AR coated NA 0.5 aspheric lens with a focal length of 4.02 mm and a transmission of 99.1 % was used to collimate the output of the laser diode to a $1/e^2$ beam diameter of 3.0 and 1.4 mm respectively in the fast and slow axes. The collimated beam was focused down using a Comar Optics 20 DQ 10 objective that has a focal length of 20 mm and a transmission of 87.1 %. The $1/e^2$ focal spot diameter was measured to be 5.4 ± 0.4 and 9.4 ± 0.4 µm respectively in the fast and slow axes (Figure 26) using the Spiricon LBA-FW SCOR 20 beam profiler. A 4.2 mm focal length lens was used to magnify the laser focal spot and the beam profiler field of view was calibrated using a microscope grating. There was no difference in the measured beam diameters when a 3 mm thick glass window was placed in between the focal point and the objective, however the focal distance from the objective to the focal point increased.

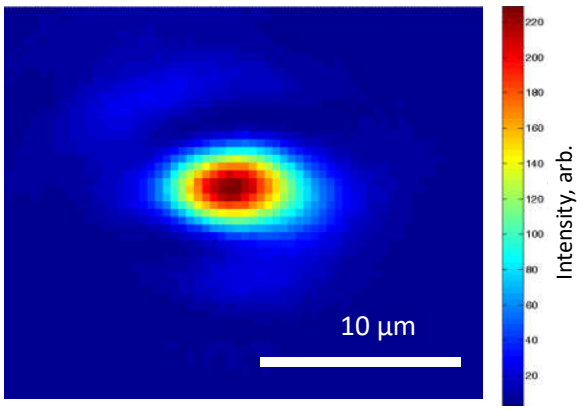

Figure 26: Measured intensity profile of focused beam spot.

The output power of the collimated beam was measured using a Coherent LM-3 air-cooled thermopile against the input current measured using a Fluke 83III Multimeter. The output power to input current relationship is seen in Figure 27. Even though the power output to current relationship is linear at 0.5 A input current, it is not advisable to run the diode laser at that operating point because heat from the diode is not dissipated well enough and a diode was broken after 20 mins at 0.5 A. The laser diode, collimating and focusing optics were mounted on an Aerotech AGS10000 XYZ stage that has a movement resolution of 1.0 µm and position repeatability of 3 µm.

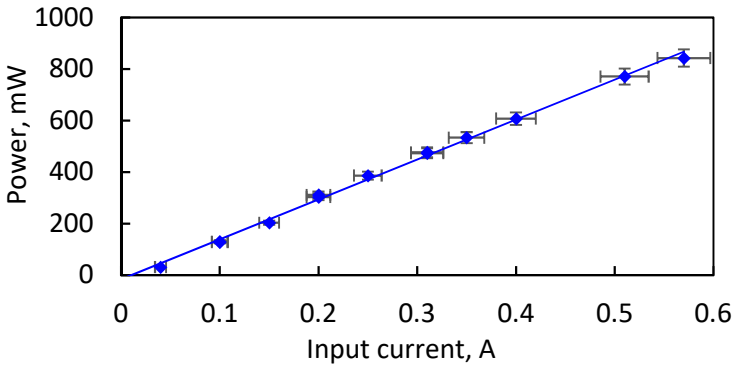

Figure 27: The output power to input current relationship of the laser diode, measured after collimating the beam.

3.2.2 1030 nm ultrafast laser

Table 7: Ultrafast laser parameters

Laser model	Amplitude Systemes Satsuma
Wavelength	1030 nm
Pulse duration	300 fs
Pulse repetition rate	502 kHz
Beam radius	2.2 mm
M^2	1.1
Maximum pulse energy	10 µJ
Maximum average power	5 W
Calculated focused diameter	6.6 µm (20 mm focal length) 33 µm (100 mm focal length)

For the ultrafast pulsed laser dissociation of the precursor, an Amplitude Systemes Satsuma laser was used. The parameters of the laser are in Table 7. The pulse duration was measured using an APE

PulseCheck autocorrelator while the laser output power was measured using a Thorlabs S121C power meter. The experimental setup using this laser is schematically shown in Figure 28. The linear polarization angle of the laser beam was controlled by rotating a half-waveplate and circular polarization was obtained by replacing the half-waveplate with a quarter waveplate. Motion of the focal point on the substrate was achieved using a XYZ Aerotech stage and fixed number of pulses control was attained through pulse synchronized output of the Aerotech controllers. The position repeatability of the XYZ Aerotech linear stages that was equipped with air-bearings was 1 μm.

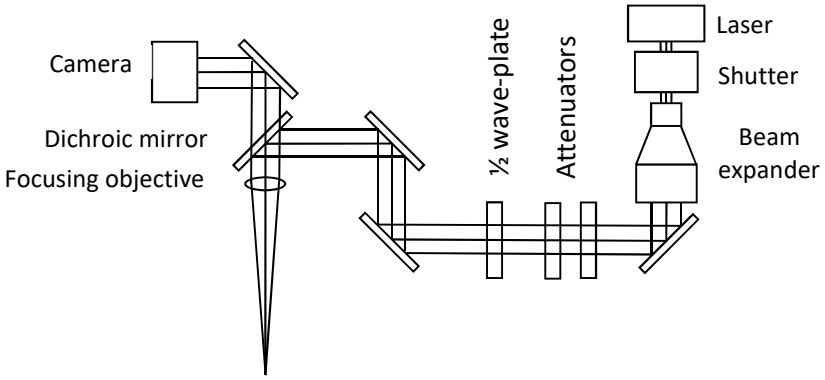

Figure 28: Schematic of the ultrafast laser setup used in the experiments.

3.3 Vacuum system

The main components of the vacuum chamber were the deposition chamber, precursor container, heaters, valves, pressure measurement devices, vacuum pipes and the vacuum pump.

3.3.1 Deposition chamber

A vacuum deposition chamber was designed and machined using SS304 with a low aspect ratio to accommodate the short focal length of the objectives used in this study (CAD in Figure 29). The laser was focussed through a 3 mm thick transparent glass window (UQG FVI-503C AR coated fused silica window or UQG WSC-503 sapphire window) to reach the substrate. A K-type thermocouple was placed externally, in a drilled hole, 1 mm under the substrate to monitor the substrate temperature. Vacuum compatible ports for connecting the thermocouple inside the vacuum system were not used because the required size of commercially available ports was too large for the required low aspect ratio design mentioned previously. Threaded pipe adapters, Pfeiffer KF to BSPP ISO G adapter with O-rings, were used to link the deposition chamber to the precursor container, pressure gauge and vacuum pump.

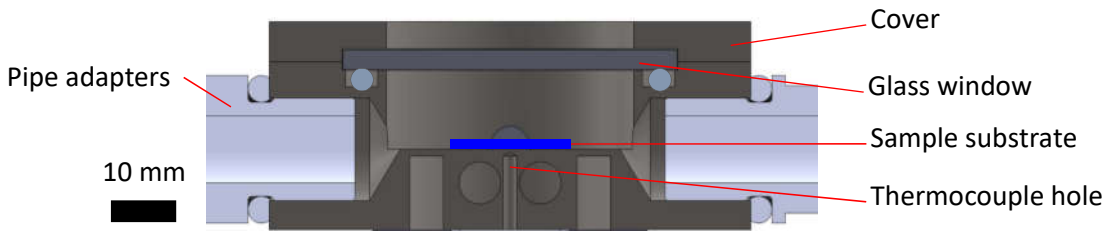

Figure 29: CAD cross-section of deposition chamber.

3.3.2 Precursor container

An early version of the vacuum deposition system used a non-refillable cylinder from Sigma Aldrich that was pre-filled with 25 g of tungsten hexacarbonyl. However, only approximately 200 mg of material was needed for each batch of experiments. Repeated heating of the precursor for each experiment, even below the dissociation temperature, could potentially contaminate and degrade the precursor. A custom designed precursor container was machined using SS304 (CAD in Figure 30). A 2 ml glass vial loaded with approximately 200 mg of tungsten hexacarbonyl fits inside the container. This vial was refilled with tungsten hexacarbonyl for each experiment. A thermocouple was placed inside a drilled hole where the wall thickness was only 1 mm to achieve temperature reading of the precursor.

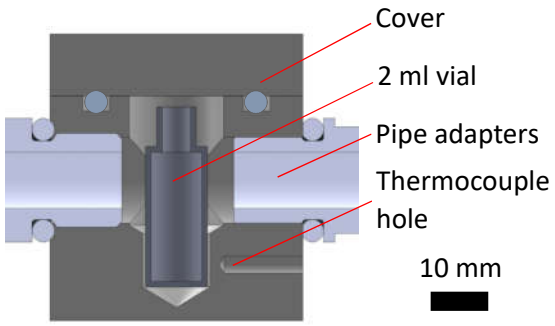

Figure 30: CAD cross-section of the precursor container.

3.3.3 Heaters

A total of five Omega Engineering CN 7800 PID controllers were wired-up (schematic and picture seen in Figure 31) to control the surface temperature of the precursor container and the deposition chamber. The precursor container heater heats the precursor to the vaporization temperature to sublime the precursor. The other heaters heat the vacuum pipes and deposition chamber to prevent condensation of the precursor on the internal walls. The heating tapes used were Omega Engineering DHT series high temperature, dual-element heating tapes that can withstand 760ºC and supply heat at a power of 2 W/cm^2. These tapes were wrapped around the external walls of the vacuum system and covered with crumpled aluminium foil that served to reduce heat loss.

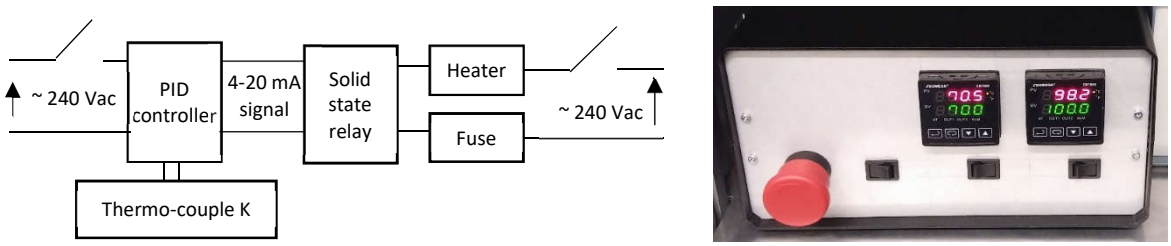

Figure 31: (left) Wiring schematic for the PID controller of the tape heater. (Right) Picture of two assembled temperature controllers panel mounted to an electrical enclosure.

3.3.4 Valves

The ball valves used in this study were Pfeiffer Vacuum ISO-KF ball valves which were specified for operating in the pressure range of 10^{-5} – 500 mBar, has a seal tightness of 10^{-6} mBar l/s and can be heated to 80 °C. The ball valves were used to shut off the flow and open the flow without adding any constriction to the pipe because the diameter of the channel through the opened ball valve was equivalent to the vacuum pipe diameter. The other type of valve used in this study were needle valves. These valves have conical regulator to control the size of the opening and flow-rate. For this study, Swagelok H series bellow sealed needle valves were used. These needle valves have been helium leak tested by the manufacturer to have a maximum leak rate of 4 x 10^{-9} cm^3/s.

3.3.5 Pressure measurement devices

Two types of pressure gauges were used in this study. The first was a Bourdon gauge from Kurt J Lesker. This gauge was a bent tube that deformed with a change in pressure. The deformation was amplified by levers to give the pressure reading. The measurement range for this gauge was between 10 – 1000 mBar of absolute pressure. This gauge was used to detect rough vacuum and atmosphere pressure especially when bleeding in nitrogen into the vacuum chamber to reach atmosphere. The second pressure gauge was a Pirani type gauge from Edward Vacuum, APG100-XLC. This gauge measures pressure by measuring the heat flux from a hot wire to the surrounding inside vacuum. The measurement range of this type of gauge was from 10^{-3} to 10 mBar. This was the main vacuum pressure gauge used in this study and the deposition pressure was measured using this gauge.

3.3.6 Vacuum pumps

The deposition pressure in the experiments were from 0.1 – 5 mBar. Due to the increase in pressure from the vacuum pipes and filter, the vacuum pump must reach a pressure one or two orders of magnitude lower than the pressure in the deposition chamber. A Leybold Trivac D4B rotary vane vacuum pump was used because these pumps can achieve pressures of 10^{-4} mBar. This model was also ATEX (European Directives for controlling explosive environments) rated to Category 3 meaning that under normal operation, there were no ignition sources inside the pump. Thus, hydrogen can be used in the vacuum system if necessary. A hose was connected to the exhaust of this vacuum pump for venting

out of the building. This was done to ensure that any precursor vapours that escapes the filter placed before the vacuum pump was vented out of the building.

3.3.7 Overall system

A plan view and picture of the vacuum deposition system is seen in Figure 32. There were two precursor containers however only precursor container #1 was used in this study. Precursor container #2 was incorporated in the final set-up for future work. Nitrogen flowed to precursor container #1 through a needle valve. Precursor container #1 was linked to the deposition chamber. The output of the deposition chamber branched to the Pirani pressure gauge and the activated carbon and HEPA filter. The Pirani pressure gauge can be shut-out using a ball valve if gases capable of damaging the gauge were used in the system.

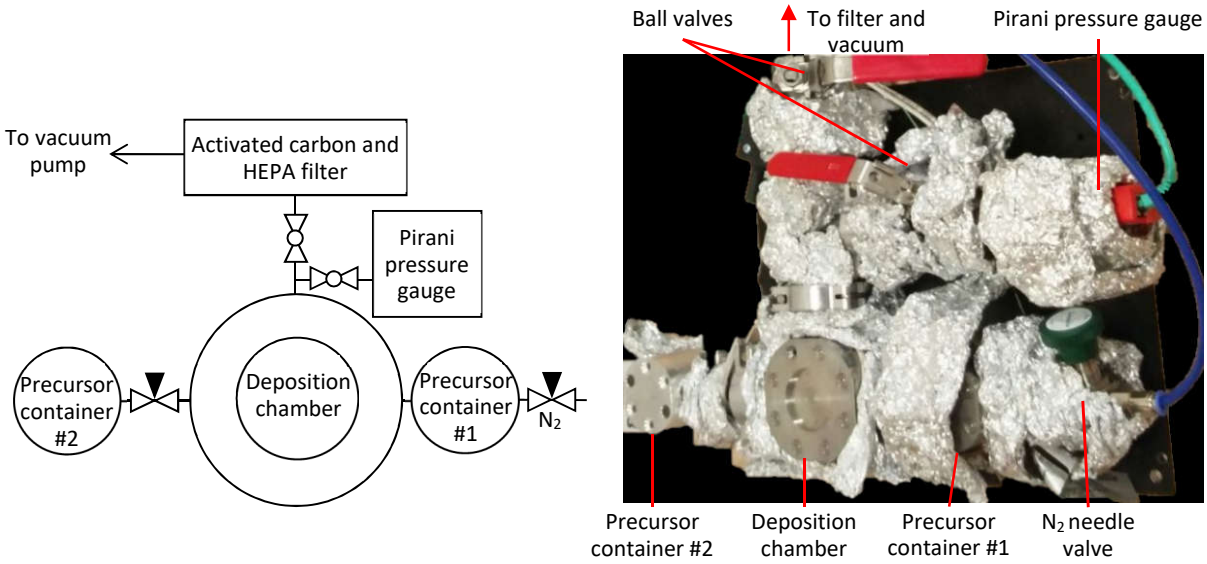

Figure 32: (left) Plan view schematic and (right) picture of vacuum deposition system.

In one of the previous set-up arrangements, there was a ball valve between the deposition chamber and precursor container #1 to shut-out the precursor from the system. During experiments, the deposition system would first be pumped down to 0.1 mBar then this ball valve was closed while the precursor container was heated to vaporise the precursor at 45-85 °C for 20 mins. When the ball valve was opened, the precursor vapour would expand adiabatically into the deposition chamber and condense the precursor vapour into microscopic powders seen in Figure 33. To avoid the condensation due to pressure differences, this ball valve was removed and the vacuum system was filled with nitrogen after pumping down to 0.1 mBar. Then the precursor container was heated to sublime the precursor and the vacuum system was pumped to the desired deposition pressure.

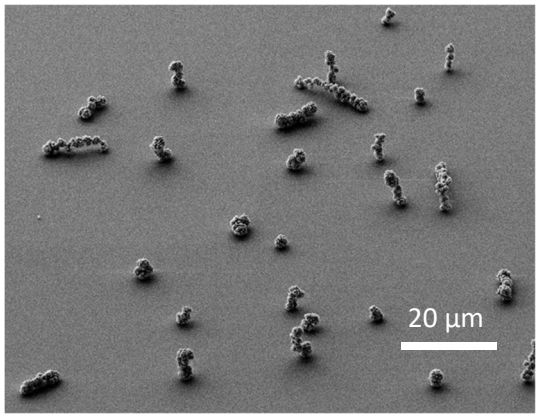

Figure 33: SEM image of the precursor condensed into powders on the substrate after the ball valve to the precursor container, heated to 85 ^{0}C, was opened.

3.4 Deposition procedure

Before the deposition experiment, the system was outgassed by heating the walls to 70 °C and vacuum pumping to 0.01 mBar for a few hours. Once the system was purged, it was filled with nitrogen to 0.5 bar above atmosphere and the precursor container was left to reach room temperature while the rest of the system was kept at 70 °C. With the nitrogen flowing, a vial with 200±20 mg of tungsten hexacabonyl was placed into the precursor container. The sample substrate along with a sacrificial focus finding substrate was placed in the deposition chamber. For the ultrafast laser, the sacrificial focus finding substrate was typically silicon wafers. However, the 405 nm CW laser does not have sufficient power to machine most materials except polyimide. Thus, a 40 µm Kapton polyimide film was placed onto another sacrificial sample and used as the focus finding material. The focus height was found by inspecting the tracks ablated by the laser at various height settings. The middle height where ablation was observed was taken as the focal point with adjustments for difference in height between the sample substrate and the sacrificial focus finding sample.

After finding the focus, the deposition system was pumped down to 0.1 mBar absolute pressure. Then, nitrogen gas was bleed into the chamber to approximately 0.5 bar above atmosphere. The precursor container was then heated to 45 – 85 °C for a heating time of 20 mins. After the heating, the valve connecting the system to the vacuum pump was gradually opened to pump the system to 0.32 mBar. Once reaching that pressure, this valve was throttled to keep the pressure inside the system at the desired deposition pressure. The laser was then scanned in focus on the sample substrate at the desired laser settings. All experiments were kept to a maximum of 30 mins because the 200 mg precursor was known to be depleted after 30 mins.

After the experiment, the valve throttling the flow to the vacuum pump was closed and the system was filled with nitrogen. The precursor container was turned off and a heat sink was placed on top of the container to aid cooling to room temperature. After 20 mins of cooling, the system was vented and refilled with nitrogen then the samples and precursor vial were removed from the system.

3.5 Analysis methods

This section explains the details of the analysis methods employed to evaluate the LCVD process and deposition results.

3.5.1 Optical microscope

The quickest analysis method was to use an optical microscope to view the LCVD written track. Almost all the sample substrates with LCVD written tracks were viewed using bright-field illumination on an Olympus BX51 optical microscope. A rough estimate of the track width can be inferred from the bright-field illumination image. If the deposits were more than a micro-meter tall, the height could be estimated by measuring the distance between the focus point at the top and bottom. The optical microscope image was also used to measure the distance of the track between two conductive pads for the resistivity measurements (section 3.5.4).

3.5.2 White light interferometry

The second most frequently used analysis method in this study was white light interferometry (WLI). For this method, a Veeco Wyko NT3300 WLI was used to vertically scan a broad-spectrum light source over the track to produce interference fringes which were interpreted by a computer to provide surface height information. This device is classified as a non-contact coherence scanning interferometry instrument under International Standard ISO 25178. The device has a vertical resolution of 0.1 nm however the accuracy is highly dependent on the surface being measured (Leach, 2011). The digital lateral resolution of the instrument is 80 nm however the lateral resolution is limited by the Rayleigh criterion to 700 nm. The areal height measurements were taken based on procedures recommended by the National Physical Laboratory Measurement Good Practice Guide (Petzing et al., 2010). A cross-section profile of the deposited track provides height, width and cross-section area information necessary to gauge the speed and quality of the deposit. A single cross-section profile (Figure 34 c) does not provide a statistically good representation of the track cross-section. Therefore, the cross-section profiles were averaged for at least 50 µm length of track. During measurements, errors in tilt was reduced by following procedures in the National Physical Laboratory Measurement Good Practice Guide (Petzing et al., 2010). However, misalignments and errors in tilt (Figure 34 a) were still present in the measurements and these were corrected (Figure 34 b) in MATLAB before the averaging process. The alignment was done by aligning the deposited track to the vertical axis of the page since the averaging was done in the vertical direction. The tilt correction was done by tilting the plane until the background substrate appeared flat. During this adjustment, the height colormap was limited to 0 - 100 nm to emphasise the tilt of the substrate, if any.

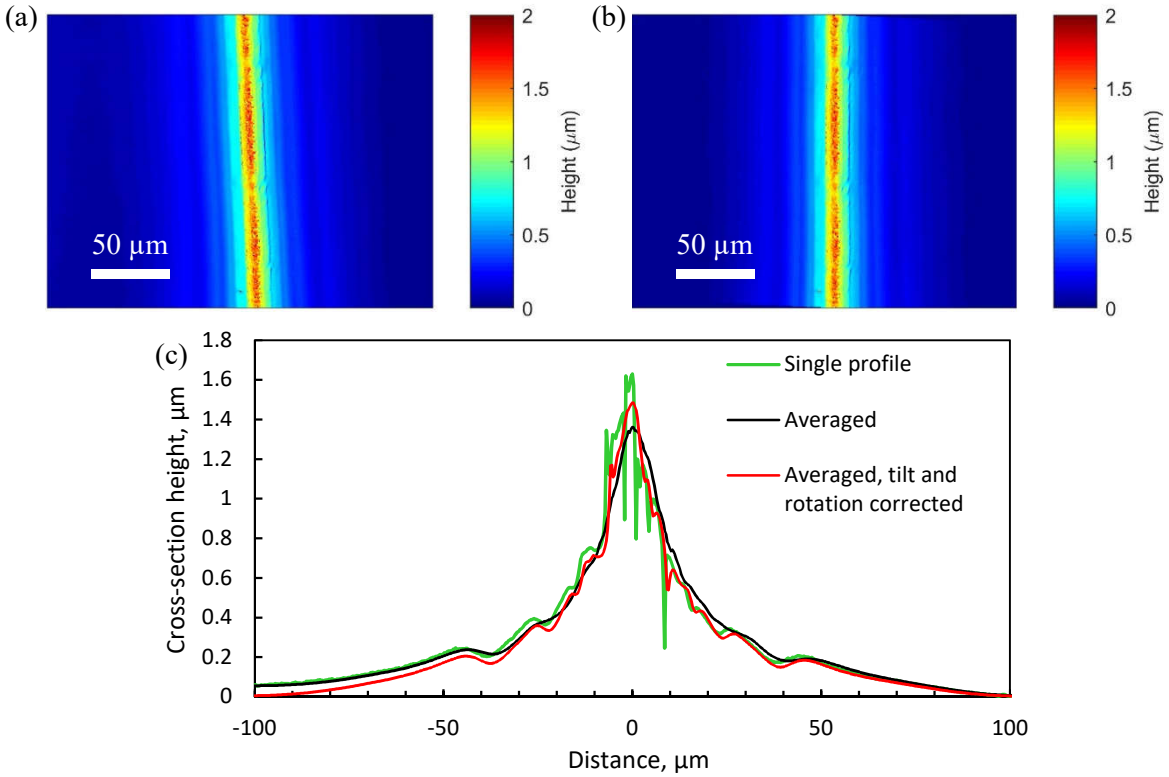

Figure 34: (a) Raw data and (b) tilt and rotation corrected surface height profiles measured through WLI. (c) Single and averaged cross-section height profiles of the raw and corrected data.

For some of the LCVD written tungsten tracks, a layer with a colour gradient was deposited outside the dark central region where the laser spot was scanned as seen in Figure 35 (a). This deposition outside the laser spot seemed to affect the WLI measurements. When the tracks were sputter coated with a thin 10 nm layer of chromium, gold and palladium to give a uniform reflective coating, the WLI measurements changed (Figure 35 b). To confirm that the coated WLI measurements were accurate, a WLI coated cross-section profile measurement was compared to two atomic force microscopy (AFM) measurements (Figure 35 c). The AFM used in this study was an Oxford Instruments Asylum Research MFP-3D AFM. The WLI coated cross-section profile gave a slightly lower surface height reading however the maximum profile height differences were within the ± 8 % uncertainty of the WLI measurements. On average, a single WLI surface area measurement of the deposited track took an acquisition time of 30 s while the AFM measurements took approximately one hour. Thus, WLI measurements were taken after coating for the bulk of the tracks deposited in this study. The coatings were done with an Emitech K575X sputter coater with chromium first at a current setting of 85 mA for ten seconds followed by gold and palladium at 65 mA for twenty seconds.

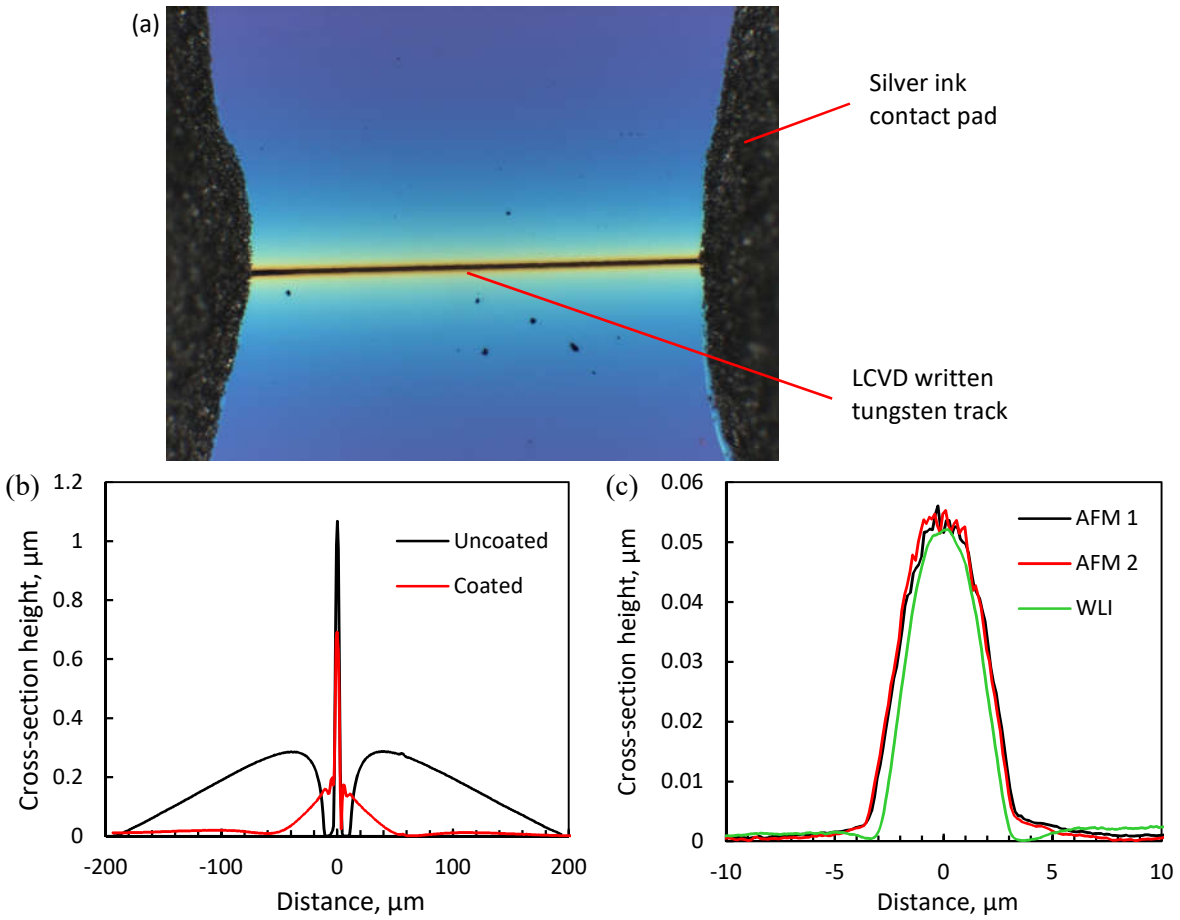

Figure 35: (a) Optical microscope image of a LCVD written tungsten track between two contact pads. (b) Average cross-section height profiles of a LCVD written track measured using a Veeco Wyko WLI system before and after the track was sputter coated with chromium, gold and palladium. (c) Comparison of average cross-section profiles for a LCVD written track measured using WLI and AFM.

Two weaknesses of WLI measurements are data dropout due to high surface gradient (Petzing et al., 2010) and the optical lateral resolution of 700 nm mentioned earlier. Due to these weaknesses, the surface height measurements of the quasi-periodic structures measured in Chapter 5 were not accurate because the structures were almost vertical, and the length periodicity was less than 500 nm. Only height data at the top of the periodic structures where obtained while the bottom of the periodic structures were missing data. Due to interpolation from neighbouring measurement points, the missing data was filled with data from the top of the periodic structures. Thus, the surface measured in the WLI for the quasi-periodic structures were that of an outer surface encompassing a porous volume filled with the quasi-periodic structures.

3.5.3 Scanning electron microscope and energy dispersive X-ray spectra

The microstructure of the deposit was observed using a Zeiss Gemini 1540 XB scanning electron microscope (SEM). The bulk of the imaging was done using an accelerating voltage of 5 kV which provided the best resolution images. For the aperture, the standard aperture of 30 µm was used. The aperture was aligned and stigmation was adjusted each time the SEM was used to ensure sharp images. To get cross-section views of the LCVD written track, the FIB column of the Zeiss Gemini 1540 XB

was used to mill the deposited track. Before the milling was done, the field of view of the SEM and FIB were aligned. Rectangle shaped mills were used with a milling for depth setting of one micro-meter. The substrate setting in the FIB software was set to silicon and the current was set to 500 pA.

The elemental composition of the deposit was analysed using an Oxford Instruments X-Max^N 80 energy dispersive X-ray spectroscope (EDX). The software retrieved SEM images and parameters from the Zeiss Gemini SEM and from there element analysis of specific locations or the entire SEM image can be processed. The beam energy was set to 20 kV to achieve a more accurate elemental analysis since more elemental peaks were detected in the broader energy spectrum. However, the high beam energy increased the penetration depth of the electrons thus the detection volume was larger than one micro-meter in diameter (Goldstein et al., 2003) and penetrated the substrate when the deposition was thin. This created inhomogeneity in the detection volume and inaccuracies in the measurement. Thus, the elemental composition results were not absolute and were only used for detection of the deposited tungsten and impurities, and comparison between different track compositions.

3.5.4 Resistivity measurements

The total resistance of the track (Schroder, 2006), R depends on the contact resistance, $R_{Contact}$ and the deposited track resistance, R_{Film} where

$$R = 2\,R_{Contact} + R_{Film} \qquad [\,9\,]$$

The resistance of the track depends on the resistivity of the deposit, ρ, the length of the film, l and the cross-section area of the film, A where

$$R_{Film} = \frac{\rho l}{A} \qquad [\,10\,]$$

Thus, the resistivity of the deposited track and the contact resistance can be measured by fitting a straight line to the total resistance against length over area of the tracks i.e.

$$R = \frac{\rho l}{A} + 2R_{Contact} \equiv mX + C \qquad [\,11]$$

where $m \equiv \rho$, $X \equiv \frac{l}{A}$, and $C \equiv \ 2R_{Contact}$. This measurement technique is known as the transfer length method or transmission line method (TLM). Another track resistance measurement technique used in this study was the four-point probe method. In this configuration, a known current was fed through a pair of source connections and the voltage drop was measured by another pair of connections. Since there was no current flow in the voltage measurement connections, there was no voltage drop due to the contact and lead resistance. The contact resistance can be calculated by taking the difference between the usual two probe resistance and the four-probe resistance.

The deposited tracks were thin films of around 1 µm thick and at least 5 µm wide, thus, these tracks were too fragile for direct contact with macro-measurement probes. Instead, silver paste was used to as

contacts. A track approximately 10 mm long was written on the substrate, then silver paste (Alfa Aesar silver conductive adhesive paste) was applied across the track to attach copper wires (Figure 34). The silver paste was spaced at a varying distance from one another to achieve the different lengths for the TLM. There were four to six terminals on each track to achieve three to five measurements in the TLM and one to three four-probe measurements. Once dried, electrical clips were attached to the copper wires and the two and four-probe resistance was measured using a Keithley 2000 multi-meter. A control set-up consisting of the substrate and the silver paste with two copper wires was made to account for the resistance in the leads, electrical clips, copper wires, silver paste, and contact resistance between those components. The resistance of this control set-up was measured to be less than 1 Ω, at least two orders of magnitude lower than typical track resistance measured in this study. From the track resistance value, the resistivity was calculated using the track length, which was measured using the optical microscope (section 3.5.1) and the cross-section area, which was measured using WLI (section 3.5.2).

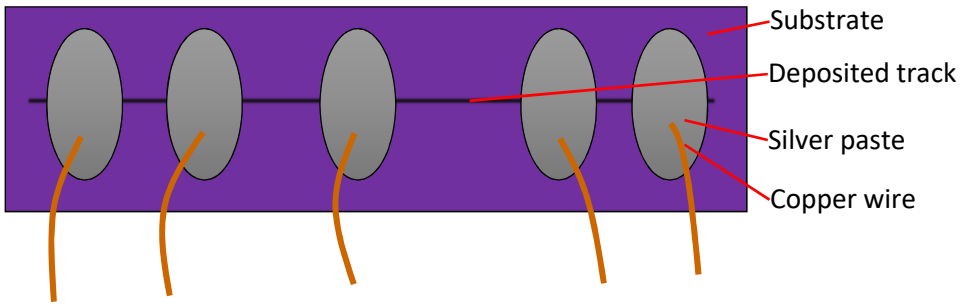

Figure 36: Schematic of substrate, deposited track, silver paste and copper wires made to measure the resistivity of the tracks.

3.5.5 Measurement uncertainty and linear regression analysis

Fitting data to a linear equation (Coleman and Glenn Steele, 2009)

$$Y = mX + c \qquad [\ 12\ ]$$

was done to find the laser modification thresholds (section 2.3.6) and resistivity (section 3.5.4). The best fit using least squares regression would give the following for the slope and Y-intercept

$$m = \frac{n\sum_{i=1}^{n} X_i Y_i - \sum_{i=1}^{n} X_i \sum_{i=1}^{n} Y_i}{n\sum_{i=1}^{n} X_i^2 - \left(\sum_{i=1}^{n} X_i\right)^2} \qquad [\ 13]$$

$$c = \frac{\sum_{i=1}^{n} X_i^2 \sum_{i=1}^{n} Y_i - \sum_{i=1}^{n} X_i \sum_{i=1}^{n} X_i Y_i}{n\sum_{i=1}^{n} X_i^2 - \left(\sum_{i=1}^{n} X_i\right)^2} \qquad [\ 14]$$

The standard error for the slope would be

$$s_m = \left(\frac{s_Y^2}{s_{XX}}\right)^{1/2} \qquad [\ 15\ ]$$

$$s_{XX} = \sum_{i=1}^{n} X_i^2 - \frac{1}{n}\left(\sum_{i=1}^{n} X_i\right)^2 \qquad [\ 16\ ]$$

$$s_Y = \left[\frac{\sum_{i=1}^{n}(Y_i - mX_i - c)^2}{n-2}\right]^{1/2} \quad [17]$$

And the standard error for the intercept is

$$s_c = \left[s_Y^2\left(\frac{1}{n} + \frac{\left(\sum_{i=1}^{n} X_i\right)^2}{n^2 s_{XX}}\right)\right]^{1/2} \quad [18]$$

For data that had multiple sources of error in the measurement, the combined uncertainty was calculated by the summation of quadrature. For the summation of multiple independent errors the combined uncertainty would be

$$\bar{u} = \sqrt{\sum_{i=1}^{n} u_i^2} \quad [19]$$

For uncertainties in products or quotients the combined uncertainty would be

$$\frac{\bar{u}}{\bar{x}} = \sqrt{\sum_{i=1}^{n}\left(\frac{u_i}{x_i}\right)^2} \quad [20]$$

This equation was used to combine the uncertainty in the slope and intercept values with the uncertainty in the measurement of the x and y values. For averaging multiple independent results with different uncertainties, the inverse variance weighted average was used where the weighted average was (Hartung et al., 2008)

$$\bar{x} = \frac{\sum_{i=1}^{n}\frac{x_i}{u_i^2}}{\sum_{i=1}^{n}\frac{1}{u_i^2}} \quad [21]$$

and the uncertainty of the weighted average would be

$$\bar{u} = \frac{1}{\sum_{i=1}^{n}\frac{1}{u_i^2}} \quad [22]$$

Table 8 shows the uncertainty level of various measurements involved in this study. Most of the uncertainty in measurements were lower than ±10 % except the pressure measurements using the Pirani pressure gauge.

Table 8: Combined uncertainty of measurements.

Measurement	Approximate uncertainty
Optical, track length ending with silver paste	±10 μm
Optical, track width	±(Maximum-minimum reading)/$\sqrt{3}$ (Bell, 2001)
WLI	±8%
Resistance	±5%
Pressure measurements	±20%
Substrate temperature measurements	±5%
Laser power measurements	±7%

3.5.6 CW laser deposition temperature simulation

To understand the temperature in the pyrolytic CW experiments, a temperature model was built in COMSOL Multiphysics 5.0. The laser heating was simulated as a moving volumetric heat source in a solid heat transfer model (COMSOL, 2013) governed by the heat equation 3 with the moving volumetric heat input of equation 12. The simulation model domain is shown in Figure 37 along with the coordinate system and the moving laser spot. The domain was a 3D symmetrical model with dimensions of 10×5×0.3 mm and tetrahedral dominant mesh elements. For the top surface, swept prismatic elements with growth factor of two and total swept depth of $3d$ were used to capture the shallow optical penetration depth of the laser. The bottom surface temperature was fixed at the vacuum deposition chamber temperature of 100 °C. Radiative and convective losses were included in the simulation.

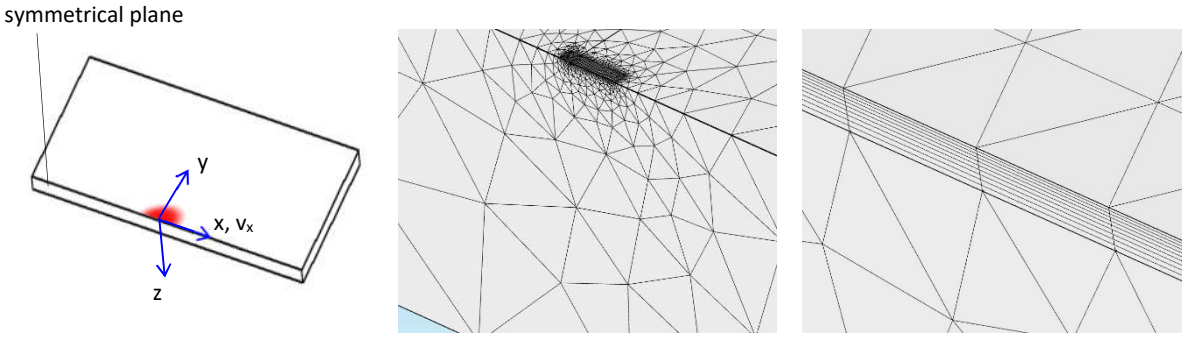

Figure 37: (Left) Simulation domain, coordinate system and laser heat spot that was used in the COMSOL heat transfer simulation. (Centre) Meshed domain with tetrahedral dominant elements and (right) close-up view of swept prismatic elements used to capture the shallow optical penetration depth of the laser.

3.5.7 Ultrafast laser deposition temperature simulation

The ultrafast pulse duration and micro-meter focal spot size of the focused ultrafast pulse made measurement of the laser spot temperature technically challenging. Instead, a heat transfer model was written in Matlab to understand the surface temperature during deposition with the pulsed ultrafast laser. This simulation could not be done in COMSOL because the author could not find a way to insert the sudden temperature rise of the ultrafast pulse and control the time step size in the software. The Matlab model numerically evaluated the heat transfer in the material through the heat diffusion equation 3 with the heat source modelled as a stationary Gaussian beam with intensity

$$I = I_0 \exp\left(-\frac{2r^2}{w^2}\right) \exp(-\alpha z) \qquad [\,23\,]$$

where $I_0 = \frac{2E}{\pi w^2 d_p t_{pulse}}$ is the peak intensity, E the pulse energy, w the $1/e^2$ beam radius, $1/\alpha$ the absorption penetration depth, t_{pulse} the pulse duration, r the distance from the centre line of the beam and z the depth into the material. This source equation was turned on during the pulse and turned off between the pulse where the material cools until the next pulse. Only one pulse was simulated at a time.

The heat transfer equation was discretized using finite volume equation 14 of section 2.3.4. The simulation domain was the same size as that of the COMSOL model (Figure 37). However, rectangular cuboids elements were used instead of tetrahedral mesh elements. Melt phases were simulated as fixed temperature cells kept at the melting temperature, accumulating latent heat during the laser pulse. Outside the pulse, the total heat loss to surrounding cells was taken from the latent heat accumulated and when a negative latent heat value was reached the cell temperature was adjusted to the corresponding temperature below melt. Radiation heat losses were not accounted for because the losses were negligible, and this assumption was backed by the model results. For example, in the simulation results in Figure 79, the energy loss due to radiation was at most 2.1×10^{-3} nJ per pulse while the input pulse energy was 11.5 nJ. Convection heat losses was expected to be $<1.7\times10^{-4}$ nJ per pulse and were also not included in the simulations.

A few time advancing schemes were tested out by adjusting the value of θ in the previous equation such as 0 (explicit, backwards time scheme), 1 (implicit, forwards time scheme) and 0.5 (Crank-Nicolson combination of explicit and implicit) (Crank and Nicolson, 1996). The time step size could be increased for the implicit models to reduce the computing time. However, the implicit models were not stable when there were melt phases because at the end of the melt phase the cell temperature was adjusted based on the negative value of the latent heat. To improve the accuracy of the explicit model, the heat transfer gradients were first evaluated at half a time step. Then the temperature change was evaluated at the full time step based on these gradients.

The model was tested against two analytical test cases. The first test case was to compare the response of the model to a step change in temperature. The model was tested against a one dimensional analytical solution of exposing a rod to a step change in temperature, T_{step} at both ends. The partial differential heat diffusion equation 3 can be solved through separation of variables to give rise in temperature as

$$\Delta T = T_{step} - \sum_{m=1}^{\infty} \frac{4T_{step}}{(2m-1)\pi} \exp\left(-\left(\frac{(2m-1)\pi d}{L}\right)^2 t\right) \sin\left((2m-1)\frac{\pi}{l}x\right) \qquad [\ 24\ ]$$

where l was the length of the rod (Kreyszig, 2010). By having a rod length, l of one metre and a step change in temperature, T_{step} of 1000 °C, the temperature response at a point 1.1 µm from the edge was calculated for various finite values of the upper summation limit of equation 32. As the upper limits were increased (Figure 38), the solution converged and does not change significantly from 10,000,000 to 100,000,000. An upper limit of 100,000,000 was used for the rest of the calculations.

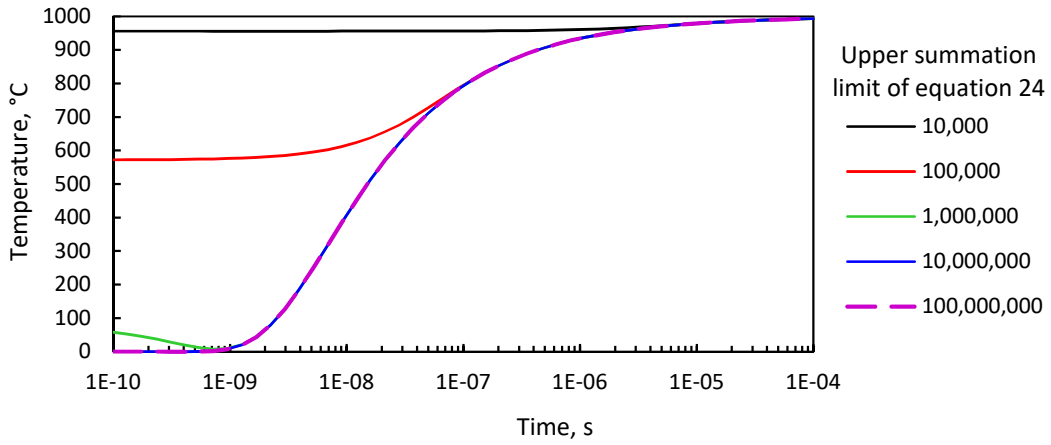

Figure 38: Temporal temperature at location 1.1 µm from the edge of a rod exposed to 1000 °C step change in temperature at t=0 s.

To simulate the rod using the Matlab model, a rectangle cuboid silicon simulation domain with a length of one metre and a face area of five by five millimetres was used. The step temperature rise of 1000 °C was applied to the two end faces at time t=0 s. It was assumed that there were no heat losses through the other surfaces of the cuboid. Figure 39 shows the temporal temperature from the simulation and analytical results at a few points near the edge of the rod exposed to the temperature step. Initially, there was a large error in temperature at the node 1.1 µm from the edge, however as the simulation progressed the error reduced and all nodes accurately simulated the temperature rise.

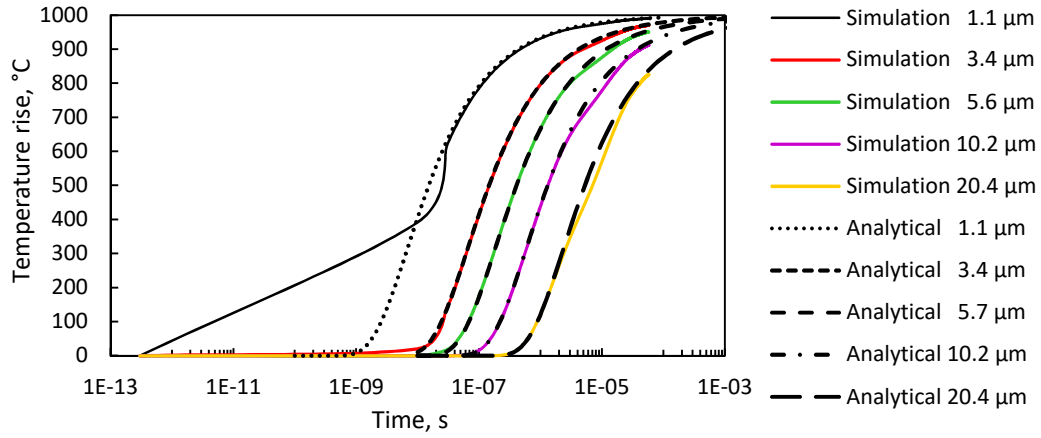

Figure 39: Temporal temperature at a few nodes <21 µm away from the edge of the rod exposed to 1000 °C step change in temperature at t=0 s for both the Matlab simulation and analytical model.

Another comparison test was the change of the steady state temperature distribution when exposed to a point heat source. This was done to demonstrate the ability of accurately simulating the spatial propagation of the heat from the laser point. For a semi-infinite plane, the partial differential heat diffusion equation 3 can be solved by superposition of impulse responses through Green's function (Cline and Anthony, 1977) to give the temperature distribution

$$T = \int_{-\infty}^{t}\int_{-\infty}^{\infty}\int_{-\infty}^{\infty}\int_{-\infty}^{\infty} \frac{2\dot{q}}{\rho C\left(4\pi d(t-t')\right)^{\frac{3}{2}}} \exp\left(-\frac{(x-x')^2+(y-y')^2+z^2}{4d(t-t')}\right) dx'dy'dz'dt' \quad [25]$$

where the $'$ superscript denotes the location of the multiple heat sources. For the case where the laser source was a single continuous point source, the integrals can be solved to give

$$T = \int_0^{\infty} \frac{P}{\rho C(4\pi dt)^{\frac{3}{2}}} \exp\left(-\frac{r^2}{4dt}\right) dt = \left[\frac{P}{4\pi kr} \operatorname{erf}\left(\frac{r}{\sqrt{4d}x}\right)\right]_0^{\infty} = \frac{P}{4\pi kr} \qquad [\,26\,]$$

This equation was compared with the Matlab simulation case where the domain was a cube, five millimetres long on each side. A point source could not be simulated, instead the laser spot radius of 3.3 µm was used. The input power was 500 mW and the material was silicon. The spatial temperature distribution for the analytical and simulation model is seen in Figure 40. A higher temperature was reached in the point source due to the higher energy density near the singularity of the analytical solution. The simulation model had a broader temperature profile due to the finite Gaussian laser heat source. The rest of the simulation result was close to the analytical solution.

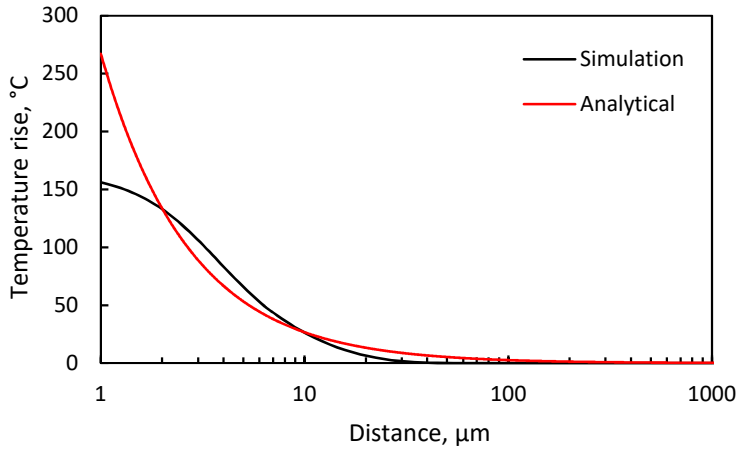

Figure 40: Comparison between steady state spatial temperature distribution between a point heat source from an analytical solution and a small Gaussian heat source from the Matlab simulation model.

3.6 Summary

In this chapter, the experiment materials, system and methods were detailed along with the analysis methods. SS304, SiO_2/Si, borosilicate glass and polyimide films were used as the sample substrates while tungsten hexacarbonyl was chosen as the precursor. The laser source for the CW control experiments was a laser diode extracted from a Pioneer BDR-209 Blu-ray disc writer and powered with a custom-made current regulator. The laser diode output was collimated and focused to an elliptical spot measuring 5.4 by 9.4 µm, with a maximum power of 850 mW and 405 nm wavelength. The laser source for the pulsed ultrafast experiments was an Amplitude Systemes Satsuma at a wavelength of 1030 nm and pulse duration of 300 fs that was focused to a calculated spot diameter of 6.6 µm. The vacuum system was custom built consisting of a deposition chamber, a precursor container, heaters, valves, pressure measurement devices, filters, pipes and vacuum pumps. The deposition chamber had a low profile to allow for the short focal length of the microscope objectives used in this study. The precursor container was built to fit a 2 ml glass vial so that the precursor can be easily refilled and safely handled using the vial. Before the experiments, the deposition system was heated to 70 °C and left to out-gas

and reach a base pressure of 0.01 mBar. For each experiment, the focal position was verified by ablating sacrificial substrates of known height difference to the sample substrate. These steps ensure repeatability of experiment results. For analysis of the deposits, an optical microscope, WLI, SEM and EDX was used. For the WLI surface height measurements, a 10 nm layer of chromium, gold and palladium was used to coat the surface. This created a uniform reflective surface for accurate surface height measurements as verified using AFM measurements. The elemental composition analysis done via EDX would not be accurate because the analysis software assumes a homogenous detection volume. However, the results can be used for the detection of tungsten deposits and for comparison between the different experiments. Resistivity measurements were done using both TLM and four-point probe measurements. To achieve better contact to the deposited track, silver paste was used to connect the track to copper wires. A heat transfer model was built in COMSOL to evaluate the temperature distribution during CW deposition experiments. Another heat transfer model was built in Matlab to understand the temperature distribution during the pulsed ultrafast experiments. This model was checked against analytical solutions to ensure the accuracy of the model.

Chapter 4 Continuous wave LCVD

In this chapter, CW deposition using the 405 nm laser (section 3.2.1) and tungsten hexacarbonyl precursor is explored on SiO_2/Si and SS304 substrates. The aim was to optimize the deposition parameters such as laser power, scanning speed, deposition pressure and substrate temperature to produce the best deposition results in terms of track resistivity, track resolution, deposition purity, and deposition rate. The best results from this chapter will then be used for comparison with the deposition done using the pulsed ultrafast laser that will be presented in the next chapter.

4.1 Temperature simulations

A starting point for the deposition parameters was found in the published work of (Nambu et al., 1990) which used the same precursor, tungsten hexacarbonyl for deposition of tungsten tracks. In that work, a 515 nm argon ion laser with a maximum power of 100 mW was focused to a spot diameter of 2 µm for scanning at a minimum speed of 100 µm/s on SiO_2/Si substrates. No measurements or simulations of the temperature at the laser spot were mentioned in the work. Based on the experiment details available, the temperature distribution on the substrate was simulated in the COMSOL model mentioned in section 3.5.6 (Figure 41). The peak temperature achieved was 500 °C, which corresponds to the temperature required for deposition of low resistivity α-phase tungsten mentioned in section 2.2.1. For the system built in this study, the CW 405 nm laser at a power of 350 mW and a scanning speed of 100 µm/s achieves a theoretical peak temperature of 533 °C. The width of the temperature distribution was wider than that of (Nambu et al., 1990) because the laser spot size was larger at 6.6 µm compared to 2 µm. There was no significant differences in the temperature distribution when the speed was increased until above 100 mm/s. Thus, a laser power of 350 mW was used for most of the experiments in this chapter.

This study focused on tungsten hexacarbonyl, however there are a variety of other precursors available for LCVD processes (Table 5). At maximum power of 650 mW and scanning at a speed of 100 µm/s, the centre of the laser spot can reach a temperature of 651 °C on silicon and 1300 °C on stainless-steel. This temperature was enough to break down various other CVD precursors such as silver, gold, copper, palladium and platinum, thus the laser diode should be able to write these materials on silicon and stainless steel.

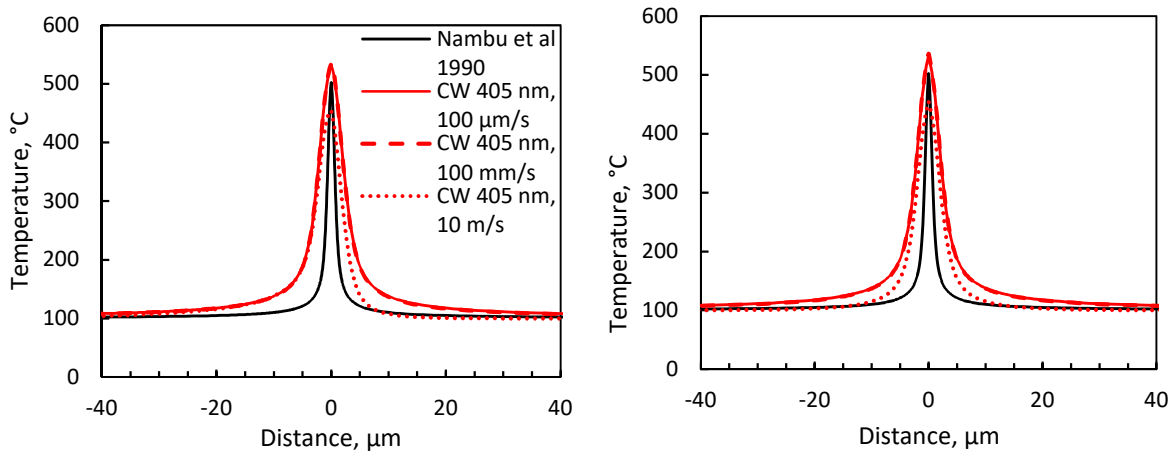

Figure 41: Temperature distribution parallel (left) and perpendicular (right) to the scanning direction showing that peak temperatures above 500 °C were achieved in both the settings used in (Nambu et al., 1990) and the CW setup used in this study.

4.2 Line deposition

Tungsten deposition from tungsten hexacarbonyl was attempted on SiO_2/Si substrates. Figure 42 shows SEM images of the deposited tungsten track. The track was made with a laser scanning speed of 10 µm s^{-1}, power of 350 mW and deposition pressure of 1 mBar. The width of the central deposition region was approximately 5 µm, comparable to the laser spot size of 6.6 µm. The high-resolution SEM image of at the centre of the track in Figure 42 (right) shows that the track consisted of circular grains that were around 100 nm in diameter. The elemental composition at this central region, discounting the Si from the substrate, was 84 wt% tungsten, 5 wt% oxygen and 11 wt% carbon.

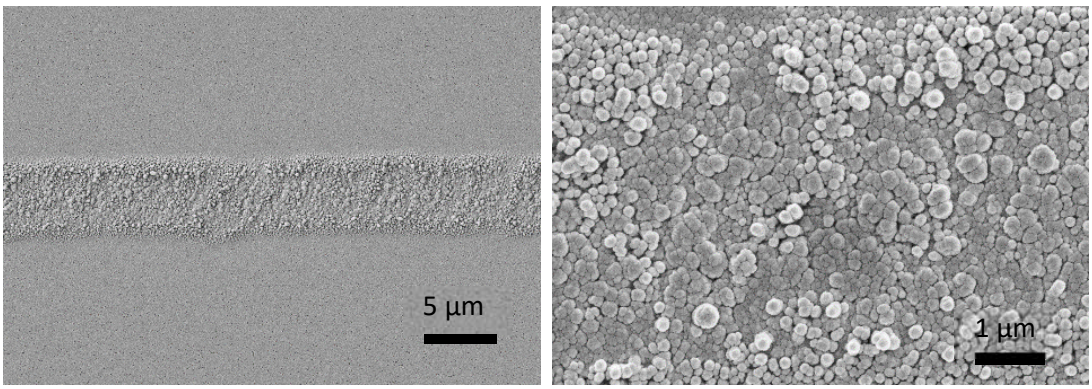

Figure 42: SEM images of tungsten deposited track with a laser power of 350 mW, a scanning speed of 10 µm s^{-1} and a deposition pressure of 1 mBar.

Figure 43 shows the FIB milled cross-section of the deposited track. A layer of platinum was FIB deposited on top of the track to achieve a flat cross-section during the milling. No swelling or damage to the underlying substrate was observed in the cross-section. However, there was significant deposition on the substrate outside the centre of the track.

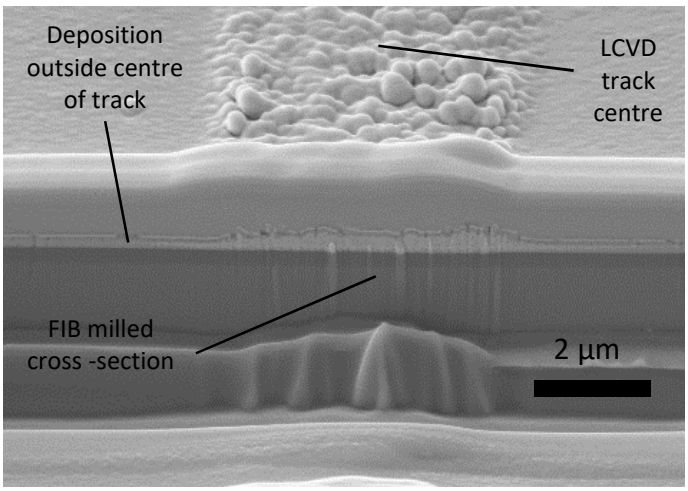

Figure 43: SEM image, at 54 ° to the substrate surface, after the track was milled using a FIB.

At higher magnification, Figure 44 (left), the deposition outside the centre of the track could be seen to consist of grains with diameters in the order of 10 nm. The EDX composition of the region was 31 wt% tungsten, 23 wt% oxygen and 46 wt% carbon (excluding silicon). This region was thought to be the deposition of partially broken-down precursors and reaction by-products. In comparison, on the substrate 1 mm away from the track, Figure 44 (right), the surface of the substrate was clean.

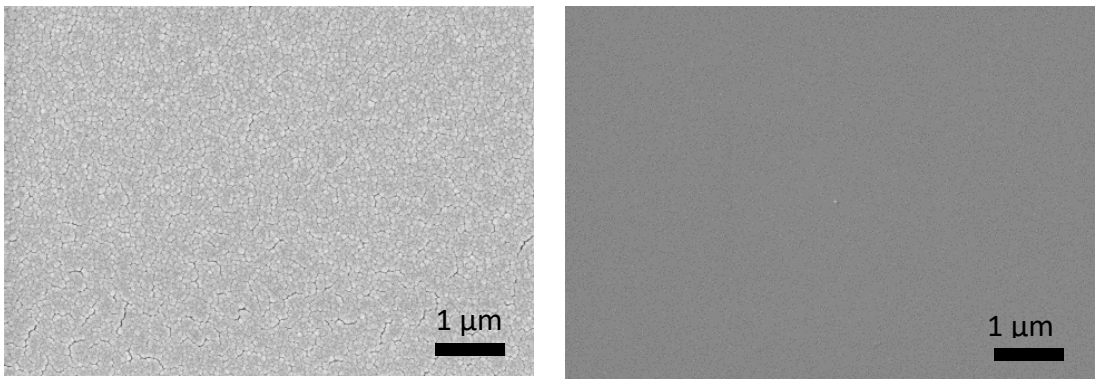

Figure 44: High resolution SEM image at a spot (left) 5 µm from the middle of the track; and (right) 1 mm away from the centre of the track.

An average WLI height profile of the deposited track is shown in Figure 45 (left). The sharp peaks and troughs in the WLI measurements (circled in red) were artefacts of the measuring technique and these peak and troughs were not seen in the FIB cross-section of Figure 43. The full width half maximum (FWHM) of the track, as measured from the WLI profile, was 5 µm. This width covers the whole central deposition region and was smaller than the effective spot diameter of 6.6 µm. For the deposition outside the central region, the height profile tapered down from a height of 150 nm to cover a width of 150 µm.

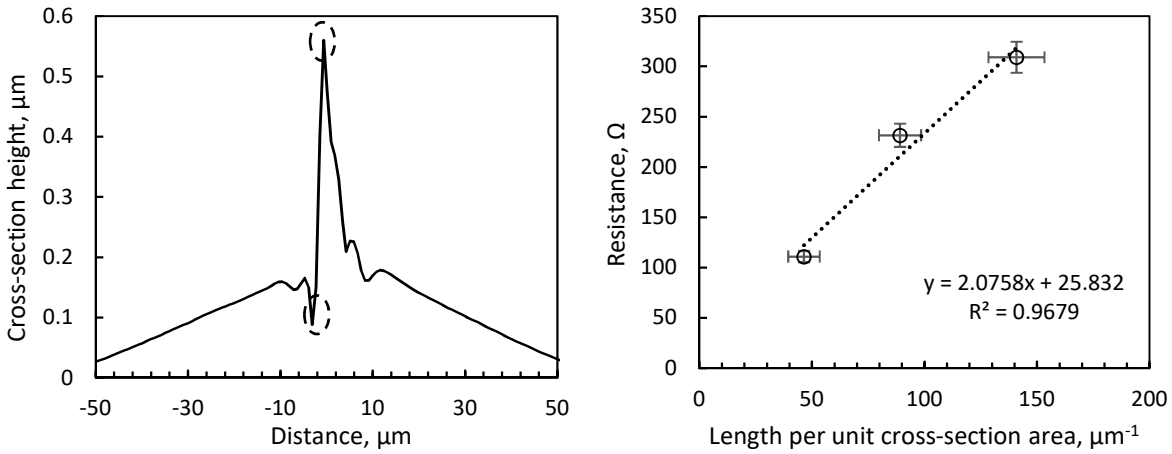

Figure 45: (left) Averaged WLI profile height measurements of the same track with the artefacts of the WLI measurement circled. The uncertainty in the height measurements was ±8 %. (right) Graph of resistance against length per unit cross-section area used to estimate the resistivity and contact resistance of the track via TLM.

The resistivity of the track was measured to be 207.6±50 µΩ cm through the TLM seen in Figure 45 (right). This value at 37.1 times bulk tungsten resistivity was high due to the significant gaps between the grains seen in Figure 42. In the following sections, the effect of scanning speed, substrate temperature, precursor temperature and pressure, laser power, background gases, and post deposition treatment were investigated to optimize the deposition results especially in terms of track smoothness, reduction of deposition outside the laser spot and electrical resistivity of the track.

4.2.1 Effect of scanning speed

Having achieve a deposition result, the scan speed was varied to study the effects on the deposition. For these experiments, the laser was fixed at a power of 350 mW and deposition pressure at 4 mBar. Figure 46 shows the geometry of the track from various experiments at different scan speeds. The maximum height of the track decreases with increasing scanning speed as seen in Figure 46 (a). At a scanning speed of 50 µm/s, the scanning speed was too fast and the deposition barely nucleates such that the maximum recorded height was only 5 nm. The linear height growth rate can be estimated from the formula

$$h = \dot{h}\frac{2w}{v_x} \qquad [\ 27\ ]$$

where h is the maximum height and $\dot{h}$ is the linear height growth rate. A growth rate of 3.8 µm/s vertically gives the best fit for the experiment data and is marked as the black dotted line in Figure 46 (a). This vertical growth rate was much higher than in CVD at 5 nm/s (Lai and Lamb, 2000). The three order of magnitude difference was due to the higher transport of the precursor in the LCVD configuration. The transport was higher due to the three dimensional diffusion pathway as opposed to the one dimensional path in the large area CVD configuration (Mazumder and Kar, 1995).

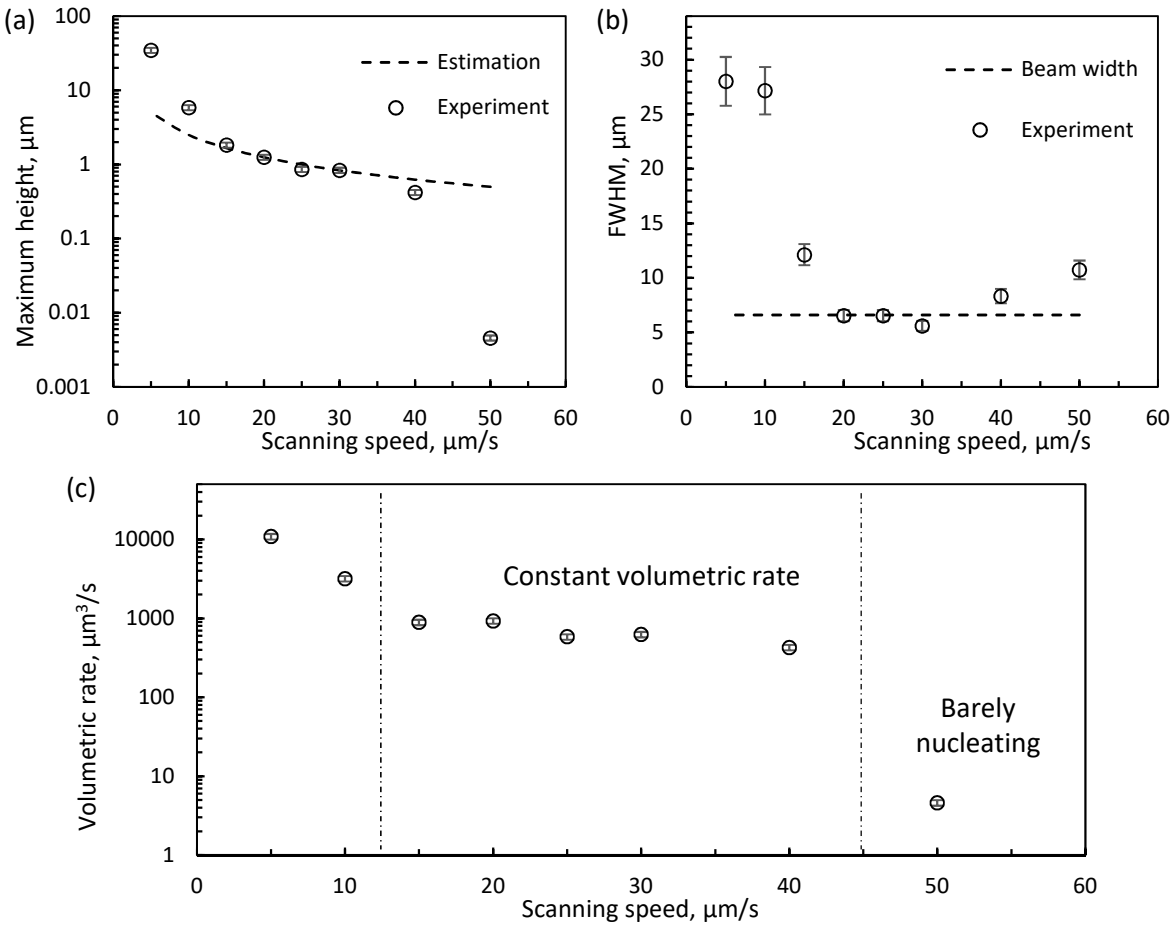

Figure 46: Deposited track (left) heights and (right) widths and (c) volumetric deposition rate at various scanning speeds done with a laser power of 350 mW and deposition pressure of 4 mBar.

Similar to the track height, the track width also decreased with increasing scan speed (Figure 46 b). The decrease in maximum height when the scanning speed was increased from 5 to 40 µm/s was approximately two orders of magnitude. For the track width, the decrease in width was less than one order of magnitude when the scan speed was increased over the same range. This happened because there was no significant change in the temperature profile perpendicular to the scan direction as confirmed by the temperature simulations in section 4.1.

Figure 46 (c) shows the volumetric deposition rate against scanning speed. The highest volumetric deposition rate was 10860 $\mu m^3/s$ when the scan speed was 5 µm/s. The volumetric deposition rate decreased when the scanning speed was increased from 5 to 15 µm/s. In the range of 15 to 40 µm/s, the volumetric rate stays approximately constant at 1000 $\mu m^3/s$. This region provides a window for stable deposition. At a scanning speed of 50 µm/s, the deposition was barely nucleating and the deposition rate was low at 5 $\mu m^3/s$. The temperature simulations in section 4.1 showed that there was no significant reduction in the peak temperature when the laser scan speed was increased from 10 µm/s to 100 mm/s. Thus, the reduction of volumetric deposition rate against scanning speed was likely due to a finite deposition nucleation time and/or a higher built rate on pre-deposited surfaces compared to the built rate on a clean substrate surface.

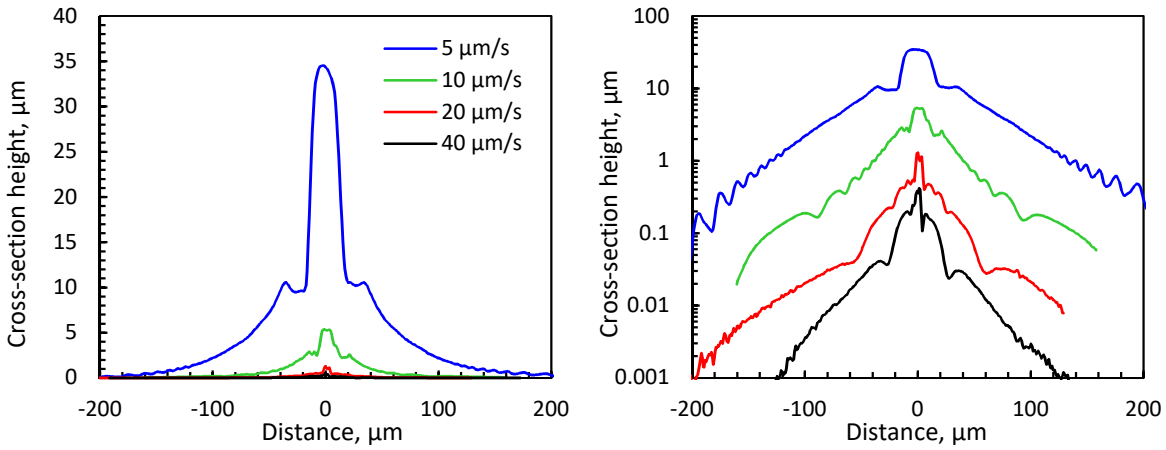

Figure 47: Cross-section height profiles, linear (right) and logarithmic (left), of the tracks made with a laser power of 350 mW and deposition pressure of 4 mBar at various scanning speeds. For all scan speeds, there is significant deposition outside the laser spot of 7 µm.

Figure 47 shows the averaged cross-section height profiles of the deposition at the investigated scan speeds. The height profiles appeared to consist of two profiles: a narrow Gaussian profile in the middle of the track and a wider Gaussian profile outside the laser spot. The two profiles were observed for all laser scanning speeds. The amount of deposition outside the laser spot covers a width of 200 to 400 µm and reduced with increasing scan speed.

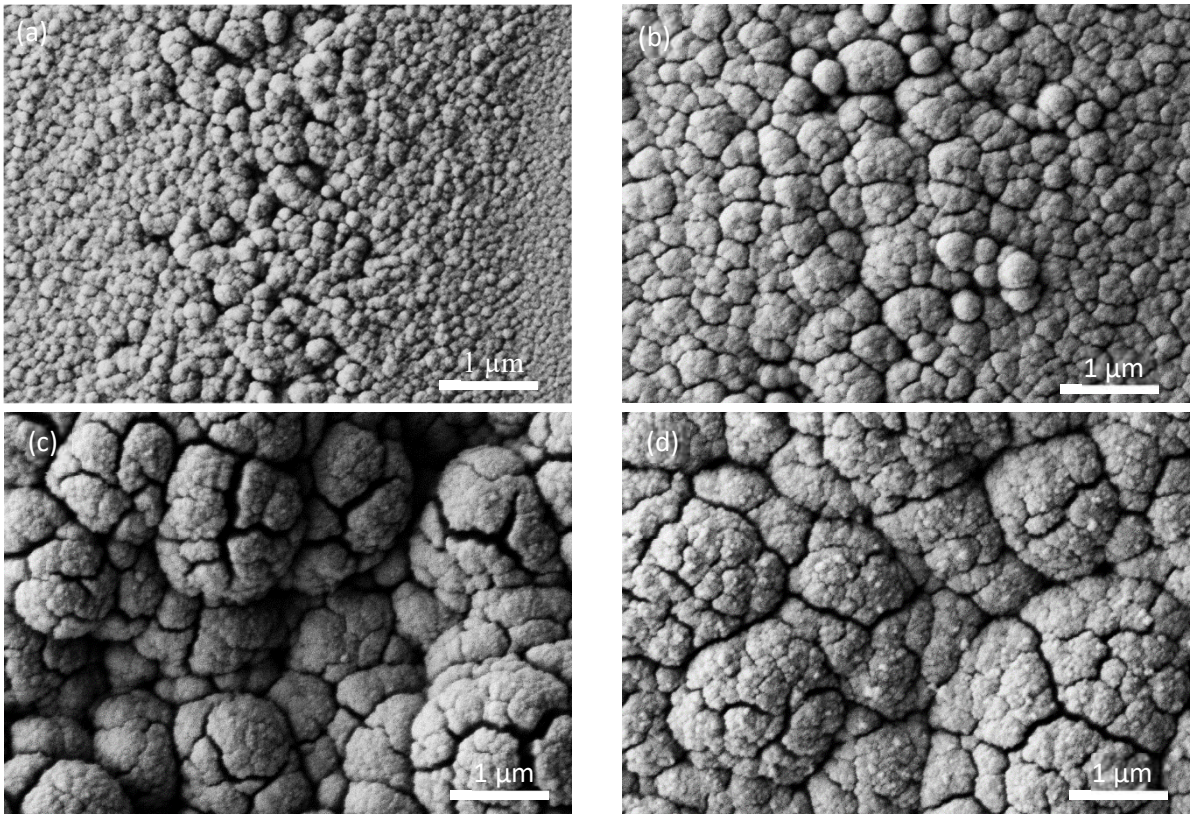

Figure 48: SEM images of the middle of the deposited track at various scanning speed showing the microstructure of the deposition. (a) 40, (b) 20, (c) 10, and (d) 5 µm/s.

The microstructure of the deposition in the middle of the track is seen in Figure 48. The deposition consists of grains that grew with reducing scan speed. At a scan speed of 40 µm/s the grains were approximately 200 nm in diameter and at a scan speed of 5 µm/s the grains were approximately 1 µm.

As the grain grew, cracks started to form within the grain, seen in the microstructure images at scan speed of 5 and 10 µm/s.

Table 9 shows the elemental composition at the middle of the track for various scan speeds measured using EDX. The purity of tungsten increased slightly with scanning speed from 77.1 % at 5 µm/s to 81.8 % at 20 µm/s. The carbon impurity stayed approximately constant at 10-13% while the oxygen impurity dropped from 10.0 % at a scanning speed of 5 µm/s to 6.2 % at a scanning speed of 40 µm/s.

Table 9: Elemental composition at the middle of the track measured using EDX.

Speed, µm/s	Excluding silicon			Silicon, wt%
	Tungsten, wt%	Carbon, wt%	Oxygen, wt%	
5	77.1	12.9	10.0	1.04
10	78.9	10.6	10.6	1.22
20	80.6	11.4	8.0	1.20
40	81.8	12.0	6.2	6.75
Clean substrate	0.0	23.2	76.8	74.00

4.2.2 Effect of substrate temperature

Other than the scanning speed, the substrate temperature would affect the pyrolytic LCVD results. For variation of the substrate temperature experiments, the laser was fixed at power of 350 mW, scanning speed of 10 µm/s, and deposition pressure was fixed at 2 mBar. Figure 49 (left) shows the change in maximum cross-section profile height when the substrate temperature was increased from 80 to 110 °. The maximum height increased with substrate temperature because the deposition rate increased with temperature. Based on the substrate temperature in the experiment, the peak temperature of the laser spot was simulated. When the maximum track height was plotted against the inverse of the peak simulated temperatures Figure 49 (right), a linear fit was observed. This indicated that the growth was limited by the substrate temperature rather than transport of precursor to the substrate (Smith, 1995).

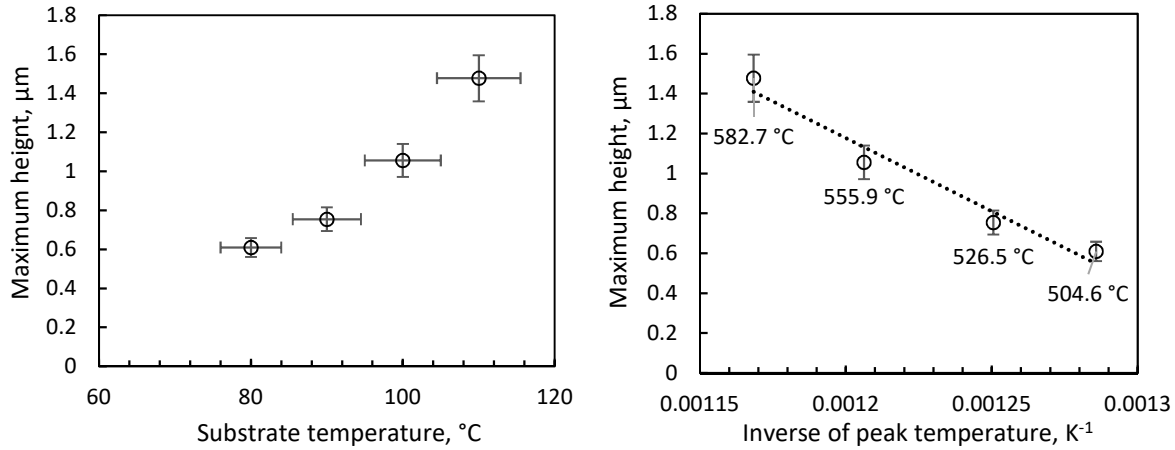

Figure 49: Maximum height against substrate temperature (left) and inverse of peak simulation temperature (right).

Figure 50 (left) shows the FWHM against substrate temperature. At a set substrate temperature of 80 °C, the FWHM of the deposition was close to the laser spot diameter of 6.6 µm. However, as the substrate

temperature was increased to 110 °C, the FWHM increased to 20 µm, approximately three times the laser spot diameter. As seen in Figure 50 (right), the volumetric deposition rate increased with substrate temperature. The deposition rate at 110 °C, 600 µm^3/s, was six times higher than the deposition rate at 80 °C.

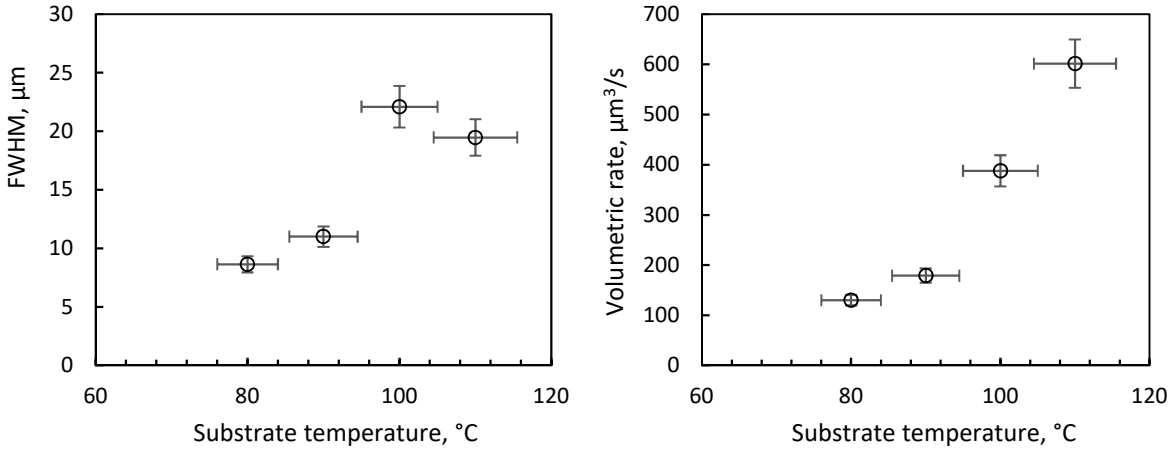

Figure 50: FWHM (left) and volumetric deposition rate (right) against substrate temperature. Both FWHM and volumetric deposition rate increased with substrate temperature.

At a substrate temperature of 80 °C, the deposition inside the laser spot appeared Gaussian in height profile while the outer deposition region was triangular (Figure 51). Reducing the substrate temperature dramatically reduced the deposition outside the laser spot. This reduction is seen in Figure 51 (right) where the width for deposition over one nano-meter thick reduced from approximately 300 µm when the substrate temperature was set to 110 °C to less than 80 µm at 80 °C.

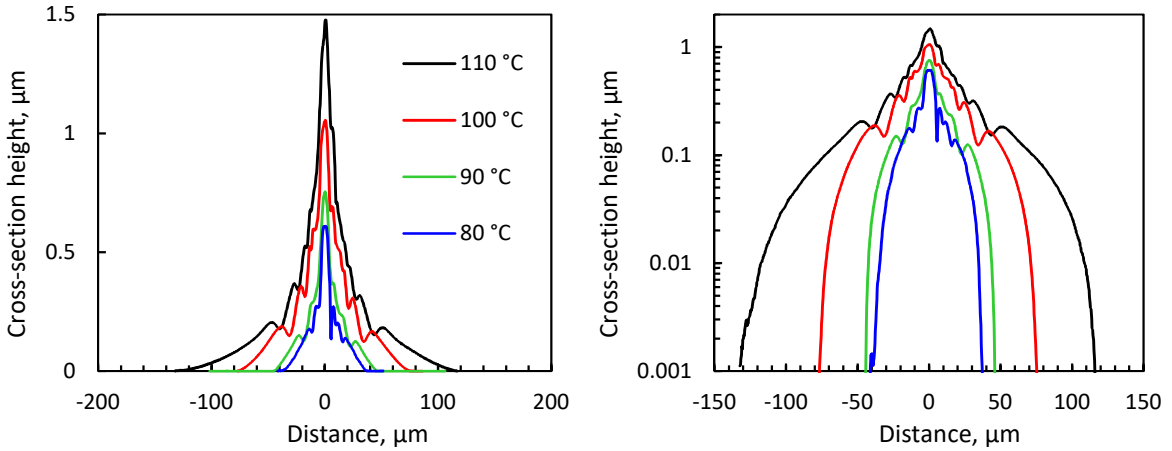

Figure 51. Cross-section height profile, linear (right) and logarithmic (left), of deposition on silicon at various stage temperatures.

Figure 52 shows SEM images of the tungsten track deposited at stage temperature of 80 °C and 110 °C. The deposits were granular, with larger granules at the centre of the track and smaller denser granules in the outer region. When the stage temperature was increased from 80 °C to 110 °C, the size of the grains at the centre of the track increased from ≈200 nm to 500 nm leading to a rougher surface. The elemental composition at the centre of the track were ≈84 wt% tungsten, ≈8 wt% carbon and ≈8 wt% oxygen (excluding silicon) with no significant variation with the stage temperature. The percentage of impurities increased in the outer region. At FWHM, the tungsten percentage for the deposit with stage

temperature of 80 °C was 52 wt% (excluding silicon). When the stage temperature was increased to 110 °C the tungsten purity at FWHM was lower at 31 wt% (excluding silicon).

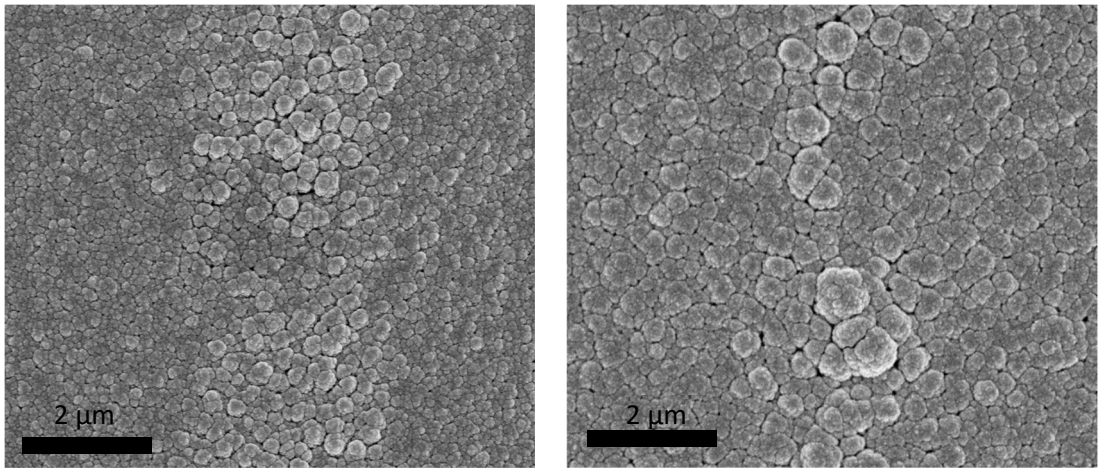

Figure 52. SEM image of tungsten deposited with stage temperature at 80 °C (left) and 110 °C (right) showing granular microstructures.

Figure 53 shows the FIB milled cross-section of the tungsten track. At 110 °C, the porosity at the top and bottom of the deposited track increased. There was no noticeable damage to the underlying silicon substrate at both stage temperatures.

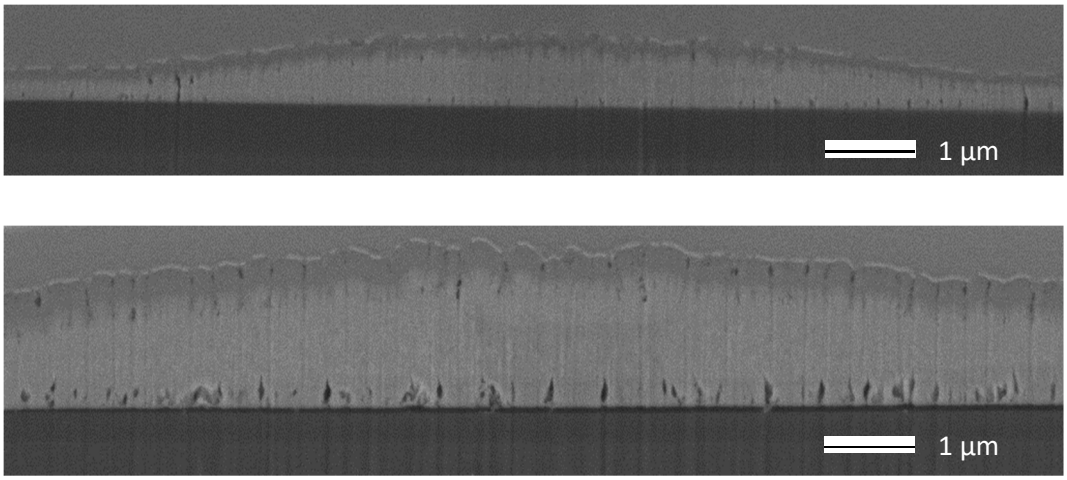

Figure 53. FIB milled cross-section of tungsten deposited with stage temperature at 80 °C (top) and 110 °C (bottom). Visually, there was higher porosity in the track deposited at a stage temperature of 110 °C.

The electrical resistivity of the tracks was measured through four probe measurements and the results are shown in Table 10. The lowest recorded resistivity of 892±45 µΩ cm was achieved at a substrate temperature of 80 °C. The electrical resistivity increased with substrate temperature. This was expected because the porosity and impurities in the deposition outside the laser spot increased with substrate temperature.

Table 10: Electrical resistivity of track deposited at various substrate temperatures.

Substrate temperature, °C	Resistivity, μΩ cm	Multiple of bulk tungsten resistivity	Resistance per unit track length, Ω/mm
70	518±26	92	625
80	892±45	159	685
90	1296±65	231	724
100	2731±137	488	704
110	3990±200	713	663

4.2.3 Effect of deposition pressure

Another variable in the pyrolytic LCVD process was the deposition pressure. To investigate the effect of changing the deposition pressure, the laser was set at power of 350 mW and a scan speed was fixed at 10 μm/s while the deposition pressure was varied from 0.2 to 4.0 mBar. Figure 54 shows the geometrical effects of the change in deposition pressure on maximum height and FWHM. The maximum height changed two orders of magnitude while the FWHM changed one order of magnitude in the pressure ranged investigated.

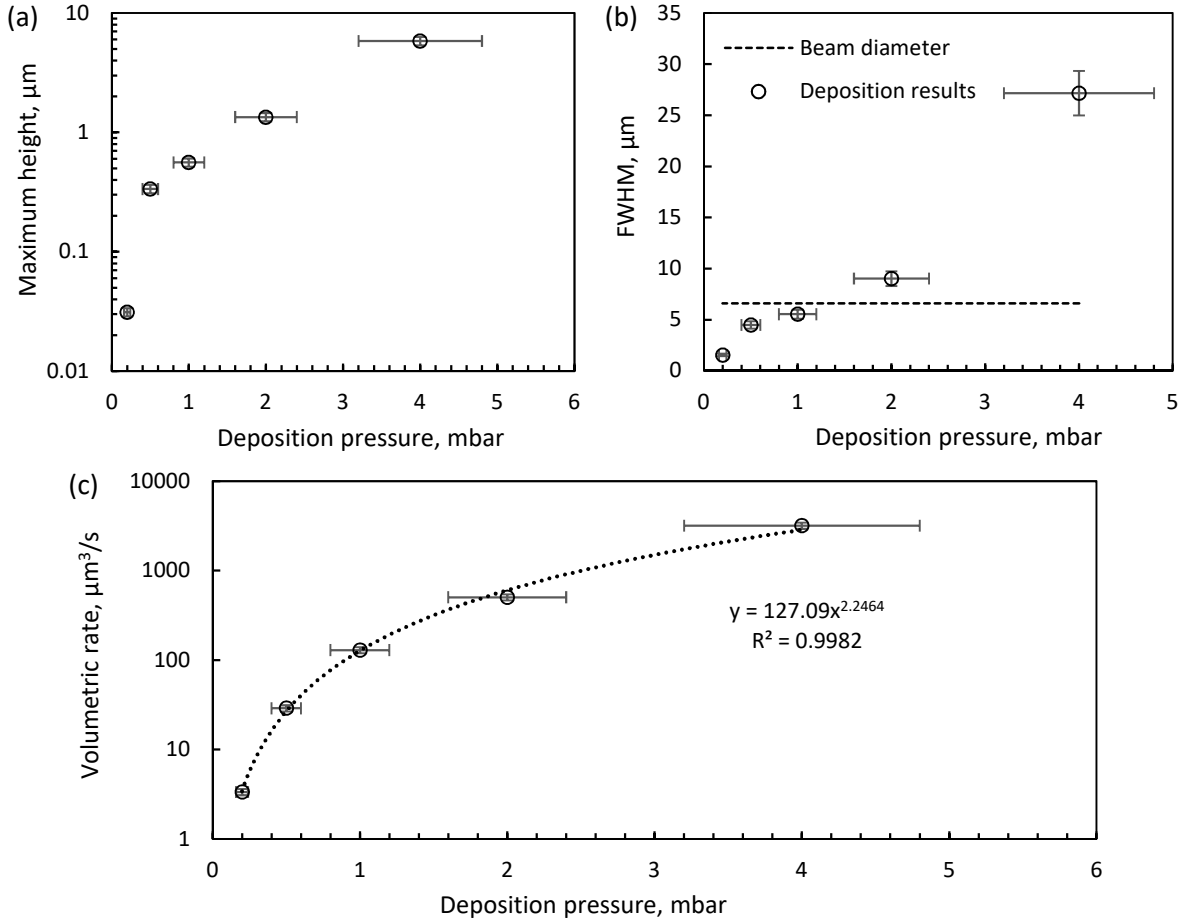

Figure 54: Graph of maximum track height (a), FWHM (b) and volumetric deposition rate (c) against deposition pressure.

Similar to the rise in the maximum profile height, the volumetric deposition rate seen in Figure 54 (c) increased with deposition pressure, with a rise of three orders of magnitude over the pressure range investigated. A power curve provided good fit to the data with a power of 2.25. This implied that the

effective deposition rate was approximately proportional to the square of the concentration and the collision of two precursor molecules was likely the rate determining step of the deposition process.

The cross-section profile of the track is seen in Figure 55. There were two deposition regions: one at the middle of the track and the other outside the laser spot. The deposition outside the laser spot reduces significantly with deposition pressure. At a pressure of 0.5 mBar, the deposition outside the laser spot reduced to a width of approximately 100 µm while at a pressure of 0.2 mBar the deposition width outside the laser spot was only approximately 50 µm.

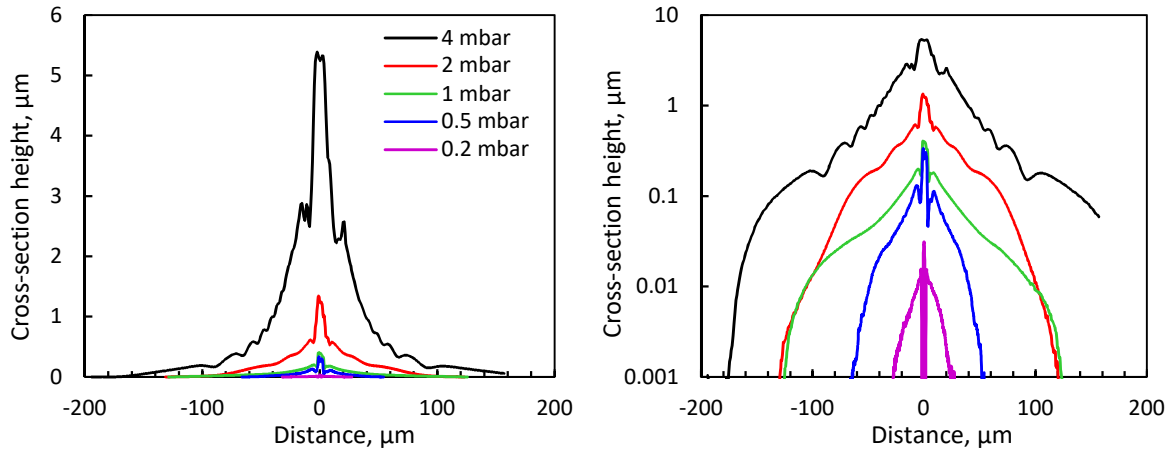

Figure 55: Cross-section height profiles, linear (right) and logarithmic (left), of the tracks made with a laser power of 350 mW and scan speed of 10 µm/s. The deposition outside the laser spot significantly reduced with deposition pressure.

Figure 56 shows the effect of changing the deposition pressure on the deposition microstructure. The size of the deposition grains and the gaps between the grains increased with deposition pressure.

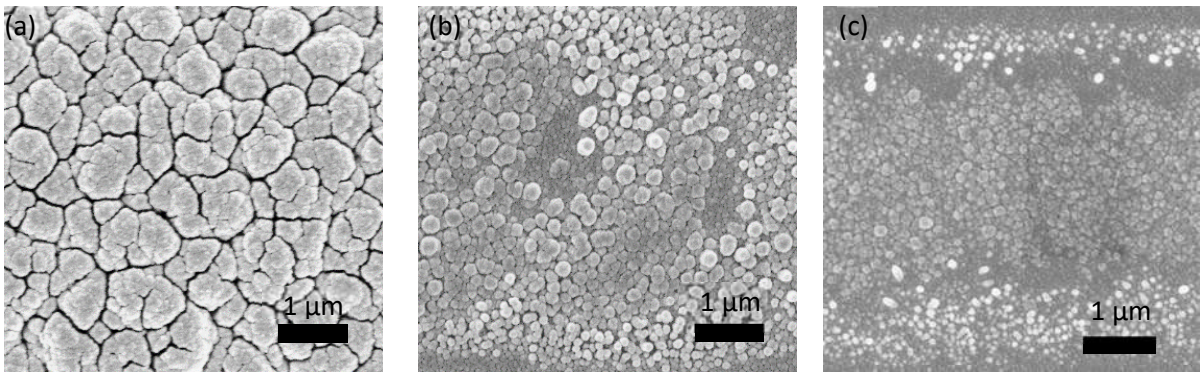

Figure 56: SEM images of tungsten deposition on SiO_2/Si substrate at a scanning speed of 10 µm/s and laser power of 350 mW at deposition pressure of 4 mBar (a), 0.5 mBar (b) and 0.2 mBar (c).

Table 11 shows the effect of decreasing the deposition pressure on the elemental composition in the middle of the track measured using EDX. The highest tungsten purity was measured at ta pressure of 1 mBar at 83.8 wt%. At a low deposition pressure of 0.2 mBar, the tungsten purity drops significantly to 42.8 wt% and the level of carbon impurities rised to 43.7 wt%.

Table 11: Elemental composition at the middle of the track measured using EDX.

Deposition pressure, mBar	Excluding silicon			Silicon, wt%
	Tungsten, wt%	Carbon, wt%	Oxygen, wt%	
4.0	79.1	10.1	10.8	0.6
2.0	83.2	8.3	8.5	1.2
1.0	83.8	10.7	5.4	7.1
0.5	81.4	13.7	4.9	18.1
0.2	42.8	43.7	13.6	58.3
Clean substrate	0.0	23.2	76.8	74.1

The resistivity of the tracks is seen in Table 12. The deposition pressure significantly affects the resistivity with the optimum resistivity achieved at a deposition pressure of 0.5 mBar at 93±27 μΩ cm or 17 times bulk tungsten resistivity. However, the lowest track resistance per unit length was the track deposited with a pressure of 2 mBar. This was due to the higher cross-section area of the track deposited at that pressure.

Table 12: Track resistivity at various deposition pressures.

Deposition pressure, mBar	Resistivity, μΩ cm	Multiple of bulk tungsten resistivity	Resistance per unit track, Ω/mm^{-1}	Contact resistance, Ω
4	6630±3167	1184	201	42±136
2	205±71	37	65	35±31
1	208±50	37	247	13±38
0.5	93±27	17	181	132±92
0.2	146±25	26	4366	819±260

4.2.4 Effect of laser power

The effect of increasing the laser power was investigated by keeping the scanning speed constant at 5 μm/s and deposition pressure at 0.5 mBar. The laser power was increased from 350 mW to 550 mW. Table 13 shows the geometrical results of the tracks done with the various laser power settings. The maximum track height, FWHM and cross-section area increased with laser power. The volumetric deposition rate with the laser power of 550 mW was more than double the deposition rate with the laser power of 350 mW.

Table 13: Geometry and rate of track deposition for the various laser powers settings.

Laser power, mW	Maximum track height, μm	FWHM, μm	Cross-section area, μm^2	Volumetric rate, $\mu m^3/s$
350	0.349	7.28	9.67	48.37
450	0.521	9.36	16.31	81.53
550	0.482	15.26	19.69	98.47

Figure 57 shows the cross-section height profile of the tracks written with the various laser powers. Although the maximum height of the tracks increased, the deposition outside the laser spot increased significantly with laser power.

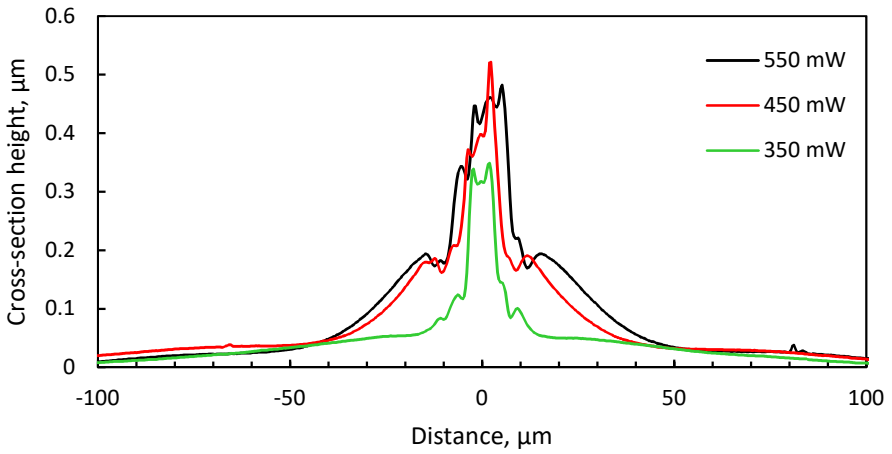

Figure 57: Cross-section profile for the tracks written with the laser powers of 350 to 550 mW.

Figure 58 consist of SEM images of the microstructure in the middle of the deposited track. There were no significant morphological differences in the microstructure of the deposits albeit the increase in grain size and gaps in between the grains when the laser power was increased.

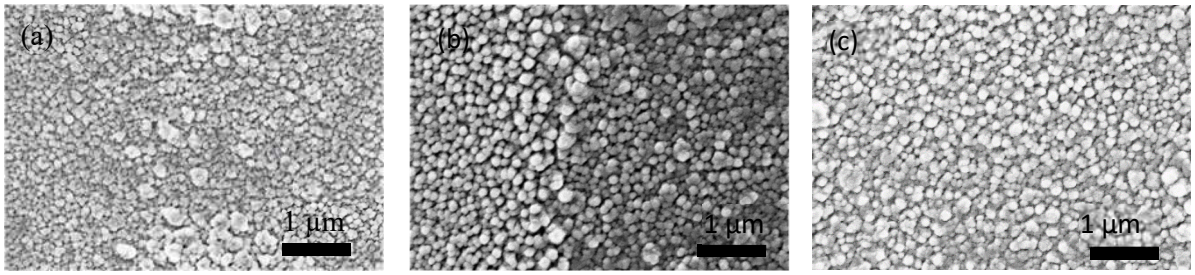

Figure 58: High resolution SEM images of the microstructure in the middle of the track for the deposition written with a laser power of 350 mW (a), 450 mW (b) and 550 mW (c).

Table 14 shows the elemental composition at the middle of the track done at the various laser powers. The tungsten purity increased with increasing laser power. The increase in tungsten purity was followed by a decrease in carbon impurities. The detected silicon substrate decreased with increasing laser power due to the increase in deposited track thickness.

Table 14: EDX elemental composition at the middle of the track deposited at various laser powers.

Laser power, mW	Excluding Si			Silicon, wt%
	Tungsten, wt%	Carbon, wt%	Oxygen, wt%	
350	85.3	9.8	5.0	16.4
450	88.8	7.1	4.1	4.8
550	91.7	4.7	3.6	3.4
Clean substrate	0.0	23.2	76.8	74.1

4.2.5 Effect of background gases

In all the previous experiments, the deposition chamber was back-filled with nitrogen while the tungsten hexacarbonyl precursor was heated. In this section, the effect of using hydrogen to back-fill the chamber was investigated. The precursor was fixed at a temperature of 80 °C, the substrate at 100 °C, the laser scanning speed at 10 µm/s, laser power at 350 mW and the deposition pressure was fixed at 1.5 mBar. Table 15 shows the geometry of the deposited tracks, while Figure 59 shows the cross-section profile of the tracks. The track produced in hydrogen background gas has a larger cross-section area and taller

maximum height. However, both track profiles were similar in terms of profiles in middle of the laser spot and deposition outside the laser spot.

Table 15: Comparison of track geometry between using nitrogen and hydrogen as the background gas.

Background gas	Cross-section area, μm^2	Maximum height, μm	FWHM, μm
Nitrogen	40.70	1.12	22.47
Hydrogen	47.71	1.35	15.92

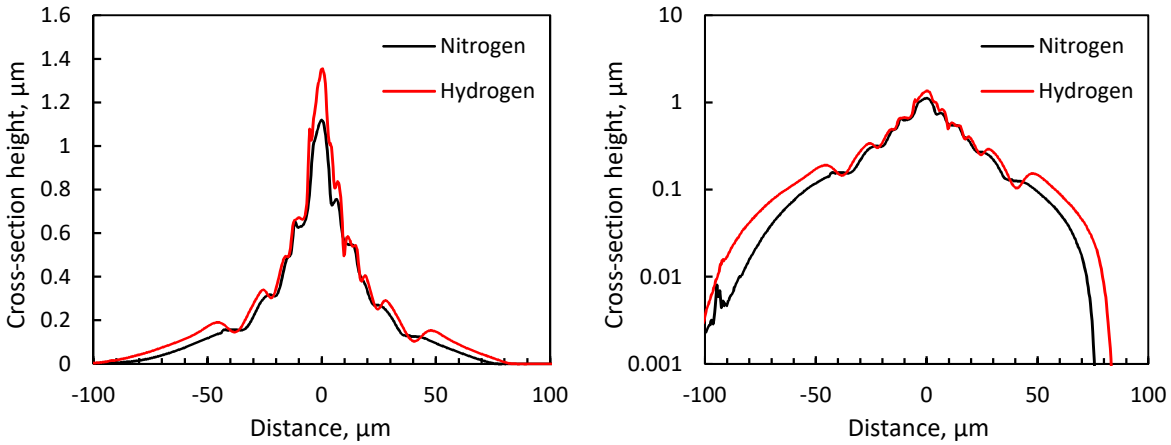

Figure 59: Cross-section height profile, linear (right) and logarithmic (left), of the track for using nitrogen and hydrogen background gas during the deposition.

Figure 60 shows SEM images of the microstructure in the middle of the deposited tracks. Both tracks consist of large grains with gaps in between the grains. However, the size of the grains for the track deposited in hydrogen background gas was larger.

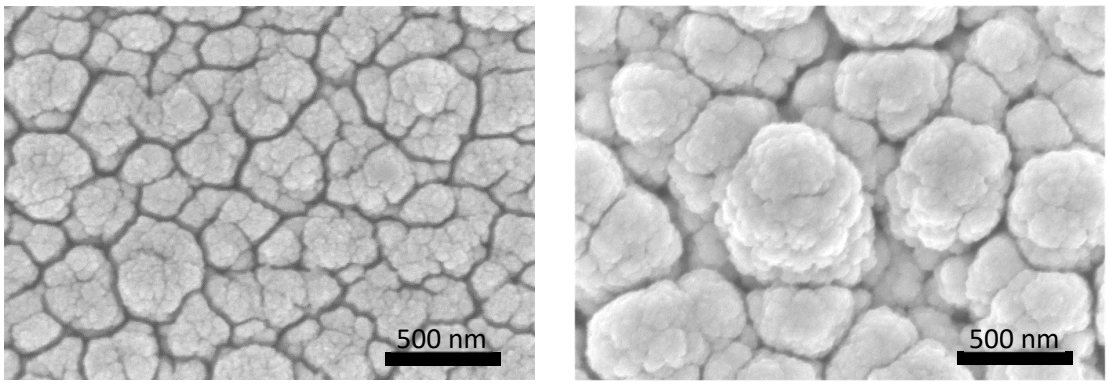

Figure 60: Comparison of microstructure for the deposition with nitrogen (left) and hydrogen (right) as background gases for deposition.

4.2.6 Post deposition treatment and annealing

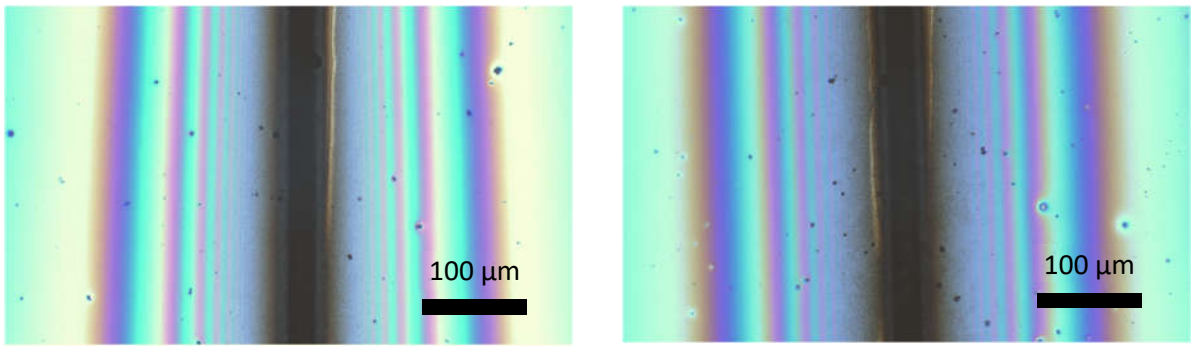

Figure 61: LCVD track on silicon that was left in the as-deposited state (left) and one which was ultrasonically cleaned for 16 mins in acetone (right).

To remove the deposition outside the laser spot, a post deposition treatment was attempted. A sample was made using a deposition pressure of 1 mBar, laser scanning speed of 10 µm/s and laser power of 350 mW and cleaved into two pieces. One was placed in an ultrasonic bath for 16 mins with acetone and blown dry, while the other was left in the as-deposited state. Figure 61 shows the optical images of both pieces. There was no significant visual difference in the samples especially in terms of deposition outside the laser spot.

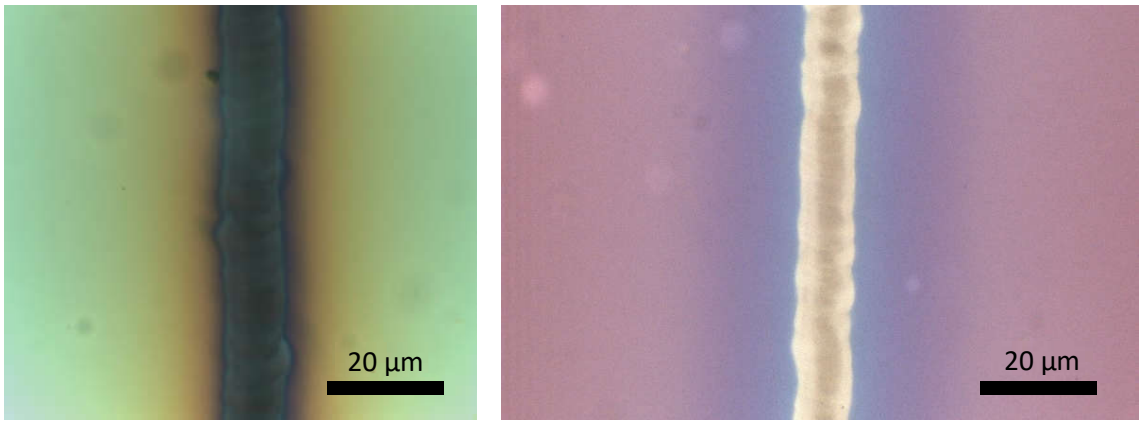

Figure 62: Optical microscope images of the as-deposited track (left) and the track annealed in hydrogen at 650 °C for 30 mins (right).

In another attempt, a sample was made and after the deposition the sample was annealed in the hydrogen at a flow-rate of 200 sccm at a temperature of 650 °C for 30 mins. These conditions were chosen because an investigation by Deutsch and Rathman, 1984 showed that annealing at 650 °C in hydrogen reduced the resistivity from 32 to 6 times bulk for tungsten deposited from tungsten hexafluoride. Figure 62 shows the optical images of the as-deposited track and that of the track after annealing. The annealing turned the middle of the track from a dark colour to a metallic surface. There was also reduction in the deposition outside the laser spot and the original pink colour of the SiO_2/Si substrate was visible.

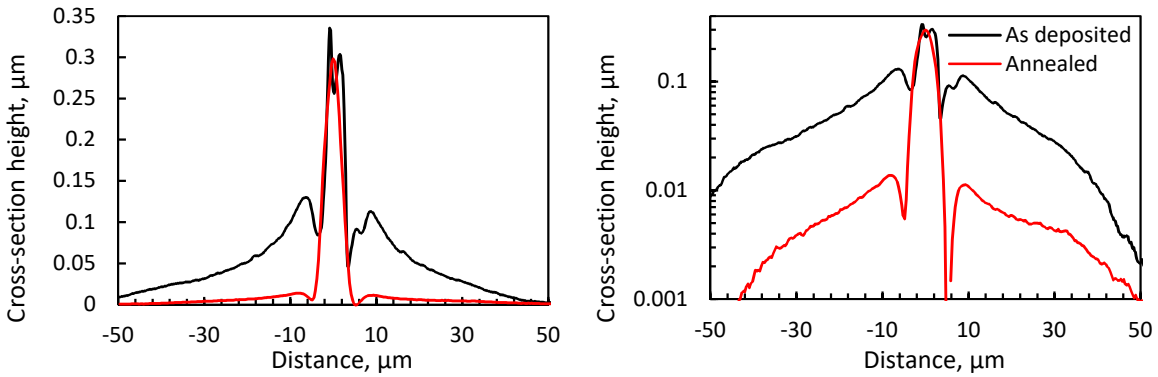

Figure 63: Cross-section profiles, linear (right) and logarithmic (left), of the as-deposited track (black) and the annealed track (red) showing a removal of deposits outside the laser spot.

Figure 63 shows the cross-section profile of the as-deposited track and the annealed track. There was no significant reduction in the track height inside the laser spot. However, there was a drastic reduction in the deposits outside the laser spot.

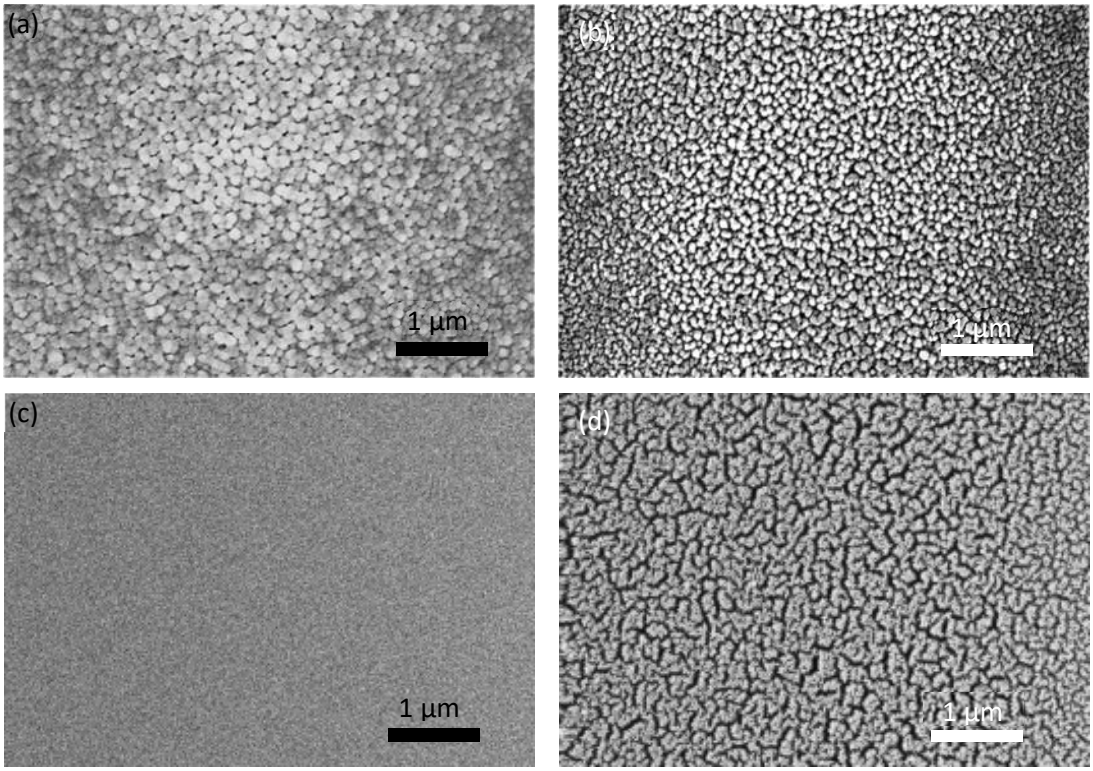

Figure 64: SEM images of track as-deposited (a, c) and after annealing with hydrogen for 30 mins at 650 °C (b, d) in the middle of the track (a, b) and 8 µm from the centre of the track (c, d).

Figure 64 shows SEM images of the as-deposited (left) and annealed track(right) at the centre of the track (top) and 8 µm from the centre of the track (bottom). The SEM images show that in the middle of the track, the annealing reduced the size of the grains and outside the laser spot, the annealing left a porous surface on the substrate.

Table 16 shows the EDX measured element composition of the as-deposited and annealed track in the middle of the track and 10 µm outside the middle of the track. Annealing increased the purity of the tungsten in the middle of the track from 83.3 to 90.6 wt%. A reduction in carbon impurities was observed

in the middle and outside the track. The element contents outside the annealed track was close to that of the clean substrate.

Table 16: EDX measured element weight percentage for the as-deposited and annealed track.

Track	Location	Excluding silicon			Silicon, wt%
		Tungsten, wt%	Carbon, wt%	Oxygen, wt%	
As-deposited	Track middle	83.3	13.4	3.3	5.8
Annealed	Track middle	90.6	8.2	1.2	8.0
As-deposited	10 µm off-middle	0.0	53.2	46.8	62.0
Annealed	10 µm off-middle	0.0	31.3	68.7	73.7
Clean substrate		0.0	23.2	76.8	74.1

Table 17 shows the electrical resistance measurements of the as-deposited and annealed track. There was a reduction in resistivity after annealing from 16.6 to 11.7 times bulk tungsten resistivity. There was a reduction in resistance per unit track length due to the reduction in the cross-section area of the track. A significant reduction in contact resistance between the silver paint and the deposited track from 132 to 2 Ω was observed. This was likely due to the annealing process removing the carbon impurities on the surface of the track as evidenced from the element composition measurements in Table 16.

Table 17: Comparison between electrical properties of the as deposited track and the annealed track.

Condition	Resistivity, µΩ cm	Multiple of bulk tungsten resistivity	Resistance per unit track, Ω/mm-1	Contact resistance, Ω
As deposited	93±27	16.6	180.8	132±92
Annealed	66±7	11.7	218.1	2±32

4.2.7 Optimum results

In terms of track resistivity, the best result was achieved when the track was scanned at a speed of 10 µm/s, laser power set at 350 mW, the substrate temperature 100 °C and the deposition pressure 0.5 mBar. These settings produced a track with a resistivity of 93±27 µΩ cm or 16.6 times bulk tungsten resistivity (section 4.2.3). At a deposition pressure of 2 mBar, the track resistivity was shown to drop when the substrate temperature was reduced from 110 to 70 °C (section 4.2.2). However, when a track was deposited at a substrate temperature of 70 °C compared to 100 °C, the resistivity increased to 110 from 16.6 times bulk tungsten resistivity.

The study done by (Nambu et al., 1990) used the same tungsten hexacarbonyl precursor at the same deposition pressure of 0.5 mBar. However, the resistivity measured in their study was in the range of 2-6 times bulk tungsten resistivity. This difference in resistivity measurement was attributed to the method used for calculating the cross-section area of the track. In the work of (Nambu et al., 1990), the track cross-section was obtained by assuming a triangular cross-section with the maximum height measured using a stylus profilometer and width measured using an optical microscope. From Figure 62, the width measured from the optical microscope image for the deposition done at to produce the best as-deposited track resistivity would have been 10.3 µm. Assuming a triangular cross-section, as done by (Nambu et

al., 1990), the cross-section area of the track would have been 1.73 μm^2 instead of the 5.14 μm^2 measured by taking the average cross-section area of the track including the deposition outside the laser spot. This lower cross-section area would imply that the resistivity of the track was 5.6 times bulk tungsten resistivity, which was within the range measured by (Nambu et al., 1990). There was no optical or electron images in the work of (Nambu et al., 1990) and there was no mention of deposition outside the laser spot. Thus, it is assumed that if the deposition outside the laser spot was accounted for, (Nambu et al., 1990) would have measured a higher resistivity value similar to that achieved in this chapter. Given that the deposition outside the laser spot contained high impurities, the tracks deposited by the CW LCVD cannot be treated as traditional thin film deposition and only the cross-section area of the deposition inside the laser spot should be used for the effective track resistivity calculations.

In the previous section, the as-deposited track resistivity was improved by annealing in hydrogen at 650 °C. After the annealing, the resistivity of the track reduced from 16.6 to 11.7 bulk tungsten resistivity (93±27 to 66±7 μΩ cm). This was the lowest track resistivity achieved in this study through deposition using CW laser deposition. In terms of resolution, the annealed track was the best with the least amount of deposition outside the laser spot. The thickness outside the laser spot was at maximum only 13 nm and tapered off to cover a width of 90 μm (Figure 63).

4.2.8 Deposition on other substrates

Besides deposition on SiO_2/Si substrates, deposition was successful on metal substrates such as copper and stainless steel. For these experiments, the laser power was fixed at 350 mW, the deposition pressure at 2 mBar and substrate temperature at 110 °C. The track on stainless steel had the largest cross-section area, tallest track height and fastest volumetric deposition rate (Table 18). This was due to the thermal diffusivity of stainless steel at 4.2 mm^2/s being the lowest, followed by silicon at 88 mm^2/s and copper at 111 mm^2/s being the highest. The low thermal diffusivity allowed a higher temperature in the laser spot and thus a higher deposition rate on stainless steel.

Table 18: Geometrical comparison between the track deposited on copper, SiO_2/Si and stainless steel.

Material	Scanning speed, μm/s	Cross section, μm^2	Max height, μm	FWHM, μm	Volumetric deposition rate, μm/s
SS	10	98.02	2.48	18.78	980.19
SiO2	10	57.07	1.34	21.52	570.74
Cu	10	17.06	0.60	14.34	170.63

Figure 65 shows the cross-section profile of the track deposition on the various substrates. For all the materials, there were significant deposition outside the laser spot.

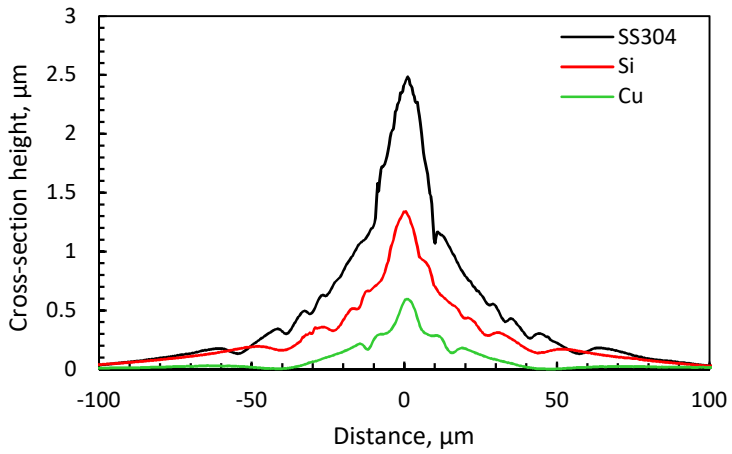

Figure 65: Cross-section height profiles of tracks deposited on stainless steel, SiO_2/Si and copper at a substrate temperature 110 °C.

Figure 66 are SEM images of the microstructure in the middle of the deposited track on the various substrate materials. The deposition on all substrate materials were granular with the biggest grains formed on stainless steel, followed by SiO_2/Si and the smallest grains were on copper. The size of the grains was largest on stainless steel because the laser spot temperature was the highest on that material. This relationship was demonstrated previously in section 4.2.2. Deposition was also attempted on transparent materials such as borosilicate and fused silica glass. However, no deposition nor damage to the glass was observed at the maximum power of the laser at 600 mW. Deposition was also attempted on polyimide, however ablation was observed at the lowest power of the CW laser at 50 mW.

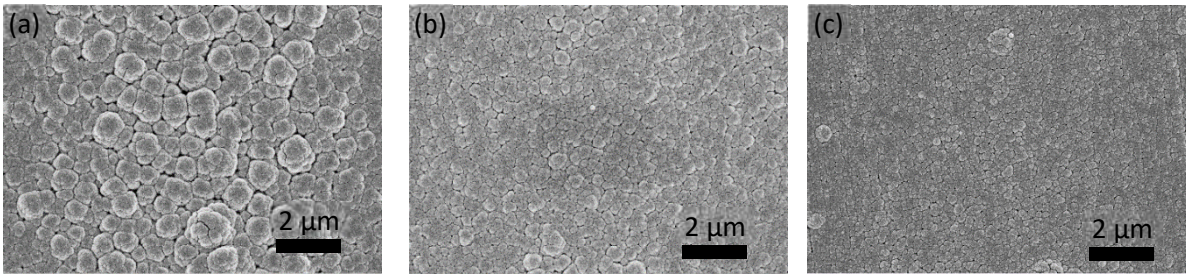

Figure 66: SEM images of the microstructure in the middle of the deposited track on stainless steel (a), SiO_2/Si (b) and copper (c).

4.3 Three-dimensional growth

In this section, the growth of spherical, conical and vertical columnar structures on the substrate was investigated. The growth of such structures has not been reported for metal based LCVD. To prevent the heat from spreading during the long dwells on a spot, SS304 substrates were used due to the low thermal diffusivity of the material. Thermal simulations were done based on the observed growth structures to provide an insight to the temperature distributions during laser exposure and possible explanations to the observed growth. In these simulations, only heat transfer from the laser was simulated, no mass transfer and actual growth were simulated.

The growth of the deposit when the laser was dwelled on the stainless-steel substrate at a stationary spot followed a few stages. The first stage observed was nucleation, which is seen in the SEM image of Figure 67 (left). At this stage, only a fine deposition layer was visible through the contrast of the SEM. As the deposited layer was only a few hundred nanometers thick, the temperature distribution on the surface was determined by the heat transfer properties of the stainless-steel substrate. Figure 67 (right) shows the cross-section temperature distribution of the simulated laser dwell. Due to the low thermal diffusivity of stainless-steel, 4 mm^2/s, the heat was concentrated within the laser spot.

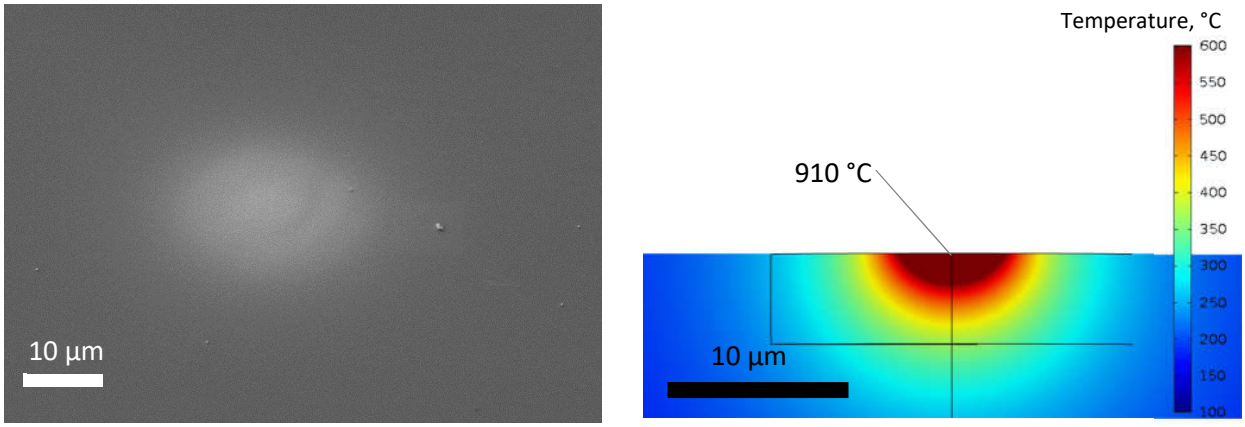

Figure 67: (left) SEM image of deposition nucleation after 5 s dwell time with a laser power of 200 mW. (right) Cross-section simulation temperature distribution of the spot dwell.

After nucleation, thin layer growth was observed. This stage occurred after approximately twenty seconds of laser exposure at a power of 200 mW (Figure 68 left). As the thickness of the deposit grew, the thermal properties of the deposit determined the temperature distribution. Bulk tungsten has a higher thermal diffusivity, 69 mm^2/s, compared to stainless-steel. The cross-section temperature distribution from simulation is seen in Figure 68 (right). Due to the higher thermal diffusivity, the peak temperature at the laser spot was lowered from 910 to 529 °C and the temperature gradient along the radial direction reduced. As a result, the deposition grew in the radial direction to form the thin layer.

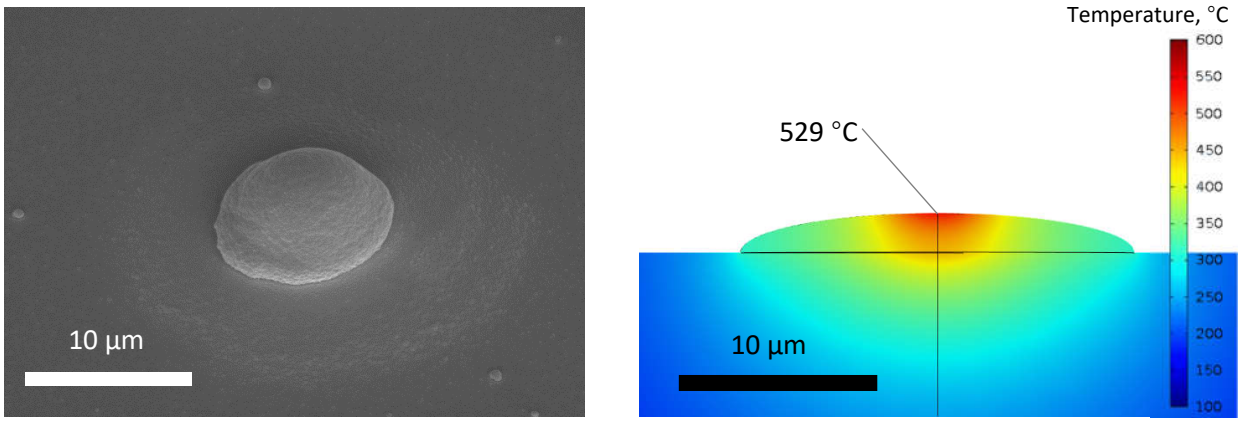

Figure 68: (left) SEM image and (right) simulation of the cross-section temperature distribution for the layer growth stage which was observed after twenty seconds of exposure to a laser at a power of 200 mW.

After the thin layer growth, spherical growth was observed. Figure 69 (left) shows an SEM image of the spherical deposit after ten seconds of exposure to the laser at a power of 300 mW. During the thin layer

growth stage, growth in the radial direction started to slow down once the temperature at the circumference of the spot was below the threshold deposition temperature of 375 °C (Lai and Lamb, 2000). As the thickness of the deposit increased, the temperature within the deposit became more even as seen in the simulated cross-section of the deposit in Figure 69 (right). The even temperature distribution encouraged uniform growth rates perpendicular to the surface of the deposit resulting in a spherical structure.

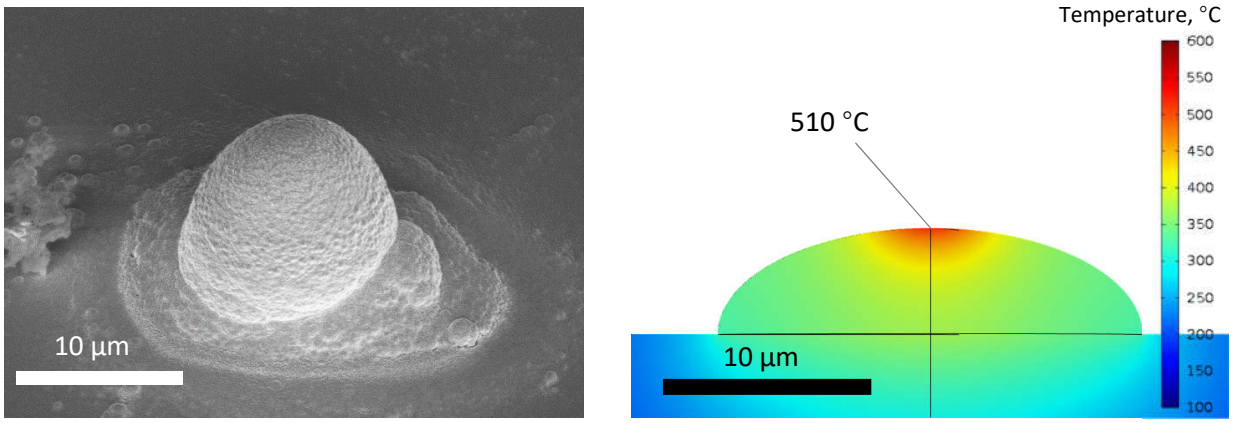

Figure 69: (left) SEM image and (right) temperature simulation of the cross-section of the spherical deposit produced after ten seconds of laser exposure at 300 mW of power.

Conical growth was observed after spherical growth as seen in Figure 70 (left) where the laser at a power of 300 mW was dwelled for 50 s. Growth in this shape was believed to be due to the deposition outside the laser spot that extends to a width of 100 µm in the line track deposition seen in the previous section (4.2). As this secondary deposition zone increased in thickness, more heat would conduct from the primary growth region, resulting in conical growth.

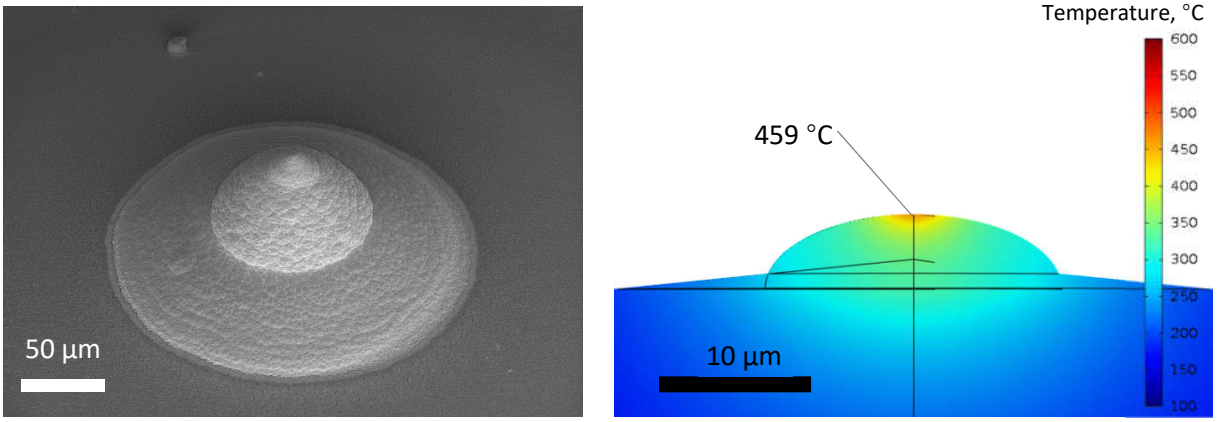

Figure 70: (left) SEM image and (right) simulated temperature distribution of the cross-section for the conical growth.

After conical growth, column growth was observed as seen in the SEM images of Figure 71. The cross-section for the temperature distribution from the simulation is seen in Figure 71. As the size of the cone increased, the temperature at the base of the cone was no longer above the threshold deposition temperature. Thus, growth was concentrated on the tip of the cone, producing a column structure.

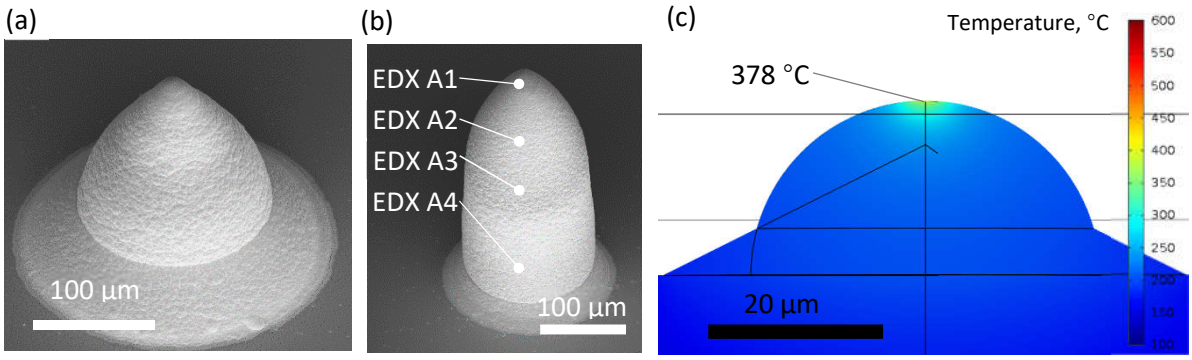

Figure 71: SEM images of cone (a) and column (b) after a dwell time of 100 and 200 s respectively using a laser with 300 mW power. EDX analysis shown in Table 19. (c) Cross-section temperature distribution in a cone-shaped deposit from simulation.

As the column grows taller, the diameter in the middle of the column increased, resulting in bulb-like growth. This is seen in the SEM image of Figure 72 (left). Figure 72 (right) shows the cross-section temperature distribution from the simulation. When the column increases in height, the aspect ratio increased. This resulted in an increase in the peak temperature at the laser spot and a rise of the temperature in the middle of the column above the threshold deposition temperature. Thus, as the tip continued to grow, the diameter in the middle of the column increased to form a bulb-like structure.

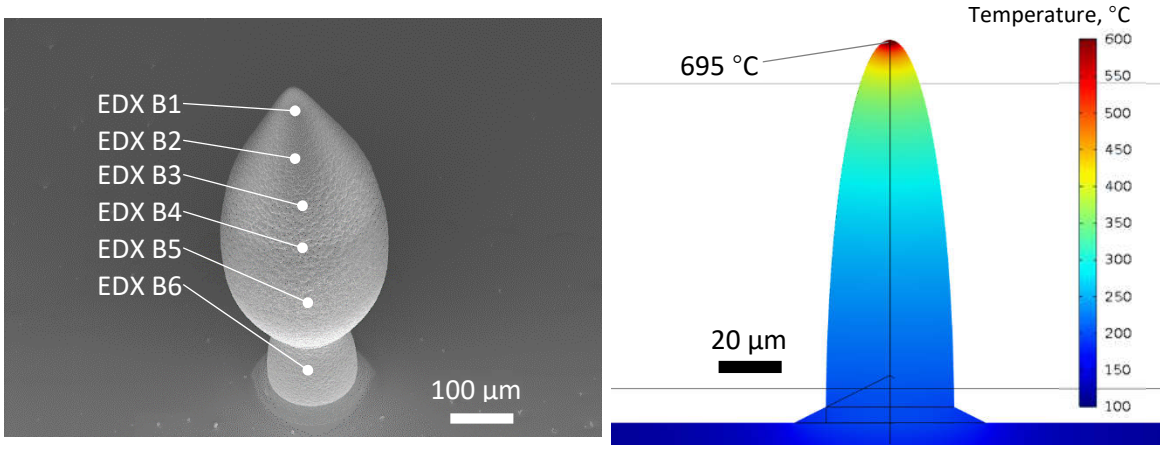

Figure 72: (left) SEM image of bulb-like growth formed after 500 s of laser dwell at a laser current of 300 mW and a deposition pressure of 3 mBar. EDX analysis shown in Table 19. (right) Cross-section of temperature distribution from simulation results.

Other than the growth stages mentioned previous, the contamination level of the substrate surface also affected the geometry of the deposits. When the substrate was not cleaned, there was less deposition outside the laser spot and higher aspect ratio structures were deposited as seen in Figure 73 (left). When the substrate was cleaned ultra-sonically for 5 mins with IPA and blown dry, a deposit with a wide base as seen in Figure 73 (right) was more prevalent.

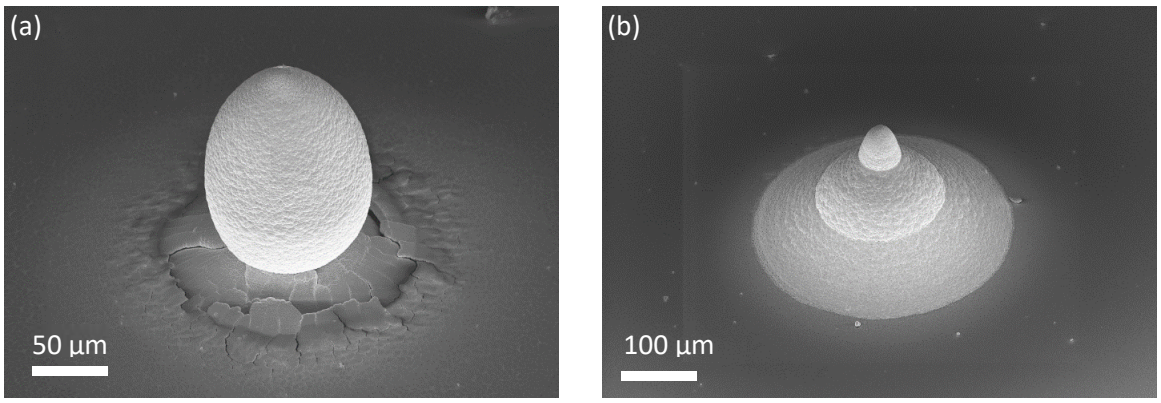

Figure 73: Deposition with a dwell time of 200 s on (a) an uncleaned substrate and (b) a substrate cleaned ultra-sonically for 5 mins in IPA.

EDX elemental analysis was done on column and bulb-like growth of Figure 71 and Figure 72 respectively and the results are seen in Table 19. Due to the higher temperature at the tip during column and bulb-like growth, there was a higher purity of tungsten at the top of the column. At the tip of the structure, the tungsten purity was as high as 93.5 wt% (excluding substrate elements).

Table 19: EDX elemental composition of the locations in Figure 72 and Figure 72.

Location	Excluding Fe, Cr, Ni, Si, Mn			Fe, wt%	Cr, wt%	Ni, wt%	Si, wt%	Mn, wt%
	W, wt%	C, wt%	O, wt%					
EDX A1	92.3	5.2	2.5	2.4	0.7	0.0	1.7	0.0
EDX A2	90.8	4.8	4.4	5.5	1.7	0.0	1.8	0.0
EDX A3	85.4	6.9	7.7	10.7	3.3	1.1	1.8	0.0
EDX A4	84.1	6.7	9.2	7.8	2.3	0.0	1.8	0.0
EDX B1	93.5	5.9	0.6	0.5	0.2	0.0	1.9	0.0
EDX B2	91.1	7.8	1.2	1.0	0.3	0.0	2.0	0.0
EDX B3	89.5	8.8	1.7	1.7	0.5	0.0	2.0	0.0
EDX B4	83.8	13.0	3.2	5.7	1.7	0.0	2.0	0.0
EDX B5	63.0	27.2	9.8	24.7	7.6	0.0	1.4	0.0
EDX B6	77.8	9.3	12.9	13.9	4.4	0.0	2.0	0.0
Substrate	0.0	100.0	0.0	68.9	19.0	9.0	1.0	2.0

4.4 Summary

In this chapter, track deposition on SiO_2/Si substrates was optimized based on laser scanning speed, substrate temperature, deposition pressure and laser power to achieve the lowest track resistivity and to reduce the deposition outside the laser spot. In terms of the microstructure of the written track, the deposit consisted of circular grains with diameters at the order of 100 nm to 1 µm. This morphology did not change with the laser scanning speed, substrate temperature, deposition pressure and laser power. However, the size of the grains increased with deposition pressure and temperature, leading to rougher and higher resistivity tracks. Deposition outside the laser spot also increased with deposition pressure and temperature. Through EDX element analysis, the deposition outside the laser spot was identified to consist of low purity tungsten with high carbon impurities. This was thought to be the deposition of partially broken-down precursor and reaction by-products. The lowest recorded as-deposited track

resistivity achieved was 93±27 μΩ cm or 16.6 times bulk tungsten resistivity for the track deposited at a laser power of 350 mW, scan speed of 10 μm/s, deposition pressure of 0.5 mBar and substrate temperature of 100 °C. This resistivity value was calculated based on the cross-section area including deposition outside the laser spot. If a triangular cross-section was assumed similar to in the work reported by (Nambu et al., 1990), then the calculated resisitivity would have been 5.6 times bulk tungsten which was within the 2-6 times bulk tungsten range reported by (Nambu et al., 1990) using a CW laser, same precursor and similar silicon substrates. Through COMSOL simulations of the laser heating, the temperature at the laser spot was estimated to be 533 °C, which was slightly higher than the estimated temperature at the laser spot for the parameters used by (Nambu et al., 1990) at 500 °C. The highest volumetric deposition rate achieved for CW deposition was in the order of 3,000 $\mu m^3/s$, however this included deposition outside the laser spot and the track resistivity was high at 1184 times bulk tungsten resistivity. The volumetric deposition rate for the lowest as-deposited track resistivity of 16.6 times bulk tungsten was 29.8 $\mu m^3/s$, 30,000 times the FIB deposition rate of the same precursor. The tungsten purity measured through EDX in the middle of that track was 81.4 wt% with 13.7 wt% carbon and 4.9 wt% oxygen excluding the measured silicon content detected from the substrate.

The usage of hydrogen instead of nitrogen gas as the background gas during the deposition did not change the deposition track geometry, microstructure morphology and amount of deposition outside the laser spot. However, by annealing in hydrogen at 650 °C for 30 mins, removal of the deposition outside the laser spot was achieved. Optical microscope images and EDX element analysis showed that the region outside the laser spot returned to the substrate composition levels after the annealing. The microstructure of the track still consisted of circular grains after the annealing, however the size of the grains reduced and larger gaps appeared between the grains likely due to removal of material during the annealing process. The annealing process increased the tungsten purity from 83.3 % to 90.6 % (excluding silicon) and reduced the resistivity from 93±27 to 66±7 μΩ cm (16.6 to 11.7 times bulk tungsten resistivity). There was also a significant reduction in the contact resistance between the deposited tungsten track and the silver paste from 132±92 to 2±32Ω. This was thought to be due to the removal of carbon impurities on the surface of the track during the annealing process that previously created an insulating barrier between the silver paste and the tungsten track.

Also explored in this chapter was growth of three dimensional structures on the substrate when the laser was dwelled on a spot. Stainless-steel substrates were chosen due to the low thermal diffusivity of the material and would thus concentrate the thermal energy on a small spot on the substrate surface. The morphology of the deposit changed from a thin layer, to a sphere, then a conical shape, a column and then a bulb-like shape. The change in morphology was attributed to the thermal diffusivity of tungsten which was approximately 17 times that of stainless-steel, resulting in a more uniform temperature distribution within the deposit.

Chapter 5 Ultrafast LCVD

The LCVD of tungsten using the 405 nm CW laser diode of the previous chapter produced deposition with significant deposition outside the laser spot. In this chapter, the deposition of tungsten using a pulsed ultrafast laser is studied. Most of the results were produced using a laser spot of 6.6 μm, pulse repetition rate of 500 kHz and deposition pressure of 0.5 mBar.

5.1 Spot dwell deposition and temperature simulation

The nucleation of the deposition through LCVD was investigated in this section by exposing the substrate to a fix number of pulses. For dielectrics like SiO_2/Si and borosilicate glass, a thin film first nucleates and on top of that the quasi-periodic structures start to form. On metal substrates like stainless steel, no thin film is formed and quasi-periodic structures grow on the surface from the start.

5.1.1 Deposition on SiO_2/Si

To understand the growth process of tungsten deposited with the ultrafast laser, the laser was set to dwell on a spot at a fix number of pulses on SiO_2/Si substrates at a pulse repetition rate of 500 kHz. The SEM images of the spot deposition are seen in Figure 74. At a peak fluence of 36 mJ/cm^2, nucleation affecting an area of 500 nm was only observed after 50 000 pulses. At 100 000 pulses, a thin film was formed on the substrate with periodic structures starting to form on top of it. At the edges of the thin film, a periodic pattern that was perpendicular to the linear polarization of the laser beam was observed. The observed period of approximately 300 nm ($\sim\lambda/3$) was shorter than the period of the quasi-periodic structures that grew on it at 500 nm ($\sim\lambda/2$). After 200 000 pulses, the diameter of the thin film and the height of the quasi-periodic structures increased. The walls appeared curvy and forked into two in certain locations. After 500 000 pulses, the quasi-periodic structures grew even higher and short branches with random orientation appeared at the edges of the quasi-periodic structure.

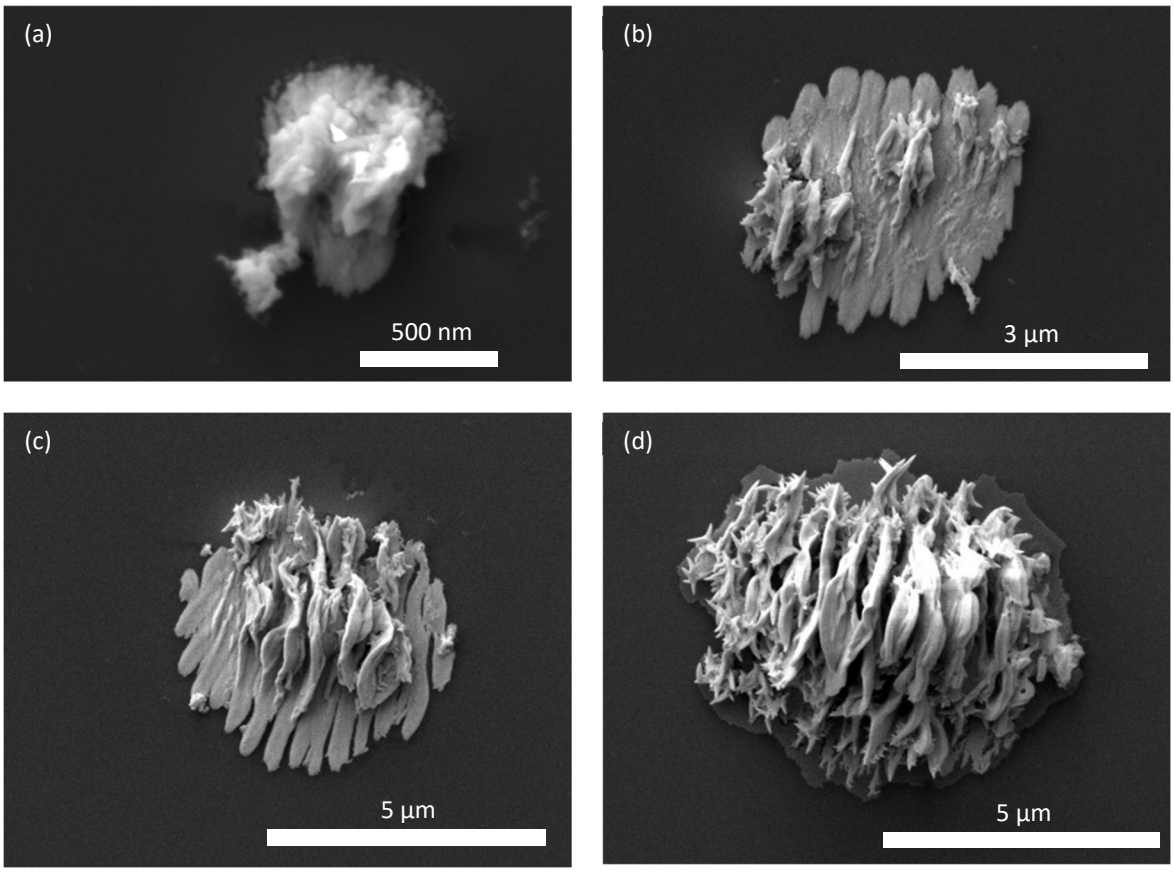

Figure 74: Spot dwelling of the laser at a peak fluence of 36 mJ/cm² for a length of (a) 50 000, (b) 100 000, (c) 200 000, and (d) 500 000 pulses.

Figure 75 shows the height growth of the spot deposition at three different power levels for SiO_2/Si substrate. There was a threshold number of pulses required to nucleate the thin film and this threshold reduced with increasing laser power. For a peak fluence of 36 mJ/cm², deposition required 50,000 pulses to nucleate. When the peak fluence was increased to 188 mJ/cm², the threshold number of pulses decreased to 5000 pulses.

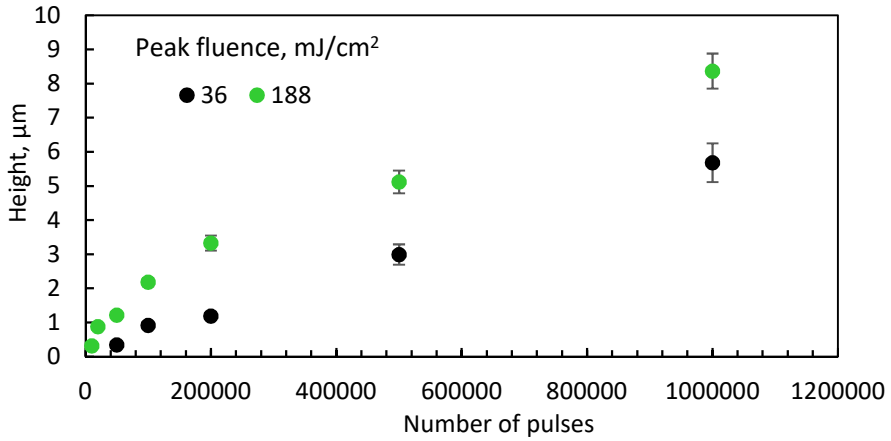

Figure 75: Height growth for spot dwell experiments at two laser powers on SiO_2/Si measured using white light interferometry.

5.1.2 Deposition on borosilicate glass

Other than SiO_2/Si substrates, deposition of tungsten using ultrafast laser pulses was also possible on borosilicate glass. The substrate was transparent at the wavelength of the laser and absorption was due to high intensity non-linear laser-material interaction at the laser spot (Ben-Yakar and Byer, 2004). Figure 76 shows SEM images of the spot dwell tungsten deposition on borosilicate glass. Similar to that seen on SiO_2/Si, a thin film formed first followed by quasi-periodic structures on the thin film.

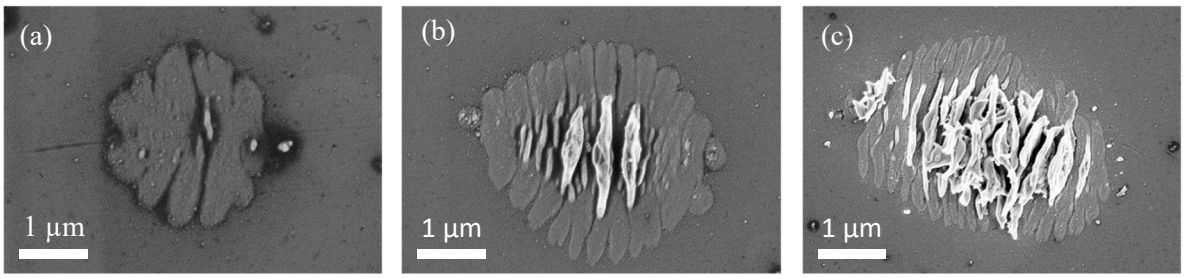

Figure 76: SEM images of spot dwell deposition on borosilicate glass. (a) Peak fluence of 110 mJ/cm² with 100,000 pulses, (b) 110 mJ/cm², 200,000 pulses, and (c) 80 mJ/cm², 500,000 pulses. A thin film was formed before the quasi-periodic structures started to grow on the thin film.

5.1.3 Deposition on stainless steel

For the spot dwells on stainless steel, a laser peak fluence of 56 mJ/cm² was used. Deposition was observed in the SEM images after 20 000 pulses (Figure 77). In the image, two ridges with a width of approximately 110 nm and separation of 150 nm were formed. After 40 000 pulses, the ridges grew to a width of 190 nm and the separation between the ridges were approximately 320 nm. At 60 000 pulses, the ridges continued to grow in width to 370 nm and the separation between the ridges increased further to approximately 500 nm. At 80 000 and 100 000 pulses, the width of the ridges was approximately 400 nm and there were clumps of larger width sections. The wavelength of the periodic structure was approximately 500 nm. The increase in the wavelength during growth was likely due to the increase in surface roughness. During nucleation, the nanoscale roughness of the stainless steel substrate promoted high spatial frequency LIPSS (Bonse et al., 2017) to form. The growth of the ridges increased the roughness of the surface such that lower spatial frequency ridges were preferred such as the dominant wavelength of 500 nm ($\sim\lambda/2$). Further growth in height of the ridges caused the periodicity to be unstable such that the ridges became wavier. Branching was also observed in the structures. This happened because localized hot spots were also created on the flanks instead of just at the top of the structures. This phenomenon is similar to the LIPSS structures created when the incident laser was placed at an angle to the substrate (Buividas et al., 2014).

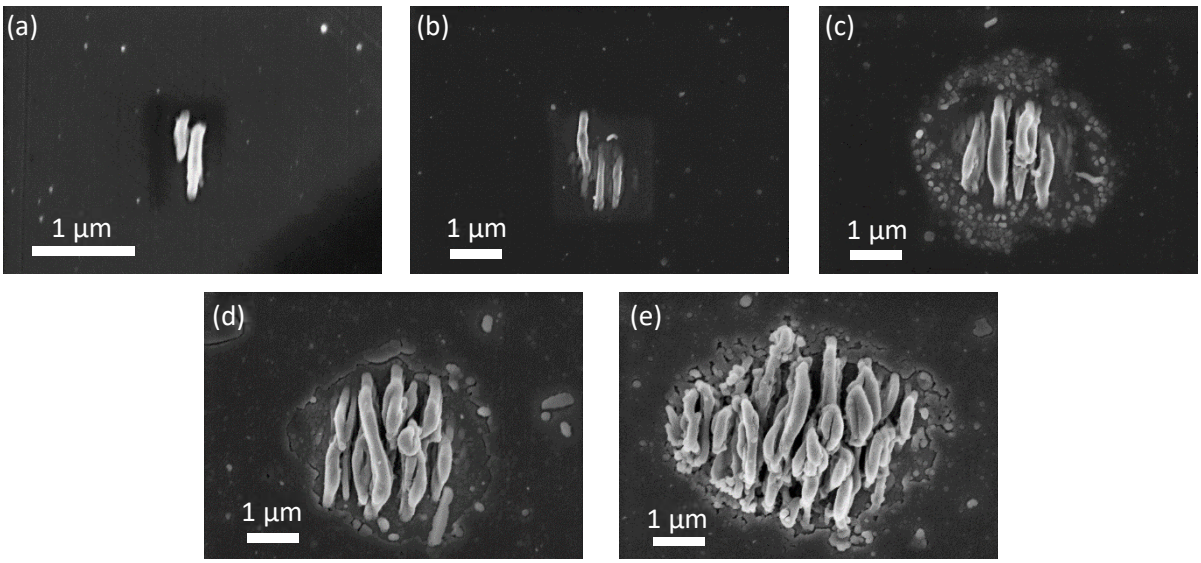

Figure 77: SEM images of spot dwelling of the laser at a peak fluence of 56 mJ/cm² for a duration of (a) 20 000, (b) 40 000, (c) 60 000, (d) 80 000, and (e) 100 000 pulses on stainless steel substrate.

Figure 78 shows the height growth of the tungsten deposit on stainless steel substrate. Similar to the growth behaviour on SiO_2/Si, a threshold number of pulses was required before a constant height growth rate was achieved. The threshold number of pulses also decreased with increasing laser power. The growth rate after reaching the threshold number of pulses increased with increasing laser power.

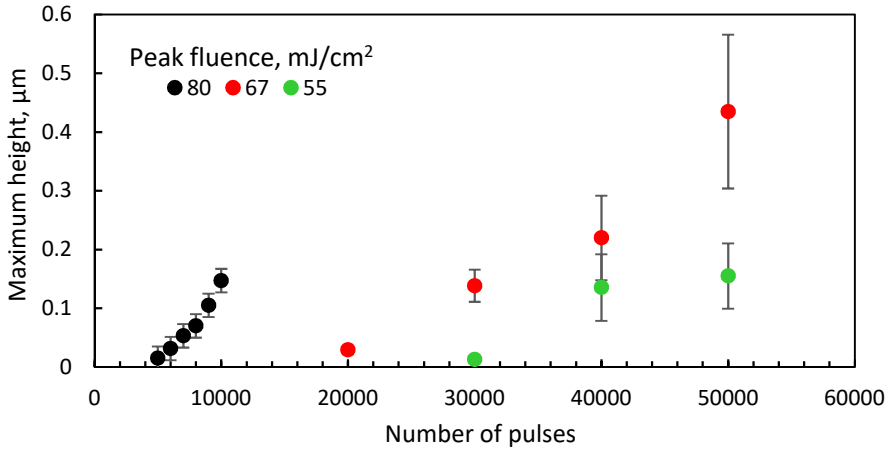

Figure 78: Height growth for spot dwell experiments at three laser powers on stainless steel substrate measured using white light interferometry.

5.1.4 Temperature simulation

The spatial and temporal temperature profile during deposition was simulated using the MATLAB model described in section 3.5.7. Figure 79 (left) shows the temperature at the centre of the laser spot on the surface of stainless steel exposed to a single laser pulse with peak fluence of 67 mJ/cm², pulse energy of 11.5 nJ and beam diameter of 6.6 µm. The temperature rose to the melting temperature of approximately 1500 °C and stayed at melt temperature for around 2 ns. After that, the temperature cooled back down to the initial temperature of 70 °C before the next pulse. Figure 79 (right) shows the spatial temperature profile at various times after the laser pulse. Due to the short laser pulse, the

temperature rise on the surface of the substrate was limited to a 6 µm radius and the rest of the substrate stays cool.

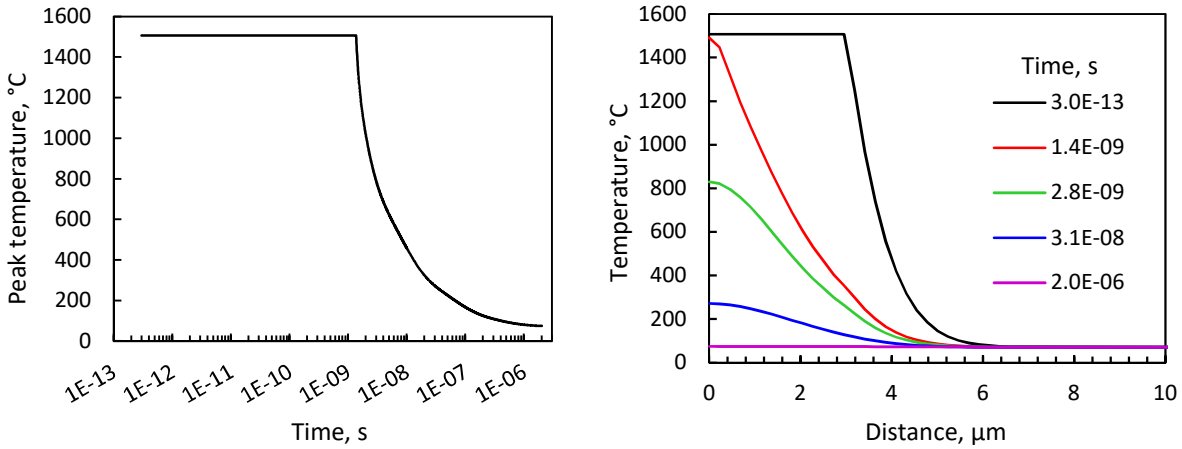

Figure 79: (Left) Temperature at the centre of the laser spot between pulses with energy of 11.5 nJ and peak fluence of 67 mJ/cm² on stainless steel showing that the peak temperature stays at melting temperature for around 2 ns. (Right) Spatial temperature profile on the surface of the substrate at various times after the laser pulse.

The deposition height growth rate can be modelled using the Arrhenius equation

$$\dot{h} = B \exp\left(-\frac{E}{\mathcal{R}T}\right) \qquad [\,28\,]$$

where the constants B and $E/\mathcal{R}$ can be estimated from the best fit of the height data and T is the temperature. The actual peak height on stainless steel can be compared to the predicted peak height from the Arrhenius equation by integrating the temporal peak temperature profile

$$h_{predict} = \eta \times \int_0^{t_{repetition}} B \exp\left(-\frac{E}{\mathcal{R}T}\right) dt \qquad [\,29\,]$$

where η is the number of pulses and $t_{repetition}$ is the time between the laser pulses, to estimate the constants B and $E/\mathcal{R}$. The best fit between the actual and predicted peak height (Figure 80) gave the values of B =2731 µm/s and $E/\mathcal{R}$ =789 K.

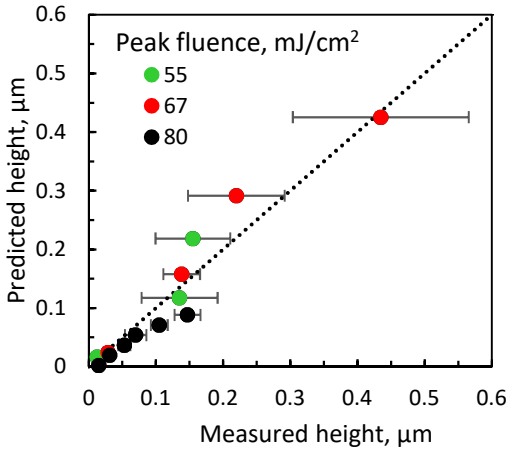

Figure 80: Graph of predicted height based on the Arrhenius constants that gave the best fit against the measured height used to estimate the Arrhenius constants.

Using the best estimate of the constants, the height profile on the surface of the substrate can be predicted in the simulations. The spatial Gaussian profile of the laser was modified to include the observed interference periodicity of 500 nm. Figure 81 shows the comparison between SEM images of the dwell results and the predicted height of the deposition using the Arrhenius constant mentioned earlier and the simulated surface temperature from the MATLAB model. The simulation could predict good resemblance of the actual results in terms of deposition area and approximate number of ridges. Slight coalescence due to the width of the ridges increasing and touching one another was also predicted. However, the waviness of the ridges was not predicted because three-dimensional light interference between the incident laser light and reflected light off the deposited structure were not included in the model.

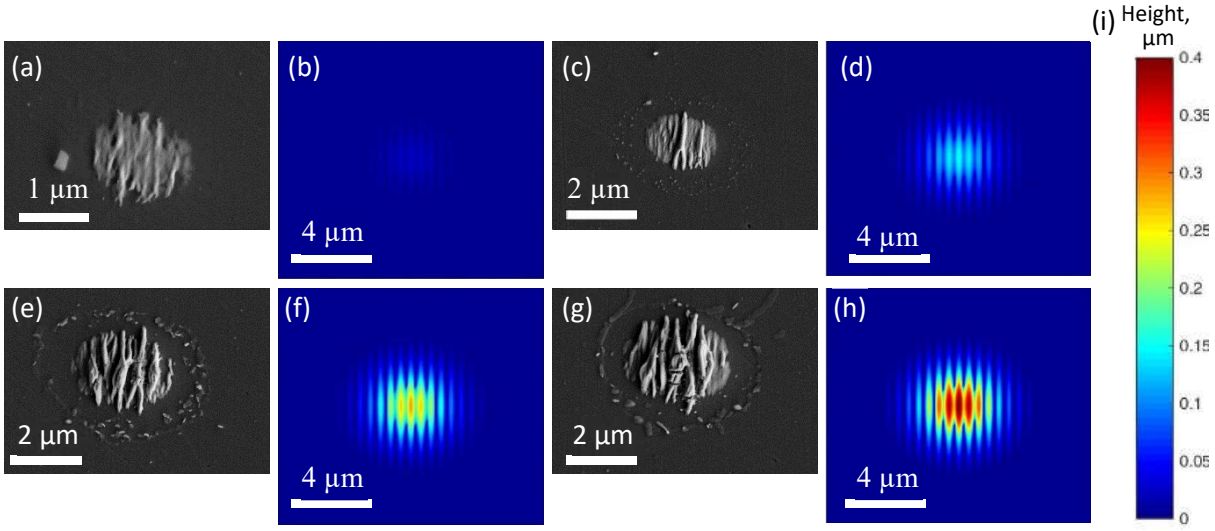

Figure 81: SEM images (a, c, e, g) along with the predicted deposition height (b, d, f, h) based on the fitted Arrhenius constants to peak height data and simulated surface temperature from the Matlab model. (i) Colour scale bar for the surface height profiles (b, d, f, h).

5.2 Track deposition on SiO_2/Si

Deposition tracks were produced by scanning the laser on the substrate. Figure 82 shows SEM images of the quasi-periodic tungsten structures deposited on the silicon wafers at a scanning speed of 30 µm/s, peak fluence of 56 mJ/cm^2 and pulse repetition rate of 502 kHz. The orientation of the periodic structures formed in LIPSS was affected by the direction of the laser beam linear polarization (Bonse et al., 2017). For strong absorbing materials, such as semiconductors and metals, the structures were orientated perpendicular to the laser beam polarization. From the images, the periodicity of the structures was around 500 nm ($\sim\lambda/2$) and the wall thickness was approximately 200 nm. Also visible was deposition outside the laser spot which was also observed in tungsten LCVD with CW 405 nm lasers. The width of this thin film reduced with increasing laser scan speed and decreasing laser power.

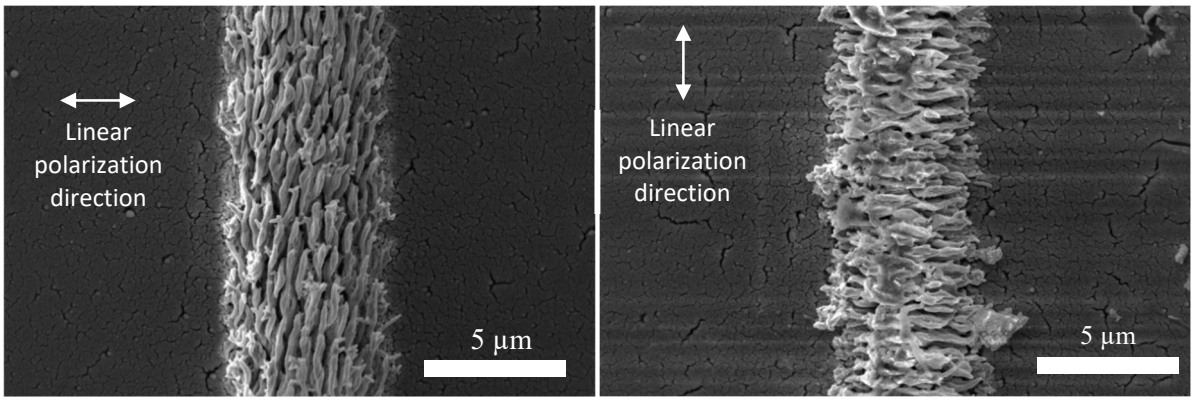

Figure 82: SEM image of quasi-periodic tungsten structures deposited on silicon dioxide coated silicon wafers with linear polarization perpendicular (left) and parallel (right) to laser scan direction.

Figure 83 shows a SEM image of the deposited track when the laser beam was circularly polarized with a scanning speed of 30 µm/s, peak fluence of 67 mJ/cm^2 and pulse repetition rate of 502 kHz. Instead of quasi-periodic grooves, short nano-wires with no specific orientation were observed. There was also more branching in the structures compared to that made with linear polarized laser beam.

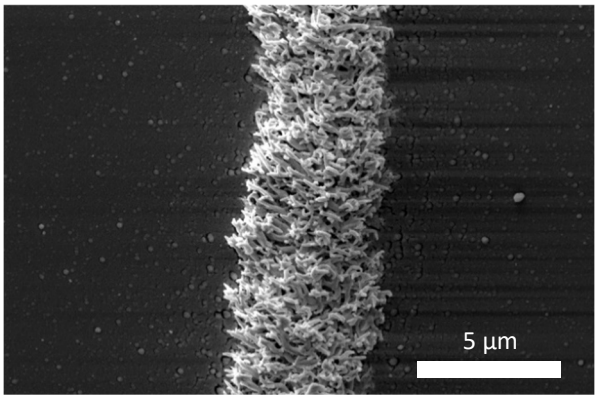

Figure 83: Plan view SEM image of tungsten structures deposited with circular laser polarization.

A 45° tilted SEM view of the cross-section of the track with laser linear polarization perpendicular to the scan direction is seen in Figure 84 (left). The track was deposited on a piece of silicon wafer and then the wafer was cleaved to reveal the cross-section. Figure 84 (right) shows the cross-section after the cleaved substrate was moulded in polymer and polished. There were significant branches in the quasi-periodic walls. The small grains in the polished sample were likely the 40 nm silica particles used in the polishing process. No damage to the underlying substrate was observed in the cross-section.

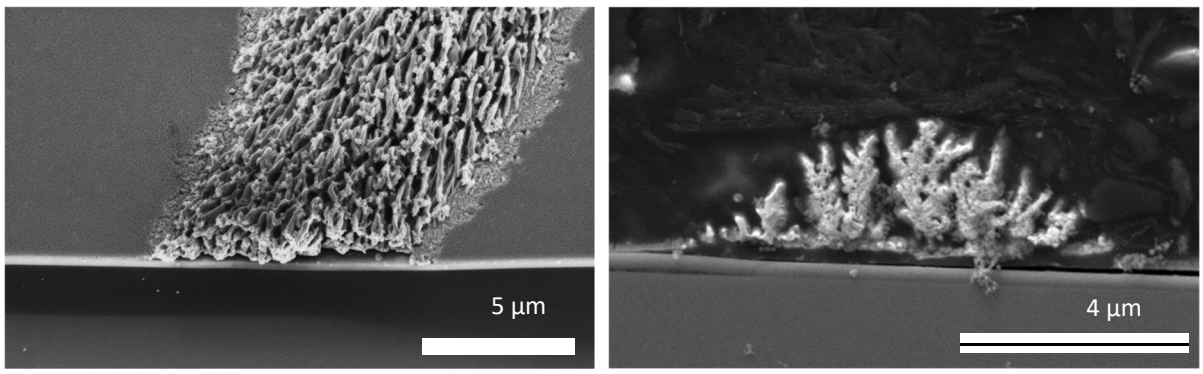

Figure 84: (left) 45° SEM tilt view of the quasi-periodic tungsten structures on substrate cleaved after deposition. (right) SEM image of track cross-section after polymer moulded and polished.

5.2.1 Deposition thresholds and regimes

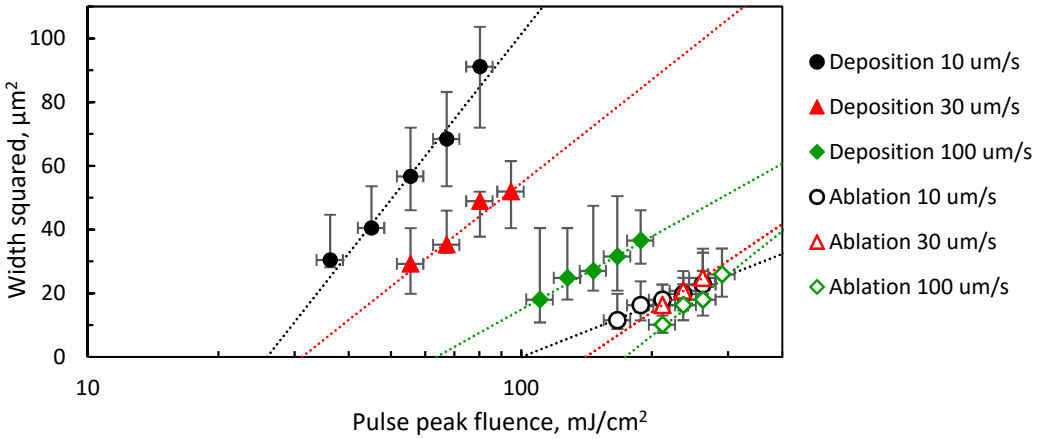

Figure 85: Plot of fluence against ablation diameter squared to measure fluence thresholds.

The threshold for ablation and tungsten deposition on silicon dioxide coated silicon wafers at various scanning speeds are shown in Figure 85 and summarized in Table 20. The ablation threshold experiments were done without the tungsten precursor with nitrogen at atmospheric pressure and the linear polarization was perpendicular to the scan direction. Up to a scan speed of 100 µm s^{-1}, the deposition threshold of tungsten on silicon was lower than the ablation threshold of silicon. This was expected because the minimum deposition temperature of tungsten, 350 °C (Lai and Lamb, 2000), was lower than the melting temperature of silicon, 1414 °C (Kun Li et al., 2014). The lowest deposition intensity threshold (≈10^{10} W/cm^2) was two orders of magnitude lower than the threshold reported for 400 nm ultrafast multi-photon dissociation of the same precursor (Green and Her, 2013).

Table 20: Ablation and deposition threshold at various scan speeds on silicon.

Regime	Scan speed, µm/s	Pulse fluence threshold, mJ/cm^2	Intensity threshold, 10^{11} W/cm^2	Pulse energy threshold, nJ
Deposition	10	26±7	0.864	4.43
Deposition	30	31±12	1.04	5.34
Deposition	100	64±46	2.12	10.90
Ablation	10	100±44	3.34	17.13
Ablation	30	141±50	4.70	24.11
Ablation	100	174±71	5.79	29.72

The spot growth experiments of section 5.1.1 showed that a thin film grew on the silicon substrate first followed by the quasi-periodic structures growing on top of it. It may be possible to limit the deposition to thin films by increasing the scan speed so that the thin film was deposited with negligible quasi-periodic structures on top of it.

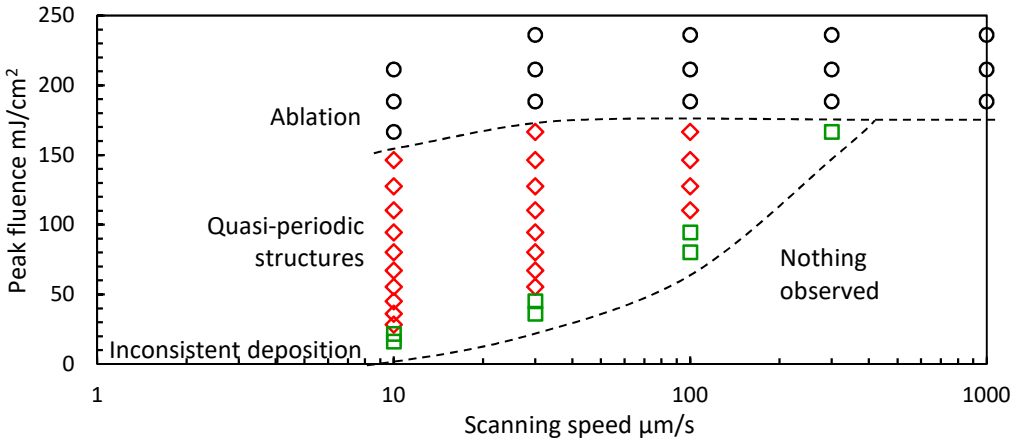

Figure 86: Plot of pulse fluence against scanning speed experiment points explored for the deposition of tungsten on silicon along with the resultant modification regimes achieved. Uncertainty of 7% in peak fluence measurements was not displayed.

The results of increasing the scan speed with various power levels are plot in Figure 86. In the experiments, a continuous ablation track without the tungsten precursor and in nitrogen was observed at an approximately constant fluence value of 190 mJ/cm^2 for scan speeds of 10 to 1000 µm/s. When the substrate was exposed to the tungsten precursor at 190 mJ/cm^2 and above, ablation in the middle of the track flanked by deposition at the sides was observed (Figure 87 a). The minimum fluence for observable deposition of quasi-periodic structures increased with scan speed, narrowing the window where deposition without ablation was observed. At low power levels, the deposition was erratic and consisted of discontinuous patches of thin film deposition with and without the quasi-periodic structures on top of them (Figure 87 b). At 300 µm/s and above, no quasi-periodic structures were observed however deposition with slight ablation in the middle of the track was observed (Figure 87 c).

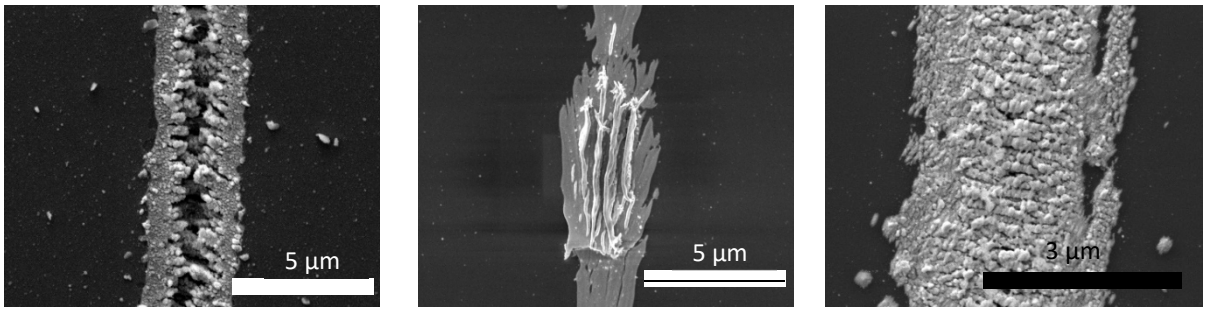

Figure 87: SEM image of (a) ablation in the presence of tungsten hexacarbonyl precursor and (b) erratic deposition with discontinuous patches of thin film deposition with and without the quasi-periodic structures. (c) SEM image of deposition at a scan speed of 300 µm/s and pulse fluence of 190 mJ/cm^2 showing slight ablation and balling of the deposits in the middle of the scanned track

5.2.2 Elemental composition

The elemental composition of the deposition was analysed in EDX to confirm the tungsten composition. A track was made by scanning the laser at speed of 15 µm/s and EDX analysis was done perpendicular to the scanned track (Figure 88). On a blank silicon wafer that was exposed to the same cleaning methods used in all samples in this study, the elemental composition measured was 73.8 wt% silicon, 20.1 wt% oxygen and 6.0 wt% carbon. The high content of oxygen on the blank samples was from the

280 nm thick thermally grown silicon dioxide layer on the surface of the wafer while the carbon content may be due to contamination from the cleaning procedures. At approximately 40 µm from the centre of the deposited track, the elemental composition was approximately 70 wt% silicon, 18 wt% oxygen and 12 wt% carbon. The increase in carbon content compared to the blank samples was likely due to deposition of precursor dissociation by-products. No tungsten was detected outside the laser spot. The tungsten composition in the middle of the track was at least 80 wt% and discounting the detected silicon the maximum measured value was 90 wt%. This tungsten content was similar to that reported in large area constant temperature CVD growth (Lai and Lamb, 2000) and FIB deposition (Langfischer et al., 2002) using the same precursor.

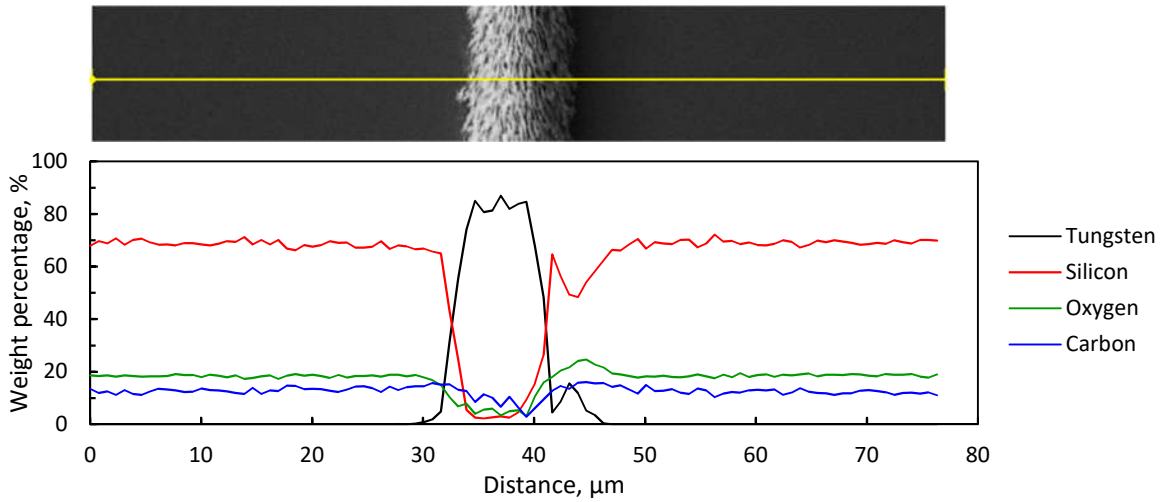

Figure 88: (Top) SEM image and (bottom) EDX element analysis of a track deposited at a scanning speed of 15 µm/s. The analysis points of the EDX were along the yellow line on the SEM image.

5.2.3 Resistivity measurements of quasi-periodic structures

For the resistivity measurements, tracks were made at a scanning speed of 30 µm/s with the linear polarization set perpendicular to the track to produce quasi-periodic structures parallel to the track. This was done to promote electrical conductivity along the deposited track. The peak fluence of the laser during the scan was 56 mJ/cm^2. The linear fit to the plot of total resistance of the track (Figure 89) estimated the resistivity of the track to be 290±60 µΩ cm, 51.8 times bulk resistivity of tungsten. This resistivity value was lower than that reported in large area CVD tungsten deposition using the same precursor at 375 °C (Lai and Lamb, 2000) and similar to the reported value from FIB deposition (Langfischer et al., 2002). The cross-section area used for the resistivity calculation included porous regions of the structure, thus resistivity of the track excluding the porous regions would have been lower.

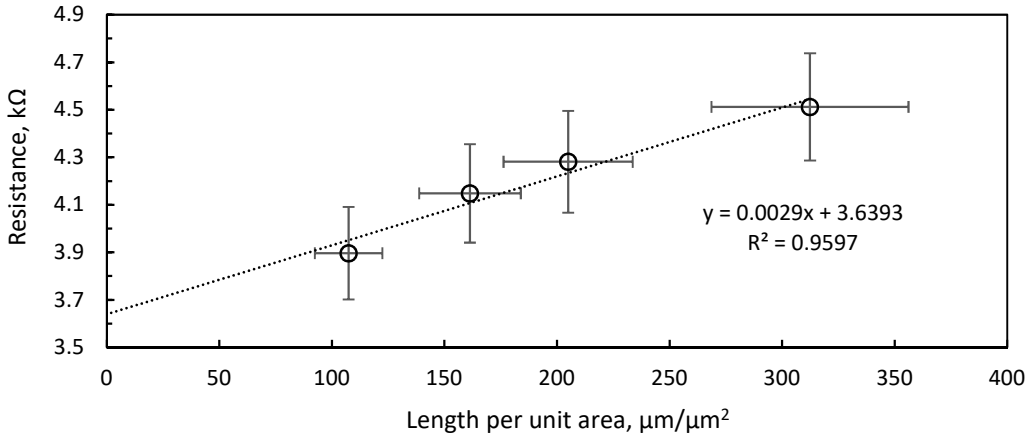

Figure 89: Plot of total resistance of the tracks deposited at 30 µm/s scanning speed, and 56 mJ/cm² peak laser fluence.

5.2.4 Effect of laser scan speed and power

The laser scan speed and peak intensity was varied to study the effects on the deposition. Figure 90 shows the maximum track height and FWHM when the laser peak fluence was fixed at 110 mJ/cm^2 while the scanning speed was increased. The track height decreased two orders of magnitude while the when the scanning speed was increased from 3 to 100 µm/s. The linear height growth rate based on the equation 35 that gave the best fit to the maximum height data was 5.5 µm/s. The linear height growth rate in these ultrafast experiments was higher than that measured in the CW experiments at 3.8 µm/s (section 4.2.1) likely due to the higher temperature at the laser spot (section 5.1.4) and porosity of the quasi-periodic structures. The FWHM stayed closed to the beam diameter of 6.6 µm when the scan speed was increased.

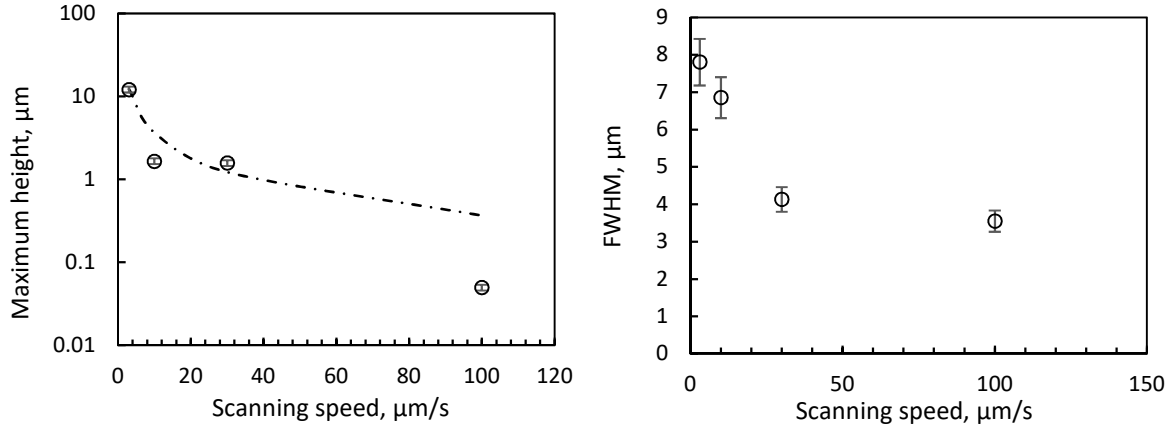

Figure 90: Maximum cross-section average height and FWHM against scanning speed for ultrafast LCVD on SiO_2/Si substrates at a laser peak fluence of 110 mJ/cm².

Figure 91 shows the cross-section profile of the track at the various scan speeds. There was deposition outside the laser spot covering a width of approximately 60 µm. The deposition outside the laser spot reduced with increasing scan speed.

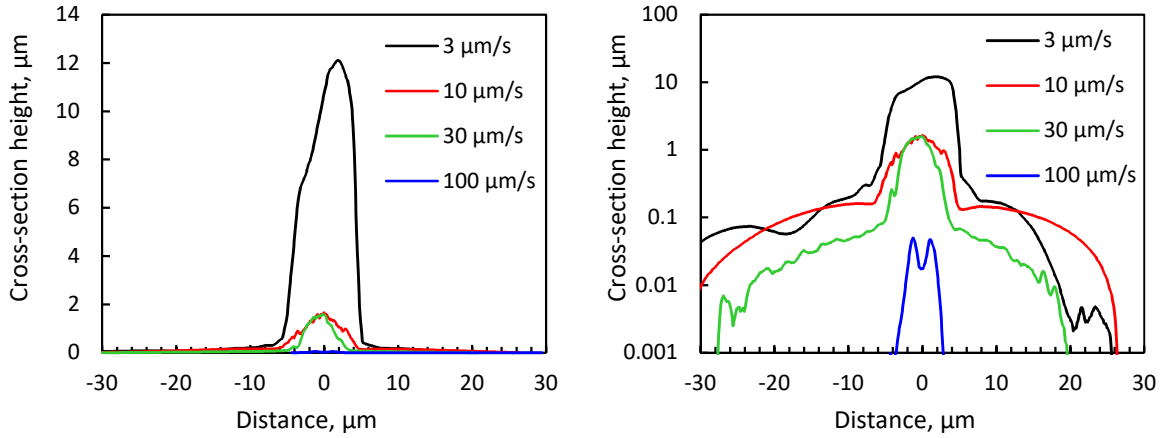

Figure 91: Average cross-section profile, linear (right) and logarithmic (left), for ultrafast LCVD on SiO_2/Si substrates at a laser peak fluence of 110.4 mJ/cm^2. The uncertainty in the height measurements was 8 %.

Figure 92 shows SEM images of the track at various scanning speeds. As the scanning speed was reduced, the thickness of the periodic structures increased and clumps of material were visible in the middle of the track at scanning speeds of 10 and 30 µm/s. At a scanning speed of 3 µm/s, there was significant branching in the quasi-periodic structures and some of the branches were orientated parallel to the linear polarization direction.

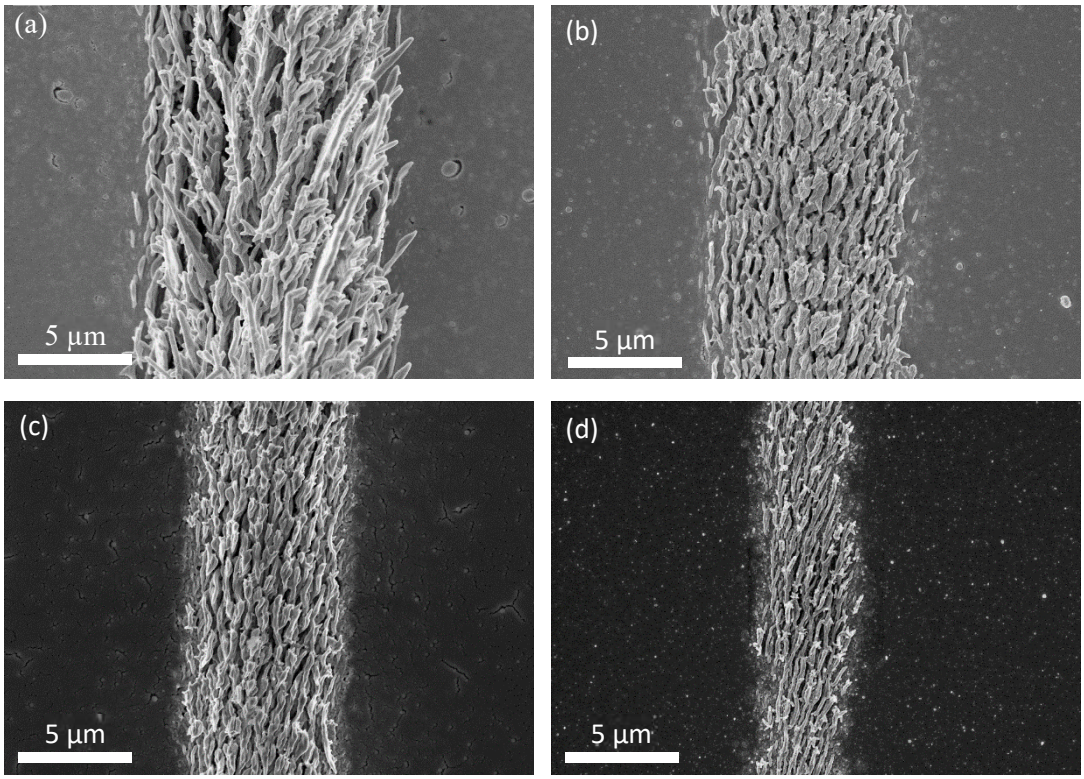

Figure 92: SEM images of deposited tracks using a laser peak fluence of 95 mJ/cm^2 at a scanning speed of (a) 3, (b) 10, (c) 30, and (d) 100 µm/s.

Figure 93 shows the cross-section track profile at various laser powers for a scan speed of 10 µm/s. The deposition outside the laser spot increased with laser power. At a laser peak fluence of 36 mJ/cm^2, there was negligible deposition outside the laser spot at a laser peak fluence of 95 mJ/cm^2 the width of the deposition outside the laser spot was approximately 60 µm.

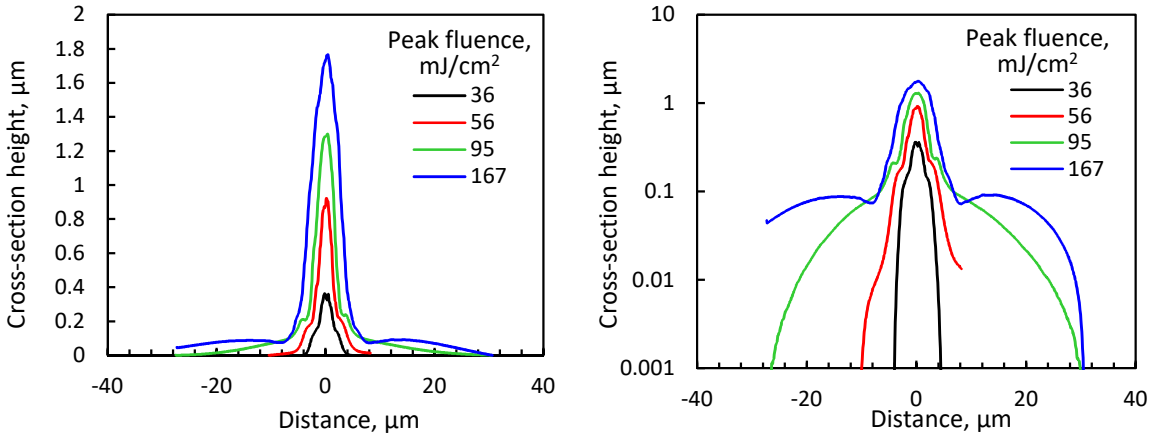

Figure 93: Average cross-section profile, linear (right) and logarithmic (left), for ultrafast LCVD on SiO_2/Si substrates at scanning speed of 10 µm/s at various laser peak fluence levels.

Figure 94 shows SEM images of the deposited track made at the various laser power levels. As the laser power was increased, the thickness of the quasi-periodic structures increased and clumps of material were visible in the middle of the track.

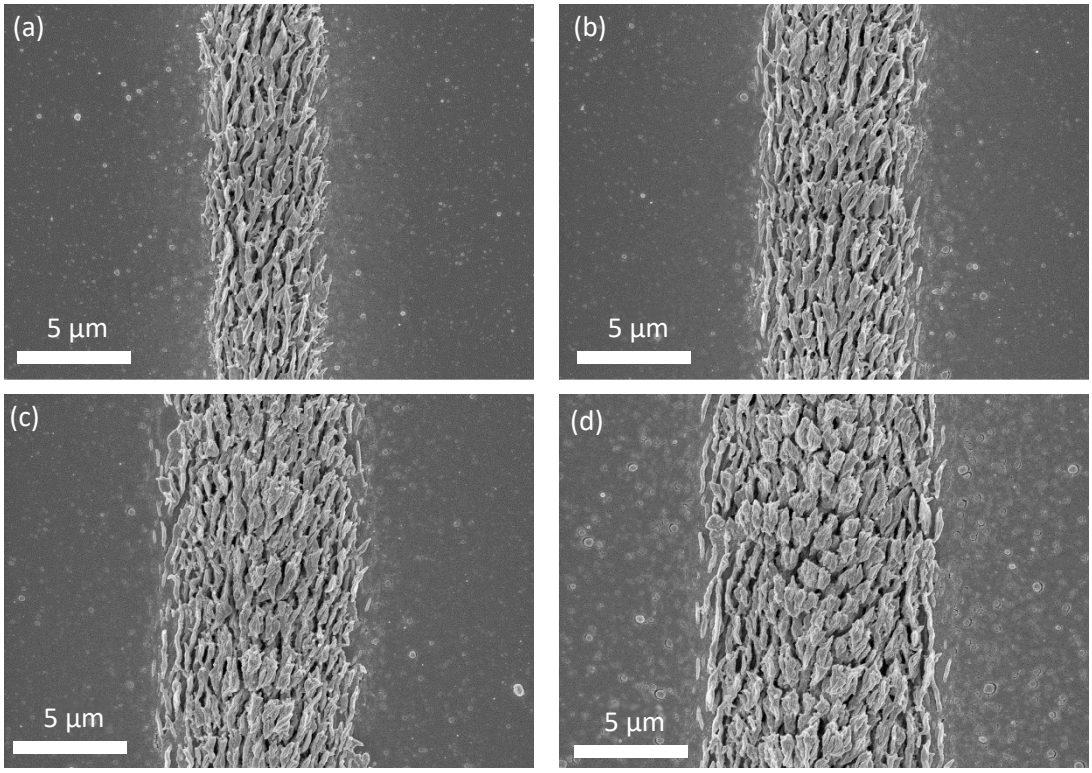

Figure 94: SEM images of deposited tracks made using as scanning speed of 10 µm/s with a laser peak fluence of (a) 36, (b) 56, (c) 95, and (d) 167 mJ/cm^2.

5.2.5 Effect of pulse repetition rate

The effect of pulse repetition rate on the deposition was investigated by comparing the deposition at 500 kHz with that of a lower repetition rate at a comparable number of pulses per spot. The settings for these experiments are seen in Table 21. The number of pulses per spot was calculated as

$$\eta = 2wf/v \qquad [38]$$

where $2w$ was the focal spot diameter, f was the laser pulse repetition rate and v was the scanning speed. Three pairs of samples were prepared.

Table 21: Laser parameters for the experiments to investigate the effect of frequency.

Label in Figure 95	Frequency, kHz	Number of pulses	Scanning speed, µm/s	Peak fluence, mJ/cm^2
a	500	330,000	10	56
b	100	220,000	3	56
c	500	33,000	100	147
d	20	44,000	3	147
e	500	11,000	300	212
F	5	11,000	3	212

Figure 95 shows SEM images of the deposition at a repetition rate of 500 kHz (top) and deposition at a lower frequency (bottom) that has the same order of magnitude for the number of pulses, η. There was similarity in terms of widths of the lines and deposition morphology showing that the formation of the quasi-periodic structures was independent of pulse repetition rate.

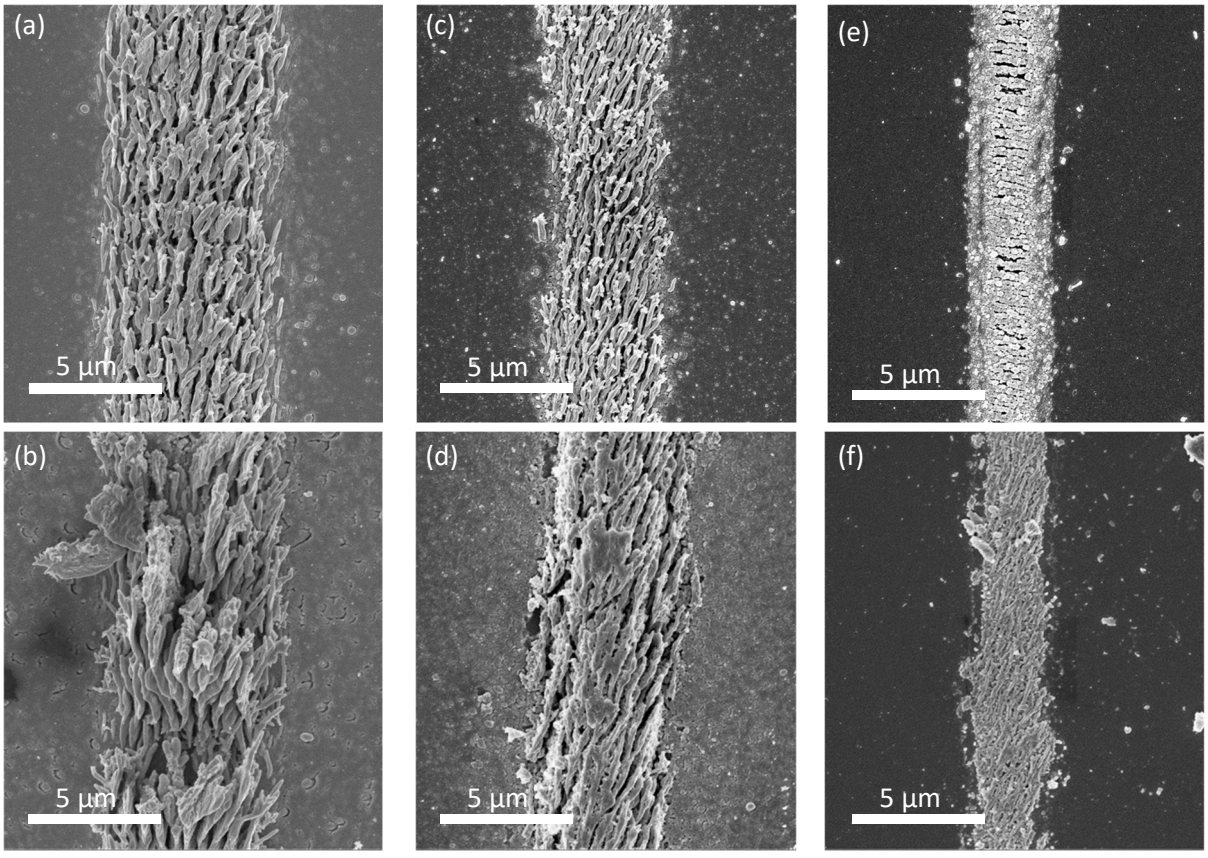

Figure 95: Tracks produced with a lower frequency (top) and tracks produced with the standard frequency of 500 kHz with comparable pulse overlap values (bottom). The details of the laser parameters are in Table 21. The morphology of the tracks produced at the lower frequency was similar to that produced at the standard frequency of 500 kHz at a comparable pulse overlap.

The measured geometrical profiles of the tracks are seen in Table 22. The track made at a frequency of 100 kHz and scan rate of 3 µm/s was compared with the track at 500 kHz and 10 µm/s, where the number of pulses was at the order of 220,000-330,000 pulses. Similarly, the track made at 20 kHz repetition rate 3 µm/s scanning speed was compared to the track made at 500 kHz 100 µm/s, where the number of pulses was at the order of 33,000-44,000 pulses. For both comparison cases, the cross-section

area and the maximum track height of the lowered frequency deposition was higher than the results of the standard 500 kHz deposition. The volumetric deposition rate of the lowered frequency deposition was of the same order of magnitude compared to the volumetric deposition rate of the standard 500 kHz deposition even though the frequency was lowered by at least a factor of five. Thus, the deposition process was likely limited by the transport of the precursor to the laser spot at higher frequencies. Increasing the pulse repetition rate above 500 kHz may not achieve significant increases in volumetric deposition rates unless the precursor pressure and flow-rate were increased.

Table 22: Comparison between deposition at 500 kHz and lower repetition rates.

Label in Figure 95	Frequency, kHz	Scanning speed, μm/s	Number of pulses	Cross-section area, μm^2	Maximum track height, μm	FWHM, μm	Volumetric deposition rate, $\mu m^3/s$
a	500	10	330,000	4.95	0.8	5.2	49.45
b	100	3	220,000	18.84	3.1	4.8	56.52
c	500	100	33,000	0.39	0.1	3.5	39.31
d	20	3	44,000	6.61	2.2	1.9	19.84

5.2.6 Thin film tracks with larger 33 μm focal spot

The previous study of scanning the beam on the SiO_2/Si was done using a focal spot diameter of 6.6 μm. With this beam size, it was not possible to write consistent thin-film tracks with no quasi-periodic structures on SiO_2/Si substrates. However, experiments with a larger focal spot of 33 μm (5 times larger) produced thin-film tracks (Figure 15) without ablation at high speeds (≥1500 μm/s). At low speeds, quasi-periodic structures were produced.

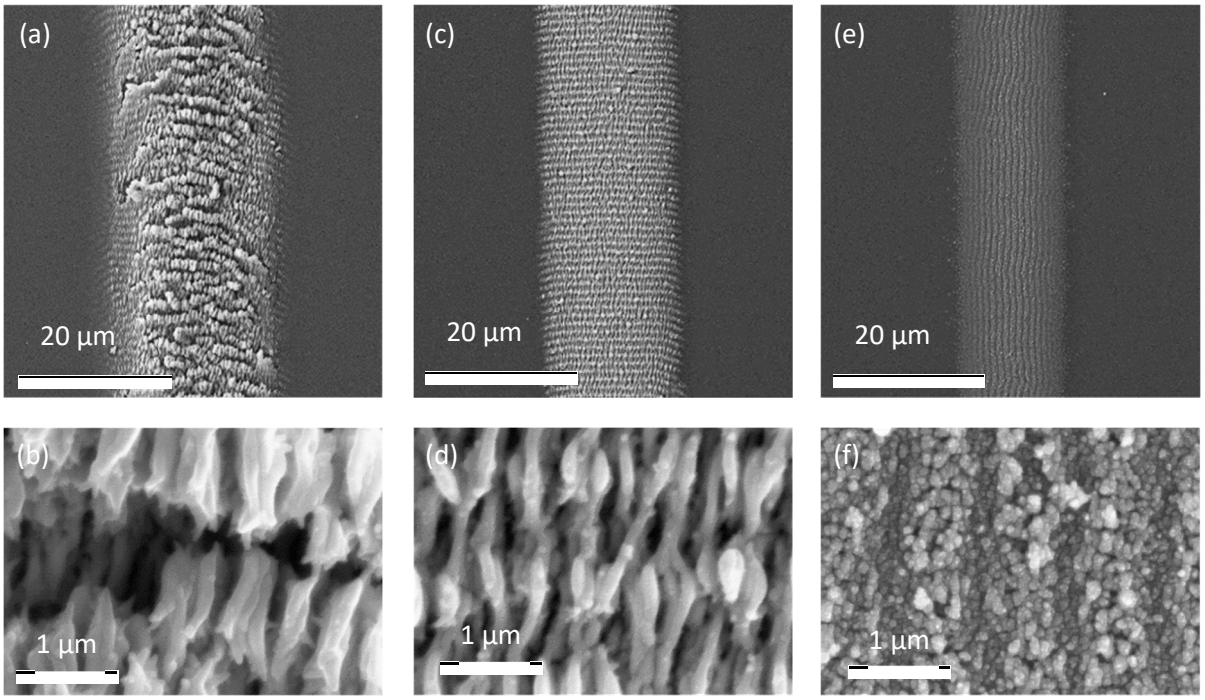

Figure 96: Microstructure of tracks deposited using a larger focal spot of 33 μm with a laser peak fluence of 80 mJ/cm² scanning at a speed of (a, b) 150, (c, d) 500, and (e, f) 1500 μm/s.

The results of using the 6.6 µm beam spot and the 33 µm are compared in Figure 97. Instead of scanning speed, the chart is plot using number of pulses, η. Due to the conversion from scanning speed to pulse overlap, the graph plotted with the number of pulses in the x-axis appears flipped about a vertical axis compared to the graph plot with the scanning speed in the x-axis seen in Figure 86. As the pulse overlap number was decreased (or scanning speed increased), the lowest fluence for observable deposition with both the 6.6 and 33 µm spot increased. However, the increase in minimum fluence for observable deposition with 33 µm spot was less than the increase with using the 6.6 µm spot. For example, the lowest intensity for observable deposition at a pulse overlap of 33,000 pulses was 42 mJ/cm^2 using a 33 µm spot and 110 mJ/cm^2 using a 6.6 µm spot. At a pulse overlap of 11,000 pulses, no deposition without ablation was observed using a 6.6 µm spot however using a 33 µm spot, thin-film deposition was observed at a fluence of 60 mJ/cm^2.

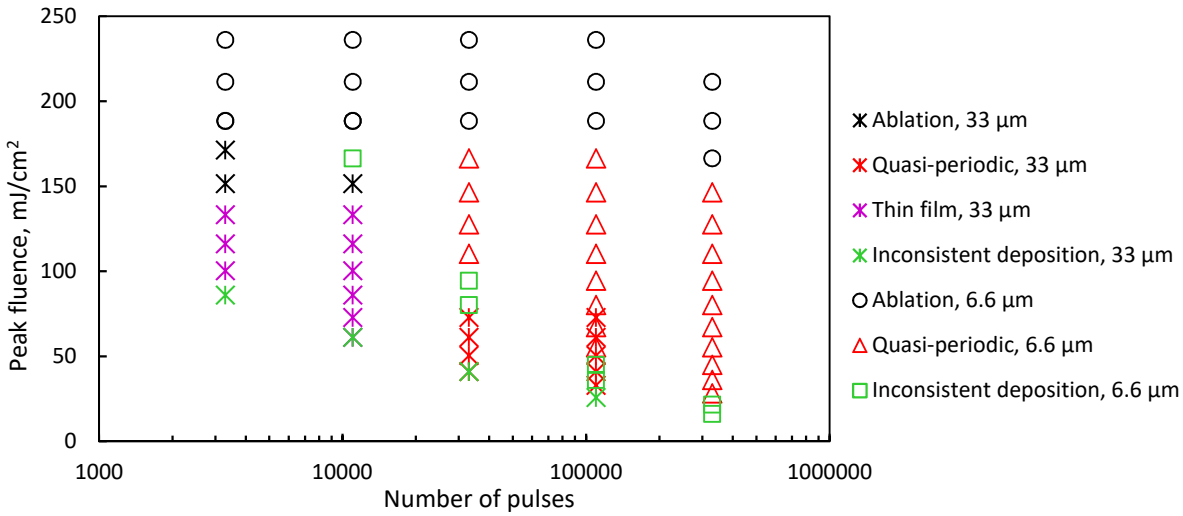

Figure 97: Plot of pulse fluence against pulse number experiment points explored for the deposition of tungsten on SiO_2/Si along with the resultant deposition morphology achieved for beam size of 6.6 and 33 µm.

The lower threshold for the deposition using the larger beam was attributed to the higher overall average power. When the spot size was increased five times from 6.6 to 33 µm, the energy per pulse increased 25 times to achieve the same peak fluence. This led to a longer time above the temperature being above the deposition temperature threshold of approximately 375 °C (Lai and Lamb, 2000) for longer as seen in Figure 98.

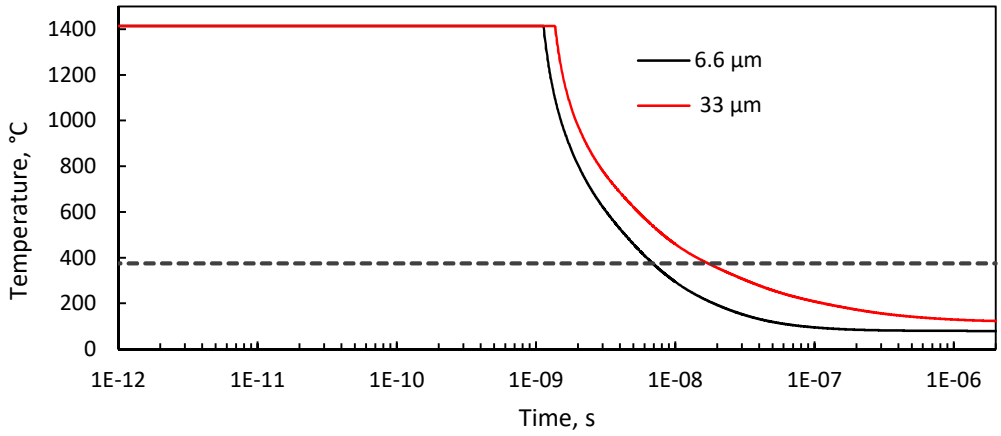

Figure 98: Simulation of peak temperature at laser spot for the 6.6 and 33 µm laser spot at peak fluence of 110 mJ/cm^2. For the 33 µm spot, the temperature stays above the 375 °C deposition temperature threshold for 12 ns compared to 6 ns for the 6.6 µm spot.

Figure 99 compares the microstructure of the quasi-periodic structures made with 33,000 pulses using a 6.6 µm (left) with that using 33 µm (right) laser spot. The spatial periodicity and directionality of the structures created by the larger focal spot appeared more regular. A periodicity parallel to the laser beam polarization was also observed in the tracks produced by the larger beam spot.

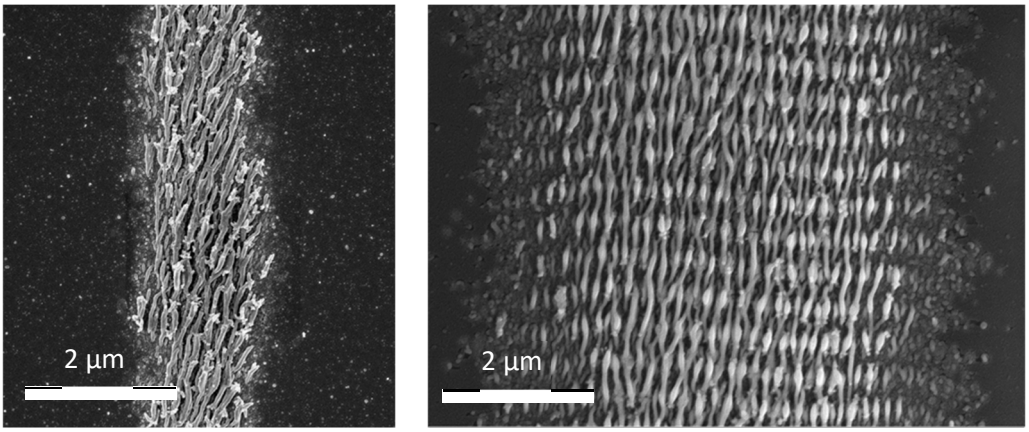

Figure 99: Comparison between tungsten tracks written with a focal spot size of 6.6 µm, peak fluence 110 mJ/cm^2 (left) and 33 µm, 51 mJ/cm^2 (right) at 33,000 number of pulses. Lower aspect ratio quasi-periodic structures were observed when with the larger beam spot.

Figure 100 compares the microstructure of the quasi-periodic structures made with 110,000 pulses using a 6.6 µm (left) with that using 33 µm (right) laser spot. Due to the high number of pulses and high laser power, the quasi-periodic structures thickened into clumps in the middle of the track.

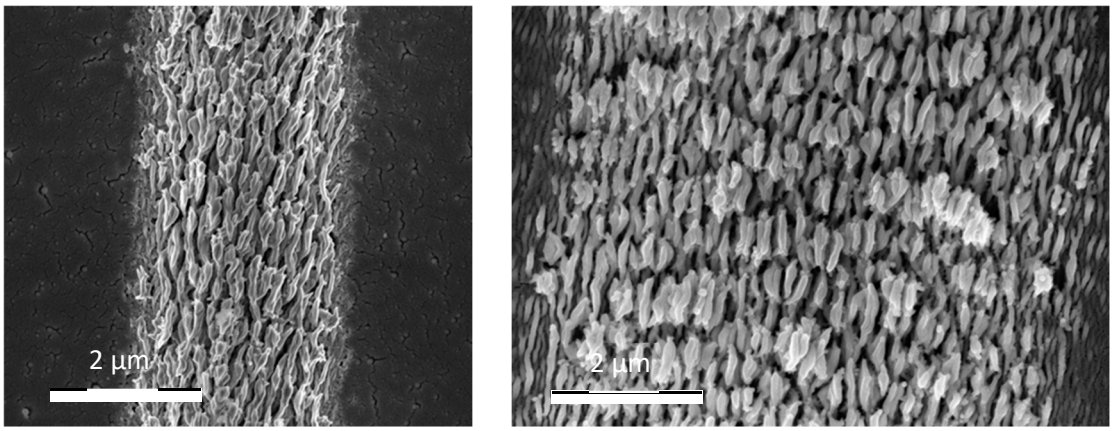

Figure 100: Comparison between tungsten tracks written with a focal spot size of 6.6 µm, peak fluence 95 mJ/cm^2 (left) and 33 µm, 51 mJ/cm^2 (right). Clumps in the middle of the track were due to the high number of pulses of 110,000 and high laser power.

Thin films were deposited with the 33 µm spot when the number of pulses was 11,000 or lower (scan speed of 1500 µm/s or higher). Figure 101 shows charts of maximum height, FWHM and volumetric deposition rate against peak pulse fluence for the thin-film deposition. The maximum height and volumetric deposition rate increased with peak pulse fluence however the FWHM stayed approximately constant at 8 µm. The highest volumetric deposition rate recorded was 2925±234 µm^3/s. Based on the maximum height values, the linear growth rate on the substrate can be calculated based on equation 35 of section 4.2.1. The average linear growth rate using the peak pulse fluence of 133 and 152 mJ/cm^2 were 0.112 and 0.133 µm/s respectively. These linear growth rate values were lower than that of the quasi periodic structures (5.5 µm/s from section 5.2.4) and CW deposition (3.8 µm/s from section 4.2.1), but higher than the linear growth rates in CVD at 5 nm/s (Lai and Lamb, 2000).

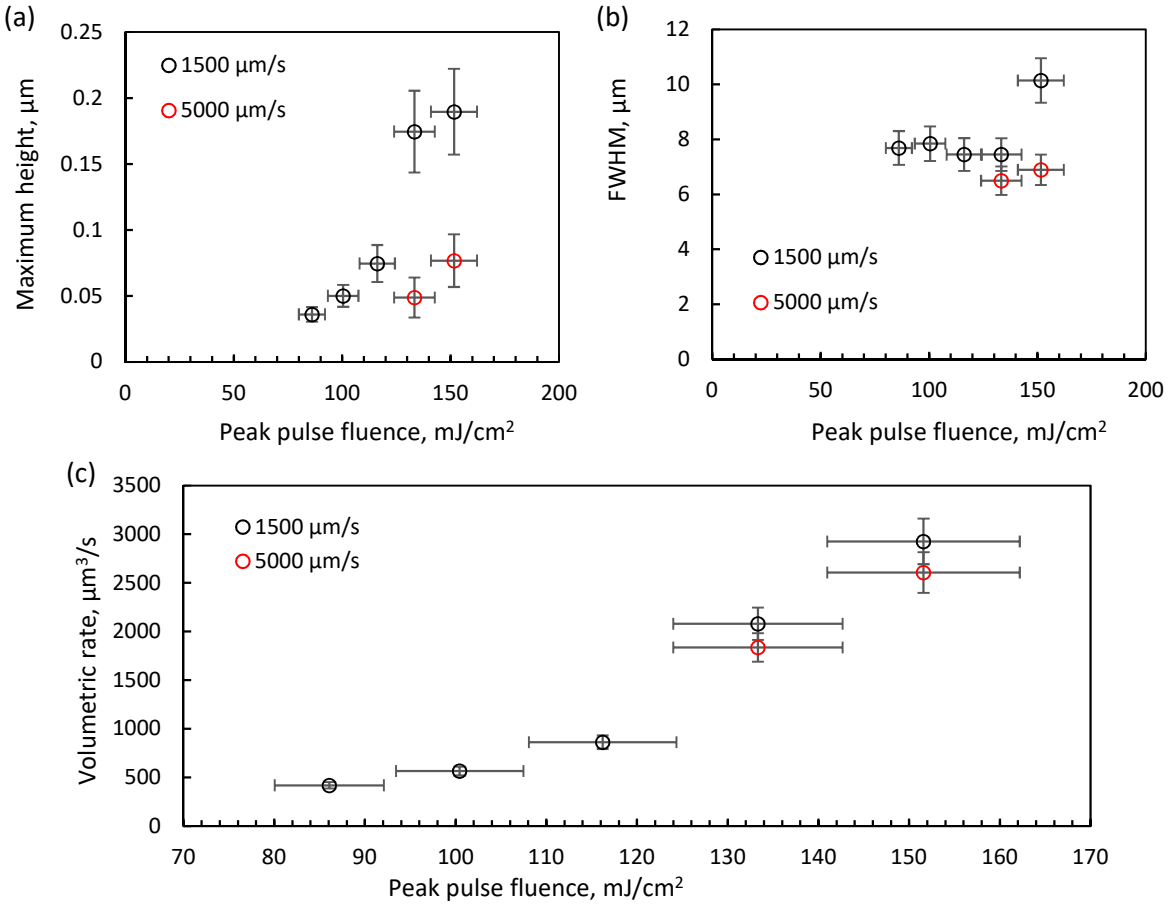

Figure 101: Graphs of maximum height (a), FWHM (b) and volumetric deposition rate (c) against peak pulse fluence for the thin films deposited at 1500 µm/s and 5000 µm/s.

Figure 102 shows SEM images that demonstrate the effect on the track microstructure of the thin-films when the laser peak fluence was increased. At the low laser peak fluence of 73 mJ/cm^2, the deposited track consisted of circular grains approximately 100 nm in diameter. Grooves spaced 1 µm ($\sim\lambda$) were visible that were orientated perpendicular to the linear polarization direction. As the laser power was increased, the circular grains grew and the periodic grooves became thinner.

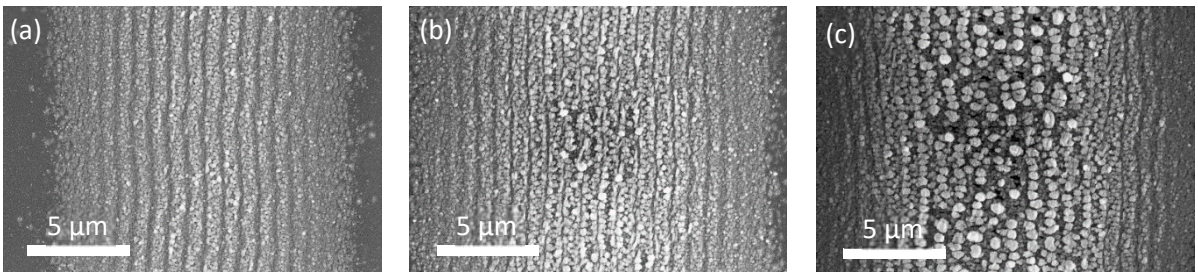

Figure 102: SEM images for the deposition using a scanning speed of 1500 µm/s at a peak fluence of (a) 73, (b) 100, (c) 133 mJ/cm^2.

Figure 103 shows SEM images of the deposition done at a laser peak fluence of 100 mJ/cm^2 and scanning speed of 5000 µm/s (left) and 1500 µm/s (right). As the scanning speed was reduced, the size of the circular grains increased, creating a rougher deposited track.

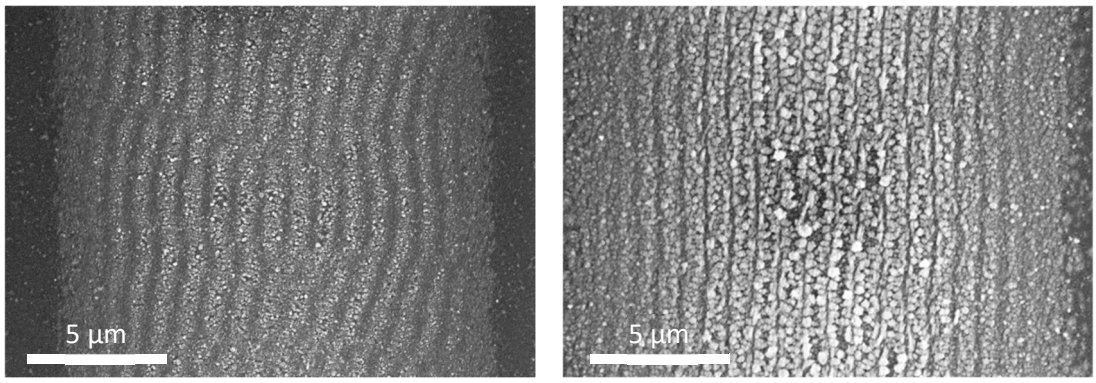

Figure 103: SEM images of the deposition at a peak fluence of 100 mJ/cm^2 at a scanning speed of 5000 µm/s (left) and 1500 µm/s (right).

Table 23 shows the elemental composition of the tracks made using the larger laser spot of 33 µm. The track made at a scan speed of 500 µm/s produced quasi-periodic structures with a tungsten purity of 85.9 wt% (excluding silicon). The highest tungsten purity for the thin film tracks was 64.6 wt%, written at a scan speed of 1500 µm/s and laser peak pulse fluence of 133 mJ/cm^2. The low measured tungsten purity of the track made with the lower pulse fluence of 73 mJ/cm^2 and that of the track made with a higher scanning speed of 5000 µm/s was due to the track being thin. Therefore, the high carbon and oxygen impurities may be that of the substrate especially since there was a high silicon content detected in the EDX measurements (>65%).

Table 23: EDX elemental composition for the track deposition using the larger laser spot of 33 µm diameter.

Deposition type	Scanning speed, µm/s	Peak pulse fluence, mJ/cm^2	Peak pulse intensity, 10^{11} W/cm^2	Excluding silicon			Si, wt%
				W, wt%	C, wt%	O, wt%	
Quasi-periodic	500	61	2.0	85.9	8.3	5.8	34.8
Thin-film	1500	73	2.4	28.3	39.8	31.9	66.6
Thin-film	1500	133	4.4	64.6	24.1	11.3	37.2
Thin-film	5000	152	5.1	20.7	35.1	44.2	65.4
(substrate before deposition)				0.0	37.5	62.5	74.0

Table 24 shows the electrical resistance measurement results of the tracks made using the larger laser spot of 33 µm. The quasi-periodic structure track had a resistivity value 525±52 µΩ cm (93.8 times bulk tungsten). This value was higher than the resistivity of the quasi-periodic track made using the standard laser spot of 6.6 µm in section 5.2.3 at 51.8 times bulk tungsten. The thin film tracks all had a low resistivity value with the lowest resistivity of 37±4 µΩ cm (6.7 times bulk tungsten) for the track written at a scan speed of 1500 µm/s and peak fluence of 73 mJ/cm^2. However, the contact resistance between the thin film track and silver paste was high at 482 Ω. The track written using the same scan speed but at a higher laser peak fluence of 133 mJ/cm^2 had the lowest contact resistance of 9±2 Ω.

Table 24: Resistivity measurements of the tracks deposited using the larger laser spot of 33 µm diameter.

Deposition type	Scanning speed, µm/s	Peak pulse fluence, mJ/cm^2	Peak pulse intensity, 10^{11} W/cm^2	Resistivity, µΩ cm	Multiple of bulk tungsten	Resistance per unit length, Ω/mm	Contact resistance, Ω
Quasi-periodic	500	61	2.04	525±52	94	637	50±10
Thin-film	1500	73	2.43	37±4	6.7	564	482±93
Thin-film	1500	133	4.44	53±5	9.5	515	9±2
Thin-film	5000	152	5.05	70±6	13	3489	68±178

5.2.7 Effect of multiple passes

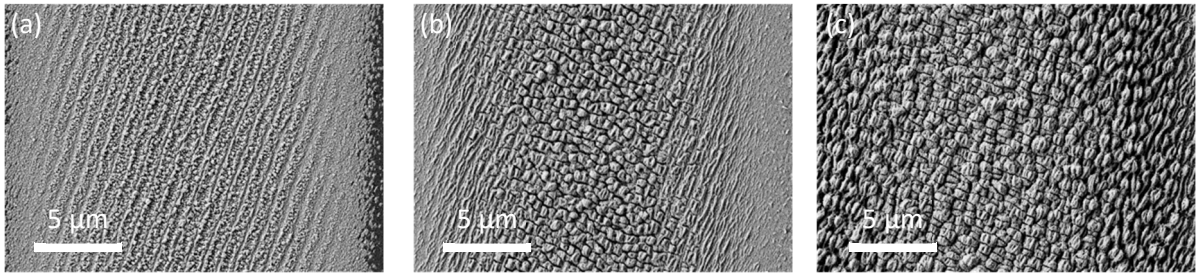

Figure 104: SEM images of track deposition results using peak fluence of 100 mJ/cm^2 for (a) one, (b) three, and (c) ten passes. The scan speed was 1500 µm/s using a beam spot of 33 µm.

Besides changing the frequency while keeping the number of pulses per spot constant, the track could be scanned multiple times while keeping the total number of pulses per spot constant. Figure 104 shows SEM images of the deposit tungsten tracks using peak fluence of 100 mJ/cm^2 for a single, triple and ten passes. For a single pass, the track consisted of granular structures. After three passes, there was evidence of the quasi-periodic structures. After ten passes, the track was covered with quasi-periodic structures with clumps that appeared to have a periodicity perpendicular to the scan direction.

Table 25: Measured track geometry of line deposition done at a speed of 1500 µm/s and peak laser fluence of 100 mJ/cm^2 for one, three and ten coatings.

Number of coatings	Maximum track height per coating, µm	FWHM, µm	Average cross-section area per coating, µm	Volumetric deposition rate per coating, µm^3/s
1	0.050	7.8	0.377	566
3	0.084	16.0	1.890	2835
10	0.103	22.2	3.672	5509

Table 25 shows the geometry measurements of the track deposited while Figure 105 shows the cross-section profile of the tracks. The maximum track height per coating and average cross-section per coating increased with number of coatings because the deposition rate was higher on already-coated substrates compared to the pure substrate. The FWHM of the tracks increased approximately three times when the number of coatings increased from one to ten. However, the FWHM was still smaller than the beam spot diameter of 33 µm. As the number of coatings increased, the deposition outside the laser spot increased significantly as seen in Figure 105. This unwanted deposition increased the cross-section area and led to the significant increase in volumetric deposition rate per coating seen in Table 25.

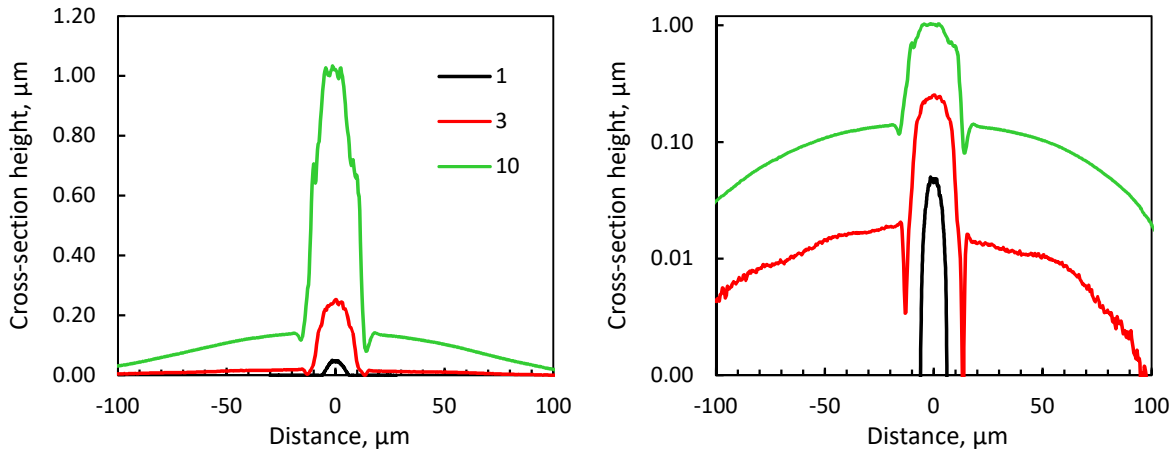

Figure 105: Averaged cross-section profile, linear (right) and logarithmic (left), of the deposition done at a speed of 1500 µm/s for one, three and ten coatings.

Table 26 shows the comparison between the resistance measurements of the single coated track and the track with ten coatings. The single track has a low resistivity value of 37±4 µΩ cm. The track with ten coatings has a higher resistivity value of 137±15 µΩ cm. This was due to the porous quasi-periodic structures forming on the track as seen in Figure 104 and the large amount of deposition outside the laser spot as seen in Figure 105. The contact resistance between the silver paste and the deposited track decreased significantly when the number of coatings was increased from one to ten. This was likely due to the increase in the width of the track and the larger surface area available from the quasi-periodic structures formed on the track.

Table 26: Comparison between resistance measurements for the tracks with a single coating and ten coatings.

Number of coatings	Cross-section area, µm^2	Resistivity, µΩ cm	Multiple of bulk tungsten	Resistance per unit length, Ω/mm	Contact resistance, Ω
1	0.66	37±4	6.65	564.0	482±93
10	11.81	137±15	24.44	115.8	2±12

The morphology of the deposit for the same total number of pulses in single and multiple passes were compared using the laser parameters seen in Table 27.

Table 27: Laser parameters for single and multiple passes at the same total number of laser pulses per spot.

Label in Figure 106	Number of passes	Total number of pulses per spot	Scanning speed, µm/s	Peak fluence, mJ/cm^2
a	3	33,000	1500	51
b	1	33,000	500	51
c	10	110,000	1500	33
d	1	110,000	150	33

Figure 106 shows SEM images that compares the microstructure of the results. The formation of thin films was favoured in the multiple coating tracks while the formation of quasi-periodic structures was favoured in the single coating tracks.

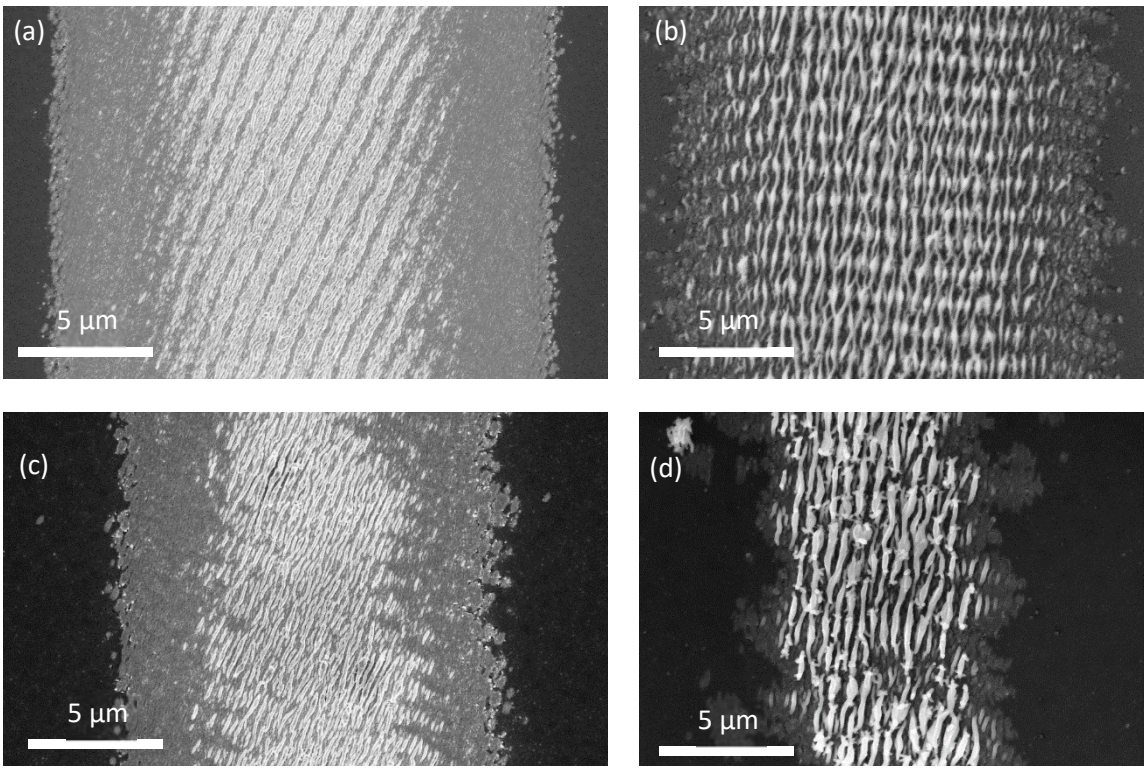

Figure 106: SEM images comparing tracks made with the laser through multiple passes (left) and a single pass (right). The other laser parameters are in Table 27. The track made using multiple passes favours the formation of thin film while the single pass favours the formation of quasi periodic structures.

5.2.8 Nanolines

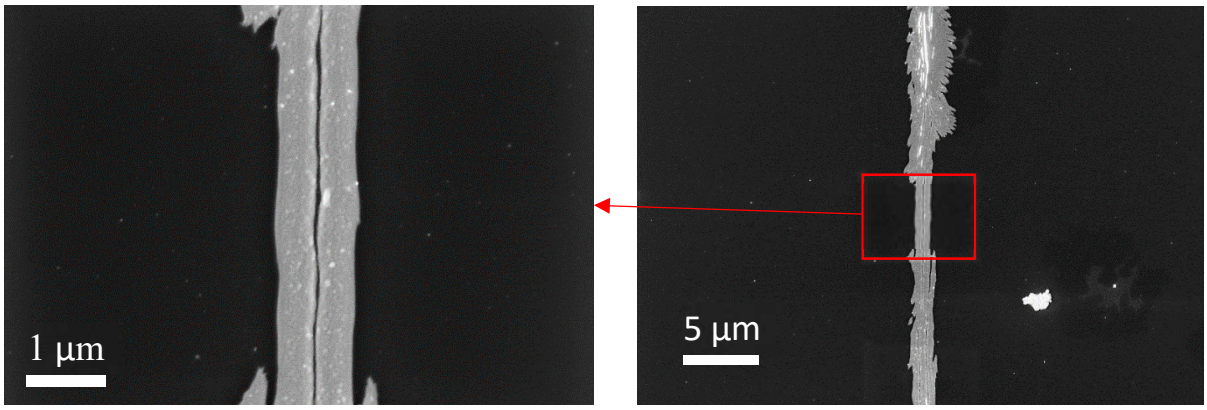

Figure 107: High resolution SEM image of two thin film tracks written by ultrafast LCVD. Each track has a width of approximately 500 nm.

A few attempts with deposition using a shorter focal length objective were done. For these, the objective used was a Mitutoyo M PLAN APO HR NIR 50x that has an effective focal length of 4 mm. The calculated spot diameter using this objective was 1.3 µm. However, due to aberration through the 3 mm thick window, the beam diameter was expected to be larger. By scanning the laser at a speed of 30 µm/s and energy per pulse of 17 nJ, a thin-film track was deposited. At certain regions of the track, two sub-micrometer lines were deposited (Figure 107). The irregularity of the line thickness may be due to instability of the laser output power. These results show that it is possible to write sub-micrometer thin film tracks using this ultrafast LCVD technique.

5.2.9 Optimum track resistivity

The lowest resistivity tungsten track written on SiO_2/Si substrates was the thin film track with electrical properties measured in Table 24. At a scanning speed of 1500 μm/s and peak laser fluence of 73 mJ/cm^2, the lowest track resistivity achieved was 37±4 μΩ cm (6.7 times bulk tungsten resistivity). However, the contact resistance between the track and the silver paste pads was measured to be 482±93 Ω. When the laser peak fluence was increased to 133 mJ/cm^2, the resistivity increased to 53±5 μΩ cm (9.5 times bulk tungsten) but the contact resistance was reduced to 9.0±2 Ω. Both thin film tracks have a lower resistivity than the optimum results produced using the 405 nm CW laser in the previous chapter (11.7 times bulk tungsten resistivity after annealing).

5.3 Track deposition on glass

For CW, borosilicate and fused silica glass are transparent at 1030 nm. However, using an ultrafast 300 femtosecond pulse, the high intensity of the laser pulse is absorbed in the glass. The effective absorption penetration depth of borosilicate glass is in the order of 240 nm for an ultrafast pulse (Ben-Yakar and Byer, 2004). Figure 108 shows plan view SEM images of the tungsten track on borosilicate made at a laser peak fluence of 128 mJ/cm² at a scanning speed of 1000, 300, 100, and 30 μm/s (η = 3300, 11 000, 33 000, and 110 000 pulses respectively). At the higher speeds of 300 and 1000 μm/s the deposition with grains of the order of 100 nm were observed. These tracks appeared smooth in the optical microscope and were considered as thin-film deposition. The size of the grains increased with decreasing scanning speeds. At the lower scanning speed of 30 and 100 μm/s, the grains grew into quasi-periodic structures. The linear polarization direction of the laser was perpendicular to the scanning direction therefore the nano-structures were aligned parallel to the laser scan direction. At the lowest scanning speed of 30 μm/s the quasi-periodic structures were taller, and had more branching in the walls.

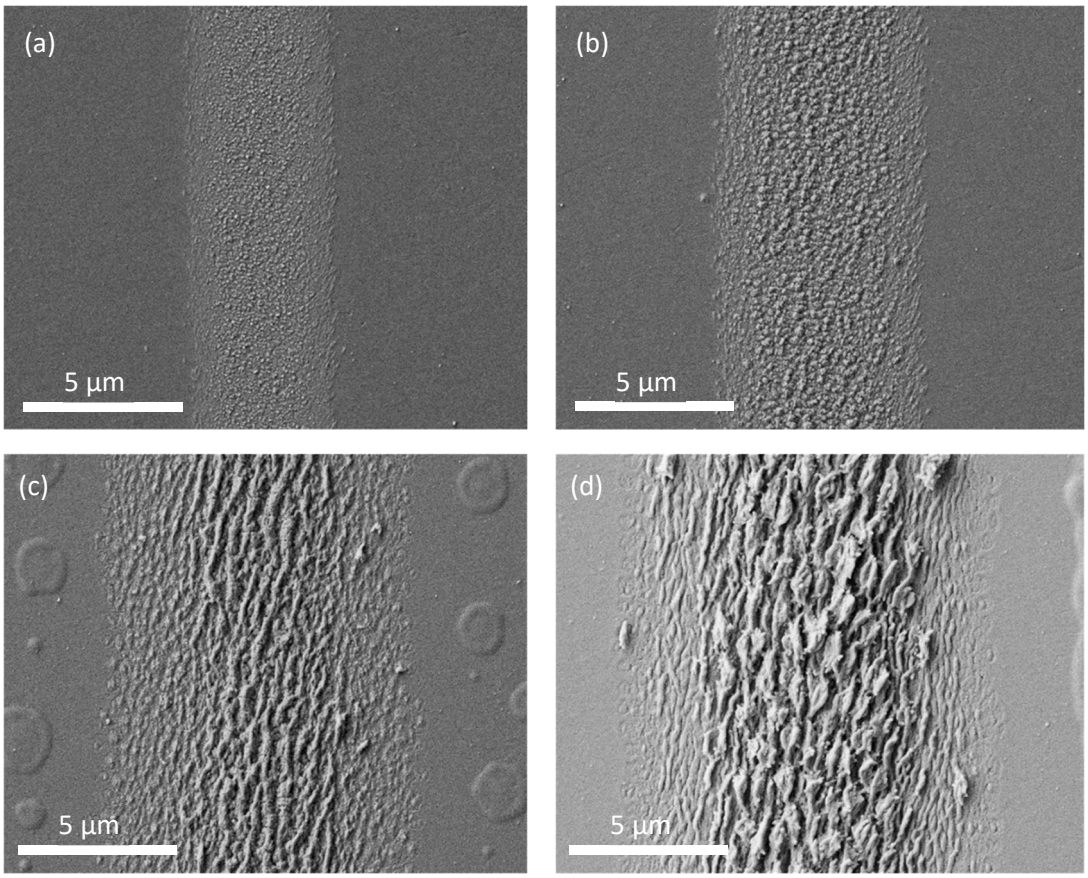

Figure 108: Deposition of quasi-periodic structures on borosilicate glass at a pulse peak fluence of 128 mJ/cm² and scan speed of (a) 1000, (b) 300, (c) 100, and (d) 30 µm/s.

Figure 109 show higher resolution SEM images of the nano-structure in the thin film deposited with the scan speed of 1000 and 300 µm/s. At a scan speed of 1000 µm/s the grains were approximately 50-100 nm in diameter and when the scan speed was decreased to 300 µm/s the grain sizes grew to approximately 100-200 nm in diameter.

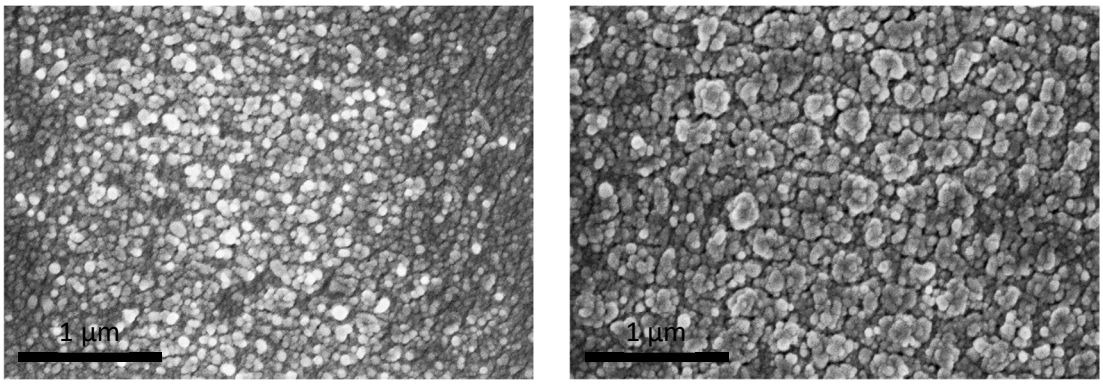

Figure 109: Plan view SEM images of nano-structure in the thin film tungsten tracks deposited with a laser peak fluence of 128 mJ/cm² at scanning speed of (left) 1000 and (right) 300 µm/s.

Figure 110 (a) shows the averaged cross-section profile measured using white light interferometry for the laser at scanning speed of 1000 (thin-films), 300 (thin-films), 100, and 30 µm/s at laser peak fluence of 128 mJ/cm^2. Generally, the maximum height of the cross-section and the FWHM of the track reduced with increasing scan speed. Figure 110 (b) shows the averaged cross-section profile for a scanning speed of 100 µm/s at various power levels. At that scanning speed, deposition was first observed at fluence of

67 mJ/cm^2. When the fluence was increased to 95 mJ/cm^2, the maximum height of the track increased. However, further increases in power reduced the maximum height and at a peak fluence of 167 mJ/cm^2, a trough was observed in the middle of the track. This was similar to the phenomenon reported in (Duty et al., 2001) where the deposition at the laser centre decreased at high laser powers due to high temperatures discouraging adsorption of the precursor onto the substrate. For the scan speed of 300 µm/s, the lowest power where deposition was observed was at a fluence of 110 mJ/cm^2 (Figure 110 c). No troughs were visible at this power level. However, as the laser fluence was increased to 128 mJ/cm^2, the profile height decreased and higher at 167 mJ/cm^2 a trough was visible in the middle of the track.

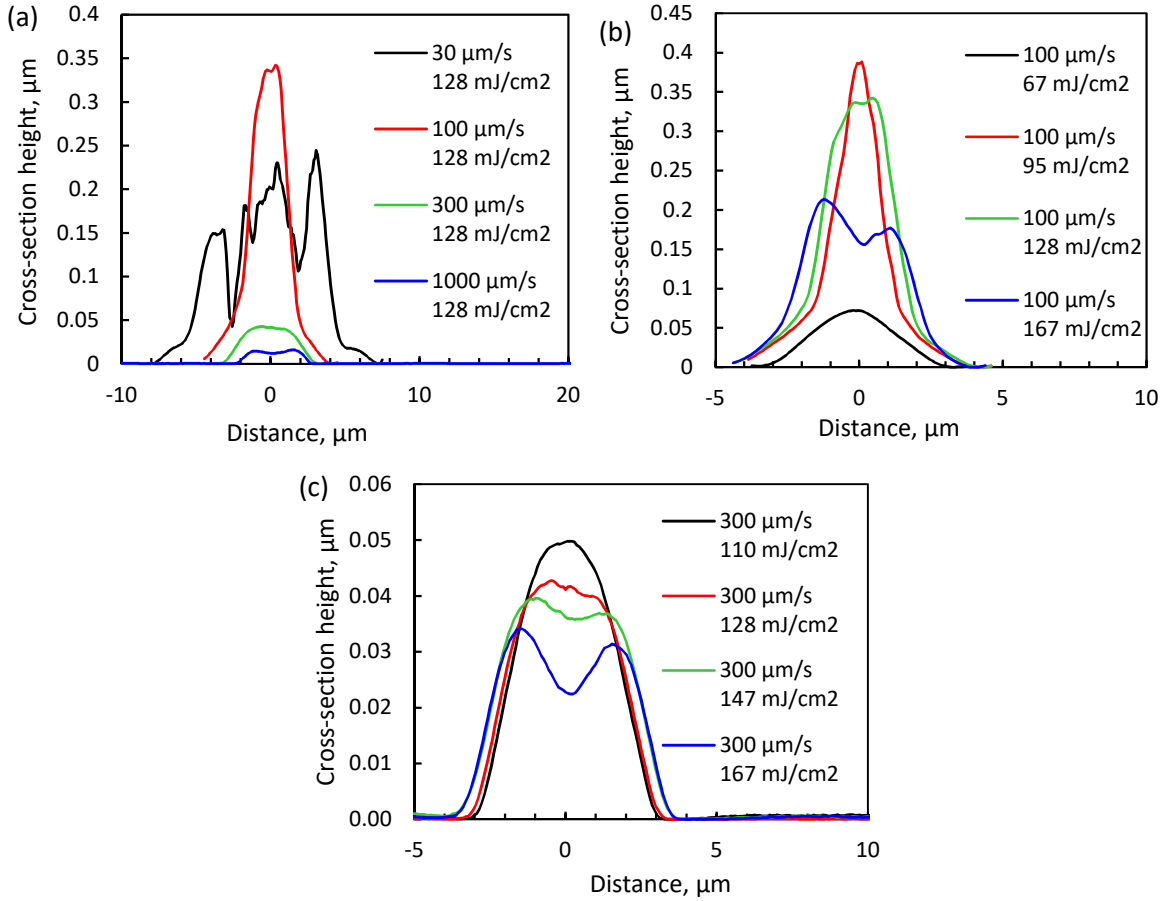

Figure 110: Averaged cross-section profile measured using white light interferometry of the tungsten track on borosilicate glass at various laser scanning speeds and laser intensities. (a) Constant laser power of 128 mJ/cm^2, and constant laser scan speed of (b) 100 µm/s, and (c) 300 µm/s (thin-films).

Figure 111 shows graphs of maximum profile height, FWHM and volumetric deposition rate based on the white light interferometer measurements. For the maximum height graph, the height reduces with laser scanning speed. This was because the effective dwell time and thus deposition time reduces with increasing scanning speed. For increasing laser power, the maximum height increased until laser peak fluence of 110 mJ/cm^2, then the maximum height started to decrease. This was because the higher temperatures caused by the higher laser power discouraged adsorption and encouraged desorption of the chemical precursor from the substrate as mentioned previously. For the FWHM, the widths increased with laser power because a wider area was above the threshold deposition intensity. The volumetric deposition rate increased with laser power until 110 mJ/cm^2 where the deposition rate remains constant

and a drop in deposition rate was observed at peak fluence of 212 mJ/cm^2. The highest deposition rate achieved was 106 µm^3/s for scanning at a speed of 100 µm/s. The average deposition rate was approximately 60 µm^3/s. At the peak fluence of 128 mJ/cm^2, the linear height growth rate of the deposit was 3.1 and 2.2 µm/s for the quasi-periodic structures and the thin-film deposition respectively. The quasi-periodic structure growth rate on borosilicate glass was lower than that on SiO_2/Si substrates (5.5 µm/s from section 5.2.4). However, the thin-film deposition rates on borosilicate glass were higher than that on SiO_2/Si substrates (0.112 µm/s from section 5.2.6).

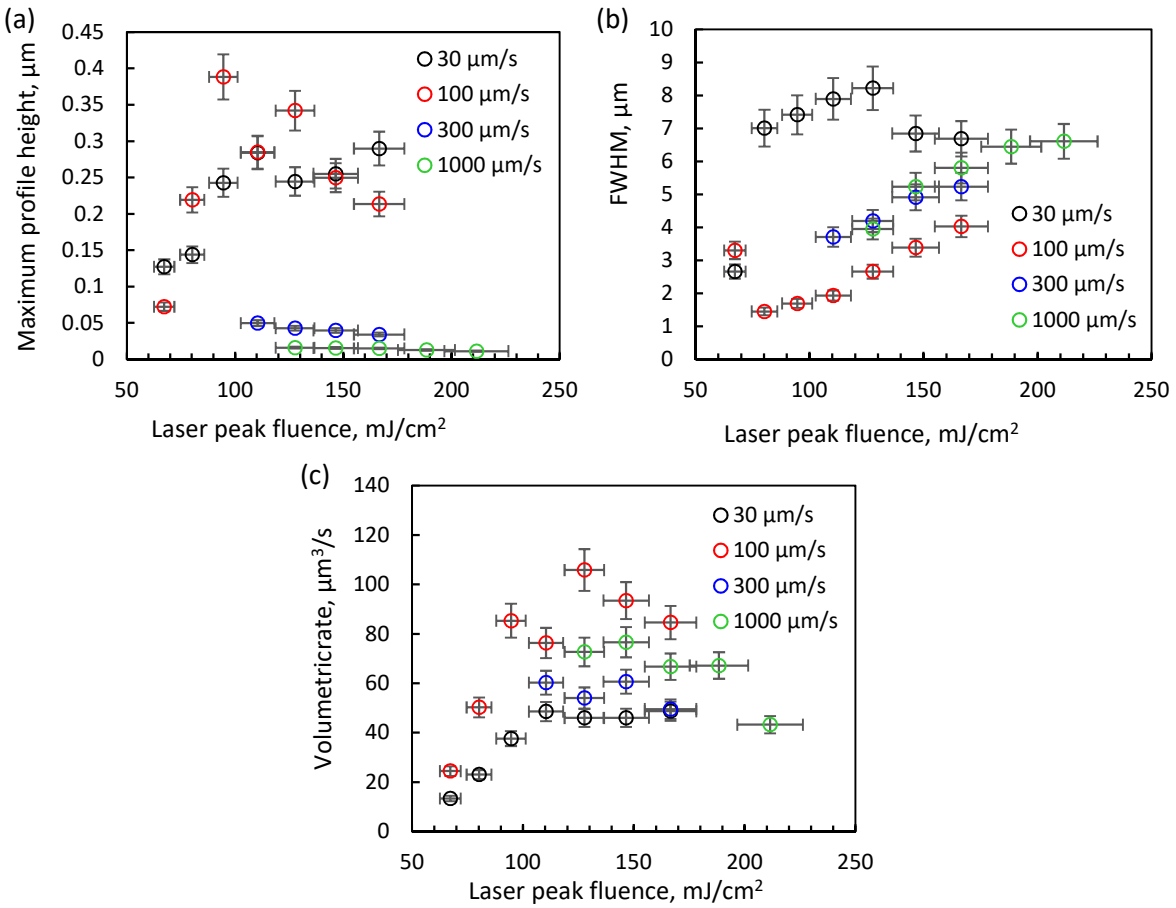

Figure 111: Maximum height (a), FWHM (b) and volumetric deposition rate (c) graphs at various scanning speeds summarized from the WLI measurements for the deposited tungsten tracks on borosilicate glass.

The deposition results of scanning the laser on borosilicate glass is summarized in Figure 112. Borosilicate glass has a higher ablation threshold compared to SiO_2/Si, thus no ablation was observed at the higher laser intensities investigated in this study. Quasi-periodic structures were produced at a scan speed of 100 µm/s and below ($\eta \geq 33{,}000$). At a speed of 300 µm/s and above ($\eta \leq 11{,}000$), thin film tracks were produced. The minimum laser power for observable deposition increased with scanning speed. Besides illumination from the front or top of the substrate, deposition was also observed when the laser was focused at the back surface of the substrate. For back illumination, thin film tracks were produced at all speeds tested. Deposition at the bottom surface was also observed when the glass was placed above another substrate such that the gap between the surfaces was less than a hundred microns.

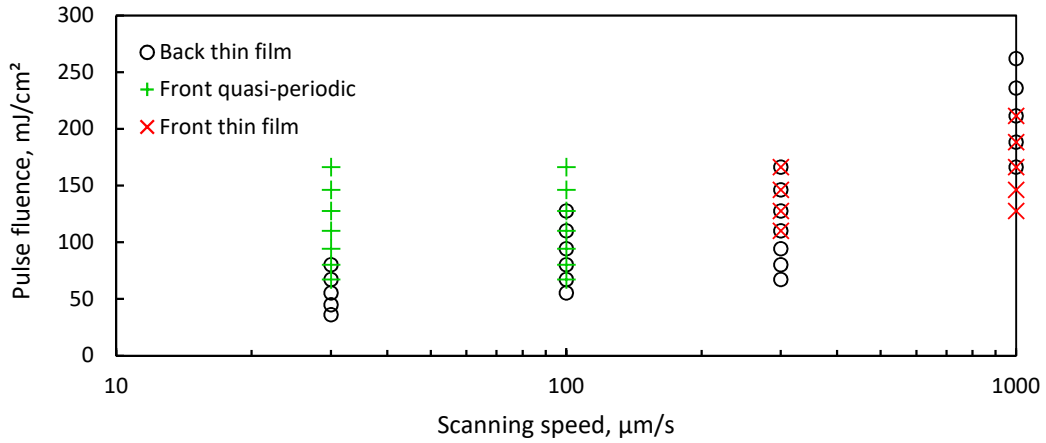

Figure 112: Plot of pulse fluence against scanning speeds experiment points explored for the deposition of tungsten on borosilicate glass along with the resultant modification regimes achieved. The uncertainty of 7 % for the pulse fluence was not displayed on the figure.

Figure 113 and Figure 114 shows SEM images of the microstructure of the tracks written with back-illumination on fused silica. The track consists of circular grains however there a less gaps in the thin compared to that of the track deposited through front-illumination in Figure 103. Generally, the occurrence of large grains increased with increasing laser power and decreasing scan speed.

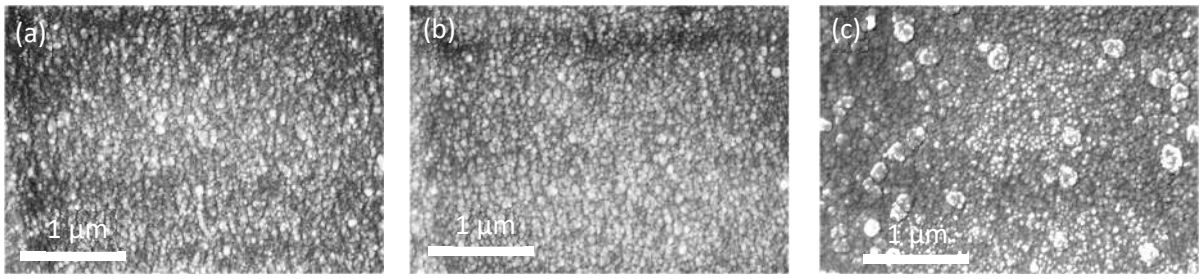

Figure 113: SEM image of the tungsten deposition on borosilicate glass through back-illumination done at a speed of 30 µm/s and laser peak fluence of (a) 36, (b) 45, and (c) 67 mJ/cm².

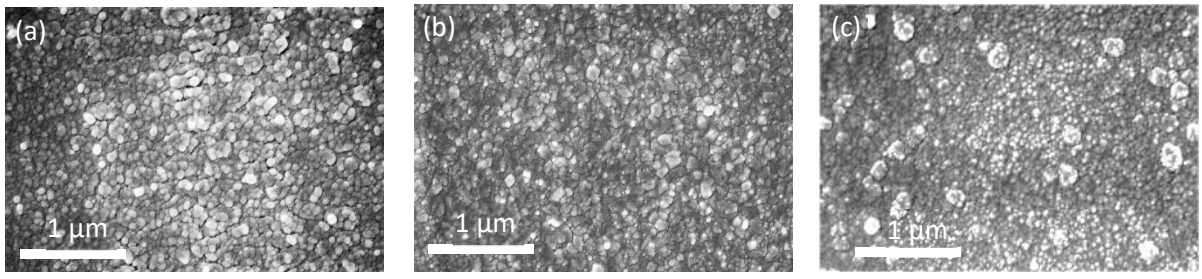

Figure 114: SEM image of the tungsten deposition on borosilicate glass through back-illumination done at a speed of (a) 300, (b) 100 and (c) 30 µm/s and laser peak fluence of 67 mJ/cm².

Figure 115 shows the cross-section profiles of the thin film tungsten tracks deposited through back-side illumination and measured through white light interferometry. The general shape of the cross-section was Gaussian except when the laser power was too high, troughs in the middle of the profile started to appear. The maximum height of the track increased with decreasing scan speed and increased with laser power before the trough in the middle of the track appeared.

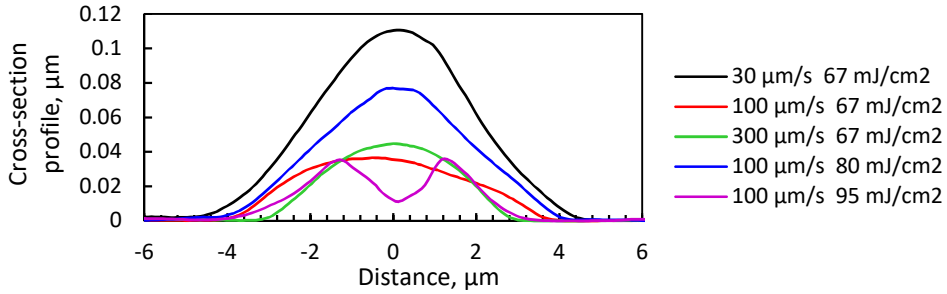

Figure 115: Averaged cross-section profile of the tungsten track on borosilicate glass deposited through back-illumination at various laser scanning speeds and laser peak fluences.

Figure 116 shows the maximum track height, FWHM and volumetric deposition rate for the back-side illumination configuration. The maximum track height increases with laser peak power until troughs or ablation in the middle of the tracks were observed. The maximum track height decreases with increasing scan speed and this was expected because the dwell time decreases. The FWHM of the tracks increased with laser peak fluence for all speeds investigated. The widths of the tracks were of the same order of the beam diameter of 6.6 µm. For the volumetric deposition rate, the deposition rate increases with laser power until troughs or ablation was observed in the middle of the tracks. The linear height growth rate at a laser peak fluence of 128 mJ/cm^2 was 1.5 µm/s, which was slightly lower than the growth rate achieved through front illumination (2.2 µm/s).

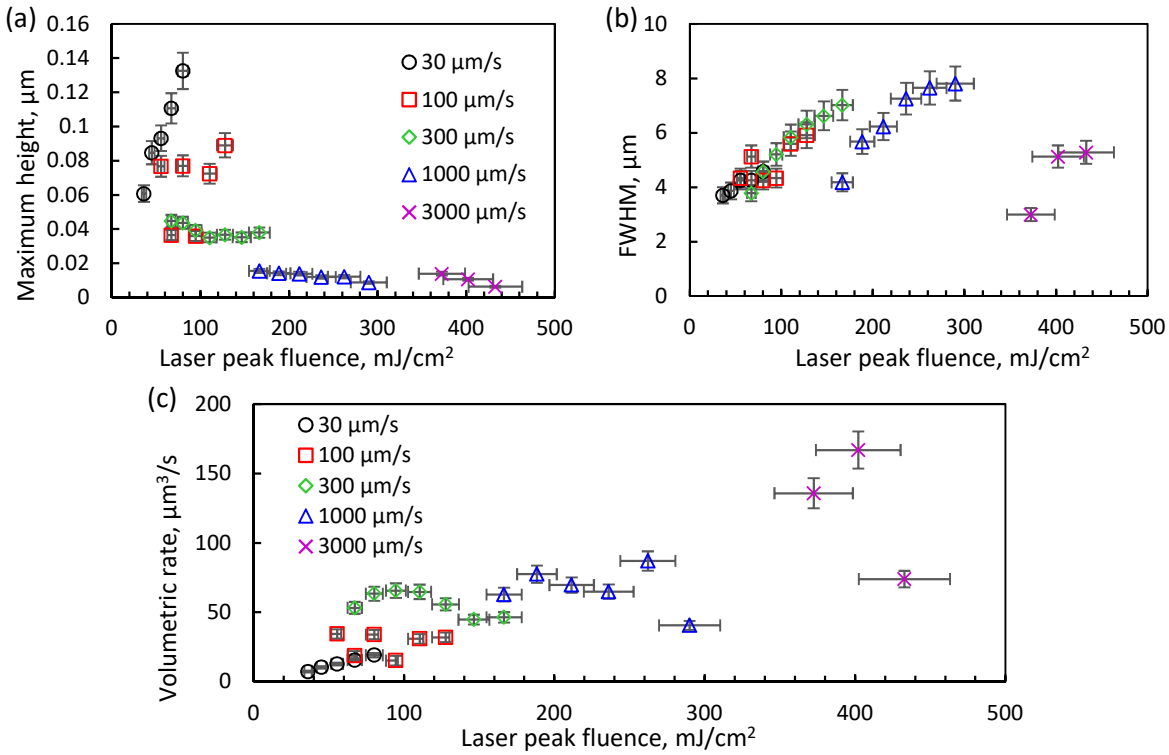

Figure 116: Maximum height (a), FWHM (b) and volumetric deposition rate (c) graphs summarized from the WLI measurements for the deposited tungsten tracks on borosilicate glass through back-illumination.

Table 28 shows the electrical resistance measurement results of the tracks written through back-illumination configuration on fused silica and borosilicate glass. The lowest resistivity was achieved on fused silica and borosilicate glass when the laser fluence was 63.9 mJ/cm^2. The track resistivity increased when the laser fluence was decreased and increased.

Table 28: Electrical track resistance of the tracks written on glass via back-illumination.

Substrate	Scan speed, µm/s	Peak fluence, mJ/cm^2	Peak intensity, 10^{11} W/cm^2	Resistivity, µΩ cm	Multiple of bulk tungsten resistivity	Resistance per unit track length, Ω/mm	Contact resistance, Ω
Fused silica	30	63.9	4.3	50±10	8.8	533.7	14±9
Fused silica	30	131.1	8.7	92±11	16.5	555.7	27±22
Borosilicate glass	30	40.1	2.7	559±41	99.7	6221.9	93±90
Borosilicate glass	300	63.9	4.3	40±4	7.2	1177.6	121±300
Borosilicate glass	3000	239.9	16.0	369±44	66.0	52771.0	150±80

5.4 Track deposition on polyimide

Tungsten LCVD using the ultrafast laser was also attempted on polyimide films. A 40 µm thick polyimide adhesive thin was pasted on a copper substrate and exposed to the laser at increasing laser power levels. The track width squared was plot against the laser peak fluence for threshold estimation as seen in Figure 117. The scanning speed was 30 µm/s. The ablation threshold was measured as 67±15 mJ/cm^2 while the deposition threshold was lower at 37±13 mJ/cm^2. Deposition on polyimide without ablation was not possible using the 405 nm CW laser in the previous chapter.

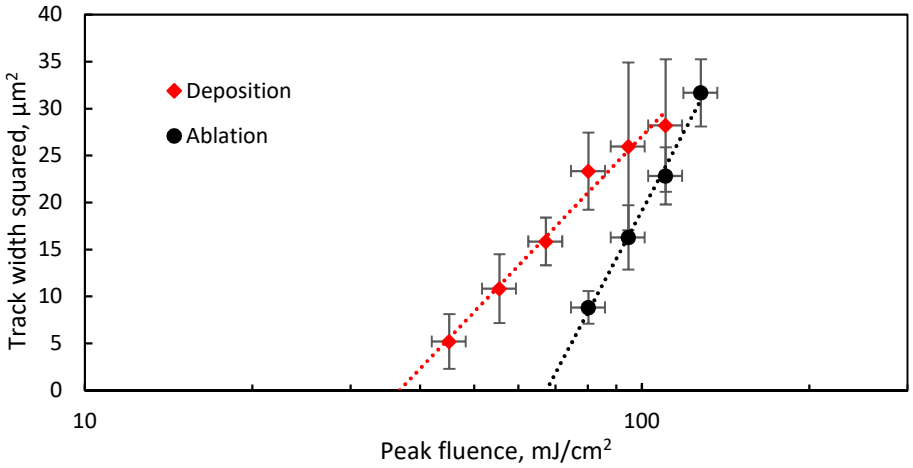

Figure 117: Graphs of track width squared against peak fluence for ablation and deposition threshold estimation of tungsten deposition on polyimide.

Figure 118 shows the microstructure of the tungsten track deposition on the polyimide substrate. The substrate was sputter coated with Au/Pd after the deposition to avoid charging in the SEM. At a laser fluence of 45 mJ/cm^2, quasi periodic structures were observed. The orientation of the structures was perpendicular to the linear polarization of the laser. When the laser power was increased, the width of the periodic structures increased until clumps of material was found in the middle of the track.

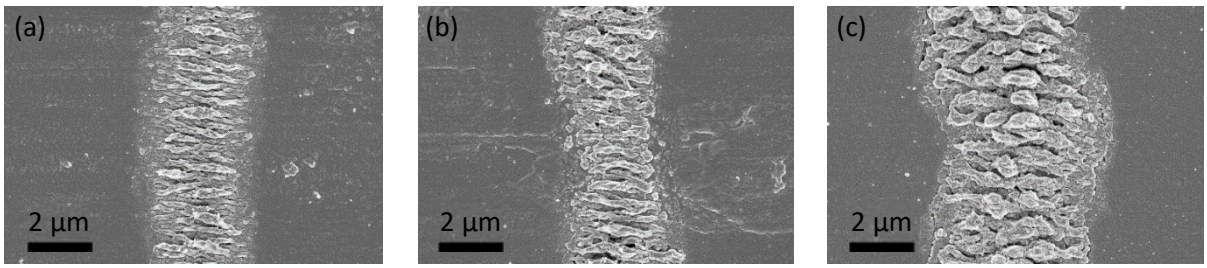

Figure 118: SEM images for the ultrafast LCVD on polyimide done with a focal spot of 6.6 µm, scanning speed of 30 µm/s and a laser power of 45, 55, and 80 mJ/cm^2.

5.5 Large area deposition

Large area deposition was attempted by scanning the successive tracks close to each other at a fixed hatch spacing. Figure 119 shows such a deposition on stainless-steel substrate by scanning the 6.6 µm laser spot at a hatch spacing of 5 µm. There was no observable change in the deposition morphology between each successive line scans.

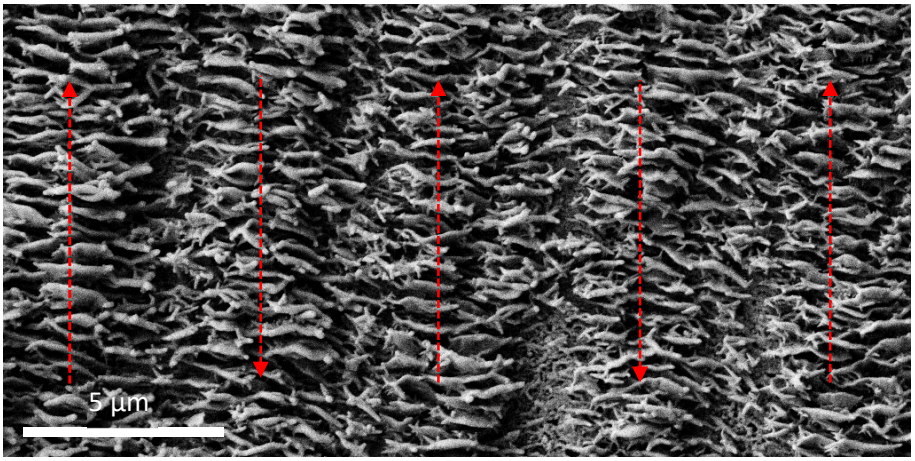

Figure 119: Large area deposition on stainless steel substrate made by scanning the 6.6 µm beam at 30 µm/s (55 mJ/cm^2 peak fluence) at a hatch spacing of 5 µm. Scan directions were labelled with red arrows.

Figure 120 shows SEM images of the large area deposition on SiO_2/Si substrates with the 33 µm laser spot. The sample on the left was made with a hatch spacing of 25 µm while that on the right has a hatch spacing of 21 µm. When the hatch spacing was reduced, the subsequent tracks became coarser due to clumping of the periodic structures. This was thought to be the due to the deposition outside the laser spot contaminating the substrate and the subsequent tracks got progressively worse.

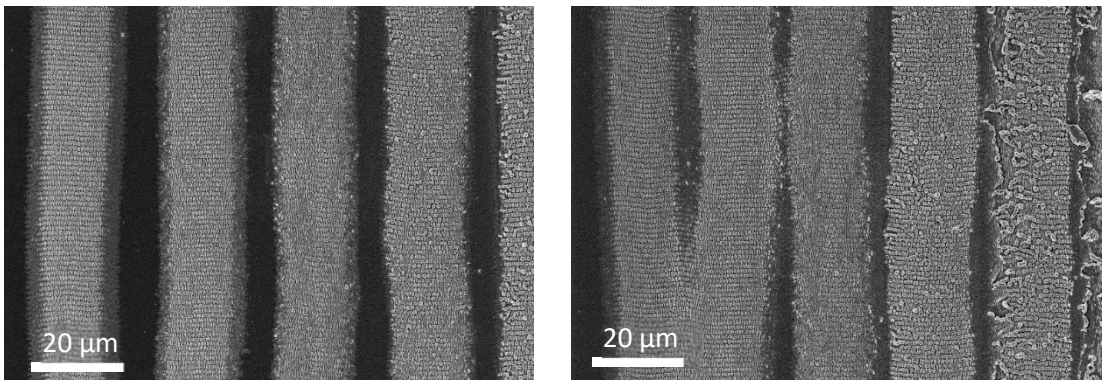

Figure 120: SEM images of large area deposition on SiO_2/Si at a hatch spacing of 25 (left) and 21 µm (right). As the hatch spacing was reduced, successive deposited lines become rougher.

The degradation of the deposition quality for subsequent track also affected the thin film deposition. Figure 121 shows an optical image of multiple successive thin film track deposition on borosilicate glass through the back-illumination configuration. The first track of the left image had a straight edge, however the fourth track had a wavy edge. The first track also appeared darker than the subsequent tracks. These observations were likely due to successive deposition outside the laser spot from the previous tracks. When the scanning speed was increased from 30 (left) to 300 µm/s (right), the deposited film was thinner and the effect of the deposition outside the laser spot was reduced.

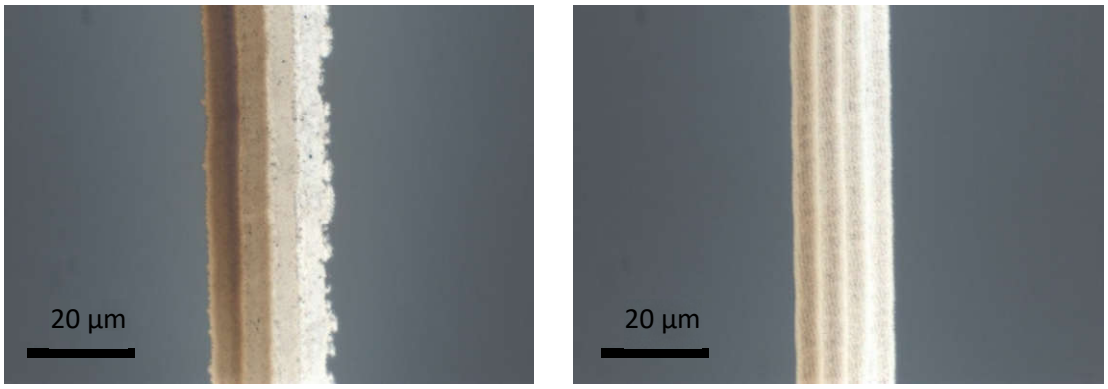

Figure 121: Multiple thin film tracks on borosilicate glass deposited through the back-illumination configuration at a scan speed of 30 µm/s (left) and 300 µm/s (right), peak fluence of 45 mJ/cm^2 (left) and 67 mJ/cm^2 (right), and hatch spacing of 8 µm.

5.6 Columns

Dwelling the laser on a spot for more than two seconds promoted the growth of the quasi-periodic structures into porous columns (Figure 122). After approximately 20 µm of column height, the periodicity and alignment of the structures became more random such that it was no longer generally aligned perpendicular to the laser linear polarization direction. These columns retained diameters close to that of the focused laser spot at 7 µm and grew vertically until approximately 32 µm tall at a dwell time of 50 s. Beyond this height, the aspect ratio of the column prevented cooling to below the threshold deposition temperature between the laser pulses. Thus, non-porous deposition was observed near the tip of the column. Through non-porous deposition, the height continued to increase until approximately

60 µm tall at a dwell time of 100 s. Beyond that height, the tip of the column grew to form a cone previously seen in the column deposition using the 405 nm CW laser (section 4.3).

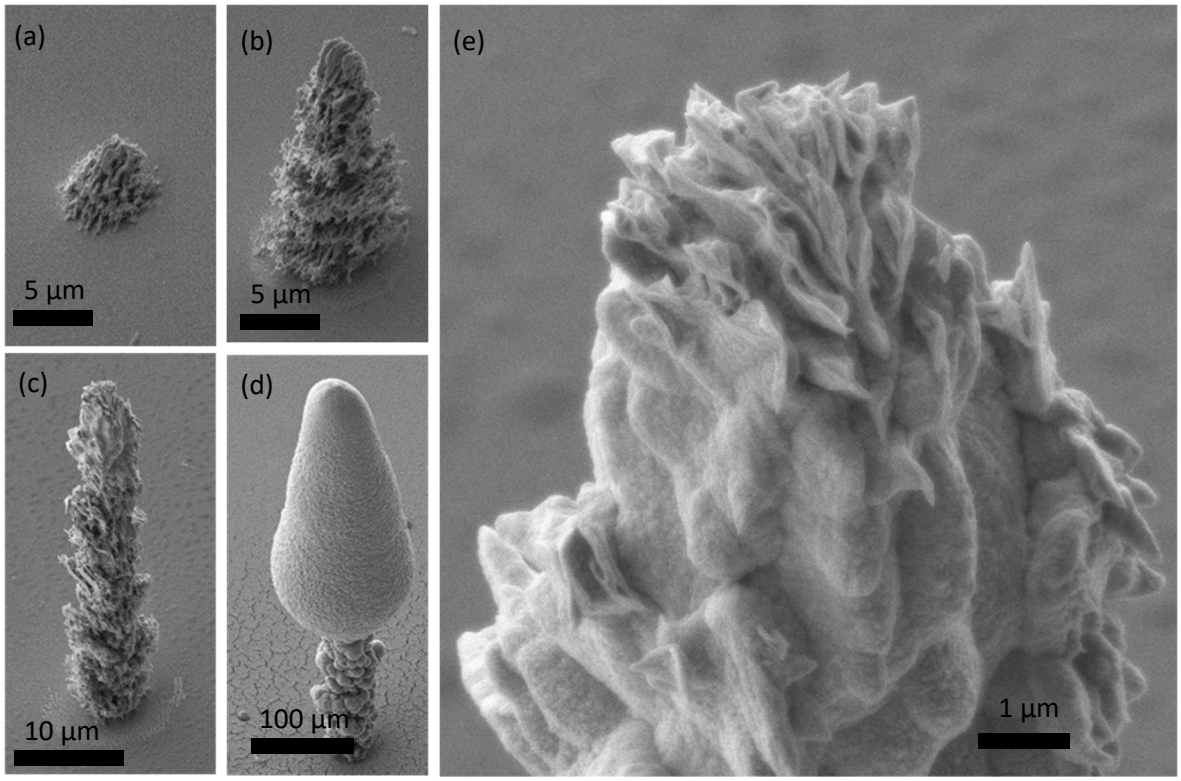

Figure 122: SEM images, at 45⁰ angle to the substrate, of tungsten porous fibres on stainless steel by dwelling the laser at a peak fluence of 30 mJ/cm² on a spot for (a) 1, (b) 5, (c) 50, and (d) 500 s. (e) Higher resolution image of (c) at the top of the column.

There were no significant differences between using linear polarized and circular polarized laser beam for the column growth experiments. Figure 123 shows the column grown by dwelling the laser on a spot for 10 s for both linear and circular polarized laser. Both columns consisted of short nanowires and quasi-periodic walls. Both had similar diameters and heights after 10 s of growth. The column produced by linear polarized light had more features orientated to perpendicular to the linear polarization direction while the column produced by circular polarized light had more features pointing in random directions.

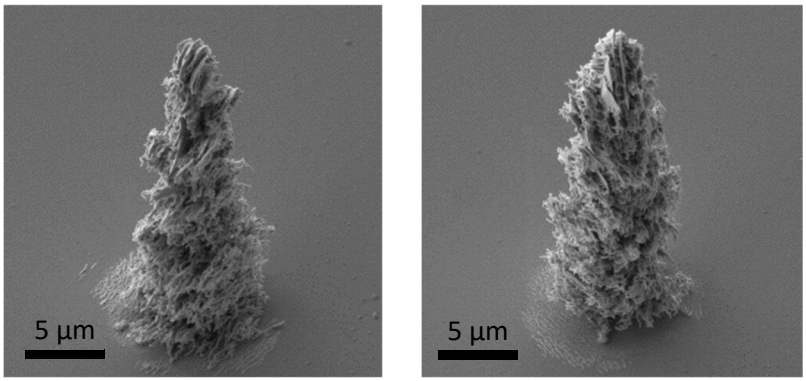

Figure 123: SEM image of column grown by dwelling the laser on a spot for 10 s using (left) linear and (right) circular polarized laser beams.

Figure 124 shows the columns after a certain time dwell using a laser peak fluence of 80 mJ/cm^2. Compared to the deposition using a lower power in Figure 122, the non-porous growth started earlier at 20 s instead of 50 s. The height of the non-porous section for the growth with the higher laser power was also shorter at 22 µm compared to 32 µm for the growth using the lower laser power. The height growth rate for the deposition with the laser power was higher than the lower laser power. After 50 s of deposition time, the height of the column with the lower laser power was 45 µm while the height of the column grown with the higher laser power was 89 µm. The columns widths for both laser powers were approximately the same. The width for the porous section was approximately 10 µm while the width for the non-porous section was approximately 20 µm.

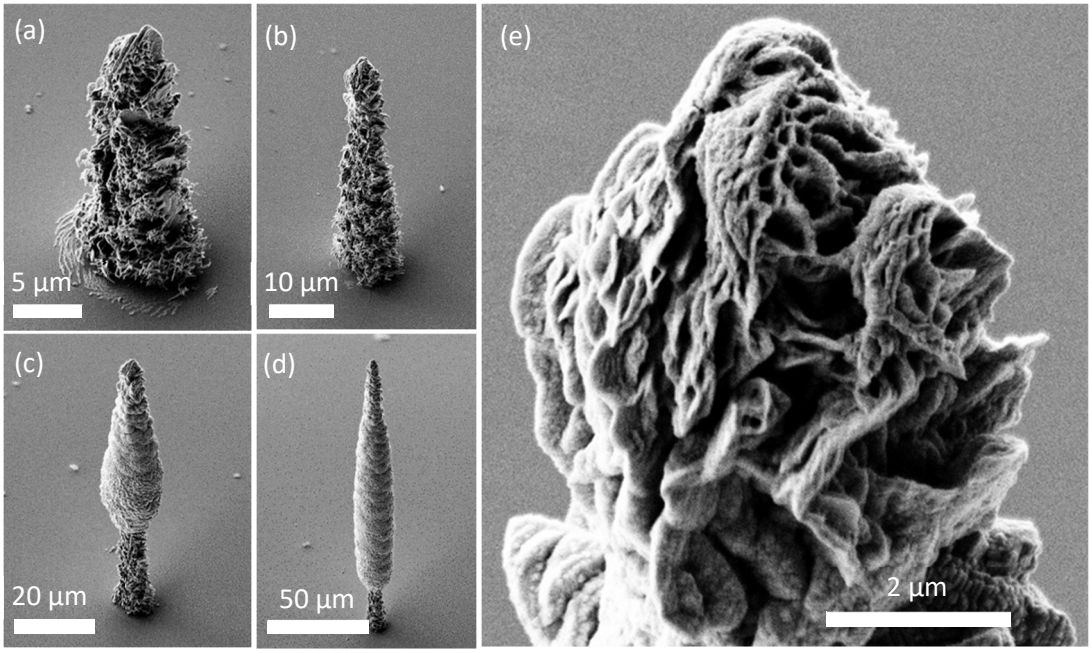

Figure 124: SEM images, at 45° angle to the substrate, of deposition using laser peak fluence of 80 mJ/cm^2 for (a) 10, (b) 20, (c) 50, and (d) 100 s. Compared to the deposition using a lower power in Figure 122, the non-porous growth started earlier at around 20 s compared to 50 s. (e) Higher resolution image of (b) at the top of the column.

5.6.1 Height growth rate

Figure 125 shows a graph of the column heights against time for both the laser powers mentioned in the previous section. The height growth rate appears the same for the first 20 s. Then the growth rate using the higher laser peak fluence of 80 mJ/cm^2 stays high at approximately 1.5 µm/s however the growth rate using the lower laser peak fluence of 30 mJ/cm^2 drops to approximately 0.14 µm/s. Since the laser was not scanned in the z-direction, the drop in the growth rate using the lower laser peak fluence was likely due to insufficient intensity once the column tip grew higher than the focal point of the laser.

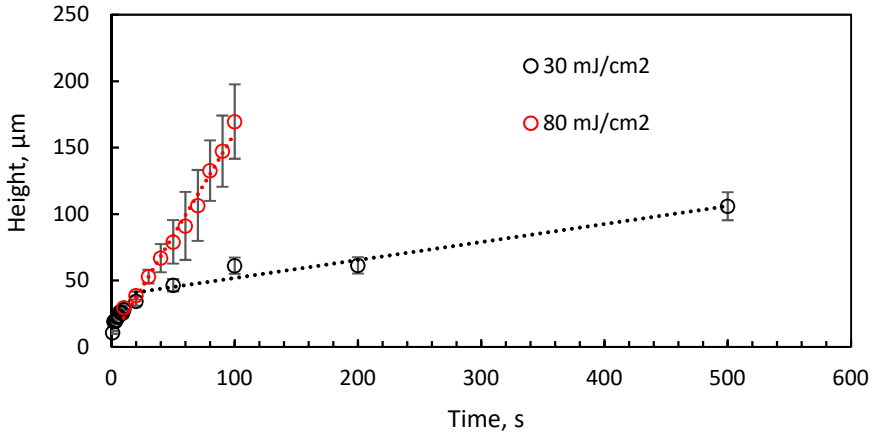

Figure 125: Height growth rate of the columns deposited with a laser power of 30 and 80 mJ/cm^2.

5.6.2 Scanning upwards in the z-direction

Instead of stationary dwells, the laser can be scanned in the z-direction. Figure 126 shows the deposition results using the same laser peak fluence of of 80 mJ/cm^2 but instead of dwelling the laser focal spot, the laser spot was moved up in the z-direction at a speed of 3 µm/s. After 100 s of deposition time, the tall column was produced. In Figure 124 where the laser spot was not moved up in the z-direction during the deposition, the column height after 100 s was 190 µm high with a diameter at the widest point of 20 µm, achieving an aspect ratio of 9.5. In Figure 126 where the laser spot was moved up in the z-direction at a speed of 3 µm/s the column height after 100 s was 330 µm with a diameter at the widest point was also approximately 20 µm. Thus a higher deposition rate was achieved by moving the focal spot in the z-direction. The higher deposition rate was achieved because by moving the laser spot the laser was focused closer to the tip of the column where growth was occuring. The column also consisted first of a porous quasi-periodic section near substrate followed by a non-porous section after reaching a height of 32 µm.

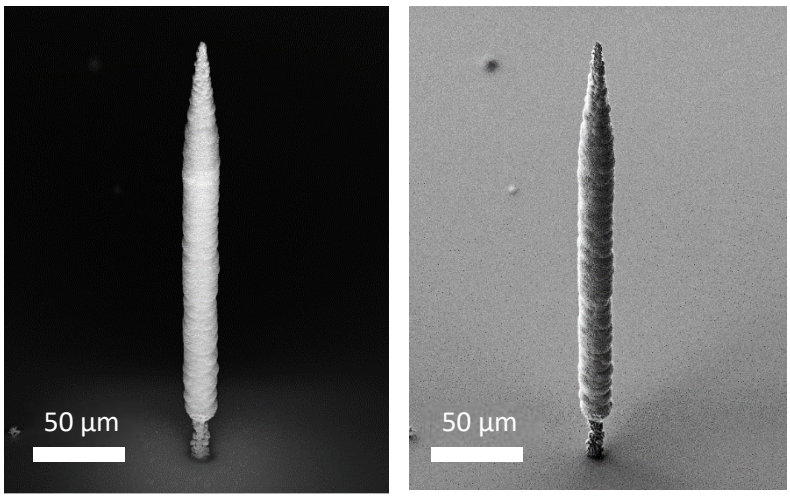

Figure 126: SEM images, at 45° angle to the substrate, of 100 s deposition using peak fluence of 80 mJ/cm^2 and focal spot scanned in the z-direction at a speed of 3 µm/s.

5.6.3 Tilted columns and multi-column structures

During the z-scans, the laser focused spot can be moved in the x- and y- direction to produce tilted columns. Figure 127 shows the deposited columns made by moving the focal spot at a speed of 2 µm/s at a direction 14° and 27° from the vertical respectively in the left and right images. When the laser scan direction was 14° from the vertical, a column tilted an angle of 12° was produced. Thus, the growth direction followed the focal laser spot. This tilted column had porous section (32 µm long) followed by non-porous sections similar to that seen in scanning the laser upwards without tilt. There was no significant build-up of material on the substrate below the tilted column. When the tilt angle was approximately doubled to 27°, a column tilted at an angle of 36.5° was produced because the growth rate in the horizontal direction was slower than the vertical direction. To increase the growth rate in the horizontal direction, the laser incident angle must be tilted closer to the required horizontal growth direction. The column was mainly porous quasi-periodic structures with no significant non-porous sections due to the low power input to the tip of the tilted column that was out of focus. There was also significant deposition of material below the tilted column because the thin column produced did not entirely block the incident laser from reaching the substrate below.

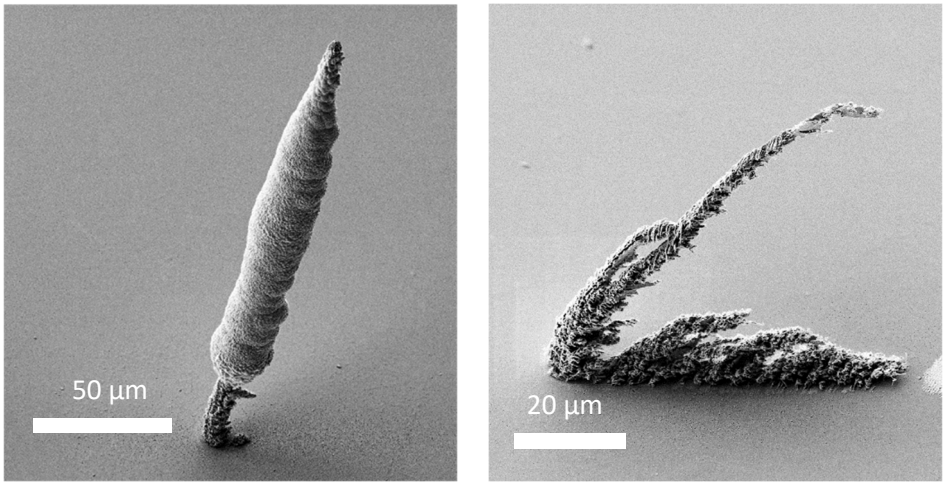

Figure 127: SEM images, at 45° angle to the substrate, of 100 s deposition using peak fluence of 80 mJ/cm^2 and focal spot moved at a (left) 14° angle and (right) 27° angle from the vertical.

The tilted columns can be combined to make more complex structures. Figure 128 shows a multiple column tower made from five columns. Four of the columns were made by scanning the laser at 14° angle to the vertical to create a four-sided pyramidal base. Each of the tilted columns was scanned at a speed of 2 µm/s for 100 s. The top section was then scanned from the tip of the four-sided pyramid at a speed of 2 µm/s in the vertical direction for 100 s. The total build time for the structure was 500 s. The four columns at the base started their growth with porous quasi-periodic structures then the deposition became non-porous after a certain column length. The fifth column on the top only consist of non-porous deposition. The top of the four base columns were not of the same diameter because the first column built blocked the incident laser from reaching the subsequent columns.

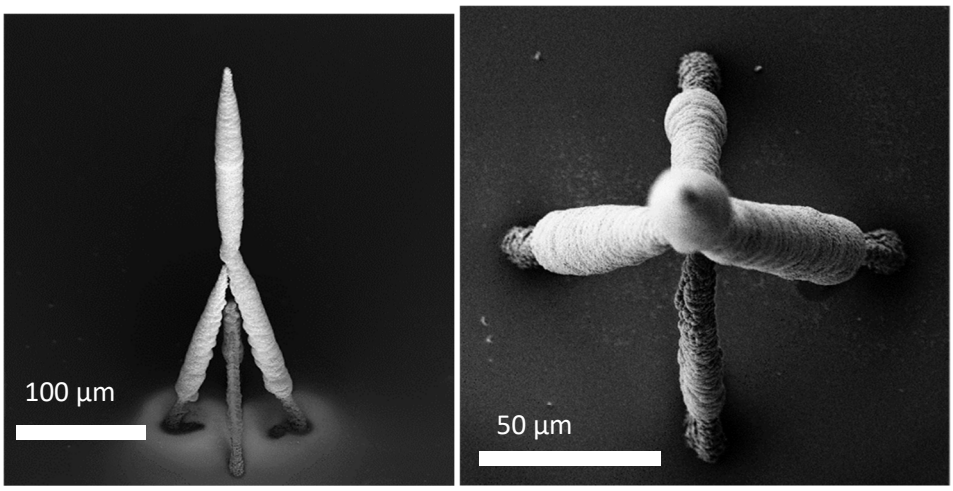

Figure 128: SEM images (left) at 45° angle to the substrate and (right) plan view, of a total of 500 s deposition time with laser peak fluence of 80 mJ/cm^2. For the four tilted columns at the base, the laser was scanned at 14° angle from the vertical at a speed of 2 µm/s for 100 s each. Then the top column was made by scanning the laser for 100 s at a speed of 2 µm/s in the vertical direction.

5.7 Walls

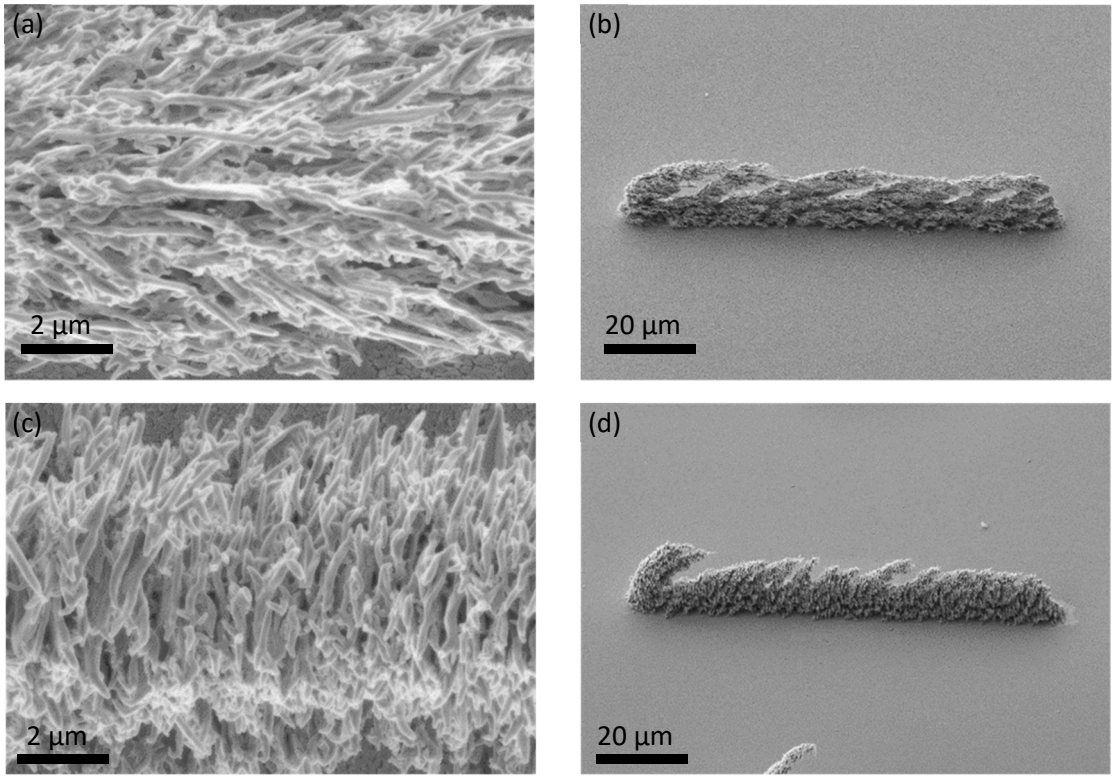

Figure 129: Scanning the laser with peak fluence 55 mJ/cm^2 and linear polarization (a, b) perpendicular and (c,d) parallel to the scan direction at a scan speed of 3 µm/s with SEM view from the top (a, c) and at a 45^o angle (b, d).

At very low scanning speeds (<1 µm/s), it was possible to tilt the columnar structures. At a slightly higher scanning speeds (1-10 µm/s) porous walls of tungsten were created (Figure 129). The porous walls consisted of curvy walls and short nano-wires with thickness of approximately 100-200 nm. As the height of the walls increased, the alignment of the nano-structures became more random however the general alignment which was perpendicular to the linear beam polarization was still observed. For

the nano-structures parallel to the scan direction, the tilt angle of the columns was shallower. The growth rate in the horizontal direction was higher than when the nano-structures were perpendicular to the scan direction. This happened because the growth rate on the pre-deposited tungsten was higher than the nucleation rate on the substrate.

5.8 Summary

This chapter explored the ultrafast pyrolytic LCVD experiments in detail. The peak intensity in a ultrafast laser pulse enabled high temperatures of up to 1500 °C at the laser spot while the immediate surrounding surface remained cool. However, the temperature inside the laser spot drops drastically after the laser pulse, dipping below the deposition threshold temperature of CVD experiments and thus the time duration for successful deposition was short. This deposition regime favours reactions that have a high deposition rates, high deposition temperatures and high ablation thresholds for the deposited material such as the deposition of tungsten using tungsten hexacarbonyl. Spot dwell experiments showed that on semiconductors and transparent glass surfaces, a thin film was first deposited and then on that thin film, quasi-periodic structures started to grow. On metallic surfaces, the quasi-periodic structures started to grow without the thin film. The orientation of the quasi-periodic structures was perpendicular to the linear polarization of the laser beam and cross-section images revealed significant branching in the structures.

Quasi periodic structures were also produced when the laser was scanned. Increasing the scan speed ($\geq$ 300 µm/s, $\eta \leq 11{,}000$) produced thin film tracks without the quasi-periodic structures on transparent glass surfaces. However, ablation was observed in the middle of the thin film tracks on SiO2/Si substrates. The lowest laser peak fluence for observable deposition at scanning speed of 100 µm/s (η=33,000) was 110 mJ/cm^2 peak fluence (3.70×10^{11} W/cm^2 intensity, 19 nJ pulse energy or 9.5 mW of average power). The ablation threshold of the SiO_2/Si substrate at this scanning speed was 174±71 mJ/cm^2. Elemental analysis of the deposits showed that the deposits were up to 90 wt% tungsten and there was insignificant tungsten deposition outside the laser spot. When the pulse repetition rate and scan speed was reduced to keep the same number of pulses per spot, the volumetric deposition rate did not drop in proportion to the drop in frequency. This suggested that the deposition process was limited by the transport of the precursor to the deposition site and higher precursor pressure or flow-rates would increase the deposition rate.

By increasing the laser spot size from 6.6 µm to 33 µm, the deposition threshold on SiO_2/Si substrate reduced and thin film deposition was possible on the substrate without ablation. For example with the larger spot size of 33 µm at a scanning speed of 500 µm/s (η=33,000), the lowest peak fluence for observable deposition was 42 mJ/cm^2 compared to 110 mJ/cm^2 when the smaller focal spot size of 6.6 µm was used. This difference was attributed to the increase in energy per pulse for the same peak fluence when the spot size was increased. When the track was scanned multiple times, thin-film

formation was favoured over the formation of quasi-periodic structures. The lowest resistivity measured for the thin-film tracks on SiO_2/Si substrates was 37±4 μΩ cm (6.7 times the bulk resistivity of tungsten), which was lower than the 66±7 μΩ cm (11.7 times bulk resistivity) achieved in the hydrogen annealed deposited track of the 405 nm CW laser diode.

For transparent glass surfaces, it was possible to focus the laser through the glass substrate to cause deposition at the bottom surface. Thin-films and quasi periodic structures were formed in top-exposure configuration. Only thin-films and no quasi-periodic structures were observed in the deposits through this configuration. Deposition at the bottom surface was also observed when the glass was placed above another substrate such that the gap between the solids was less than a hundred microns. This showed that it is possible to write the tungsten tracks in the inner wall of transparent tight channels. Analysis of the deposition microstructure (section 5.2.6) in the scanned tracks showed that for the thin films the grain size was less than 400 nm thus the deposited tracks appears smooth in optical images.

For polyimide films, deposition of quasi-periodic structures was possible at a scanning speed of 30 μm/s. The deposition threshold of 37±13 mJ/cm^2 was lower than the ablation threshold of the material at 67±15 mJ/cm^2.

Dwelling the laser on a spot longer than one second created porous towers due to growth of the quasi-periodic structures. The porous towers grew up to an aspect ratio of four. From then on, the tower growth continued through non-porous deposition. This was thought to be due to the increase in the aspect ratio, the temperature at the tip of the laser did not cool down sufficiently after the laser pulse. Thus, significant deposition that were unaffected by the laser interference continued between the laser pulses. By moving the laser spot 2 μm/s at a tilt of 14° from the vertical, tilted towers were grown. These tilted columns could be combined to form more complex structures. At higher scan speeds (<10 μm/s) porous walls of quasi-periodic structures were created.

Chapter 6 Ultrafast LCVD on graphene

In this chapter, the feasibility of using the ultrafast LCVD deposition, detailed in the previous chapter, for depositing contact metals on graphene is explored. The aim was to successfully deposit the metal on graphene and measure the contact resistance between the metal and graphene. In this study, the graphene was produced through CVD in a cold wall reactor (Aixtron Black Magic Pro 4) using 25 μm thick copper catalyst foils at 1065 °C similar to the methods published in (Braeuninger-Weimer et al., 2016), (Van Veldhoven et al., 2016) and (Tao et al., 2012). The graphene films were then transferred to 280 nm SiO_2/Si wafers using a wet transfer method. PMMA, which was used as the sacrificial transfer layer, was then removed using acetone and isopropanol.

6.1 Large area graphene patterning

The graphene grown in CVD and transferred to SiO_2/Si substrates required patterning to create uniform shapes for accurate electrical measurements. Results for stripping graphene on SiO_2/Si using a laser have been reported for single tracks (Dong et al., 2016), however parameters for large area removal of graphene through hatching of the line scans have not been reported. In this section, the laser with focal spot of 33 μm was first used to remove a single track of graphene. Then the track was scanned multiple times at a fixed hatch spacing to remove a larger area of graphene. Figure 130 shows optical images of the single ablation tracks scanned at a speed of 12.5 mm/s, 5 kHz repetition rate laser at various power levels. At low fluence of 68 mJ/cm^2, a track with jagged edges was produced. At a higher fluence level of 134 mJ/cm^2, the edges of the track were smoother. When the fluence level was increased to 170 mJ/cm^2 and above, damage to the underlying SiO_2/Si substrate was visible.

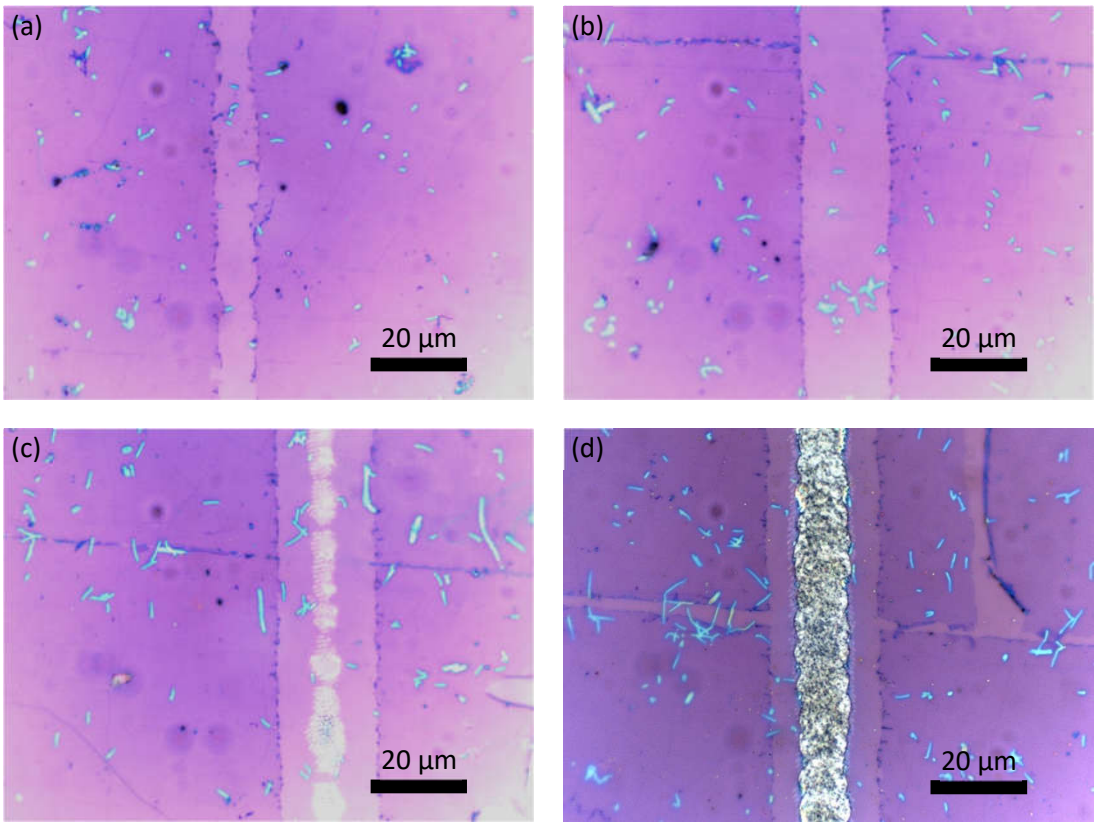

Figure 130: Optical microscope images of graphene on SiO_2/Si ablation at a scanning speed of 12.5 mm/s, pulse repetition rate of 5 kHz using a peak pulse fluence of (a) 68, (b) 134, (c) 170, and (d) 225 mJ/cm^2.

To confirm the removal of graphene, Raman analysis was done at a few locations across the ablated track. Figure 131 (a) shows a zoomed in image of the track made at peak fluence of 134 mJ/cm^2 along with locations where Raman analysis were done. Figure 131 (b) shows the Raman peak 2D intensity of those spots against distance perpendicular to the ablated track. Figure 131 (c) shows the full Raman spectrum for the measurement spots on the right edge of the ablated track. The narrow 2D peak in the Raman spectrum indicates single layer graphene (Ferrari et al., 2006). Inside the ablated track, the 2D peak intensity decreased until spectrum no. 15 where the 2D peak was no longer observed, indicating that the graphene was completely removed. Spectrum no. 15 was similar to the bare SiO_2/Si spectrum and there was no evidence of amorphous carbon (Figure 24 b). The width of the track measured from the optical microscope image was marked by the arrow in Figure 131 (b), and the good match with the dip in the peak 2D intensity showed that the optical measurement method was valid. The dip and rise in the peak 2D intensity were approximately 1 µm wide. This indicated that the minimum width of a narrow strip that can be manufactured using this technique was approximately 2 µm. The rise in the D peak in the spectrum no. 20 compared to the unexposed graphene was due to the increase in the presence of graphene edges (Cancado et al., 2008) and/or defects (Lucchese et al., 2010). The decrease in the 2D to G peak ratio intensity compared to the unexposed graphene indicated that the graphene was slightly doped after the laser ablation process (Beams et al., 2015).

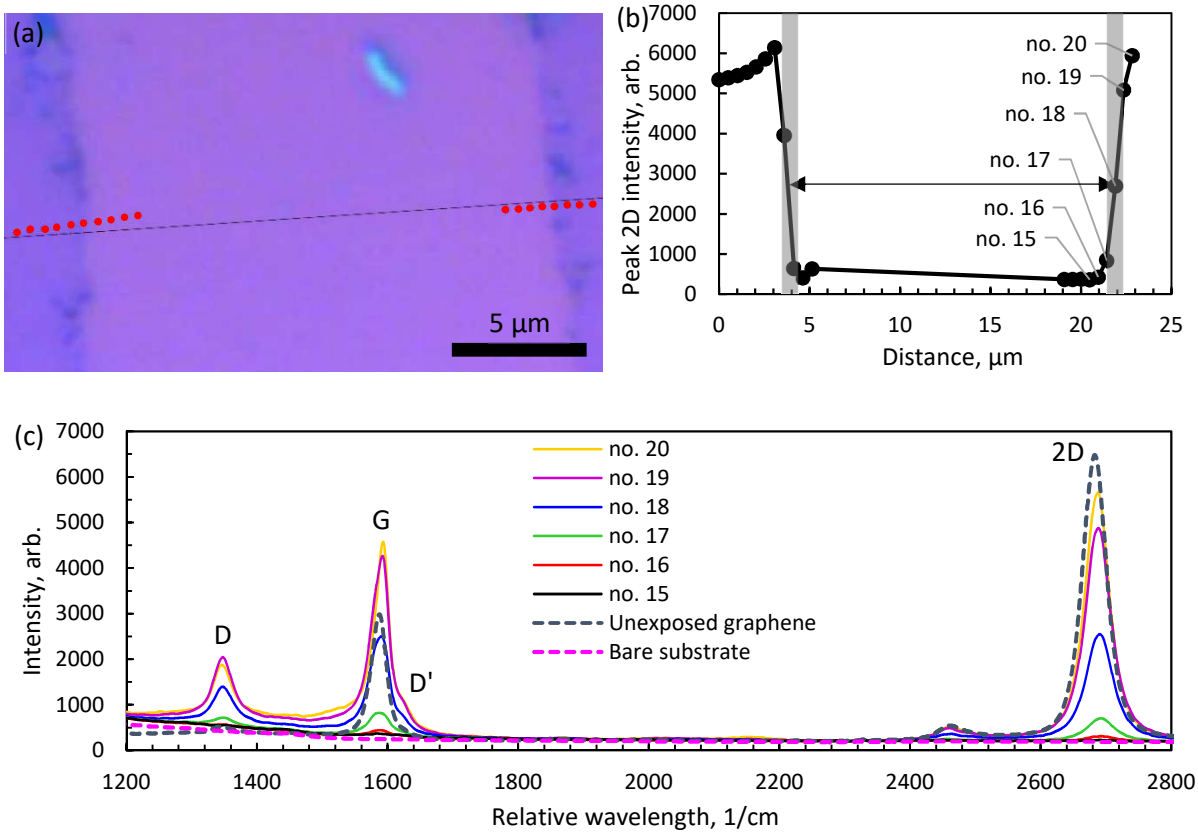

Figure 131: (a) Close-up optical microscope image of ablated graphene track scanned at a speed of 12.5 mm/s and laser peak fluence of 134 mJ/cm^2 showing spots (red circles) were Raman analysis were done. (b) Peak 2D intensity Raman intensity and (c) Raman spectrum of those spots. The arrow and greyed areas were the width and width uncertainty of the track measured using the optical microscope.

Figure 132 shows the graph of ablation track width squared against peak fluence in the logarithmic scale to find the thresholds based on equation 16. The scanning speed for the pulse repetition rates of 1 kHz and 5 kHz were 2.5 and 12.5 mm/s respectively to keep the number of pulses per spot the same in both settings. The ablation threshold of graphene was measured to be 60±10 and 57±8 mJ/cm^2 for 1 and 5 kHz respectively. These threshold values were slightly lower than the 66-120 mJ/cm^2 value measured by Dong et al., 2016 using a smaller beam diameter of 4.16 µm, scanning speed of 1.5 mm/s, and pulse repetition rate of 5 kHz. The ablation threshold of SiO_2/Si was approximately 2.8 times higher at 160±33 to 161±39 mJ/cm^2 for 1 and 5 kHz respectively.

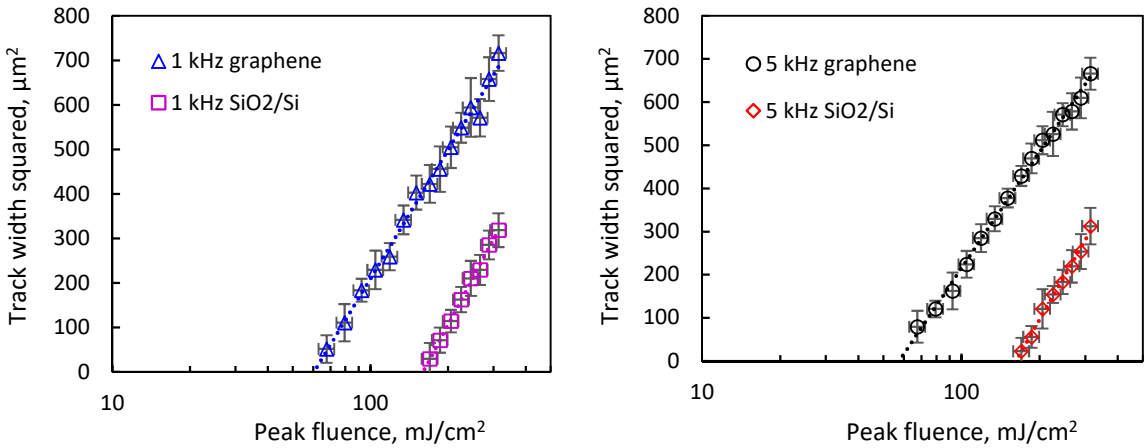

Figure 132: Graph of track width squared against peak fluence extrapolated to estimate the ablation thresholds of graphene and the underlying SiO_2/Si substrate at 1 kHz (left) and 5 kHz (right) pulse repetition rate. The ablation threshold of the underlying SiO_2/Si dropped negligibly from 160±33 to 161±39 mJ/cm² when the pulse repetition rate was increased from 1 kHz to 5 kHz. For graphene, the ablation threshold dropped from 60±10 to 57±8 mJ/cm² when the pulse repetition rate was increased from 1 kHz to 5 kHz.

A peak fluence of 134 mJ/cm², which was below the SiO_2/Si ablation threshold measured previously, was chosen for the large area patterning of graphene. The width of the ablated graphene track at that fluence level, scanning at 12.5 mm/s with a pulse repetition rate of 5 kHz was 18±1 µm. Using these parameters, the maximum graphene area removal rate was 225,000±12,500 µm²/s (nearly two orders of magnitude higher than that reported by Dong et al., 2016). A hatch spacing of 10 µm was chosen to give an overlap of 44.4 % between the tracks. Figure 133 shows a 20 µm wide strip of graphene that was left after the hatch processing. The width of the graphene strip was consistent with that image for the whole processing length of 5 mm.

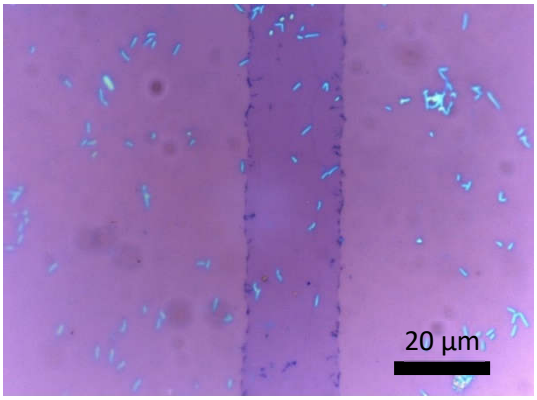

Figure 133: Optical image of a graphene strip approximately 20 µm wide made by removing the surrounding graphene at scanning speed of 12.5 mm/s, pulse repetition rate of 5 kHz and hatch spacing of 10 µm.

Figure 134 (a) shows a zoomed microscope image of the graphene strip with the locations where Raman analysis was done. Figure 134 (b) shows the peak 2D Raman intensity of those spots and Figure 134 (c) shows the Raman spectrum of a few of those spots. The spectrum no.1 have no observable 2D and G peaks indicating that the graphene was completely ablated outside the graphene strip. Inside the strip, the D, G and 2D peaks were visible. Compared to the unexposed graphene Raman spectrum, the rise in the D peak indicated presence of edges (Cançado et al., 2004) and/or defects (Lucchese et al., 2010) in

the graphene layer. The decrease in the 2D to G peak ratio intensity compared to the unexposed graphene indicated that the graphene was slightly doped after the laser ablation process (Beams et al., 2015).

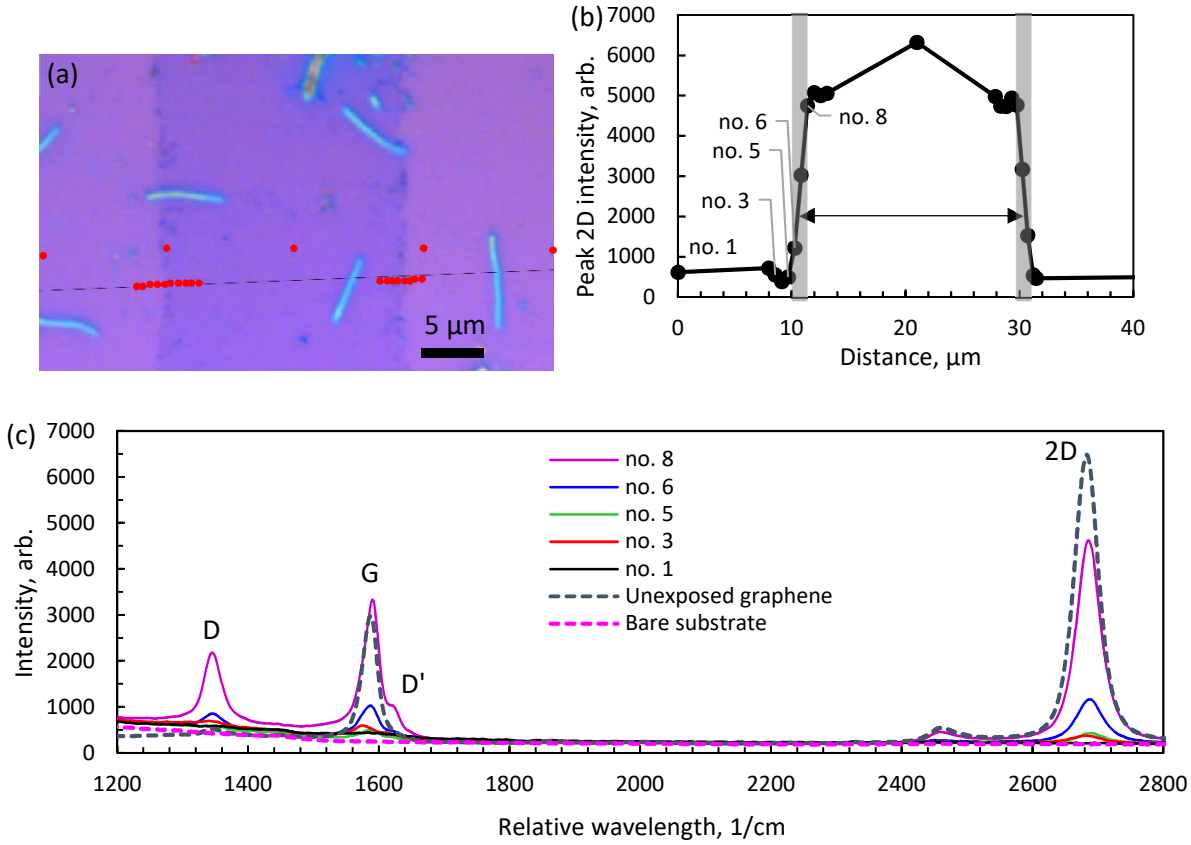

Figure 134: (a) Zoomed optical microscope image of the graphene strip with locations (red circles) of Raman analysis. (b) Peak 2D intensities of the Raman spectrum from those locations with the width measured from the optical microscope image marked by the arrow. (c) Raman spectrum at a few of those locations. The arrow and greyed areas in the top right image were the width and width uncertainty of the track measured using the optical microscope.

6.2 Damage threshold of graphene at 500 kHz

The ablation threshold of graphene exposed to ultrafast pulses measured in the previous section and reported by Dong et al., 2016 was for a pulse repetition rate of 5 kHz. The thin-film deposition investigated in section 5.2 was optimised for a pulse repetition rate of 500 kHz. Threshold at these high repetition rates (500 kHz) and high pulse overlap ($\eta \geq 11{,}000$) have not been reported in literate and is studied in this section. Figure 135 shows optical images of the graphene on SiO_2/Si after scanning the laser over at a speed of 1500 µm/s at various peak fluence levels. At a low fluence of 92 mJ/cm^2, a vague narrow track was observed. When the peak fluence was increased to 118 mJ/cm^2, the track became more obvious. However, no clear edges were detected in the images which suggested that the graphene was not removed. When the peak fluence was increased to 170 mJ/cm^2, an ablated track of SiO_2/Si was seen. The ablation track grew wider when the peak fluence was increased to 205 mJ/cm^2. The SiO_2/Si track appeared dark compared to that seen in Figure 130 likely due to thermal effects caused by the higher pulse overlap (η =11,000 here compared with η =13.2 in Figure 130).

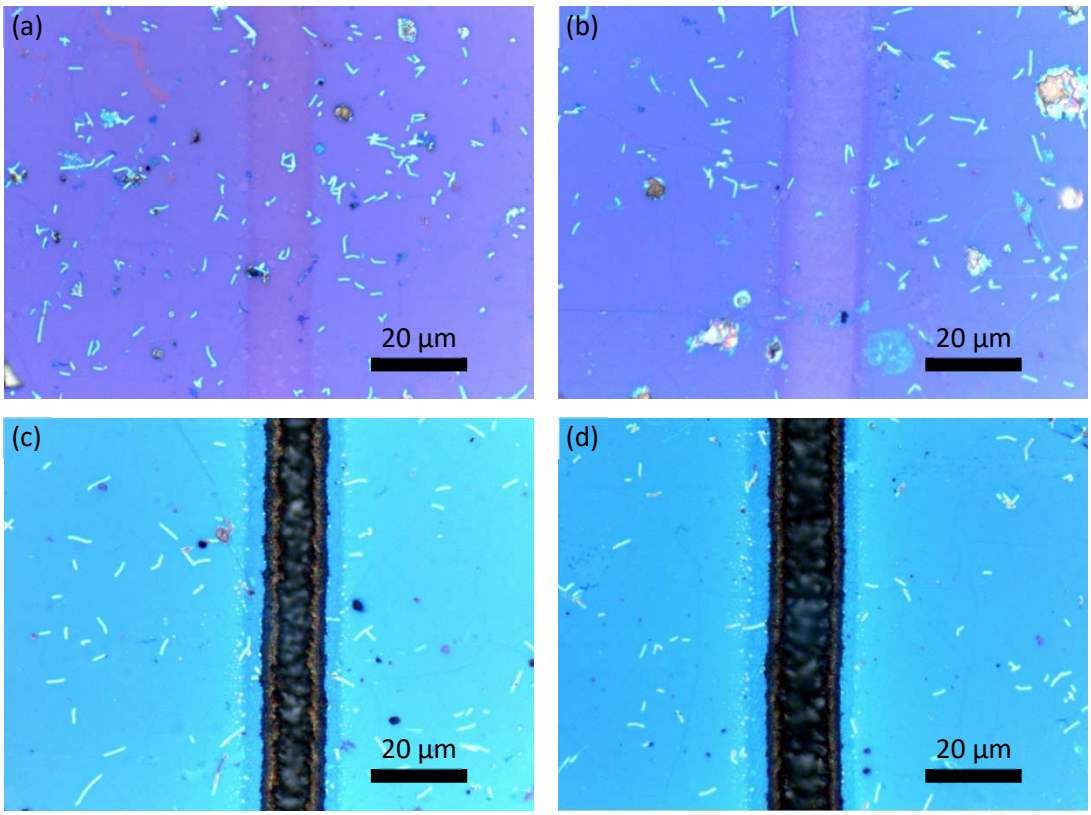

Figure 135: Optical images of the damage on graphene when the laser was scanned at a speed of 1500 µm/s with a pulse repetition rate of 500 kHz and peak fluence of (a) 92, (b) 118, (c) 170, and (d) 205 mJ/cm^2.

Figure 136 (a) shows the optical microscope image of the track scanned with a peak fluence of 92 mJ/cm^2 with points where Raman analysis was done. Figure 136 (b) shows the peak 2D Raman intensity of those points against the relative distance perpendicular to the track scan direction. Figure 136 (c) shows the Raman spectrum of a few of those points. In the middle of the track (point no. 20), G and 2D peaks were detected in the Raman spectrum. This indicated that graphene was present in the middle of the track where the fluence was at the highest. Towards the edge of the track (no. 41), the spectrum resembled the spectrum of the unexposed graphene with slightly higher D, G and 2D peaks. The width of the track measured from the optical image (indicated by the arrow in Figure 136 (top right)) was smaller than the damage width where the peak 2D intensity decreased. Thus, the damage threshold estimated through the linear regression of equation 16 would be an overestimate of the actual damage threshold.

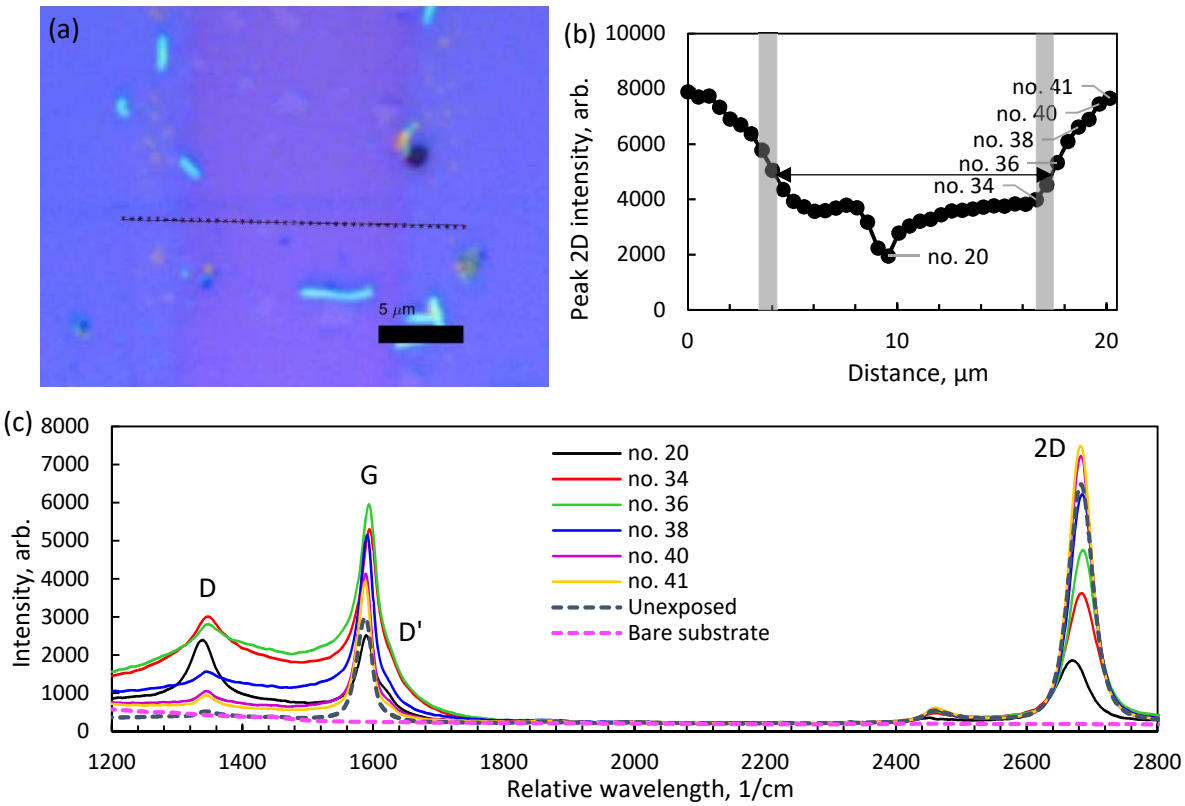

Figure 136: (a) Zoomed in optical microscope image of the graphene track scanned with the laser at a speed of 1500 μm/s and peak fluence of 92 mJ/cm² with locations where Raman analysis were done (black asterisks). (b) Peak 2D Raman intensity at those points against distance perpendicular to the scanned track. (c) Raman spectrum of a few of those points. The arrow and greyed areas in the top right image were the width and width uncertainty of the track measured using the optical microscope.

Figure 137 shows the damaged graphene track widths squared, which were measured through optical microscope images, against the peak fluence in logarithmic scale. From those points, the estimate of the graphene damage threshold was 53±7 and 59±9 mJ/cm^2 for a laser scanning speed of 500 and 1500 μm/s. These values were overestimates of the actual graphene damage threshold because the widths measured were smaller than actual damage width mentioned previously. The SiO_2/Si substrate damage threshold was measured to be 106±14 and 101±12 mJ/cm^2 for a laser scanning speed of 500 and 1500 μm/s respectively.

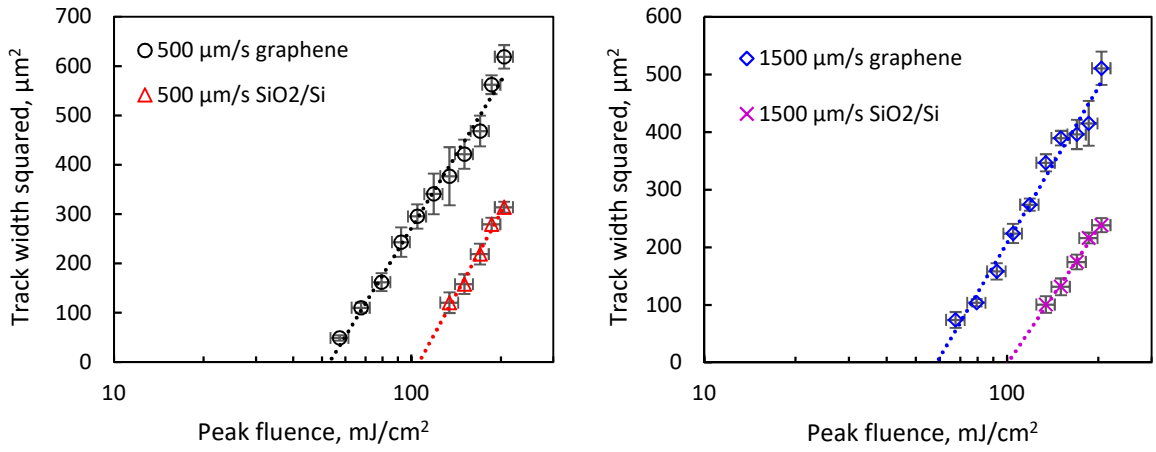

Figure 137: Graph of damaged graphene track width squared against peak fluence in logarithmic scale. The damage threshold for graphene was estimated to be 53±7 and 59±9 mJ/cm² for scanning speed of 500 and

1500 µm/s respectively while the ablation threshold of the SiO_2/Si substrate was 106±14 and 101±12 mJ/cm^2 respectively.

6.3 Deposition on graphene and ablated graphene surfaces

Ultrafast LCVD of tungsten on SiO_2/Si substrates have been studied in the previous chapter, however the deposition threshold was expected to change due to the presence of graphene and other residue on the surface. Figure 138 shows thin film tungsten tracks written on a graphene on SiO_2/Si substrate where the top half of the graphene was ablated using the settings from section 6.1. The width of the track was larger on the graphene side.

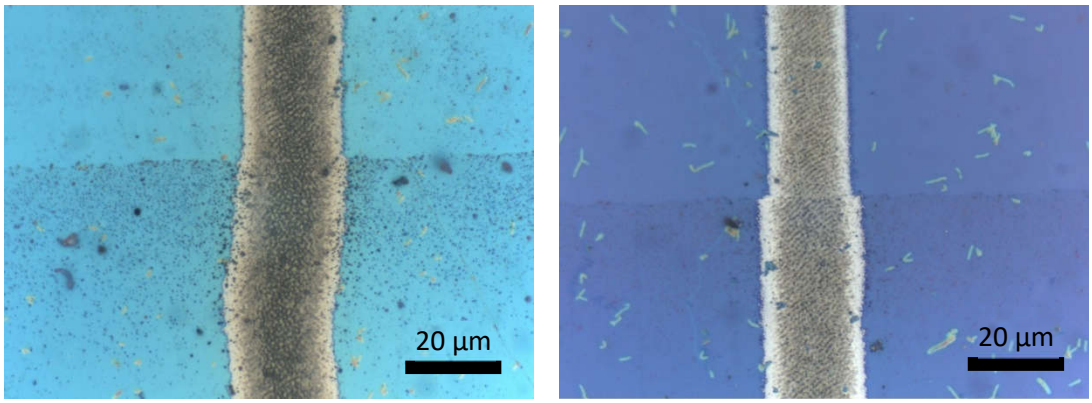

Figure 138: Optical microscope images of ultrafast LCVD of tungsten on graphene and ablated graphene surfaces using a scanning speed of 500 µm/s and peak pulse fluence of 79 mJ/cm^2 (left) and 1500 µm/s at 92 mJ/cm^2 (right).

Figure 139 shows graphs of thin-film track width squared against laser peak fluence in the logarithmic scale to find the threshold using equation 16 for various scanning speeds and substrates. The deposition threshold on the unablated graphene surface was 30±6 and 34±7 mJ/cm^2 at scan speed of 500 and 1500 µm/s respectively. The deposition threshold on the ablated graphene surface was higher at 38±8 and 55±12 µm/s for scan speed of 500 and 1500 µm/s. For both scan speeds, the deposition threshold on clean SiO_2/Si was lowest, followed by on graphene and the deposition threshold on ablated graphene was the highest.

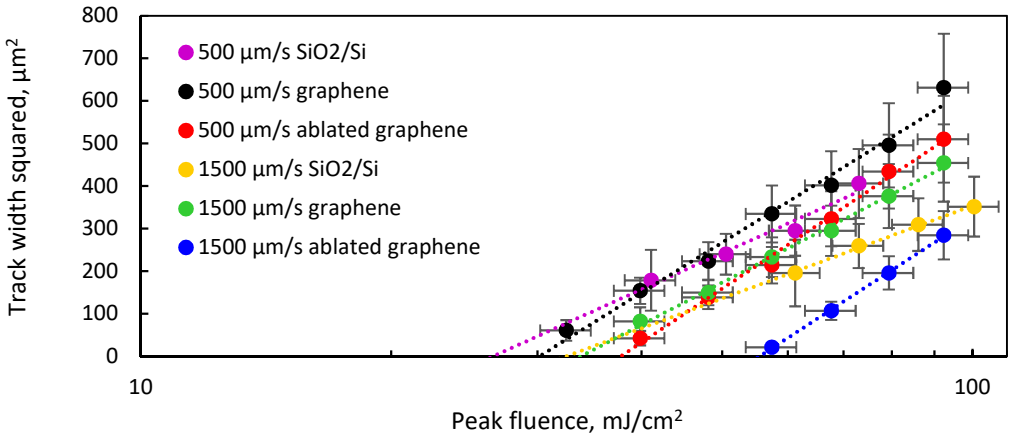

Figure 139: Graph of track width squared against peak fluence extrapolated to show the deposition threshold at scanning speeds of 500 µm/s and 1500 µm/s on unablated and ablated graphene on SiO_2/Si surfaces. The

deposition threshold at 500 µm/s was 27±6, 30±6 and 38±8 mJ/cm² on clean SiO₂/Si, graphene and ablated graphene respectively. The deposition threshold for 1500 µm/s was higher at 33±7, 34±7 and 55±12 mJ/cm² on clean SiO₂/Si, graphene and ablated graphene respectively.

Figure 140 (a) shows the zoomed optical microscope image of the track deposited on graphene at 500 µm/s scan speed and 79 mJ/cm² peak fluence along with points where Raman analysis was done. Figure 140 (b) shows the 2D peak intensity of those points against distance perpendicular to the deposited track. The arrow in the chart is the width of the deposited track measured from the optical microscope image. Figure 140 (c) shows the Raman spectrum of a few of those points. The figures show that up until the deposited track, graphene with a slightly higher D peak was detected. This indicated that there was a good possibility that the graphene and tungsten metal were in contact.

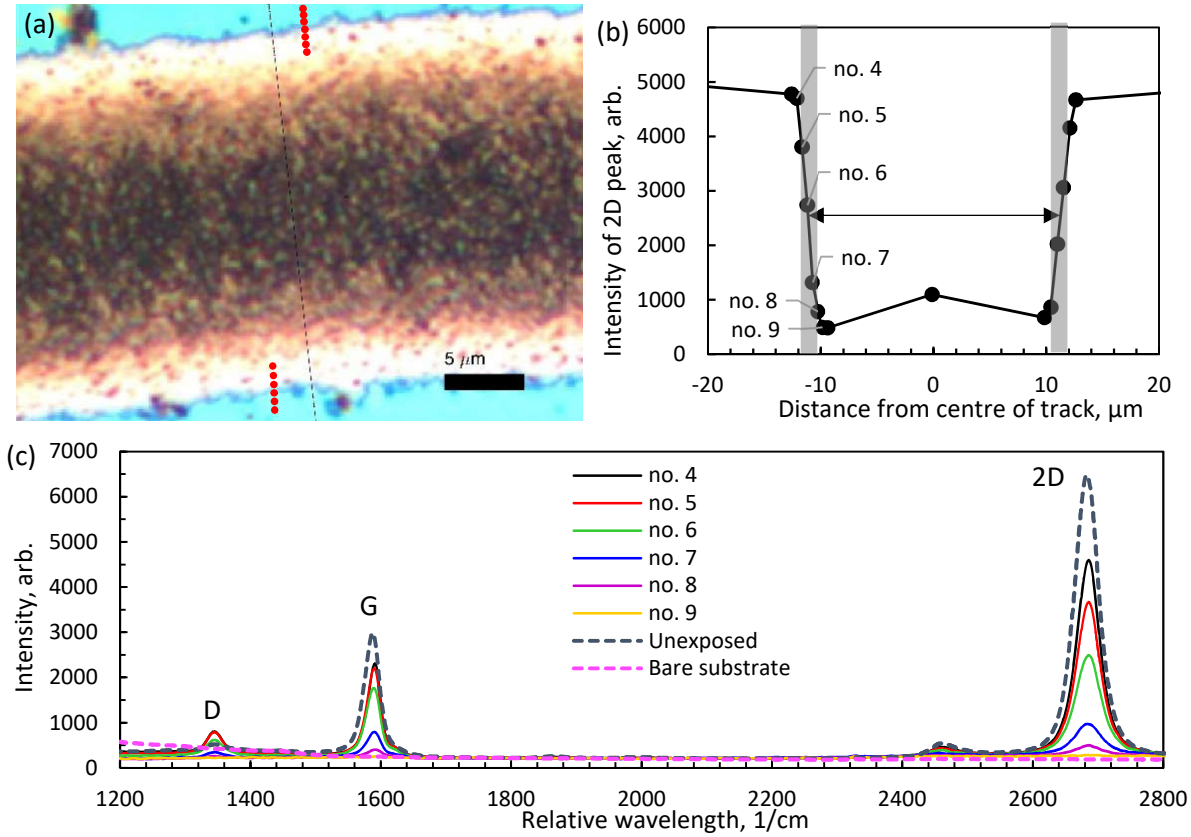

Figure 140: (a) Zoomed in optical microscope image of deposition on graphene done at 500 µm/s and peak fluence of 79 mJ/cm² along with points (red circles) where Raman analysis was done. (b) Peak 2D Raman intensity of those points against distance perpendicular to the track. (c) Raman spectrum at a few of those points. The arrow and greyed areas in the top right image were the width and width uncertainty of the track measured using the optical microscope.

Figure 141 (a) shows the zoomed optical microscope image of the track deposited on graphene at 1500 µm/s scan speed and 92 mJ/cm² peak fluence along with points where Raman analysis was done. Figure 141 (b) shows the 2D peak intensity of those points against distance perpendicular to the deposited track. The arrow in the chart is the width of the deposited track measured from the optical microscope image. Figure 141 (c) shows the Raman spectrum of a few of those points. Similar to Figure 140, Figure 141 show that up until the deposited track, graphene with a slightly higher D peak was detected indicating good contact with the deposited tungsten. The increase in the D peak compared to

the unexposed graphene sampled indicated an increase in edges (Cançado et al., 2004) and/or defects (Lucchese et al., 2010).

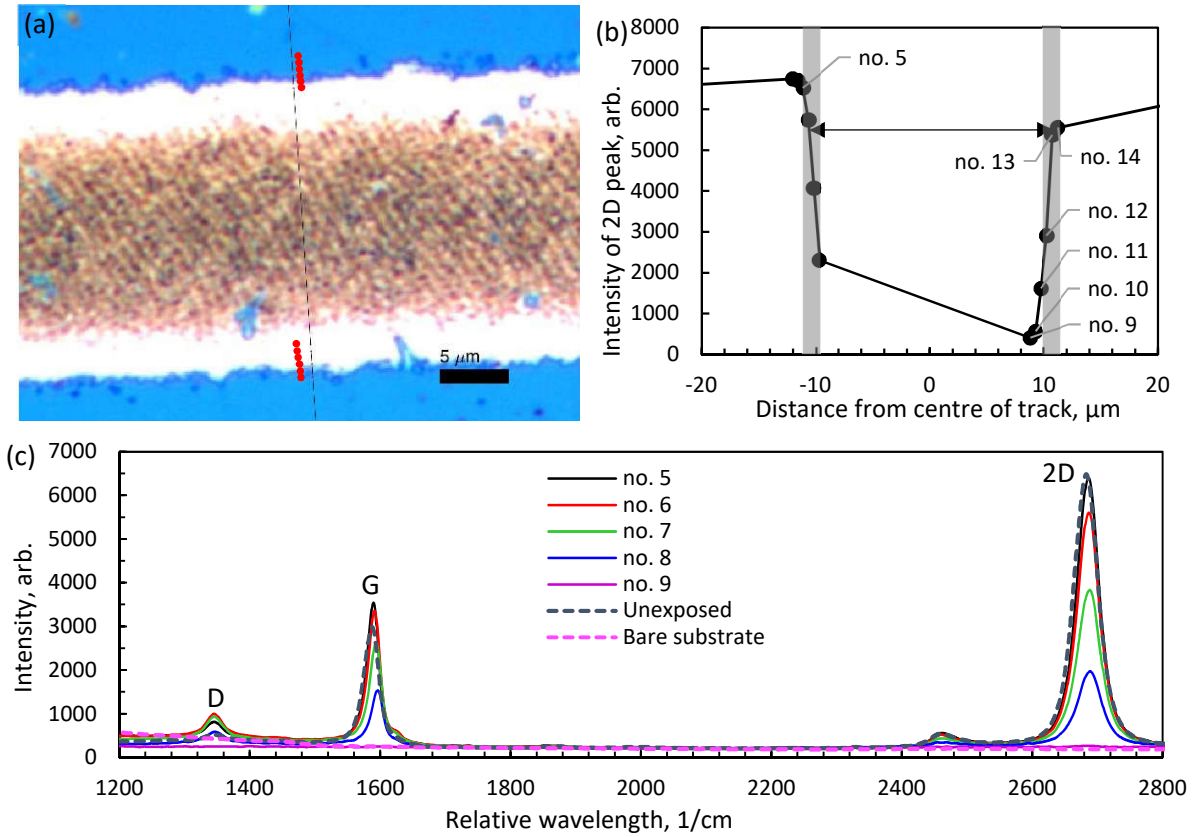

Figure 141: (a) Zoomed in optical microscope image of deposition on graphene done at 1500 μm/s and peak fluence of 92 mJ/cm^2 along with points (red circles) where Raman analysis was done. (b) Peak 2D Raman intensity of those points against distance perpendicular to the track. (c) Raman spectrum at a few of those points. The arrow and greyed areas in the top right image were the width and width uncertainty of the track measured using the optical microscope.

6.4 Condition of graphene under deposited tungsten

To understand the nature of the graphene-metal contact, it was necessary to examine the condition of the graphene under the deposited tungsten. Tungsten can be dissolved in hydrogen peroxide (Yang et al., 2015) within minutes. Multi-layer graphene on nickel substrates and transmission electron microscopy grids were degraded by hydrogen peroxide only after 10-25 hours of exposure (Xing et al., 2014). Thus, there was a possibility to dissolve the deposited tungsten while negligibly damaging the underlying graphene. A controlled experiment was done to understand the effects of hydrogen peroxide on the single layer graphene on SiO_2/Si sample used in this study. Figure 142 shows the Raman spectrum of a graphene sample left in air and the Raman spectrum of a graphene sample exposed to 30 wt% hydrogen peroxide for one hour then blown dry. There were no significant differences between the carbon D and G peaks, and there was a slight improvement in the 2D peak showing that the one hour exposure to hydrogen peroxide did not degrade the graphene.

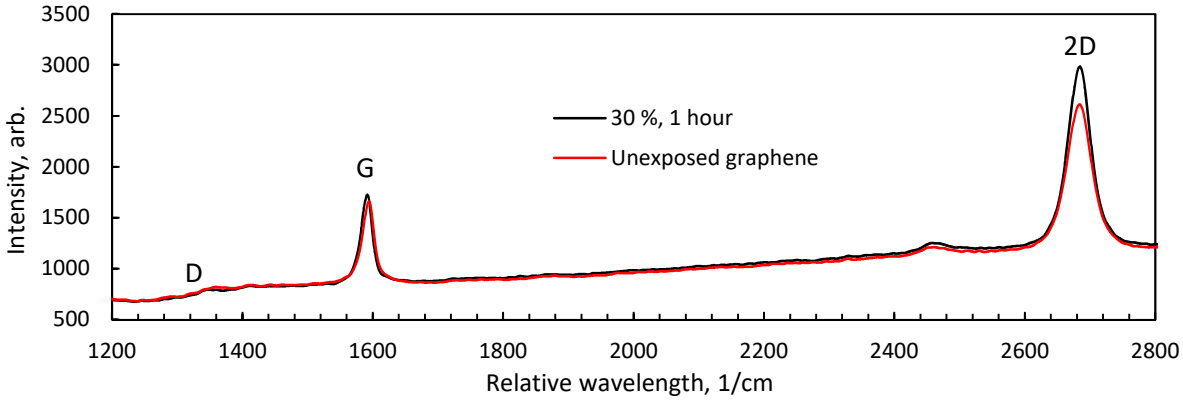

Figure 142: Raman spectrum of graphene on SiO_2/Si substrate that was dipped in 30 wt% H_2O_2 for 1 hour and another that was left in air.

Figure 143 shows the intensity of the 2D Raman peak against distance perpendicular to the track on the graphene sample with no tungsten deposition, with tungsten deposition and with the tungsten deposition removed by H_2O_2 . The sample scanned a speed of 500 µm/s with peak fluence of 79 mJ/cm^2 on the left and the sample scanned at 1500 µm/s and 92 mJ/cm^2 on the right. As mentioned in section 6.2, the graphene was damaged but not removed in the sample that had no precursor for deposition. However, after removing the deposited tungsten track, no graphene was detected under the track. The trough in the Raman 2D peak intensity against distance graph for the sample with deposition and with the deposition removed were similar.

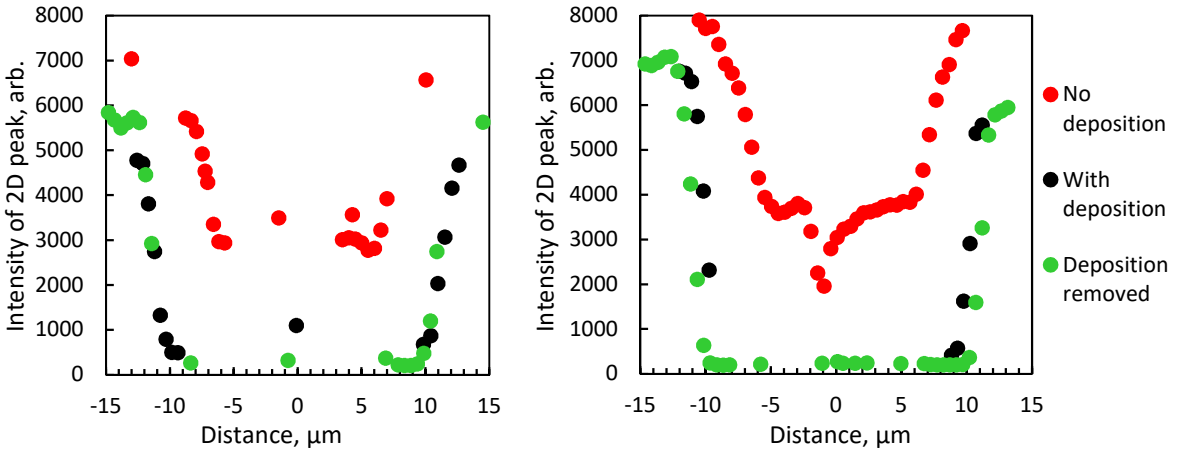

Figure 143: Intensity of 2D peak of Raman spectrum against distance perpendicular to the track where there was no deposition, with deposition and with deposition removed for a scanning speed of 500 µm/s and peak fluence of 79 mJ/cm^2 (left) and 1500 µm/s at 92 mJ/cm^2 (right).

Tungsten carbide has been reported to dissolve in hydrogen peroxide (Nakajima et al., 1999) and there was a possibility that the graphene under the deposited tungsten track reacted with the tungsten to form tungsten carbide. No tungsten carbide peaks were found from the Raman spectrum of the tungsten track. However, this may be due to the low tungsten carbide yield from the single layer graphene or the Raman signal blocked by the thick tungsten layer above. In another sample where tungsten was deposited on a drop-casted multi-layer reduced graphene oxide sample, tungsten carbide peaks at 709 and 806 cm^{-1} were detected (Figure 144). No peak tungsten carbide peaks were seen in the area outside the deposited track. As the laser power was increased, the tungsten carbide signal got weaker and disappeared likely because the tracks were thicker.

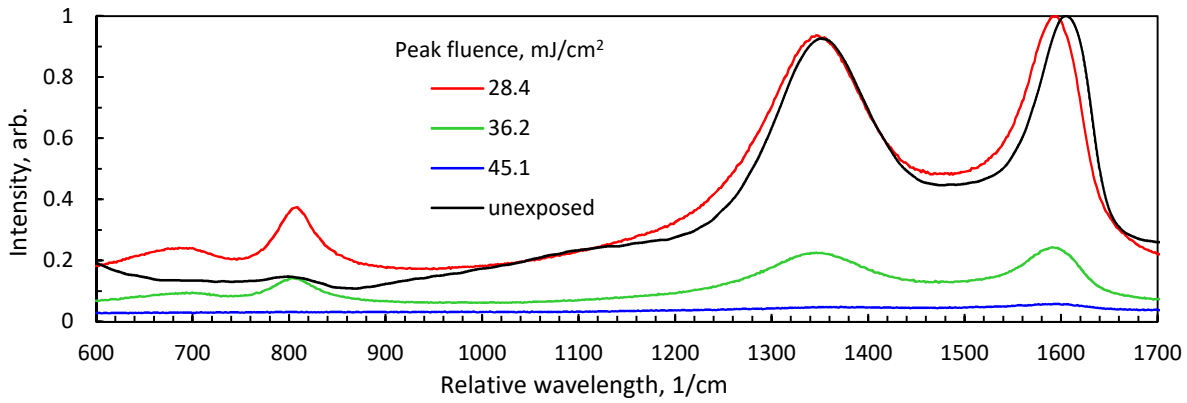

Figure 144: Raman spectrum of tungsten thin film deposited on reduced graphene oxide coated sample showing tungsten carbide peaks at 709 and 806 cm^{-1} (Yan et al., 2013).

6.5 Graphene tungsten contact resistance

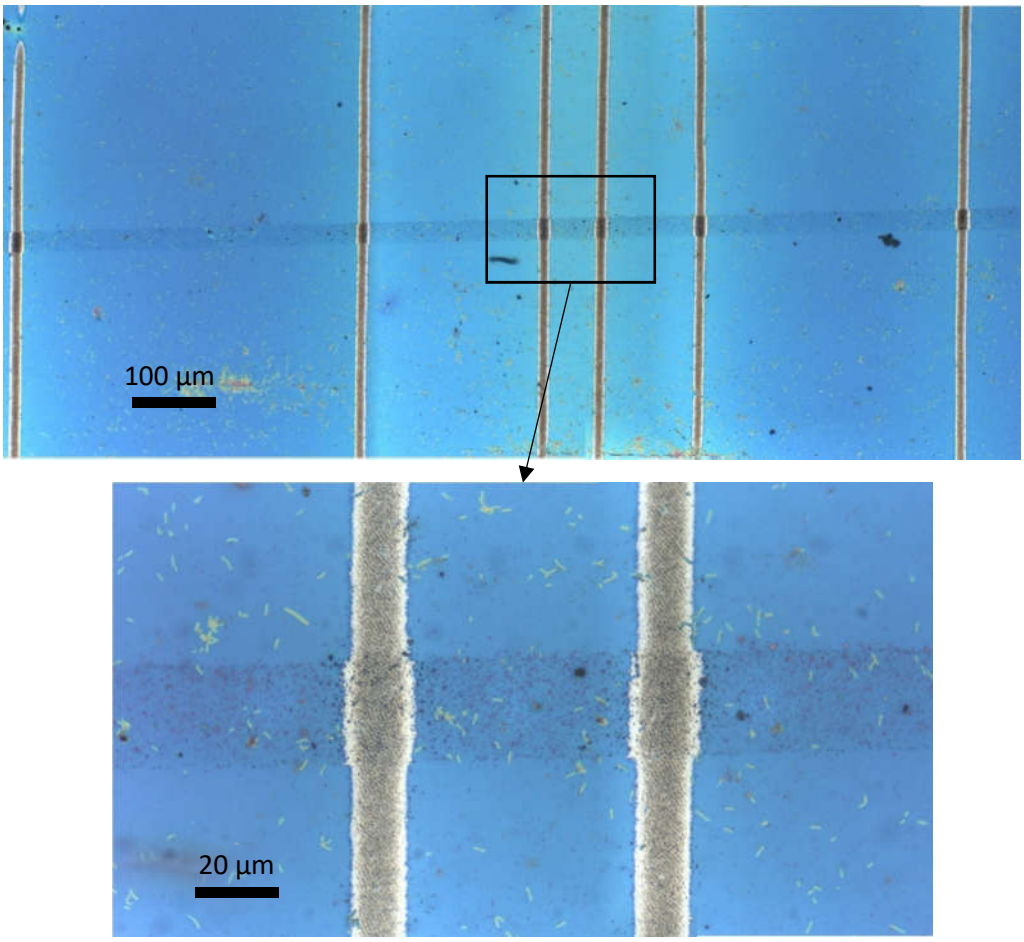

Figure 145: Optical images (top) and zoomed inset (bottom) of ultrafast LCVD tungsten tracks across the graphene strip. The tungsten tracks were deposited at 1500 µm/s scanning speed and 92 mJ/cm^2 peak pulse fluence. These tracks were used to measure the contact resistance between tungsten and graphene through the transfer length method and four-point probe method.

Another method of analysing the contact between the graphene and deposited metal was to measure the electrical contact resistance between them. Two strips of graphene were patterned to a width of approximately 20 µm based on the parameters described in section 6.1. Next, the laser was used to deposit tungsten tracks perpendicular to the graphene strip. One sample was scanned at a speed of

500 µm/s and peak fluence of 79 mJ/cm^2 (setting 1), while the other sample was scanned at 1500 µm/s and peak fluence of 92 mJ/cm^2 (setting 2). Figure 145 shows the sample with the tungsten deposited at speed of 1500 µm/s. Due to the lower deposition threshold on the graphene compared to the ablated graphene surface mentioned in section 6.3, the tungsten track on graphene was wider.

Due to the higher deposition threshold and thus a lower width on the ablated graphene surface, the resistance per unit length of deposited track would be lower compared to the electrical measurements made in the previous chapter. To obtain accurate values, the track resistance was measured on samples where the graphene was completely ablated from the surface. Table 29 shows the electrical measurement results of those tracks. The track written at the lower speed of 500 µm/s would have created a thicker tungsten track based on the study in the previous chapter, thus the expected resistance per unit length was lower. The contact resistance between the track and the silver paste pad were low (<12 Ω) for both tracks.

Table 29: Electrical resistance measurements of tungsten tracks on the ablated graphene surface.

Setting	Scan speed, µm/s	Peak pulse fluence, mJ/cm^2	Peak pulse power, ×10^{11} W/cm^2	Resistance per unit length, Ω/mm	Contact resistance, Ω
1	500	79	2.64	193±6	12±1
2	1500	92	3.08	756±38	2±6

The electrical resistance between the graphene and deposited tracks were then measured. Figure 146 shows graphs of electrical resistance measurements against length per unit width of the graphene strip for both settings. The original measurements of the track resistance were corrected to account for the tungsten track lengths and electrical properties mentioned in Table 29. The correction for the tungsten track written at 1500 µm/s speed was larger due to the higher track resistance per unit length of the track at that setting.

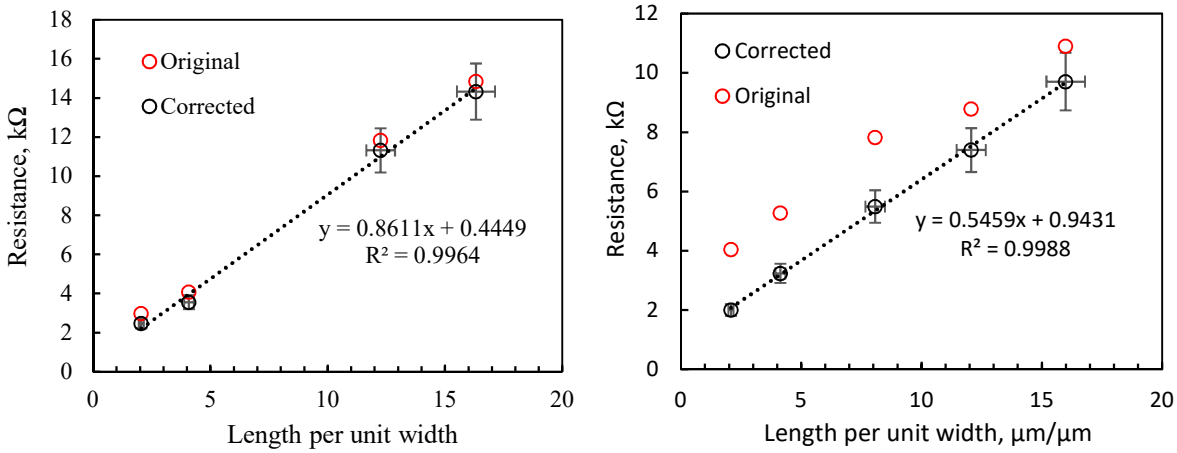

Figure 146: Resistance against length per unit graphene strip width for the tungsten tracks written at 500 µm/s speed and 79 mJ/cm^2 peak fluence (left) and 1500 µm/s and 92 mJ/cm^2 (right). The original measurements were corrected based on the tungsten track length and tungsten track resistance values in Table 29.

Table 30 shows the electrical measurements for the contact between the tungsten and graphene for both tungsten write settings and using both TLM and four-point probe method. The average sheet resistance measured for the graphene was 558±27 and 641±26 Ω per square for the writing speed of 500 and

1500 µm/s respectively. These were close to the 670 Ω per square value measured using Au/Pd contacts deposited through electron beam lithography (Peng et al., 2015). The average contact resistance of the graphene and tungsten metal was measured to be 14±1 and 4.3±0.4 kΩ µm for the writing speed of 500 and 1500 µm/s respectively. The higher writing speed produced lower contact resistance. These values were close to the contact resistance between nickel and graphene at 9.3±1.0 kΩ µm (Politou et al., 2015) where nickel carbide was formed at the contact. However, these contact resistance values were larger compared to noble metal-graphene contacts such as palladium at 2.8±0.4 kΩ µm (Politou et al., 2015).

To ensure that the track resistance measurements were not affected by deposition outside the laser spot, a control study was done. The graphene on SiO_2/Si substrates for another two samples were completely ablated based on parameters in section 6.1. Next, tungsten was deposited in the configuration similar to that seen in Figure 145 using the two tungsten deposition settings in this chapter. Next, silver paste was painted at the edges of the tungsten tracks and once dried, the electrical resistance between the tracks were measured. All electrical measurements were two orders of magnitude higher (>1 MΩ) than the samples with the 20 µm graphene strip. These results showed that the electrical measurements in Figure 146 and Table 30 were due to the presence of the graphene strip and not due to the deposition outside the laser track or conduction through the SiO_2/Si substrate.

Table 30: Resistance results for the tungsten metal to graphene contact.

Setting	Scan speed, µm/s	Peak pulse fluence, mJ/cm^2	Measurement type	Resistivity, Ω per square	Contact resistance, kΩ µm
1	500	79	Transfer length method	861±103	4±5
1	500	79	Four-point probe joint 2-3	474±35	19±2
1	500	79	Four-point probe joint 3-4	651±48	13±2
Inverse variance weighted average				558±27	14±1
2	1500	92	Transfer length method	546±62	12±2
2	1500	92	Four-point probe joint 2-3	642±47	7±1
2	1500	92	Four-point probe joint 3-4	693±51	7±1
2	1500	92	Four-point probe joint 4-5	650±48	3.0±0.4
Inverse variance weighted average				641±26	4.3±0.4

6.6 Summary

In literature, photolithography and metal evaporation are typically used to pattern and deposit metal on graphene. In this chapter, an alternative fabrication route using ultrafast lasers for patterning and metal deposition on graphene was explored.

Graphene grown on copper catalyst films and transferred to SiO_2/Si substrates required patterning to create shapes compatible with the electrical contact measurements. The ablation threshold of graphene on SiO_2/Si substrates was determined to be 57±8 mJ/cm^2 using a 300 fs, 33 µm laser spot with a pulse repetition rate of 5 kHz and scanning speed of 12.5 mm/s. The track width produced by using a peak fluence of 134 mJ/cm^2 (lower than SiO_2/Si ablation threshold at 161±39 mJ/cm^2) was 18±1 µm which

translated to a graphene area removal rate of 225,000±12,500 $\mu m^2/s$ (nearly two orders of magnitude higher than previously reported results Dong et al., 2016). By scanning the tracks one after the other at that fluence setting at a hatch spacing of 10 µm (44.4 % overlap), large area graphene removal was possible and a 5 mm long 20 µm wide graphene strip was patterned on the SiO_2/Si substrate. Raman analysis on the graphene from the single ablation tracks and the remaining graphene strip showed a rise in the D peak compared to the unexposed graphene and a decrease in the 2D to G peak ratio. The rise in the D peak was due to the increase in the presence of graphene edges (Cançado et al., 2004) and/or defects (Lucchese et al., 2010). While the decrease in the 2D to G peak ratio intensity indicated that the graphene was slightly doped after the laser ablation process (Beams et al., 2015).

For the pulse repetition rate of 500 kHz used in the ultrafast LCVD of tungsten, the graphene was not ablated but detected via Raman in the middle of the track. Compared to the pristine graphene, in the middle of the track the graphene had more edges and/or defects as identified by the Raman signal. The damage threshold for the graphene was estimated to be less than 53±7 and 59±9 mJ/cm^2 for a laser scanning speed of 500 and 1500 µm/s respectively. The tungsten deposition threshold on the unablated graphene surface was 30±6 and 34±7 mJ/cm^2 at scan speed of 500 and 1500 µm/s respectively. For both scan speeds, the deposition threshold on clean SiO_2/Si was lowest, followed by on graphene and the deposition threshold on ablated graphene was the highest. Two tungsten deposition settings were tested on graphene: (setting 1) 500 µm/s scan speed with 79 mJ/cm^2 peak fluence and (setting 2) 1500 µm/s scan speed with 92 mJ/cm^2 peak fluence. For both deposition settings, Raman analysis just outside the edge of the deposited track showed presence of graphene. After dissolving the tungsten with hydrogen peroxide, which was proven to not affect the graphene, no graphene was found under the tungsten track. Thus, the graphene likely reacted with the deposited tungsten to form tungsten carbide which does dissolve in hydrogen peroxide. The average contact resistance between the graphene deposited tungsten metal was measured to be 14±1 and 4.3±0.4 kΩ µm for settings 1 and 2 respectively. These values were close to the figures reported in literature for metal that formed carbides with graphene such nickel at 9.3±1.0 kΩ µm but higher than noble metals such as palladium at 2.8±0.4 kΩ cm.

Chapter 7 Conclusion and future work

The aim of this study as set out in section 1.2 was to investigate the feasibility of using pulsed ultrafast lasers for pyrolytic LCVD. For comparison, deposition using CW lasers using the same precursor was done. The novelty in the CW laser deposition was the usage of high power high wall plug efficiency laser diodes. Deposition using the pulsed ultrafast lasers were possible on various substrates including SS304, SiO_2/Si, glass and polymers. An application that was explored for the pulsed ultrafast laser was the deposition of tungsten metal contacts on graphene. In this chapter, the conclusions are highlighted and suggestions for future work directions are proposed.

7.1 Continuous wave LCVD conclusions

In the CW LCVD chapter, the optimum substrate temperature and deposition pressure was established for the ultrafast pulsed laser experiments. The track with the lowest resistivity was also used as a comparison standard to the ultrafast laser deposition results. These are the conclusions drawn from that chapter.

- The microstructure of the CW LCVD of tungsten consisted of circular grains with diameters at the order of 100 nm to 1 μm. This morphology did not change with the laser scanning speed, substrate temperature, deposition pressure and laser power. However, the size of the grains increased with deposition pressure and temperature, leading to rougher and higher resistivity tracks.
- There was significant deposition outside the laser spot, this was thought to be due to deposition of partially broken-down precursors and by-products of the pyrolytic dissociation. Deposition outside the laser spot increased with deposition pressure and temperature.
- The lowest recorded as-deposited track resistivity achieved was 93±27 μΩ cm (16.6 times bulk tungsten resistivity) for the track deposited at a laser power of 350 mW, scan speed of 10 μm/s, deposition pressure of 0.5 mBar and substrate temperature of 100 °C. The volumetric deposition rate at these settings was 51.4 $\mu m^3/s$ .The tungsten purity measured through EDX in the middle of that track was 81.4 wt% with 13.7 wt% carbon and 4.9 wt% oxygen excluding the measured silicon content detected from the substrate. If a triangular deposition profile was assumed without counting the cross-section area due to deposition outside the laser spot as done by (Nambu et al., 1990), then the calculated resistivity would have been 5.6 times bulk tungsten which was within the 2-6 times bulk tungsten range reported by (Nambu et al., 1990).
- Through COMSOL simulations of the laser heating, the temperature at the laser spot was estimated to be 533 °C, which was slightly higher than the estimated temperature at the laser spot for the

parameters used by (Nambu et al., 1990) at 500 °C. This deposition temperature was high enough to deposit the low resistivity α-phase tungsten mentioned in literature.

- The usage of hydrogen instead of nitrogen gas as the background gas during the deposition did not change the deposition track geometry, microstructure morphology and amount of deposition outside the laser spot. However, by annealing in hydrogen at 650 °C for 30 mins, removal of the deposition outside the laser spot was achieved. Optical microscope images and EDX element analysis showed that the region outside the laser spot returned to the substrate composition levels after the annealing. The annealing process increased the tungsten purity from 83.3 % to 90.6 % (excluding silicon) and reduced the resistivity from 93±27 to 66±7 μΩ cm (16.6 to 11.7 times bulk tungsten resistivity). There was also a significant reduction in the contact resistance between the deposited tungsten track and the silver paste from 132±92 to 2±32Ω.
- When the laser was dwelled on the spot to create structures perpendicular to the substrate, the deposit grew from a thin layer, to a sphere, then a conical shape, a column and then a bulb-like shape as the deposition time increased. The change in morphology was attributed to the temperature distribution on the surface of the deposit during growth due to the higher diffusivity of tungsten compared with stainless steel.

7.2 Ultrafast LCVD conclusions

The deposition on SS304, SiO_2/Si, glass and polyimide film was studied in the ultrafast LCVD chapter. These are the conclusions from that chapter.

- The peak intensity in a ultrafast laser pulse enables high temperatures of up to 1500 °C at the laser spot while the immediate surrounding surface remains cool. However, the temperature inside the laser spot drops drastically after the laser pulse, dipping below the deposition threshold temperature of CVD experiments after a few nanoseconds. This deposition regime favours reactions that have a high deposition rates, high deposition temperatures and high ablation thresholds for the deposited material such as the deposition of tungsten using tungsten hexacarbonyl.
- Spot dwell experiments showed that on semiconductors and transparent glass surfaces, a thin film was first deposited and then on that thin film, quasi-periodic structures started to grow. On metallic surfaces, the quasi-periodic structures started to grow without the thin film.
- The orientation of the quasi-periodic structures was perpendicular to the linear polarization of the laser beam and cross-section images revealed significant branching in the structures.
- The lowest laser peak fluence for observable deposition when the laser was scanned at speed of 100 μm/s (η = 33,000) was 110 mJ/cm^2 peak fluence (3.70×10^{11} W/cm^2 intensity, 19 nJ pulse energy or 9.5 mW of average power). The ablation threshold of the SiO_2/Si substrate at this scanning speed was 174±71 mJ/cm^2.

- Elemental analysis of the deposits showed that the deposits were up to 90 wt% tungsten and there was insignificant tungsten deposition outside the laser spot.
- When the pulse repetition rate and scan speed was reduced to keep the same number of pulses per spot, the volumetric deposition rate did not drop in proportion to the frequency. This suggested that the deposition process was limited by the transport of the precursor to the deposition site and higher precursor pressure or flow-rates would increase the deposition rate.
- By increasing the laser spot size from 6.6 μm to 33 μm, the deposition threshold on SiO_2/Si substrate reduced and thin-film deposition was possible on the substrate without ablation. The lower threshold was attributed to the increase in energy per pulse for the same peak fluence when the spot size was increased.
- When the track was scanned multiple times, thin-film formation was favoured over the formation of quasi-periodic structures.
- The lowest resistivity measured for the thin-film tracks on SiO_2/Si substrates was 37±4 μΩ cm (6.7 times the bulk resistivity of tungsten), which was lower than the 66±7 μΩ cm (11.7 times bulk resistivity of tungsten) achieved in the annealed deposited track of the 405 nm CW laser diode.
- For transparent glass surfaces, besides deposition on the top surface, it was possible to focus the laser through the glass substrate to cause deposition at the bottom surface.
- For polyimide films, deposition of quasi-periodic structures was possible at a scanning speed of 30 μm/s. The deposition threshold of 37±13 mJ/cm^2 was lower than the ablation threshold of the material at 67±15 mJ/cm^2.
- Dwelling the laser on a spot longer than one second created porous towers due to growth of the quasi-periodic structures. The porous towers grew up to an aspect ratio of four. From then on, the tower growth continued through non-porous deposition. This was thought to be due to significant growth in between the laser pulses because the aspect ratio prevents the top temperature from cooling below the threshold deposition temperature.
- By moving the laser spot at 3 μm/s upwards in the z-direction, tall columns with height of 190 μm, diameter of 20 μm and aspect ratio of 9.5 were made. By moving the laser spot 2 μm/s at a tilt of 14° from the vertical, tilted towers were grown. These tilted columns could be combined to form more complex structures.

7.3 Ultrafast LCVD on graphene conclusions

One application of the pulsed ultrafast LCVD of tungsten was explored in this study. Here are the conclusions of the experiments.

- Graphene grown on copper catalyst films and transferred to SiO_2/Si substrates required patterning to create shapes compatible with the electrical contact measurements. The ablation threshold of graphene on SiO_2/Si substrates was determined to be 57±8 mJ/cm^2 using a 300 fs, 33 μm laser spot

with a pulse repetition rate of 5 kHz and scanning speed of 12.5 mm/s. The track width produced by using a peak fluence of 134 mJ/cm^2 (lower than SiO_2/Si ablation threshold at 161±39 mJ/cm^2) was 18±1 μm which translated to a graphene removal area of 225,000±12,500 μm^2/s (nearly two orders of magnitude higher than previously reported results Dong et al., 2016).

- By scanning the tracks one after the other at that fluence setting at a hatch spacing of 10 μm (44.4 % overlap), large area graphene removal was possible and a 5 mm long 20 μm wide graphene strip was patterned on the SiO_2/Si substrate.
- Raman analysis on the graphene from the single ablation tracks and the remaining graphene strip showed a rise in the D peak compared to the unexposed graphene and a decrease in the 2D to G peak ratio. The rise in the D peak was due to the increase in the presence of graphene edges (Cançado et al., 2004) and/or defects (Lucchese et al., 2010). While the decrease in the 2D to G peak ratio intensity indicated that the graphene was slightly doped after the laser ablation process (Beams et al., 2015).
- For the laser parameters used in the ultrafast LCVD of tungsten (500 μm/s scan speed and 79 mJ/cm^2 peak fluence or 1500 μm/s and 92 mJ/cm^2), the graphene was not ablated but detected via Raman in the middle of the track. Compared to the pristine graphene, in the middle of the track the graphene had more edges and/or defects as identified by the Raman signal. The damage threshold for the graphene was estimated to be less than 53±7 and 59±9 mJ/cm^2 for a laser scanning speed of 500 and 1500 μm/s respectively.
- The tungsten deposition threshold on the unablated graphene surface was 30±6 and 34±7 mJ/cm^2 at scan speed of 500 and 1500 μm/s respectively, which was lower than the damage threshold. For both scan speeds, the deposition threshold on clean SiO_2/Si was the lowest, followed by on graphene and the deposition threshold on ablated graphene was the highest.
- Two tungsten deposition settings were tested on graphene: (setting 1) 500 μm/s scan speed with 79 mJ/cm^2 peak fluence and (setting 2) 1500 μm/s scan speed with 92 mJ/cm^2 peak fluence. For both deposition settings, Raman analysis up just outside the edge of the deposited track showed presence of graphene. After dissolving the tungsten with hydrogen peroxide, which was proven to not affect the graphene, no graphene was found under the tungsten track. Thus, the graphene likely reacted with the deposited tungsten to form tungsten carbide which does dissolve in hydrogen peroxide.
- The average resistivity of the graphene strip was measured to be 558±27 and 641±26 Ω per square for settings 1 and 2 respectively. The average contact resistance between the graphene deposited tungsten metal for setting 2 was measured to be 4.3±0.4 kΩ μm, while that of setting 1 was higher at 14±1 kΩ μm. These values were close to the values reported in literature for metals that formed carbides with graphene such nickel at 9.3±1.0 kΩ μm but higher than noble metals such as palladium at 2.8±0.4 kΩ cm.

7.4 Future work

This study focused on understanding the fundamentals of the pyrolytic ultrafast LCVD process. There were only sufficient resources to investigate one application of the technology, deposition of metal contacts to graphene. Potentially, there are numerous other suitable applications for the process. Besides applications, the usage of other precursors should also be investigated. By combining the tungsten precursor with a sulphur source, it may be possible to direct write tungsten disulphide which is a transition metal dichalcogenides (TMD).

7.4.1 Gaps in current work

Reduction or removal of the deposition outside the laser spot to achieve consistent large area thin-film deposition through hatching of multiple scan lines is important. This would enable one to make a large deposition area suitable for wire-bonding contacts or macro probes.

The deposition of tungsten on graphene produced electrical contact. Due to deposition outside the laser spot, the effect on graphene needs more study. Another step would be the manufacture and test of a field-effect graphene transistor using with the tungsten metal contacts deposited via ultrafast LCVD.

7.4.2 Investigation of other precursors

CW LCVD are not suitable for precursors that require a high temperature for deposition. This was due to the spreading of heat from the laser spot to the surrounding areas. However, there are recent developments in CVD precursors that require lower deposition temperatures and have not been investigated in LCVD. This include palladium hexafluoroacetylacetonato which has a thermal deposition temperature as low as 80 °C (Garcia and Goto, 2003). Preliminary results using this precursor showed promising results (Figure 147). However, the results were difficult to reproduce due to reactivity of the precursor with the hydrogen gas used as the reducing agent. The deposition was limited to the laser spot and there was no deposition seen outside the laser spot in the optical microscope image. This was likely due to the low laser power of 150 mW which was estimated to achieve a peak substrate temperature of 180 °C. The low deposition temperature would be suitable for deposition on polymers for direct writing onto flexible electronics in roll to roll productions systems.

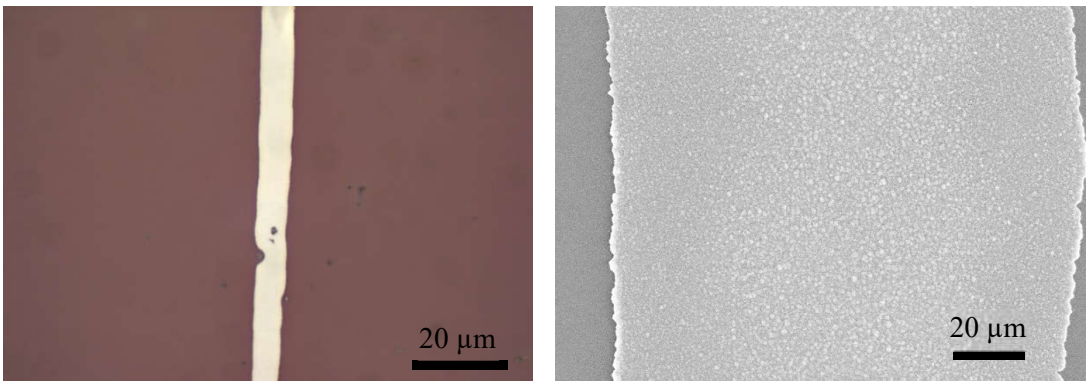

Figure 147: Optical (left) and (electron) microscope images of the deposition of palladium on SiO_2/Si substrate using the 405 nm CW laser diode with a laser power of 150 mW and scanning speed of 10 µm/s.

When the palladium hexafluoroacetylacetonato precursor was used in the ultrafast LCVD, the deposition consisted of nucleated grains that did not coalesce well with one another to form a smooth film (Figure 148). This was either due to the ultrafast LCVD process favouring high temperature dissociation precursors or the palladium that was deposited was ablated by the laser. Investigations with more precursors in both the CW and ultrafast lasers is needed to reveal the difference between them.

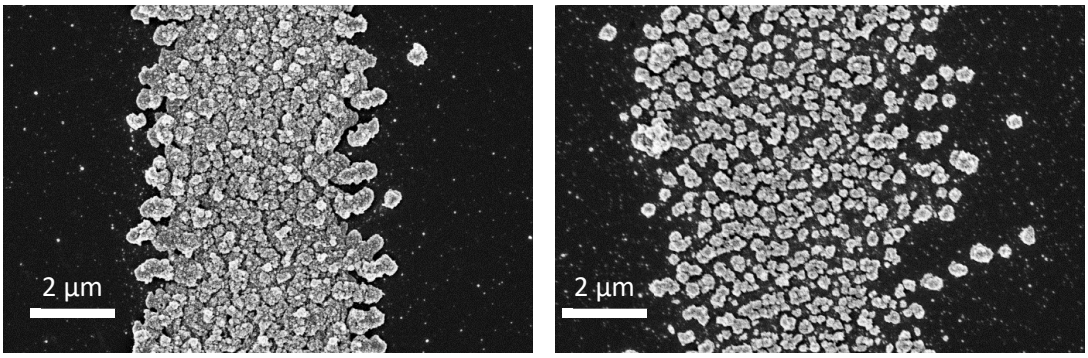

Figure 148: Ultrafast LCVD of palladium using palladium hexafluoroacetylacetonato at a scanning speed of 10 µm/s (left) and 100 µm/s (right).

7.4.3 Laser post-deposition treatment

Another topic that would be good to explore is the use of the laser for post-deposition treatment. In section 4.2.6, annealing in hydrogen was done in a furnace to reduce the resistivity of the CW LCVD track from 32 to 6 times bulk tungsten resistivity and reduce the deposition outside the track. Potentially, this annealing step can be done with the laser inside the deposition chamber with hydrogen gas. Besides annealing, the laser can also be used to ablate the high impurity deposition outside the laser spot and trim the tracks to increase the potential resolution of the deposition.

7.4.4 Other potential applications of tungsten ultrafast LCVD

One potential application of the process is for filling through silicon vias (TSV) with metal contacts in three-dimensional circuit integration (3DCI). 3DCI combines multiple planar circuit layers using TSVs (Garrou, 2012). The benefits of this include better electrical performance due to increased signal speed

and reduction in memory latency; lower power consumption and noise due to shorter wire lengths; smaller form factor; possible reduction in cost; and increase in functionality (Garrou et al., 2012). TSVs are made either during or after integrated circuit fabrication (Garrou and Bower, 2012). The holes for the TSVs are first made using either deep reactive ion etching techniques (Roozeboom et al., 2012) or laser ablation techniques (Lo and Chang, 2012). After drilling the holes, the walls of the hole needs to be passivated using dielectrics such as SiO_2 (Wieland, 2012) or parylene (Garrou and Bower, 2012). Then the TSVs are filled either using copper plating (Ritzdorf et al., 2012) or CVD of tungsten and copper (Klumpp et al., 2012). There is the opportunity to develop an integrated laser drilling and deposition system to fabricate the TSVs. First the silicon substrate is drilled using ultrafast lasers (Tan et al., 2009). Then the holes are passivated with a dielectric and filled with a conductor via LCVD. The tall columns built in section 5.6.2 would be promising in this area. This process may achieve a higher throughput and quality compared with high aspect ratio etching and deposition techniques.

Many fluidic devices control liquid and particle flow and sensing through electrical principles such as electrochemical- or impedance-based sensing, particle manipulation based on dielectrophoresis, electrokinetic separation, electroosmotic flow generation, and droplet manipulation by electrowetting (Temiz et al., 2015). Section 5.3 showed that it was possible to focus the laser on the bottom surface of a transparent medium (such as glass) for deposition on that surface. Thus, the ultrafast LCVD technique can be used to write conductive tracks inside hollow channels. This opens the technique for manufacture of electrical components for micro-fluidic devices.

Tungsten is one of the materials used in X-ray sources. The accuracy of X-ray micro-computed tomography scans depends on stable X-ray sources. If the X-ray source is small in size, better accuracy can be achieved (Zhou et al., 2016). Ultrafast LCVD may be used to deposit micro-scaled geometries of tungsten on transparent X-ray substrates.

Another potential application of the tungsten ultrafast LCVD is to take advantage of the nano-porosity of the quasi-periodic structures. These porous structures increase the surface area and may be functionalized with other materials. The large surface area holds potential as battery electrodes, large area surface catalyst, scaffolds for cell growth or even biological/chemical sensors.

7.4.5 Pyrolytic ultrafast synthesis of tungsten disulphide

An interesting usage of pyrolytic ultrafast LCVD is the synthesis of TMDs such as tungsten disulphide. TMDs are semiconductors of type MX_2 where M is the transition metal atom (such as Mo or W) and X is a chalcogen atom (such as S, Se, or Te) (Manzeli et al., 2017). Two dimensional TMDs have electronic bandgaps that graphene lacks. Interesting physical properties of TMDs include atomic scale thickness, direct bandgap, strong spin-orbit coupling and favourable electronic and mechanical properties. These properties are sort after for applications in high-end electronics, spintronics, optoelectronics, energy harvesting, flexible electronics, DNA sequencing and personalized medicine.

The main synthesis routes for TMDs are molecular beam epitaxy and CVD. Single layer form of this TMDs are most sort after because the absence of interlayer coupling plus the lack of inversion symmetry leads to optical and electronic properties that differ markedly from those of the bulk (Berkdemir et al., 2013). Single, double and triple layer and bulk tungsten disulphide can be differentiated through Raman analysis (Berkdemir et al., 2013).

A preliminary study was done to synthesize tungsten disulphide by depositing tungsten on substrates covered with sulphur flakes. Figure 149 shows the SEM image of the ultrafast tungsten LCVD on the sulphur flake placed on the SiO_2/Si substrate. The quasi-periodic structures observed in the ultrafast tungsten LCVD was not observed on the sulphur flake. Instead clumps of nanostructures were observed in the high-resolution SEM image.

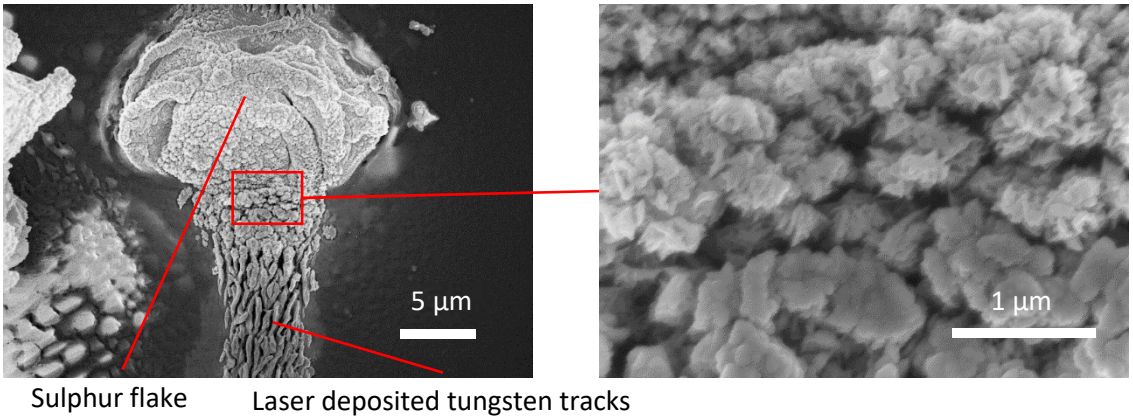

Figure 149: SEM images of the ultrafast tungsten LCVD track over a sulphur flake on the SiO_2/Si substrate.

Raman analysis was used to determine the composition of the product. Figure 150 shows the Raman spectrum on the ultrafast tungsten LCVD track on top of the sulphur flake. The sample produced was likely a three layer or thicker tungsten disulphide sample. The Raman spectrum on the sulphur flake but outside the ultrafast tungsten LCVD track only showed peaks of sulphur (Eder et al., 2014). These preliminary results showed that tungsten disulphide was successfully synthesized using ultrafast LCVD. There is an opportunity to explore replacing the sulphur solid flakes with a sulphur chemical vapour source such as dimethyl sulphide for direct writing of tungsten disulphide.

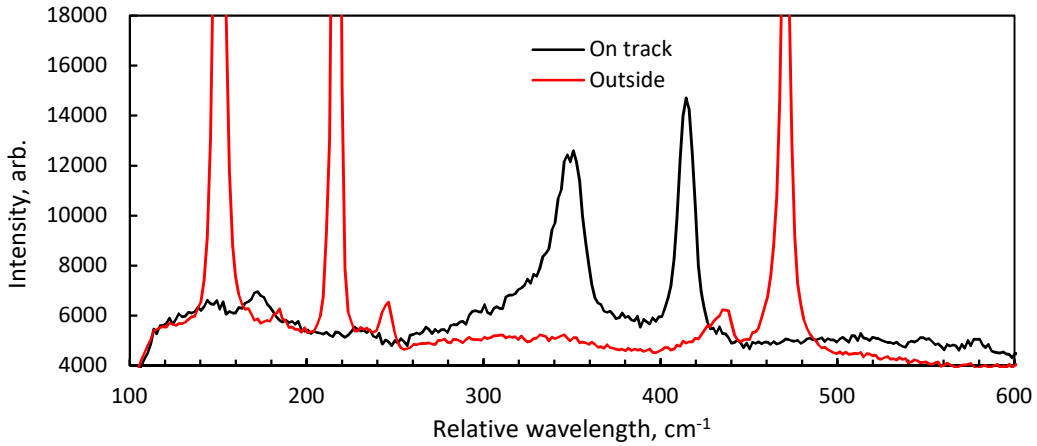

Figure 150: Raman spectrum on and outside the ultrafast tungsten LCVD using an excitation wavelength of 633 nm. A triple layer or thicker tungsten disulphide was detected in the Raman signal.

7.4.6 Nano lithography through ultrafast LCVD

In section 5.2.8, the sub-micron width line using the ultrafast LCVD was explored. The resolution of such lines would be limited by the size of the laser focus spot at approximately 500 nm. Sub-wavelength deposition features were observed in the quasi-periodic structures deposited using ultrafast LCVD. Recently, researchers have shown progress in controlling LIPSS produced through ultrafast laser ablation. For example, (Öktem et al., 2013) demonstrated the ability to control the non-linear feedback mechanism in LIPSS to stitch nano-structures seamlessly, enabling coverage of indefinitely large areas with sub-nanometre uniformity in periodicity. They first created these nano-structures on titanium dioxide and tungsten oxide substrates. Then went on to demonstrate the ability on stainless steel for tribological surfaces (Gnilitskyi et al., 2016) and on titanium for aligners for nematic liquid crystals (Pavlov et al., 2018). In these studies, the LIPSS created were done through ablation. Ultrafast LCVD can be employed to create uniform nanostructures through LIPSS deposition. Interference patterns on the surface of the substrate may also be further enhanced using spatial light modulators so that hologram patterns on the surface can be employed to create specific nanostructures through ultrafast deposition. Success in this area may reduce the cost of prototyping nano-structured devices and may be employed in developing qubits for quantum computers (Veldhorst et al., 2015), plasmonic pixels for next generation displays (James et al., 2016) (Duan et al., 2017) and molecule-specific nano-sensors (Im et al., 2014). In parallel, the production speed of non-linear laser lithography could potentially be increased so that this technology would be ready for high volume, high mix production of low-cost nano-devices.

References

Albrecht, A., Rivadeneyra, A., Abdellah, A., Lugli, P., Salmerón, J.F., 2016. Inkjet printing and photonic sintering of silver and copper oxide nanoparticles for ultra-low-cost conductive patterns. J. Mater. Chem. C 4, 3546–3554. https://doi.org/10.1039/C6TC00628K

Alexandrov, S.E., Hitchman, M.L., 2008. Chapter 12. Plasma Enhanced Chemical Vapour Deposition Processes, in: Jones, A.C., Hitchman, M.L. (Eds.), Chemical Vapour Deposition. Royal Society of Chemistry, Cambridge, pp. 494–534.

Allen, M.J., Tung, V.C., Kaner, R.B., 2010a. Honeycomb Carbon: A Review of Graphene. Chem. Rev. 110, 132–145. https://doi.org/10.1021/cr900070d

Allen, M.J., Tung, V.C., Kaner, R.B., 2010b. Honeycomb Carbon: A Review of Graphene. Chem. Rev. 110, 132–145. https://doi.org/10.1021/cr900070d

Allen, S.D., 1981. Laser chemical vapor deposition: A technique for selective area deposition. J. Appl. Phys. 52, 6501–6505. https://doi.org/10.1063/1.328600

Alm, O., 2007. Heterogeneous Photolytic Synthesis of Nanoparticles.

Alm, O., Carlsson, J.-O., Boman, M., 2005. Laser-assisted chemical vapor deposition of carbon coated cobalt nanoparticles, in: Symposium R – Assembly at the Nanoscale – Toward Functional Nanostructured Materials, MRS Online Proceedings Library. https://doi.org/10.1557/PROC-0901-Ra09-03

Au, M.-K., Hackett, P.A., Humphries, M., John, P., 1984. Infrared multiphoton dissociation of unsubstituted metal carbonyls at 5 μm. Appl. Phys. B 33, 43–49. https://doi.org/10.1007/BF00690024

Bado, P., Clark, W., Said, A., 2011. Micromachining Handbook [WWW Document]. Clark-MXR Inc. URL http://www.cmxr.com/Education/Introduction.html (accessed 3.18.14).

Balandin, A.A., Ghosh, S., Bao, W., Calizo, I., Teweldebrhan, D., Miao, F., Lau, C.N., 2008. Superior Thermal Conductivity of Single-Layer Graphene. Nano Lett. 8, 902–907. https://doi.org/10.1021/nl0731872

Baum, T.H., Comita, P.B., 1992. Laser-induced chemical vapor deposition of metals for microelectronics technology. Thin Solid Films 218, 80–94. https://doi.org/10.1016/0040-6090(92)90907-S

Baum, T.H., Comita, P.B., Larson, C.E., III, G.W.T., 1995. Laser interconnection of circuits on transparent substrate. US5407710 A.

Baum, T.H., Comita, P.B., Sr, J.R.L., Redmond, T.F., Wassick, T.A., Jackson, R.L., 1993. Laser-induced chemical vapor deposition of thin-film conductors. US5246745 A.

Beams, R., Cançado, L.G., Novotny, L., 2015. Raman characterization of defects and dopants in graphene. J. Phys. Condens. Matter 27, 083002. https://doi.org/10.1088/0953-8984/27/8/083002

Beard, M.C., Turner, G.M., Schmuttenmaer, C.A., 2000. Transient photoconductivity in GaAs as measured by time-resolved terahertz spectroscopy. Phys. Rev. B 62, 15764–15777. https://doi.org/10.1103/PhysRevB.62.15764

Bell, S.A., 2001. A beginner's guide to uncertainty of measurement. National Physical Laboratory, UK.

Ben-Yakar, A., Byer, R.L., 2004. Femtosecond laser ablation properties of borosilicate glass. J. Appl. Phys. 96, 5316–5323.

Berkdemir, A., Gutiérrez, H.R., Botello-Méndez, A.R., Perea-López, N., Elías, A.L., Chia, C.-I., Wang, B., Crespi, V.H., López-Urías, F., Charlier, J.-C., Terrones, H., Terrones, M., 2013. Identification of individual and few layers of WS_2 using Raman Spectroscopy. Sci. Rep. 3, srep01755. https://doi.org/10.1038/srep01755

Bonaccorso, F., Colombo, L., Yu, G., Stoller, M., Tozzini, V., Ferrari, A.C., Ruoff, R.S., Pellegrini, V., 2015. Graphene, related two-dimensional crystals, and hybrid systems for energy conversion and storage. Science 347, 1246501. https://doi.org/10.1126/science.1246501

Bonse, J., Baudach, S., Krüger, J., Kautek, W., Lenzner, M., 2002. Femtosecond laser ablation of silicon–modification thresholds and morphology. Appl. Phys. A 74, 19–25. https://doi.org/10.1007/s003390100893
Bonse, J., Höhm, S., Kirner, S., Rosenfeld, A., Krüger, J., 2017. Laser-induced Periodic Surface Structures (LIPSS) - A Scientific Evergreen. IEEE J. Sel. Top. Quantum Electron. 23, 900615. https://doi.org/10.1364/CLEO_SI.2016.STh1Q.3
Bonse, J., Krüger, J., 2010. Pulse number dependence of laser-induced periodic surface structures for femtosecond laser irradiation of silicon. J. Appl. Phys. 108, 034903. https://doi.org/10.1063/1.3456501
Boutros, K.S., Roberts, J.C., Bedair, S.M., 1996. Direct writing of GaAs optical waveguides by laser-assisted chemical vapor deposition. Appl. Phys. Lett. 68, 2041–2042. https://doi.org/10.1063/1.116296
Braeuninger-Weimer, P., Brennan, B., Pollard, A.J., Hofmann, S., 2016. Understanding and Controlling Cu-Catalyzed Graphene Nucleation: The Role of Impurities, Roughness, and Oxygen Scavenging. Chem. Mater. 28, 8905–8915. https://doi.org/10.1021/acs.chemmater.6b03241
Braichotte, D., Bergh, H. van den, 1987. Growth rates and electrical conductivity of microscopic ohmic contacts fabricated by laser chemical vapor deposition of platinum. Appl. Phys. A 44, 353–359. https://doi.org/10.1007/BF00624603
Branham, M.S., 2008. Semiconductors and sustainability : energy and materials use in integrated circuit manufacturing (Thesis). Massachusetts Institute of Technology.
Brueck, S.R.J., Ehrlich, D.J., 1982. Stimulated Surface-Plasma-Wave Scattering and Growth of a Periodic Structure in Laser-Photodeposited Metal Films. Phys. Rev. Lett. 48, 1678–1681. https://doi.org/10.1103/PhysRevLett.48.1678
Buividas, R., Mikutis, M., Juodkazis, S., 2014. Surface and bulk structuring of materials by ripples with long and short laser pulses: Recent advances. Prog. Quantum Electron. 38, 119–156. https://doi.org/10.1016/j.pquantelec.2014.03.002
Cancado, L.G., Beams, R., Novotny, L., 2008. Optical measurement of the phase-breaking length in graphene. ArXiv Prepr. ArXiv08023709.
Cançado, L.G., Pimenta, M.A., Neves, B.R.A., Dantas, M.S.S., Jorio, A., 2004. Influence of the Atomic Structure on the Raman Spectra of Graphite Edges. Phys. Rev. Lett. 93. https://doi.org/10.1103/PhysRevLett.93.247401
Cao, L.X., Feng, Z.C., Liang, Y., Hou, W.L., Zhang, B.C., Wang, Y.Q., Li, L., 1995. Laser chemical vapour deposition of TiN and TiC films. Thin Solid Films 257, 7–14. https://doi.org/10.1016/0040-6090(94)06343-5
Chang, M., 2014. Annual Report 2014 (Annual Report). Taiwan Semiconductor Manufacturing Company, Ltd.
Chapman, G.H., 2010. Silicon wafers: Basic unit [WWW Document]. URL http://www2.ensc.sfu.ca/~glennc/e495/e495l2j.pdf
Chen, C.J., 1987. Kinetic theory of laser photochemical deposition. J. Vac. Sci. Technol. A 5, 3386–3398. https://doi.org/10.1116/1.574201
Chen, Y.D., Reisman, A., Turlik, I., Temple, D., 1995. Cu CVD from Copper (II) Hexafluoroacetylacetonate I. A Cold Wall Reactor Design, Blanket Growth Rate, and Natural Selectivity. J. Electrochem. Soc. 142, 3903–3911.
Chichkov, B.N., Momma, C., Nolte, S., Alvensleben, F. von, Tünnermann, A., 1996. Femtosecond, picosecond and nanosecond laser ablation of solids. Appl. Phys. A 63, 109–115. https://doi.org/10.1007/BF01567637
Chu, T.-Y., Zhang, Z., Tao, Y., 2018. Printing Silver Conductive Inks with High Resolution and High Aspect Ratio. Adv. Mater. Technol. 3, 1700321. https://doi.org/10.1002/admt.201700321
Clark, R.L., Jr, R.N.D., 2001. Three dimensional micromachined electromagnetic device and associated methods. US6271802 B1.
Clean Room Technology, 2010. TSMC strats construction of Gigafab in Taiwan [WWW Document]. URL http://www.cleanroomtechnology.com/news/article_page/TSMC_starts_construction_of_Gigafab_in_Taiwan/56230
Cline, H.E., Anthony, T.R., 1977. Heat treating and melting material with a scanning laser or electron beam. J. Appl. Phys. 48, 3895–3900. https://doi.org/10.1063/1.324261

Coleman, H.W., Glenn Steele, W., 2009. Experimentation and uncertainty analysis for engineers, Third Edition. ed. New Jersey.
COMSOL, 2013. COMSOL Multiphysics Reference Manual.
Crank, J., Nicolson, P., 1996. A practical method for numerical evaluation of solutions of partial differential equations of the heat-conduction type. Adv. Comput. Math. 6, 207–226. https://doi.org/10.1007/BF02127704
Dean, J., Robert N., Nordine, P.C., Christodoulou, C.G., 1999. Novel method for fabricating 3D helical THz antennas directly on semiconductor substrates. pp. 67–77. https://doi.org/10.1117/12.347110
Denes, G., 2009. Design for Semiconductor Reliability [WWW Document]. URL http://www.ewh.ieee.org/r6/scv/rl/articles/Design%20for%20Semiconductor%20Reliability%20(01.12.09).ppt
Derrien, T.J., Sarnet, T., Sentis, M., Itina, T.E., 2011. Application of a two-temperature model for the investigation of the periodic structure formation on Si surface in femtosecond laser interaction. J. Optoelectron. Adv. Mater. 12, 610–615.
Deutsch, T.F., Ehrlich, D.J., Jr, R.M.O., 1979. Laser photodeposition of metal films with microscopic features. Appl. Phys. Lett. 35, 175–177. https://doi.org/10.1063/1.91026
Deutsch, T.F., Rathman, D.D., 1984. Comparison of laser-initiated and thermal chemical vapor deposition of tungsten films. Appl. Phys. Lett. 45, 623–625. https://doi.org/10.1063/1.95333
Dong, T., Sparkes, M., Durkan, C., O'Neill, W., 2016. Evaluating femtosecond laser ablation of graphene on SiO2/Si substrate. http://dx.doi.org/10.2351/1.4944510
Du, Y., Yang, L., Zhang, J., Liu, H., Majumdar, K., Kirsch, P.D., Ye, P.D., 2014. Field-Effect Transistors With Graphene/Metal Heterocontacts. IEEE Electron Device Lett. 35, 599–601. https://doi.org/10.1109/LED.2014.2313340
Duan, X., Kamin, S., Liu, N., 2017. Dynamic plasmonic colour display. Nat. Commun. 8, 14606. https://doi.org/10.1038/ncomms14606
Duty, C., Jean, D., Lackey, W.J., 2001. Laser chemical vapour deposition: materials, modelling, and process control. Int. Mater. Rev. 46, 271–287. https://doi.org/10.1179/095066001771048727
Duty, C., Johnson, R., Gillespie, J., Fedorov, A., Lackey, J., 2003. Heat and mass-transfer modeling of an angled gas-jet LCVD system. Appl. Phys. A 77, 697–705. https://doi.org/10.1007/s00339-002-1887-5
Eder, S.H.K., Gigler, A.M., Hanzlik, M., Winklhofer, M., 2014. Sub-Micrometer-Scale Mapping of Magnetite Crystals and Sulfur Globules in Magnetotactic Bacteria Using Confocal Raman Micro-Spectrometry. PLOS ONE 9, e107356. https://doi.org/10.1371/journal.pone.0107356
Ehrlich, D.J., Jr, R.M.O., Deutsch, T.F., 1982. Photodeposition of metal films with ultraviolet laser light. J. Vac. Sci. Technol. 21, 23–32. https://doi.org/10.1116/1.571724
Ehrlich, D.J., Osgood, R.M., Deutsch, T.F., 1981. Direct Writing of Refractory Metal Thin Film Structures by Laser Photodeposition. J. Electrochem. Soc. 128, 2039–2041. https://doi.org/10.1149/1.2127793
Ehrlich, D.J., Tsao, J.Y., 1983. A review of laser–microchemical processing. J. Vac. Sci. Technol. B 1, 969–984. https://doi.org/10.1116/1.582718
Escribano, R., Sloan, J.J., Siddique, N., Sze, N., Dudev, T., 2001. Raman spectroscopy of carbon-containing particles. Vib. Spectrosc. 26, 179–186. https://doi.org/10.1016/S0924-2031(01)00106-0
Feng, J., Li, W., Qian, X., Qi, J., Qi, L., Li, J., 2012. Patterning of graphene. Nanoscale 4, 4883–4899. https://doi.org/10.1039/C2NR30790A
Ferrari, A.C., Bonaccorso, F., Fal'ko, V., Novoselov, K.S., Roche, S., Bøggild, P., Borini, S., Koppens, F.H.L., Palermo, V., Pugno, N., Garrido, J.A., Sordan, R., Bianco, A., Ballerini, L., Prato, M., Lidorikis, E., Kivioja, J., Marinelli, C., Ryhänen, T., Morpurgo, A., Coleman, J.N., Nicolosi, V., Colombo, L., Fert, A., Garcia-Hernandez, M., Bachtold, A., Schneider, G.F., Guinea, F., Dekker, C., Barbone, M., Sun, Z., Galiotis, C., Grigorenko, A.N., Konstantatos, G., Kis, A., Katsnelson, M., Vandersypen, L., Loiseau, A., Morandi, V., Neumaier, D., Treossi, E., Pellegrini, V., Polini, M., Tredicucci, A., Williams, G.M., Hong, B.H., Ahn, J.-H., Kim, J.M., Zirath, H., Wees, B.J. van, Zant, H. van der, Occhipinti, L., Matteo, A.D., Kinloch, I.A., Seyller, T., Quesnel, E., Feng, X., Teo, K., Rupesinghe, N., Hakonen, P., Neil, S.R.T., Tannock, Q., Löfwander, T., Kinaret, J., 2015. Science and technology roadmap for graphene,

related two-dimensional crystals, and hybrid systems. Nanoscale 7, 4598–4810. https://doi.org/10.1039/C4NR01600A
Ferrari, A.C., Meyer, J.C., Scardaci, V., Casiraghi, C., Lazzeri, M., Mauri, F., Piscanec, S., Jiang, D., Novoselov, K.S., Roth, S., Geim, A.K., 2006. Raman Spectrum of Graphene and Graphene Layers. Phys. Rev. Lett. 97, 187401. https://doi.org/10.1103/PhysRevLett.97.187401
Filmetrics Inc, 2015. Refractive index database.
Fischer, J., Wegener, M., 2011. Three-dimensional direct laser writing inspired by stimulated-emission-depletion microscopy [Invited]. Opt. Mater. Express 1, 614–624. https://doi.org/10.1364/OME.1.000614
Foresight, 2013. Future of manufacturing: a new era of opportunity and challenge for the UK. The Government Office for Science, London.
Fowlkes, J.D., Rack, P.D., 2010. Fundamental Electron-Precursor-Solid Interactions Derived from Time-Dependent Electron-Beam-Induced Deposition Simulations and Experiments. ACS Nano 4, 1619–1629. https://doi.org/10.1021/nn901363a
Franklin, A.D., Han, S., Bol, A.A., Perebeinos, V., 2012. Double Contacts for Improved Performance of Graphene Transistors. IEEE Electron Device Lett. 33, 17–19. https://doi.org/10.1109/LED.2011.2173154
Gao, L., Härter, P., Linsmeier, C., Gstöttner, J., Emling, R., Schmitt-Landsiedel, D., 2004. Metalorganic chemical vapor deposition of silver thin films for future interconnects by direct liquid injection system. Mater. Sci. Semicond. Process., Papers presented at the E-MRS 2004 Spring Meeting Symposium C: New Materials in Future Silicon Technology 7, 331–335. https://doi.org/10.1016/j.mssp.2004.09.128
Garcia, J.R.V., Goto, T., 2003. Chemical Vapor Deposition of Iridium, Platinum, Rhodium and Palladium. Mater. Trans. 44, 1717–1728. https://doi.org/10.2320/matertrans.44.1717
Garrou, P., 2012. Introducton to 3D Integration, in: Handbook of 3D Integration. Wiley-VCH Verlag GmbH & Co. KGaA, Weinheim, Germany.
Garrou, P., Bower, C., 2012. Overview of 3D Integration Process Technology, in: Handbook of 3D Integration. Wiley-VCH Verlag GmbH & Co. KGaA, Weinheim, Germany.
Garrou, P., Vitkavage, S., Arkalgud, S., 2012. Drivers for 3D Integration, in: Handbook of 3D Integration. Wiley-VCH Verlag GmbH & Co. KGaA.
Gattass, R.R., Mazur, E., 2008. Femtosecond laser micromachining in transparent materials. Nat. Photonics 2, 219–225. https://doi.org/10.1038/nphoton.2008.47
Gilgen, H.H., Cacouris, T., Shaw, P.S., Krchnavek, R.R., Osgood, R.M., 1987. Direct writing of metal conductors with near-uv light. Appl. Phys. B 42, 55–66. https://doi.org/10.1007/BF00694811
Giubileo, F., Di Bartolomeo, A., 2017. The role of contact resistance in graphene field-effect devices. Prog. Surf. Sci. 92, 143–175. https://doi.org/10.1016/j.progsurf.2017.05.002
Gnilitskyi, I., Rotundo, F., Martini, C., Pavlov, I., Ilday, S., Vovk, E., Ilday, F.Ö., Orazi, L., 2016. Nano patterning of AISI 316L stainless steel with Nonlinear Laser Lithography: Sliding under dry and oil-lubricated conditions. Tribol. Int. 99, 67–76. https://doi.org/10.1016/j.triboint.2016.03.011
Goldstein, J., Newbury, D.E., Joy, D.C., Lyman, C.E., Echlin, P., Sawyer, L., Michael, J.R., 2003. Scanning Electron Microscopy and X-ray Microanalysis, Third Edition. ed. Springer US, New York, NY.
Grant-Jacob, J.A., Mills, B., Feinaeugle, M., Sones, C.L., Oosterhuis, G., Hoppenbrouwers, M.B., Eason, R.W., 2013. Micron-scale copper wires printed using femtosecond laser-induced forward transfer with automated donor replenishment. Opt. Mater. Express 3, 747. https://doi.org/10.1364/OME.3.000747
Green, M., Her, T.-H., 2013. On the role of laser heating and adatom diffusion in femtosecond laser induced tungsten nanogratings, in: Synthesis and Photonics of Nanoscale Materials X. Presented at the Proc. of SPIE 2013, pp. 86090M1-7. https://doi.org/10.1117/12.2005682
Green, N.S., Norton, M.L., 2015. Interactions of DNA with graphene and sensing applications of graphene field-effect transistor devices: A review. Anal. Chim. Acta 853, 127–142. https://doi.org/10.1016/j.aca.2014.10.023
Griffin, G.L., Maverick, A.W., 1994. CVD of Copper from Cu(II) Precursors, in: Kodas, T.T., Hampden-Smith, rk J. (Eds.), The Chemistry of Metal CVD. Wiley-VCH Verlag GmbH, pp. 175–238.
GWI, 2009. Global Water Intelligence Magazine. Glob. Water Intell. 10.

Haight, R., Longo, P., Wagner, A., 2003. Metal deposition with femtosecond light pulses at atmospheric pressure. J. Vac. Sci. Technol. A 21, 649–652. https://doi.org/10.1116/1.1564026
Han, J., Jensen, K.F., 1994. Combined experimental and modeling studies of laser-assisted chemical vapor deposition of copper from copper(I)-hexafluoroacetylacetonate trimethylvinylsilane. J. Appl. Phys. 75, 2240–2250. https://doi.org/10.1063/1.356287
Han, J., Jensen, K.F., Senzaki, Y., Gladfelter, W.L., 1994. Pyrolytic laser assisted chemical vapor deposition of Al from dimethylethylamine-alane: Characterization and a new two-step writing process. Appl. Phys. Lett. 64, 425–427. https://doi.org/10.1063/1.111119
Handy, J., 2014. Why Are Computer Chips So Expensive? [WWW Document]. Forbes. URL http://www.forbes.com/sites/jimhandy/2014/04/30/why-are-chips-so-expensive/ (accessed 8.12.15).
Harrison, S., Marcus, H.L., 1999. Gas-phase selective area laser deposition (SALD) joining of SiC. Mater. Des. 20, 147–152.
Hartung, J., Knapp, G., Sinha, B.K., 2008. Statistical meta-analysis with applications, Wiley series in probability and statistics. Wiley, Hoboken, N.J.
He, M., Lu, T.-M., 2012. Metal–Dielectric Diffusion Processes: Fundamentals, in: Metal-Dielectric Interfaces in Gigascale Electronics. Springer New York, New York, NY, pp. 11–22. https://doi.org/10.1007/978-1-4614-1812-2_2
Hitosugi, T., Mizuno, T., 2005. Femtosecond-Laser-Assisted Chemical Vapor Deposition of Cr Metal. Jpn. J. Appl. Phys. 44, L596–L598. https://doi.org/10.1143/JJAP.44.L596
Houle, F.A., Jones, C.R., Baum, T., Pico, C., Kovac, C.A., 1985. Laser chemical vapor deposition of copper. Appl. Phys. Lett. 46, 204–206. https://doi.org/10.1063/1.95685
Huang, M., Zhao, F., Cheng, Y., Xu, N., Xu, Z., 2009. Origin of Laser-Induced Near-Subwavelength Ripples: Interference between Surface Plasmons and Incident Laser. ACS Nano 3, 4062–4070. https://doi.org/10.1021/nn900654v
Im, H., Shao, H., Park, Y.I., Peterson, V.M., Castro, C.M., Weissleder, R., Lee, H., 2014. Label-free detection and molecular profiling of exosomes with a nano-plasmonic sensor. Nat. Biotechnol. 32, 490–495. https://doi.org/10.1038/nbt.2886
ITRS, 2013. International Technology Roadmap for Semiconductors 2013.pdf (Executive summary). ITRS.
James, T.D., Mulvaney, P., Roberts, A., 2016. The Plasmonic Pixel: Large Area, Wide Gamut Color Reproduction Using Aluminum Nanostructures. Nano Lett. 16, 3817–3823. https://doi.org/10.1021/acs.nanolett.6b01250
Janz, S., 2004. Silicon-Based Waveguide Technology for Wavelength Division Multiplexing, in: Silicon Photonics, Topics in Applied Physics. Springer Berlin Heidelberg, pp. 323–360.
Jean, D., Duty, C., Fuhrman, B., Lackey, W.J., 1999. Precision LCVD system design with real time process control, in: Tenth Annual Solid Freeform Fabrication Symp. pp. 59–65.
Johansson, S., Schweitz, J.-Å., Westberg, H., Boman, M., 1992. Microfabrication of three-dimensional boron structures by laser chemical processing. J. Appl. Phys. 72, 5956–5963. https://doi.org/10.1063/1.351904
Jones, C.R., Houle, F.A., Kovac, C.A., Baum, T.H., 1985. Photochemical generation and deposition of copper from a gas phase precursor. Appl. Phys. Lett. 46, 97–99. https://doi.org/10.1063/1.95811
Kahng, Y.H., Lee, S., Park, W., Jo, G., Choe, M., Lee, J.-H., Yu, H., Lee, T., Lee, K., 2012. Thermal stability of multilayer graphene films synthesized by chemical vapor deposition and stained by metallic impurities. Nanotechnology 23, 075702. https://doi.org/10.1088/0957-4484/23/7/075702
Keller, C., Ferrari, M., 1994. Milli-scale polysilicon structures HEXSIL. Presented at the Technical Digest: 1994 Solid State Sensor and Actuator Workshop, Hilton Head Island.
Kerse, C., Kalaycıoğlu, H., Elahi, P., Çetin, B., Kesim, D.K., Akçaalan, Ö., Yavaş, S., Aşık, M.D., Öktem, B., Hoogland, H., Holzwarth, R., Ilday, F.Ö., 2016. Ablation-cooled material removal with ultrafast bursts of pulses. Nature 537, 84–88. https://doi.org/10.1038/nature18619
Kim, K., Regan, W., Geng, B., Alemán, B., Kessler, B.M., Wang, F., Crommie, M.F., Zettl, A., 2010. High-temperature stability of suspended single-layer graphene. Phys. Status Solidi RRL – Rapid Res. Lett. 4, 302–304. https://doi.org/10.1002/pssr.201000244
Kim, Y.D., Kim, H., Cho, Y., Ryoo, J.H., Park, C.-H., Kim, P., Kim, Y.S., Lee, S., Li, Y., Park, S.-N., Shim Yoo, Y., Yoon, D., Dorgan, V.E., Pop, E., Heinz, T.F., Hone, J., Chun, S.-H., Cheong,

H., Lee, S.W., Bae, M.-H., Park, Y.D., 2015. Bright visible light emission from graphene. Nat. Nanotechnol. 10, 676–681. https://doi.org/10.1038/nnano.2015.118
Klumpp, A., Wieland, R., Ecke, R., Schulz, S.E., 2012. Metalization by Chemical Vapour Deposition of W and Cu, in: Handbook of 3D Integration. Wiley-VCH Verlag GmbH & Co. KGaA, Weinheim, Germany.
Kodas, T.T., Baum, T.H., Comita, P.B., 1987. Kinetics of laser-induced chemical vapor deposition of gold. J. Appl. Phys. 62, 281–286. https://doi.org/10.1063/1.339141
Kreyszig, E., 2010. Advanced Engineering Mathematics, 10th Edition, 10th ed. John Wiley & Sons.
Kun Li, Sparkes, M., O'Neill, W., 2014. Comparison Between Single Shot Micromachining of Silicon With Nanosecond Pulse Shaped IR Fiber Laser and DPSS UV Laser. IEEE J. Sel. Top. Quantum Electron. 20, 29–35. https://doi.org/10.1109/JSTQE.2013.2295352
Lackey, W.J., Rosen, D., Duty, C., Jean, D., Bondi, S., Elkhatib, T., Johnson, R., Jiang, M., Mi, J., Gillespie, J., Harvey, R., 2002. Laser CVD System Design, Operation, and Modeling, in: Lin, H.-T., Singh, M. (Eds.), 26th Annual Conference on Composites, Advanced Ceramics, Materials, and Structures: B: Ceramic Engineering and Science Proceedings. John Wiley & Sons, Inc., pp. 23–33.
Lai, K.K., Lamb, H.H., 2000. Tungsten chemical vapor deposition using tungsten hexacarbonyl: microstructure of as-deposited and annealed films. Thin Solid Films 370, 114–121. https://doi.org/10.1016/S0040-6090(00)00943-3
Langfischer, H., Basnar, B., Hutter, H., Bertagnolli, E., 2002. Evolution of tungsten film deposition induced by focused ion beam. J. Vac. Sci. Technol. A 20, 1408–1415. https://doi.org/10.1116/1.1486230
Larson, C.E., Baum, T.H., Jackson, R.L., 1987. Chemical Vapor Deposition of Gold. J. Electrochem. Soc. 134, 266–266. https://doi.org/10.1149/1.2100427
Le Harzic, R., Dörr, D., Sauer, D., Stracke, F., Zimmermann, H., 2011. Generation of high spatial frequency ripples on silicon under ultrashort laser pulses irradiation. Appl. Phys. Lett. 98, 211905. https://doi.org/10.1063/1.3593493
Leach, R., 2011. Optical measurement of surface topography. Springer.
Lehmann, O., Stuke, M., 1994. Three-dimensional laser direct writing of electrically conducting and isolating microstructures. Mater. Lett. 21, 131–136. https://doi.org/10.1016/0167-577X(94)90206-2
Lehmann, O., Stuke, M., 1991. Generation of three-dimensional free-standing metal micro-objects by Laser Chemical processing. Appl. Phys. A 53, 343–345. https://doi.org/10.1007/BF00357199
Li, W., Hacker, C.A., Cheng, G., Liang, Y., Tian, B., Hight Walker, A.R., Richter, C.A., Gundlach, D.J., Liang, X., Peng, L., 2014. Highly reproducible and reliable metal/graphene contact by ultraviolet-ozone treatment. J. Appl. Phys. 115, 114304. https://doi.org/10.1063/1.4868897
Lo, W.-C., Chang, S.M., 2012. Laser Ablation, in: Handbook of 3D Integration. Wiley-VCH Verlag GmbH & Co. KGaA, Weinheim, Germany.
Longtin, R., Carignan, L.-P., Fauteux, C., Therriault, D., Pegna, J., 2007. Selective area synthesis of aligned carbon nanofibers by laser-assisted catalytic chemical vapor deposition. Diam. Relat. Mater. 16, 1541–1549. https://doi.org/10.1016/j.diamond.2006.12.055
Lucchese, M.M., Stavale, F., Ferreira, E.H.M., Vilani, C., Moutinho, M.V.O., Capaz, R.B., Achete, C.A., Jorio, A., 2010. Quantifying ion-induced defects and Raman relaxation length in graphene. Carbon 48, 1592–1597. https://doi.org/10.1016/j.carbon.2009.12.057
Luo, B., Gladfelter, W.L., 2008a. Chapter 7. Chemical Vapor Deposition of Metals: W, Al, Cu and Ru, in: Jones, A.C., Hitchman, M.L. (Eds.), Chemical Vapour Deposition. Royal Society of Chemistry, Cambridge, pp. 320–356.
Luo, B., Gladfelter, W.L., 2008b. Chapter 7. Chemical Vapor Deposition of Metals: W, Al, Cu and Ru, in: Jones, A.C., Hitchman, M.L. (Eds.), Chemical Vapour Deposition. Royal Society of Chemistry, Cambridge, pp. 320–356.
Luoh, T., Su, C.-T., Yang, T.-H., Chen, K.-C., Lu, C.-Y., 2008. Advanced tungsten plug process for beyond nanometer technology. Microelectron. Eng. 85, 1739–1747. https://doi.org/10.1016/j.mee.2008.04.030
Mack, C., 2007. Introduction to Semiconductor Lithography, in: Fundamental Principles of Optical Lithography. John Wiley & Sons, Ltd, pp. 1–28.
Madou, M.J., 2011. Manufacturing Techniques for Microfabrication and Nanotechnology. CRC Press.

Mak, K.F., Sfeir, M.Y., Wu, Y., Lui, C.H., Misewich, J.A., Heinz, T.F., 2008. Measurement of the Optical Conductivity of Graphene. Phys. Rev. Lett. 101, 196405. https://doi.org/10.1103/PhysRevLett.101.196405
Malinauskas, M., Žukauskas, A., Hasegawa, S., Hayasaki, Y., Mizeikis, V., Buividas, R., Juodkazis, S., 2016. Ultrafast laser processing of materials: from science to industry. Light Sci. Appl. 5, e16133. https://doi.org/10.1038/lsa.2016.133
Manzeli, S., Ovchinnikov, D., Pasquier, D., Yazyev, O.V., Kis, A., 2017. 2D transition metal dichalcogenides. Nat. Rev. Mater. 2, natrevmats201733. https://doi.org/10.1038/natrevmats.2017.33
Martin, G.D., Hutchings, I.M., 2012. Fundamentals of Inkjet Technology, in: Hutchings, I.M., D.rtin, G. (Eds.), Inkjet Technology for Digital Fabrication. John Wiley & Sons, Ltd, pp. 21–44.
Maruo, S., Nakamura, O., Kawata, S., 1997. Three-dimensional microfabrication with two-photon-absorbed photopolymerization. Opt. Lett. 22, 132–134.
Maxwell, J., Larsson, K., Boman, M., Hooge, P., Williams, K., Coane, P., 1998. Rapid prototyping of functional three-dimensional microsolenoids and electromagnets by high-pressure laser chemical vapor deposition, in: Solid Freeform Fabrication Symposium Proceedings. pp. 529–536.
Maxwell, J.L., 2010. Method of fabrication of fibers, textiles and composite materials. US20100055352 A1.
Maxwell, J.L., Boman, M., Williams, K., Larsson, K., Jaikumar, N., Saiprasanna, G., 1999. High-speed laser chemical vapor deposition of amorphous carbon fibers, stacked conductive coils, and folded helical springs. pp. 227–235. https://doi.org/10.1117/12.361225
Mazumder, J., Kar, A., 1995. Theory and Application of Laser Chemical Vapor Deposition, Lasers, Photonics, and Electro-Optics. Springer US, New York. https://doi.org/10.1007/978-1-4899-1430-9_1
Mi, J., Lackey, W.J., 2009. SiC line deposition using laser CVD. J. Mater. Process. Technol. 209, 3818–3829. https://doi.org/10.1016/j.jmatprotec.2008.08.041
Michaelson, H.B., 1977. The work function of the elements and its periodicity. J. Appl. Phys. 48, 4729–4733. https://doi.org/10.1063/1.323539
Mizeikis, V., 2014. Realization of Structural Color by Direct Laser Write Technique in Photoresis. J. Laser MicroNanoengineering 9, 42–45. https://doi.org/10.2961/jlmn.2014.01.0009
Moilanen, H., Leppävuori, S., Uusimäki, A., 1994. Laser-induced chemical vapour deposition in piezoresistive pressure sensor fabrication. Sens. Actuators Phys., Proceedings of eurosensors VII 41, 150–155. https://doi.org/10.1016/0924-4247(94)80104-5
Morishige, Y., Kishida, S., 1994. Thick gold-film deposition by high-repetition visible pulsed-laser chemical vapor deposition. Appl. Phys. A 59, 395–399. https://doi.org/10.1007/BF00331718
Morita, T., Kometani, R., Watanabe, K., Kanda, K., Haruyama, Y., Hoshino, T., Kondo, K., Kaito, T., Ichihashi, T., Fujita, J., Ishida, M., Ochiai, Y., Tajima, T., Matsui, S., 2003. Free-space-wiring fabrication in nano-space by focused-ion-beam chemical vapor deposition. J. Vac. Sci. Technol. B 21, 2737–2741. https://doi.org/10.1116/1.1630329
Nair, R.R., Blake, P., Grigorenko, A.N., Novoselov, K.S., Booth, T.J., Stauber, T., Peres, N.M.R., Geim, A.K., 2008. Fine Structure Constant Defines Visual Transparency of Graphene. Science 320, 1308–1308. https://doi.org/10.1126/science.1156965
Nakajima, H., Kudo, T., Mizuno, N., 1999. Reaction of Metal, Carbide, and Nitride of Tungsten with Hydrogen Peroxide Characterized by 183W Nuclear Magnetic Resonance and Raman Spectroscopy. Chem. Mater. 11, 691–697. https://doi.org/10.1021/cm980544o
Nambu, Y., Morishige, Y., Kishida, S., 1990. High-speed laser direct writing of tungsten conductors from W(CO)6. Appl. Phys. Lett. 56, 2581–2583. https://doi.org/10.1063/1.102848
Nan, H.Y., Ni, Z.H., Wang, J., Zafar, Z., Shi, Z.X., Wang, Y.Y., 2013. The thermal stability of graphene in air investigated by Raman spectroscopy. J. Raman Spectrosc. 44, 1018–1021. https://doi.org/10.1002/jrs.4312
Novoselov, K.S., Geim, A.K., Morozov, S.V., Jiang, D., Zhang, Y., Dubonos, S.V., Grigorieva, I.V., Firsov, A.A., 2004. Electric Field Effect in Atomically Thin Carbon Films. Science 306, 666–669. https://doi.org/10.1126/science.1102896
Okamuro, K., Hashida, M., Miyasaka, Y., Ikuta, Y., Tokita, S., Sakabe, S., 2010. Laser fluence dependence of periodic grating structures formed on metal surfaces under femtosecond laser pulse irradiation. Phys. Rev. B 82, 165417. https://doi.org/10.1103/PhysRevB.82.165417

Öktem, B., Pavlov, I., Ilday, S., Kalaycıoğlu, H., Rybak, A., Yavaş, S., Erdoğan, M., Ilday, F.Ö., 2013. Nonlinear laser lithography for indefinitely large-area nanostructuring with femtosecond pulses. Nat. Photonics 7, 897–901. https://doi.org/10.1038/nphoton.2013.272
Olander, J., Ottosson, L.M., Heszler, P., Carlsson, J.-O., Larsson, K.M.E., 2005. Laser-Assisted Atomic Layer Deposition of Boron Nitride Thin Films. Chem. Vap. Depos. 11, 330–337. https://doi.org/10.1002/cvde.200506365
O'Neill, W., Li, K., 2009. High-Quality Micromachining of Silicon at 1064 nm Using a High-Brightness MOPA-Based 20-W Yb Fiber Laser. IEEE J. Sel. Top. Quantum Electron. 15, 462–470. https://doi.org/10.1109/JSTQE.2009.2012269
Osgood, R.M., Ehrlich, D.J., 1982. Optically induced microstructures in laser-photodeposited metal films. Opt. Lett. 7, 385–387. https://doi.org/10.1364/OL.7.000385
Park, J., Hann, S., Lu, Y., 2014. Synthesis of graphene pattern using laser-induced chemical vapor deposition, in: SPIE LASE. International Society for Optics and Photonics, pp. 896813-896813–5. https://doi.org/10.1117/12.2038059
Park, J.B., Xiong, W., Gao, Y., Qian, M., Xie, Z.Q., Mitchell, M., Zhou, Y.S., Han, G.H., Jiang, L., Lu, Y.F., 2011. Fast growth of graphene patterns by laser direct writing. Appl. Phys. Lett. 98, 123109. https://doi.org/10.1063/1.3569720
Paschotta, R., 2017. Wall-plug efficiency [WWW Document]. Encycl. Laser Phys. Technol. URL https://www.rp-photonics.com/wall_plug_efficiency.html (accessed 1.18.18).
Pavlov, I.A., Rybak, A.S., Dobrovolskiy, A.M., Kadan, V.M., Blonskiy, I.V., Kazantseva, Z.I., Gvozdovskyy, I.A., 2018. High-quality alignment of nematic liquid crystals using periodic nanostructures created by nonlinear laser lithography. J. Mol. Liq. https://doi.org/10.1016/j.molliq.2018.02.058
Peng, S., Jin, Z., Ma, P., Zhang, D., Shi, J., Niu, J., Wang, X., Wang, S., Li, M., Liu, X., Ye, T., Zhang, Y., Chen, Z., Yu, G., 2015. The sheet resistance of graphene under contact and its effect on the derived specific contact resistivity. Carbon 82, 500–505. https://doi.org/10.1016/j.carbon.2014.11.001
Petzing, J., Coupland, J., Leach, R., 2010. Measurement Good Practice Guide No. 116: The Measurement of Rough Surface Topography using Coherence Scanning Interferometry 131.
Politou, M., Asselberghs, I., Radu, I., Conard, T., Richard, O., Lee, C.S., Martens, K., Sayan, S., Huyghebaert, C., Tokei, Z., Gendt, S.D., Heyns, M., 2015. Transition metal contacts to graphene. Appl. Phys. Lett. 107, 153104. https://doi.org/10.1063/1.4933192
Polo, J. a., Lakhtakia, A., 2011. Surface electromagnetic waves: A review. Laser Photonics Rev. 5, 234–246. https://doi.org/10.1002/lpor.200900050
Potter, E.D., Herek, J.L., Pedersen, S., Liu, Q., Zewail, A.H., 1992. Femtosecond laser control of a chemical reaction. Nature 355, 66–68. https://doi.org/10.1038/355066a0
Randolph, S.J., Fowlkes, J.D., Rack, P.D., 2006. Focused, Nanoscale Electron-Beam-Induced Deposition and Etching. Crit. Rev. Solid State Mater. Sci. 31, 55–89. https://doi.org/10.1080/10408430600930438
Reddy, D., Register, L.F., Carpenter, G.D., Banerjee, S.K., 2011. Graphene field-effect transistors. J. Phys. Appl. Phys. 44, 313001. https://doi.org/10.1088/0022-3727/44/31/313001
Rekštytė, S., Malinauskas, M., Juodkazis, S., 2013. Three-dimensional laser micro-sculpturing of silicone: towards bio-compatible scaffolds. Opt. Express 21, 17028–17041. https://doi.org/10.1364/OE.21.017028
Rethfeld, B., Ivanov, D.S., Garcia, M.E., Anisimov, S.I., 2017. Modelling ultrafast laser ablation. J. Phys. Appl. Phys. 50, 193001. https://doi.org/10.1088/1361-6463/50/19/193001
Ritzdorf, T., Beica, R., Sharbono, C., 2012. Copper Plating, in: Handbook of 3D Integration. Wiley-VCH Verlag GmbH & Co. KGaA, Weinheim, Germany.
Rizvi, N.H., 2003. Femtosecond laser micromachining: Current status and applications. RIKEN Rev. 50, 107–112.
Roberts, N.A., Gonzalez, C.M., Fowlkes, J.D., Rack, P.D., 2013. Enhanced by-product desorption via laser assisted electron beam induced deposition of W(CO)6 with improved conductivity and resolution. Nanotechnology 24, 415301. https://doi.org/10.1088/0957-4484/24/41/415301
Roland Berger Strategy Consultants, 2013. Additive Manufacturing: A game changer for the manufacturing industry?
Roozeboom, F., Blauw, M.A., Lamy, Y., van Grunsven, E., Dekkers, W., Verhoeven, J.F., van den Heuvel, E.F., van der Drift, E., Kessels, E.W.M.M., van de Sanden, R.M.C.M., 2012. Deep

Reactive Ion Etching of Through Silicon Vias, in: Handbook of 3D Integration. Wiley-VCH Verlag GmbH & Co. KGaA, Weinheim, Germany.
Rothenbach, C.A., Gupta, M.C., 2012. High resolution, low cost laser lithography using a Blu-ray optical head assembly. Opt. Lasers Eng. 50, 900–904. https://doi.org/10.1016/j.optlaseng.2011.12.004
Rothschild, M., Bloomstein, T.M., Fedynyshyn, T.H., Kunz, R.R., Liberman, V., Switkes, M., Efremow, N.N., Palmacci, S.T., Sedlacek, J.H., Hardy, D.E., others, 2003. Recent trends in optical lithography. Linc. Lab. J. 14, 221–236.
Schroder, D.K., 2006. Semiconductor Material and Device Characterization, 3rd ed. Wiley-IEEE Press.
Shang, H., White, M.H., Guarini, K.W., Solomon, P., Cartier, E., McFeely, F.R., Yurkas, J.J., Lee, W.-C., 2001. Interface studies of tungsten gate metal–oxide–silicon capacitors. Appl. Phys. Lett. 78, 3139–3141. https://doi.org/10.1063/1.1372340
Simmonds, M.G., Gladfelter, W.L., 1994. Chemical Vapor Deposition of Aluminum, in: Kodas, T.T., Hampden-Smith, rk J. (Eds.), The Chemistry of Metal CVD. Wiley-VCH Verlag GmbH, pp. 45–103.
Singmaster, K.A., Houle, F.A., Wilson, R.J., 1990. Photochemical deposition of thin films from the metal hexacarbonyls. J. Phys. Chem. 94, 6864–6875. https://doi.org/10.1021/j100380a060
Smith, D., 1995. Thin-Film Deposition: Principles and Practice. McGraw Hill Professional, New York.
Song, S.M., Park, J.K., Sul, O.J., Cho, B.J., 2012. Determination of Work Function of Graphene under a Metal Electrode and Its Role in Contact Resistance. Nano Lett. 12, 3887–3892. https://doi.org/10.1021/nl300266p
Steen, W.M., Mazumder, J., 2010. Laser Material Processing. Springer London, London.
Tan, B., Panchatsharam, S., Venkatakrishnan, K., 2009. High repetition rate femtosecond laser forming sub-10 μm diameter interconnection vias. J. Phys. Appl. Phys. 42, 065102. https://doi.org/10.1088/0022-3727/42/6/065102
Tang, M., Zhang, H., Her, T.-H., 2007. Self-assembly of tunable and highly uniform tungsten nanogratings induced by a femtosecond laser with nanojoule energy. Nanotechnology 18, 485304. https://doi.org/10.1088/0957-4484/18/48/485304
Tao, L., Lee, J., Holt, M., Chou, H., McDonnell, S.J., Ferrer, D.A., Babenco, M.G., Wallace, R.M., Banerjee, S.K., Ruoff, R.S., Akinwande, D., 2012. Uniform Wafer-Scale Chemical Vapor Deposition of Graphene on Evaporated Cu (111) Film with Quality Comparable to Exfoliated Monolayer. J. Phys. Chem. C 116, 24068–24074. https://doi.org/10.1021/jp3068848
Temiz, Y., Lovchik, R.D., Kaigala, G.V., Delamarche, E., 2015. Lab-on-a-chip devices: How to close and plug the lab? Microelectron. Eng., Micro and Nanofabrication Breakthroughs for Electronics, MEMS and Life Sciences 132, 156–175. https://doi.org/10.1016/j.mee.2014.10.013
Temple, D., Reisman, A., 1989. Chemical Vapor Deposition of Copper from Copper (II) Hexafluoroacetylacetonate. J. Electrochem. Soc. 136, 3525–3529. https://doi.org/10.1149/1.2096498
Thiyagarajan, M., Thompson, S., 2012. Optical breakdown threshold investigation of 1064 nm laser induced air plasmas. J. Appl. Phys. 111, 073302. https://doi.org/10.1063/1.3699368
Toda, K., Furue, R., Hayami, S., 2015. Recent progress in applications of graphene oxide for gas sensing: A review. Anal. Chim. Acta 878, 43–53. https://doi.org/10.1016/j.aca.2015.02.002
Toenshoff, H.K., Ostendorf, A., Nolte, S., Korte, F., Bauer, T., 2000. Micromachining using femtosecond lasers. Presented at the First International Symposium on Laser Precision Microfabrication, International Society for Optics and Photonics, pp. 136–140. https://doi.org/10.1117/12.405700
Tung, R.T.(董梓則), 2014. The physics and chemistry of the Schottky barrier height. Appl. Phys. Rev. 1, 011304. https://doi.org/10.1063/1.4858400
Van Veldhoven, Z.A., Alexander-Webber, J.A., Sagade, A.A., Braeuninger-Weimer, P., Hofmann, S., 2016. Electronic properties of CVD graphene: The role of grain boundaries, atmospheric doping, and encapsulation by ALD. Phys. Status Solidi B 253, 2321–2325. https://doi.org/10.1002/pssb.201600255

Veldhorst, M., Yang, C.H., Hwang, J.C.C., Huang, W., Dehollain, J.P., Muhonen, J.T., Simmons, S., Laucht, A., Hudson, F.E., Itoh, K.M., Morello, A., Dzurak, A.S., 2015. A two-qubit logic gate in silicon. Nature 526, 410–414. https://doi.org/10.1038/nature15263

Venkataraman, B., Hou, H., Zhang, Z., Chen, S., Bandukwalla, G., Vernon, M., 1990. A molecular beam study of the one, two, and three photon photodissociation mechanism of the group VIB (Cr,Mo,W) hexacarbonyls at 248 nm. J. Chem. Phys. 92, 5338–5362. https://doi.org/10.1063/1.458513

Visser, C.W., Pohl, R., Sun, C., Römer, G.-W., Veld, B.H. in 't, Lohse, D., 2015. Toward 3D Printing of Pure Metals by Laser-Induced Forward Transfer. Adv. Mater. 27, 4087–4092. https://doi.org/10.1002/adma.201501058

Wallace, D.B., 2013. Manufacturing of micro-electro-mechanical systems (MEMS), in: Inkjet Technology for Digital Fabrication. John Wiley & Sons, p. 141.

Wallenberger, F.T., Nordine, P.C., Boman, M., 1994. Inorganic fibers and microstructures directly from the vapor phase. Compos. Sci. Technol., Special Issue Advances in Inorganic Fibre Technology 51, 193–212. https://doi.org/10.1016/0266-3538(94)90190-2

Wang, S., Mao, D., Jin, Z., Peng, S., Zhang, D., Shi, J., Wang, X., 2015. A more reliable measurement method for metal/graphene contact resistance. Nanotechnology 26, 405706. https://doi.org/10.1088/0957-4484/26/40/405706

Watanabe, E., Conwill, A., Tsuya, D., Koide, Y., 2012. Low contact resistance metals for graphene based devices. Diam. Relat. Mater. 24, 171–174. https://doi.org/10.1016/j.diamond.2012.01.019

Westberg, H., Boman, M., Johansson, S., Schweitz, J.-Å., 1993. Free-standing silicon microstructures fabricated by laser chemical processing. J. Appl. Phys. 73, 7864–7871. https://doi.org/10.1063/1.353937

Wheatley, P.O., Gerald, C.F., 2004. Applied numerical analysis, 7th ed. Pearson Addison-Wesley, Boston.

Wieland, R., 2012. SiO2, in: Handbook of 3D Integration. Wiley-VCH Verlag GmbH & Co. KGaA, Weinheim, Germany.

Williams, K., Maxwell, J., Larsson, K., Boman, M., 1999. Freeform fabrication of functional microsolenoids, electromagnets and helical springs using high-pressure laser chemical vapor deposition, in: Twelfth IEEE International Conference on Micro Electro Mechanical Systems, 1999. MEMS '99. Presented at the Twelfth IEEE International Conference on Micro Electro Mechanical Systems, 1999. MEMS '99, pp. 232–237. https://doi.org/10.1109/MEMSYS.1999.746821

Willis, D.A., 2018. Laser-Induced Forward Transfer of Metals, in: Laser Printing of Functional Materials. Wiley-VCH Verlag GmbH & Co. KGaA, Weinheim, Germany, pp. 149–174. https://doi.org/10.1002/9783527805105.ch7

Wilson, R.J., Houle, F.A., 1985. Composition, Structure, and Electric Field Variations in Photodeposition. Phys. Rev. Lett. 55, 2184–2187. https://doi.org/10.1103/PhysRevLett.55.2184

Windhorn, L., Witte, T., Yeston, J.S., Proch, D., Motzkus, M., Kompa, K.L., Fuß, W., 2002. Molecular dissociation by mid-IR femtosecond pulses. Chem. Phys. Lett. 357, 85–90. https://doi.org/10.1016/S0009-2614(02)00444-X

Winer, P., Livengood, R.H., 2000. Method and apparatus for editing an integrated circuit. US6159753 A.

Wrighton, M., 1974. Photochemistry of metal carbonyls. Chem. Rev. 74, 401–430. https://doi.org/10.1021/cr60290a001

Xing, W., Lalwani, G., Rusakova, I., Sitharaman, B., 2014. Degradation of Graphene by Hydrogen Peroxide. Part. Part. Syst. Charact. 31, 745–750. https://doi.org/10.1002/ppsc.201300318

Yan, Y., Xia, B., Qi, X., Wang, H., Xu, R., Wang, J.-Y., Zhang, H., Wang, X., 2013. Nano-tungsten carbide decorated graphene as co-catalysts for enhanced hydrogen evolution on molybdenum disulfide. Chem. Commun. 49, 4884–4886. https://doi.org/10.1039/C3CC41031E

Yang, M., Zhang, X., Grosjean, A., Soroka, I., Jonsson, M., 2015. Kinetics and Mechanism of the Reaction between H2O2 and Tungsten Powder in Water. J. Phys. Chem. C 119, 22560–22569. https://doi.org/10.1021/acs.jpcc.5b07012

Yao, N. (Ed.), 2007a. Chapter 3 - Gas assisted ion beam etching and deposition, in: Focused Ion Beam Systems: Basics and Applications. Cambridge University Press, Cambridge.

Yao, N. (Ed.), 2007b. Chapter 1 - Introduction to the focused ion beam system, in: Focused Ion Beam Systems: Basics and Applications. Cambridge University Press, Cambridge.
Yeo, J., Hong, S., Wanit, M., Kang, H.W., Lee, D., Grigoropoulos, C.P., Sung, H.J., Ko, S.H., 2013. Rapid, One-Step, Digital Selective Growth of ZnO Nanowires on 3D Structures Using Laser Induced Hydrothermal Growth. Adv. Funct. Mater. 23, 3316–3323. https://doi.org/10.1002/adfm.201203863
Zewail, A.H., 2000. Femtochemistry: Atomic-Scale Dynamics of the Chemical Bond. J. Phys. Chem. A 104, 5660–5694. https://doi.org/10.1021/jp001460h
Zhang, G.Q., Szörényi, T., Bäuerle, D., 1987. Kr+ laser-induced chemical vapor deposition of W. J. Appl. Phys. 62, 673–675. https://doi.org/10.1063/1.339767
Zhang, H., Tang, M., McCoy, J., Her, T.-H., 2007. Deposition of tungsten nanogratings induced by a single femtosecond laser beam. Opt. Express 15, 5937–5947. https://doi.org/10.1364/OE.15.005937
Zhou, R., Zhou, X., Li, X., Cai, Y., Liu, F., 2016. Study of the Microfocus X-Ray Tube Based on a Point-Like Target Used for Micro-Computed Tomography. PLOS ONE 11, e0156224. https://doi.org/10.1371/journal.pone.0156224
Zinn, A.A., Brandt, L., Kaesz, H.D., Hicks, R.F., 1994a. Chemical Vapor Deposition of Platinum, Palladium and Nickel, in: Kodas, T.T., Hampden-Smith, rk J. (Eds.), The Chemistry of Metal CVD. Wiley-VCH Verlag GmbH, pp. 329–355.
Zinn, A.A., Brandt, L., Kaesz, H.D., Hicks, R.F., 1994b. Chemical Vapor Deposition of Platinum, Palladium and Nickel, in: Kodas, T.T., Hampden-Smith, rk J. (Eds.), The Chemistry of Metal CVD. Wiley-VCH Verlag GmbH, pp. 329–355.